WILEY

WIND LOADS ON STRUCTURES

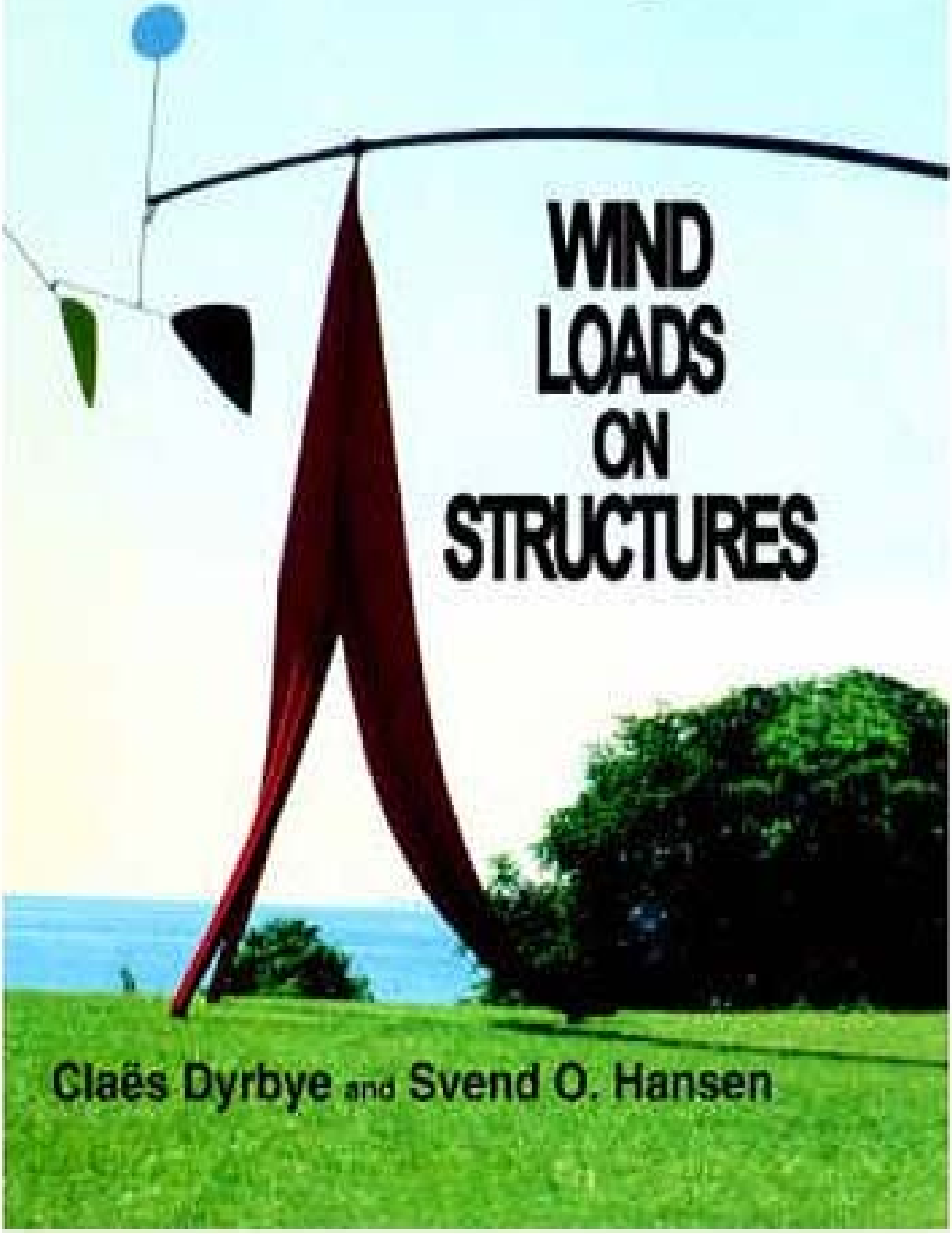

Claës Dyrbye and Svend O. Hansen

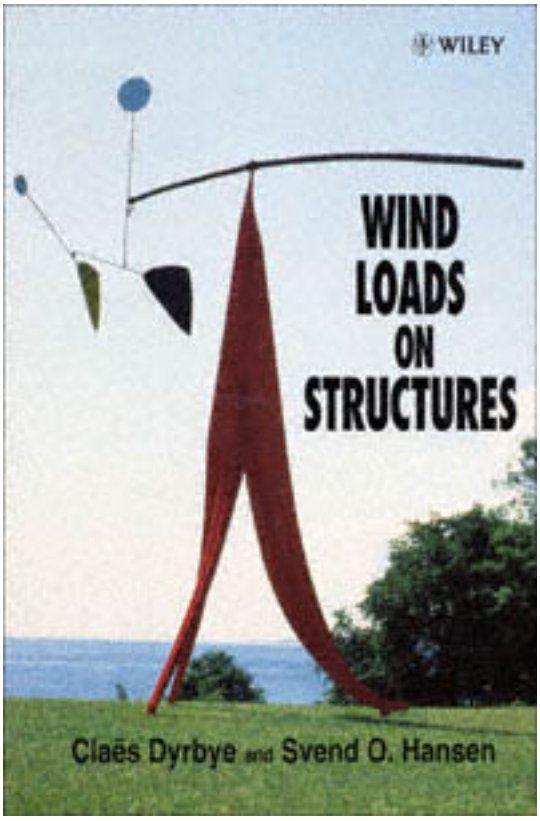

Start of Citation[PU]John Wiley & Sons, Ltd. (UK)[/PU][DP]1997[/DP]End of Citation

---

title :
author :
publisher :
isbn10 | asin :
print isbn13 :
ebook isbn13 :
language :
subject
publication date :
lcc :
ddc :
subject :

Wind Loads on Structures

Claës Dyrbye

Department of Structural Engineering and Materials
Technical University of Denmark, Lyngby, Denmark

Svend Ole Hansen

Svend Ole Hansen, Consulting Engineers,
Copenhagen, Denmark

JOHN WILEY & SONS

Chichester • New York • Weinheim • Brisbane • Toronto • Singapore

Start of Citation[PU]John Wiley & Sons, Ltd. (UK)[/PU][DP]1997[/DP]End of Citation

Originally published in Danish as *Vindlast pa * bærende konstruktioner* © 1989 Statens Byggeforskningsinstitut

Reprinted with corrections June 1999

Other Wiley Editorial Offices

John Wiley & Sons, Inc., 605 Third Avenue,
New York, NY 10158-0012, USA

WILEY-VCH Verlag GmbH, Pappelallee 3,
D-69469 Weinheim, Germany

Jacaranda Wiley Ltd, 33 Park Road, Milton,
Queensland 4064, Australia

John Wiley & Sons (Asia) Pte Ltd, 2 Clementi Loop #02-01,
Jin Xing Distripark, Singapore 129809

John Wiley & Sons (Canada) Ltd, 22 Worcester Road,
Rexdale, Ontario M9W 1L1, Canada

Library of Congress Cataloguing-in-Publication Data

Dyrbye, Claës.
Wind loads on structures / Claës Dyrbye, Svend Ole Hansen.
p. cm.
Includes bibliographical references and index.
ISBN 0 471 95651 1 (alk. paper)
1. Wind-pressure. 2. Structural dynamics. I. Hansen, Svend Ole.
II. Title.
TA654.5.D97 1996
624.1 '75dc20 96-30346
CIP

British Library Cataloguing in Publication Data

A catalogue record for this book is available from the British Library

ISBN 0 471 95651 1

Typeset in 10/12pt Times from the authors' disk by Laser Words, Madras, India Printed and bound in Great Britain by Bookcraft (Bath) Ltd. This book is printed on acid-free paper responsibly manufactured from sustainable forestation, for which at least two trees are planted for each one used for paper production.

Start of Citation[PU]John Wiley & Sons, Ltd. (UK)[/PU][DP]1997[/DP]End of Citation

< previous page | page_iv | next page >

Preface

This book is intended as a guide for consulting engineers designing wind-exposed structures. It may also be useful for students at an advanced level.

The book started out as an English version of *Vindlast pa * bærende konstruktioner* by the same authors, published in Danish in 1989. However, during the preparation of the manuscript the differences between the Danish edition and the present book evolved considerably. We thank the Danish Building Research Institute for their positive attitude towards this English version.

The authors have received a great deal of help during the preparation of the manuscript. Valuable advice about presenting different aspects of the subject was provided by Professor Erik Hjorth-Hansen at the Norwegian University of Science and Technology in Trondheim, Mr. Brian W. Smith, senior partner at Flint & Neill Partnership, Consulting Civil and Structural Engineers in the United Kingdom and Lars T. Thorbek B.Sc. at Svend Ole Hansen, Consulting Engineers in Denmark. Time histories of wind velocities measured at selected sites were kindly made available by the Department of Meteorology and Wind Energy at Riso *National Laboratory in Denmark.

Mrs. Esther Martens prepared many of the drawings, Mrs. Inge Sorensen *typed a major part of the manuscript, and Ms. Helen Dyrbye eliminated more than a few linguistic errors. We express our thanks for their important assistance.

Start of Citation[PU]John Wiley & Sons, Ltd. (UK)[/PU][DP]1997[/DP]End of Citation

Contents

Start of Citation[PU]John Wiley & Sons, Ltd. (UK)[/PU][DP]1997[/DP]End of Citation

Start of Citation[PU]John Wiley & Sons, Ltd. (UK)[/PU][DP]1997[/DP]End of Citation

Start of Citation[PU]John Wiley & Sons, Ltd. (UK)[/PU][DP]1997[/DP]End of Citation

Start of Citation[PU]John Wiley & Sons, Ltd. (UK)[/PU][DP]1997[/DP]End of Citation

Symbols

a(t)	stochastic amplitude function
A	area
A	scale parameter
*A**	aerodynamic derivatives
b	length of horizontal structure or bridge-deck width
B	spectral bandwidth
cd	dynamic coefficient
ce	exposure coefficient
cf	force coefficient
cpe	external pressure coefficient
cpi	internal pressure coefficient
ctt	topography coefficient
C	shape factor
C	decay constant
Coh	coherence
$\tilde{C}_L$	standard deviation of the normalized lift force CL
d	width of structure
E{ }	expected value

f	non-dimensional frequency
fc	Coriolis parameter
F	wind load
Fr	Froude number
g	acceleration of gravity
g( )	effect influence function
h	height of structure
H( )	frequency response function
*H**	aerodynamic derivatives
I	mass moment of inertia
IR( )	response-influence function
Iu	turbulence intensity
J2b	non-dimensional response variance

Start of Citation[PU]John Wiley & Sons, Ltd. (UK)[/PU][DP]1997[/DP]End of Citation

Je	Jensen number
|J( )|2	joint acceptance function
k	structural stiffness
k	turbulence factor
k( )	co-influence function
kp	peak factor
kT	terrain factor
K	reduced frequency
Ks( )	size reduction function
l	length
L	integral length scale
m	mass
n	frequency in Hz
ne	natural frequency
ns	frequency of vortex shedding
p	pressure
p	probability of excedance
q	velocity pressure
Q( )	generalized fluctuating load
r	separation

R	response
Re	Reynolds number
RN	non-dimensional power spectral density function
s	non-dimensional distance
S( )	spectrum
Sc	Scruton number
St	Strouhal number
t	time
T	time interval
T	time scale
u	fluctuating wind velocity in the wind direction
*u**	friction velocity
U	10-minute mean wind velocity
*U*bas	reference wind velocity with return period of 50 years
Ur	reduced wind velocity
v	fluctuating wind velocity in the lateral direction
w	fluctuating wind velocity in the vertical direction
x	axis in wind direction
y	horizontal axis normal to the wind direction
z	vertical axis
z0	roughness length

Start of Citation[PU]John Wiley & Sons, Ltd. (UK)[/PU][DP]1997[/DP]End of Citation

< previous page | page_xii | next page >

α	exponent in power law profile
α	angle
$\alpha( )$	torsional mode shape
αdef	angular rotation of structure
γ	Euler's constant
γI	non-dimensional, normalized mass moment of inertia
γm	non-dimensional, normalized mass
$\gamma\omega$	frequency ratio
ξ	logarithmic decrement
ζ	damping ratio
θ	factor concerning response
κ	von Kármáns constant
λ	non-dimensional length parameter
μ	mean value
ν	frequency and kinematic viscosity of air
$\xi( )$	flexural mode shape
ξdef	deflection of structure
ρ	density of air
$\rho( )$	correlation function
σ	standard deviation

τ	time lag
φ	gust factor
ϕ	non-dimensional parameter
x2( )	aerodynamic admittance function
ψ	normalized co-spectrum
ω	angular frequency

Subscripts

a	aerodynamic
ALT	altitude
b	background
c	critical flutter
crit	critical vortex shedding
d	damping
d	design value
div	divergence
D	aerodynamic drag
DIR	direction
e	equivalent
geo	geostrophic
gr	gradient
L	aerodynamic lift

m	motion-induced
max	characteristic
min	minimum
M	aerodynamic moment
p	pressure

Start of Citation[PU]John Wiley & Sons, Ltd. (UK)[/PU][DP]1997[/DP]End of Citation

q	mean wind load pressure
r	resonance
red	reduced
ref	reference
R	response
s	structure
t	turbulence
tot	total
TEM	temporary (seasonal)
u	longitudinal turbulence component
v	vortex shedding or lateral turbulence component
w	vertical turbulence component
x	longitudinal
y	lateral
z	vertical
α	rotation
ξ	deflection

Start of Citation[PU]John Wiley & Sons, Ltd. (UK)[/PU][DP]1997[/DP]End of Citation

1 Introduction

Wind loads have a great deal of influence on building design and the design of other kinds of civil engineering structures. Many whole structures or parts of structures that fail, do so because inadequate thought was given to wind action at the design stage.

As this subject is very wide-ranging, we have had to limit our discussion of the subject. We therefore recommend that readers also consult other books which deal in much more detail with specific problems. Some chapters may seem rather lengthy, but this is either due to the difficult nature of the subject or because we hope the additional information will prove useful.

Wind and wind response

The concept of a wind-load chain was introduced by A.G. Davenport, see Figure 1.1. Each link is necessary when wind actions and the response to actions are to be calculated. The chain gives a picture of the particular task facing the designer. The concept of a chain symbolizes that the total design process is only as reliable as the least reliable of the links. Figure 1.1 also indicates some interactions between different phenomena in the chain.

Each link deals with random parameters, so statistically based methods are recommended. Appendix A gives an explanation of some of these statistical concepts, including stochastic processes.

Wind climate

This term covers the general wind conditions in different geographical regions, a subject dealt with briefly in Chapter 2. The term includes only variations in wind velocities

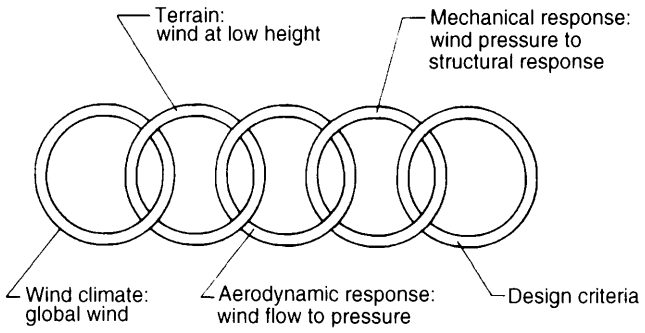

Fig. 1.1 *The wind-load chain. (Reproduced by permission of Danish Building Research Institute).*

averaged over a period of at least 10 min. The reference wind velocity is determined mainly by the wind climate.

Terrain conditions

The roughness of the terrain exerts a major influence on the wind. The mean wind velocity is reduced by the roughness of the ground, but at the same time the wind becomes turbulent and more difficult to describe. Mean wind velocity increases with the height above the ground.

Usually, the terrain can only be described in a very coarse way by introducing different categories. These are then identified by the so-called roughness length z_0. As the terrain surrounding the structure in question characterizes the roughness, possible changes, such as the erection or demolition of nearby buildings, which may take place during the lifetime of the structure, may affect wind loads.

Chapter 3 is about the influence of the terrain.

Wind loads

Structural geometry has an important influence on wind load. This influence is most easily measured by means of wind tunnel experiments, cf. Chapter 10. As reported values exist for a large variety of structures, many problems may be solved by referring to the literature, e.g. Cook, 1985. The determination of static wind load is discussed in Chapter 4.

Wind loads vary in space and time over the surface of structures. Dynamic analysis, i.e. taking the product of structural mass and acceleration (inertial forces) into account — is much more time consuming than static analysis. Therefore, an equivalent static calculation may be used if this can be justified. For vibrating structures, the wind load may also depend on structural motions. The aerodynamic response, i.e. the conversion from wind velocities to loads, may be greatly influenced by the motions of the structure, cf. Chapters 7 to 9.

Mechanical response

In wind engineering, the mechanical response means the structural response caused by wind load. Moderately stiff structures may vibrate in different ways when subjected to wind loading. E.g. along-wind vibrations called buffeting may occur in connection with the turbulence. This phenomenon is dealt with in Chapters 5 and 6.

Slender structures are especially susceptible to cross-wind vibrations caused by vortex shedding, and within certain ranges of wind velocities, the wind load perpendicular to the wind direction may be in resonance with the structure. Crosswind vibration is discussed in Chapter 7.

Cable-supported bridges and some other structures may vibrate when vertical and torsional movements are coupled. This phenomenon, called classical flutter, occurs only at high wind velocities. However, bridges where flutter is likely to occur must be studied in wind-tunnel experiments, as flutter can cause the structure to collapse completely. Wind-induced bridge vibrations are dealt with in Chapter 8. Of special interest is the section on suspension bridges under construction, as this appears not to have been published in any other textbook.

Design

Although design is as important as any of the other links in the wind-load chain, this subject does not come within the scope of this book.

Codes

The importance of wind action is recognized in the codes of practice, and in 1995, a preliminary Eurocode: Actions on structures–Wind actions, was published throughout Europe. This preliminary Eurocode is officially called European Prestandard ENV 1991-2-4, but for convenience it is referred to in this book by its popular title, Eurocode 1. According to plan, it will be replaced by a European Standard in late 1998.

Eurocode 1 pays a great deal of attention to wind action and is likely to form the basis for design against wind actions in Europe. However, in order to make reasonable use of the codes, we need to understand the reasoning behind the clauses and rules of application. One of the objectives of this book is to provide just such a background.

2 Wind Climate

Some knowledge of meteorology, in particular of the formation and duration of heavy storms, is needed for a realistic prediction of wind load on structures.

This chapter reviews the most important meteorological phenomena.

2.1 METEOROLOGICAL CLASSIFICATION

Atmospheric motion usually takes place in such a way that different patterns of motion are mutually independent both in time and in space. Figure 2.1 shows that the patterns of atmospheric motion range from turbulence, (vortices of air in the range of a few metres with a characteristic lifetime of some minutes), to local weather systems and large planetary waves, which may circumvent the entire globe and have a lifetime of several days. These phenomena are referred to as microscale, convective scale and macroscale respectively, as shown in Figure 2.1.

The autospectrum for wind velocity is a useful tool for illustrating micro- and macroscales. The autospectrum shows the variance of the wind as a function of the

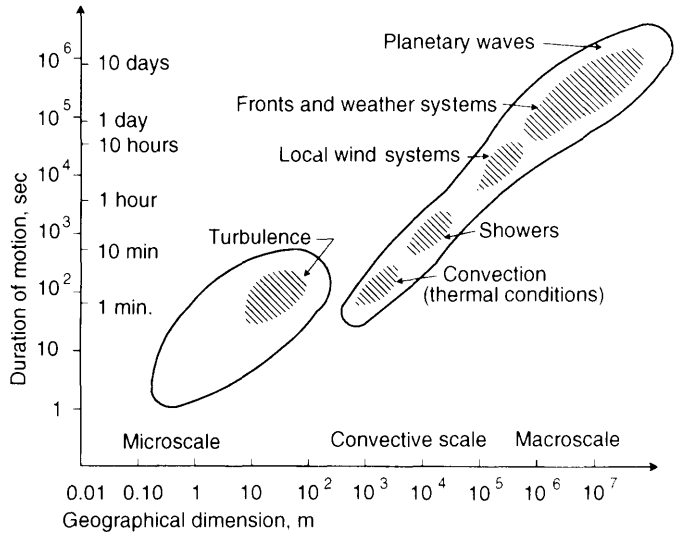

Fig. 2.1 *Orders of magnitude in space and time for different patterns of motion in the atmosphere. (After Fortak (1982). Reproduced by permission of Dietrich Reimer Verlag).*

different frequencies, see Appendix A.3. There appears to be a distinction between the high frequencies in the microscale and the low frequencies in the macroscale.

Figure 2.2 shows two different autospectra. The full curve is based upon measurements during one year on open terrain at Lammefjorden in Denmark, at 30 m height. The dotted curve shows the Van der Hoven spectrum, which is based on measurements at about 100 m height. The wind velocities were affected both by the wind climate (the first element of the wind-load chain) and by turbulence in the atmospheric boundary layer (the second element of the wind-load chain). Some important properties of the autospectra are observed:

- There is a great deal of variance in movements lasting approximately 4 days, the same lifetime as fully developed weather systems. In addition to this, the Lammefjorden spectrum has a clear peak at a period of 1 day. The Van der Hoven spectrum shows a peak at a period of $\frac{1}{2}$ day.

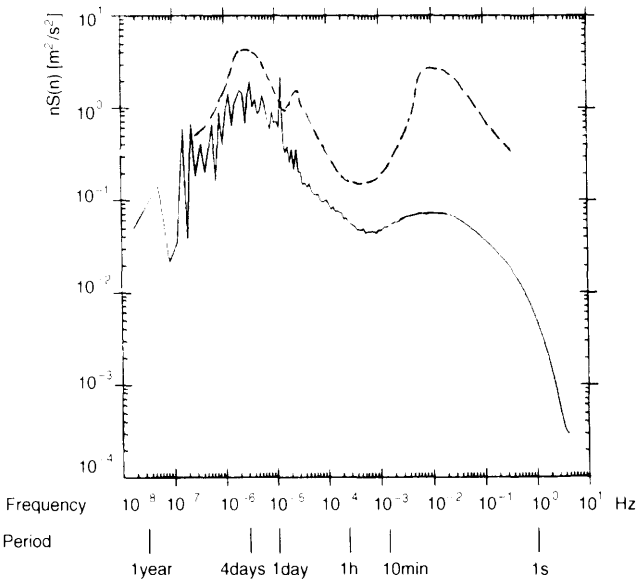

Fig. 2.2 *Autospectra for the wind velocity. The ordinate is the frequency n multiplied by the autospectrum S(n) for the horizontal wind velocity. The full curve corresponds to the autospectrum for wind measured at 30 m height at an open terrain (z_0 = approximately 0.05 m) at Lammefjord, Denmark, see Courtney and Troen (1990). The dotted line is a spectrum for wind velocities based on measurements at about 100 m height at Brookhaven, NY, USA, see van der Hoven (1957). The two spectra resemble each other for periods in the range between about 10 minutes and 1 year. The Lammefjord spectrum shows a distinct peak at a period of 1 day, and both spectra have high values at periods of 4 to 5 days. In a range from about 10 minutes to some hours, the van der Hoven spectrum takes rather low values, this phenomenon is referred to as the spectral gap. This tendency is not quite as obvious as from the Lammefjord spectrum. The rather high values of the van der Hoven spectrum at periods of about 1–2 minutes are probably due to turbulence and cannot be related to the wind climate.*

- In both spectra, the amount of variance in periods between approximately 10 minutes and about 5–10 hours is very low. This is referred to as a spectral gap.
- The van der Hoven spectrum takes rather high values corresponding to periods between some seconds and about 5 minutes. This must be due to turbulence. The Lammefjord spectrum has the same tendency, but much less pronounced.

Similar spectra from other locations show that the above-mentioned properties are typical in temperate zones.

The spectral gap means that the wind climate and the turbulence in the atmospheric boundary layer are mutually independent, so they may be treated separately and superimposed. Figure 2.3 shows how the turbulence in the boundary layer in a typical measurement of wind superimposes the variation from the wind climate.

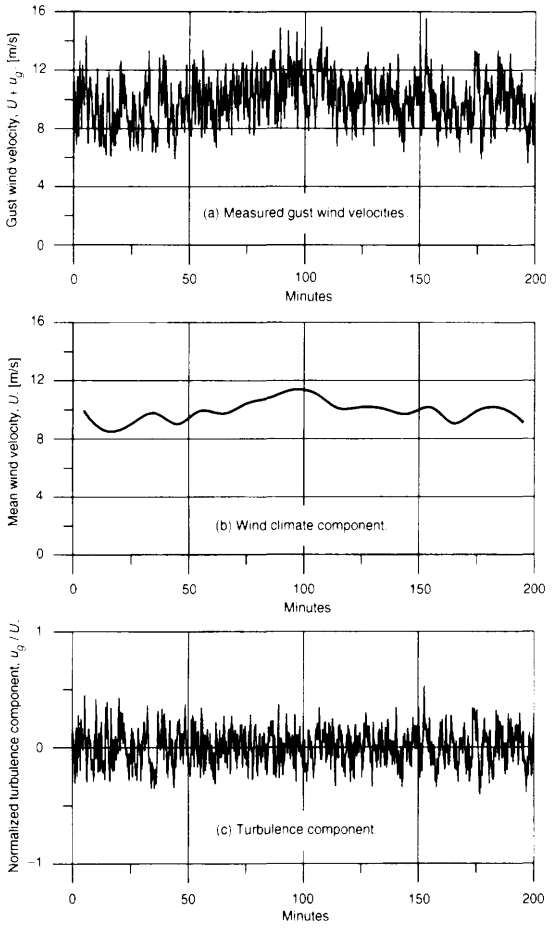

Fig. 2.3 *The gust wind velocity $U + u_g$ is separated into a wind climate component U and a turbulence component u_g. The wind climate component U is the 10 minute mean wind velocity and the turbulence component u_g is here calculated using an average time of 10 s, i.e. $u_g = u_m(T = 10\ s, t_1) - u_m(T = 600\ s, t_1)$ in equation (2.1.1). The measurements shown are the Lammefjord data also used in Figure 2.2. The wind velocities used in this figure were supplied by Risø National Laboratory, Denmark.*

As a consequence of the spectral gap, mean wind velocities based upon a period of 10 minutes, as assumed in Eurocode 1, or based upon 1 hour periods, as assumed in the Canadian code, will not show much difference. Extreme mean wind velocity estimates for open exposure based on 1-hour averaging periods are typically approximately 5% less than estimates based on 10-minute averaging periods. If the wind velocity at the time t at a certain point is called $u_a(t)$, then the mean value over a time interval T is defined as

$$u_m(T, t_1) = \frac{1}{T} \int_{t_1}^{t_1+T} u_a(t)\, dt \tag{2.1.1}$$

This mean value depends on the interval T and on the starting time t_1. If t_1 varies such that a storm event is covered, then the maximum value of u_m will decrease if the interval length T is increased, e.g. from 10 minutes to 1 hour. Furthermore, the variation of u_m with the time t_1 will decrease as T increases. The statistics of extreme wind velocities are treated in Section 3.4.

2.2 GLOBAL ATMOSPHERIC CIRCULATION

Wind arises as a result of pressure differences in the atmosphere. A kind of "feedback" effect occurs, because the wind itself then causes considerable changes in atmospheric pressure. For this reason, one phenomenon cannot be used to predict the other, so the distribution of pressure and flow must be understood as an entity.

For the Earth as a whole, there is equilibrium between the energy received from the Sun and the energy which is radiated from the Earth into space. There is a surplus of energy near the Equator and a deficiency near the poles. At the Equator, ground-level air is heated, it expands, rises and flows away, leaving low pressure. Similarly, at the poles, ground-level air cools and contracts, so at higher levels, air flows in and high pressure results, see Figure 2.4.

This chapter deals with conditions in the Northern Hemisphere. Notice that the large continents in the Northern Hemisphere cause important deviation from the simplified explanation of pressures and flow given above. Analogous, but far less complicated, conditions are found in the Southern Hemisphere. On the whole, the wind systems of the Northern and Southern Hemispheres can be generally seen as separate.

Trade winds

In the equatorial region, warm air flows upwards. At high altitudes it flows away from the Equator. Due to the rotation of the Earth, often explained by means of a fictitious force named the Coriolis force, the flow is diverted eastwards. As the friction is negligible in the higher layers of air, the deviation is complete at 30°–40° latitude, giving a westerly wind at high altitudes. The permanent subtropical high pressure in this region initiates a flow towards the Equator at ground level. This flow is bent westwards by the Coriolis force, and forms a trade wind, so the trade wind is an easterly wind, i.e. coming from the east.

Subtropical high-pressure zones

The subtropical high-pressure zone in the Northern Hemisphere at approximately 30° latitude occurs because the flow away from the Equator at high altitude cannot penetrate further north due to the Coriolis force.

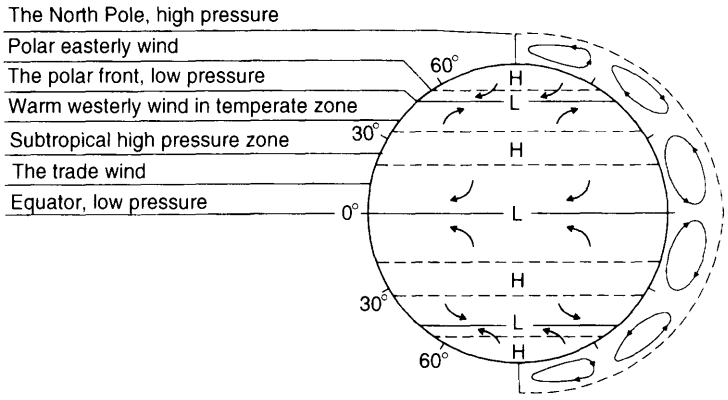

Fig. 2.4 *The general features in the global, atmospheric circulation (Jensen, 1985). The arrows shown inside the circle describe wind conditions close to the Earth's surface. H and L stand for high and low pressure respectively. The part of the figure shown to the right of the circle indicates the flow generated by air returning from the higher levels of the troposphere. The scale in vertical direction is extremely exaggerated, as the whole phenomenon takes place below 10–15 km altitude. In the figure this would correspond to less than 0.1 mm. (Reproduced by permission of Teknisk Forlag).*

In the layers near the ground, flow is directed towards the north by the subtropical high-pressure zone. Due to the Coriolis force, it is then diverted eastwards and becomes a westerly wind in the temperate zone.

Easterly polar winds

From the high pressure at the North Pole, the air flows to the south at low altitudes. The flow is then diverted to the west and becomes the cold, easterly polar wind. The two main flows, the west wind in the temperate zone and the easterly polar wind, pass along each other at 50°–60° northern latitude, thereby forming the polar front.

The polar front

Schematically, the polar front is a surface which meets the ground along a latitude. A warm westerly wind flows to the south of the polar front and a cold easterly wind flows to the north of the front. Due to the temperature difference between the air masses separated by the polar front, the front is inclined to flow northwards. This means that the warm air flows above the cold air and vice versa.

The equilibrium at this front is very sensitive to changes in temperature, velocity and the humidity of the two air masses. If the temperature of the warm air decreases, the polar front becomes steeper, as the warm air pushes the base of the front to the north. The cooling of warm air in one particular region causes a bulge in the polar front. Such a bulge is unstable. The further development of such instabilities is illustrated in Figure 2.5.

Warm and cold fronts

In Figure 2.5(c), a vertical section of the system of fronts is shown below a horizontal section of pressure at ground level and fronts. On the right, i.e. towards east, the warm

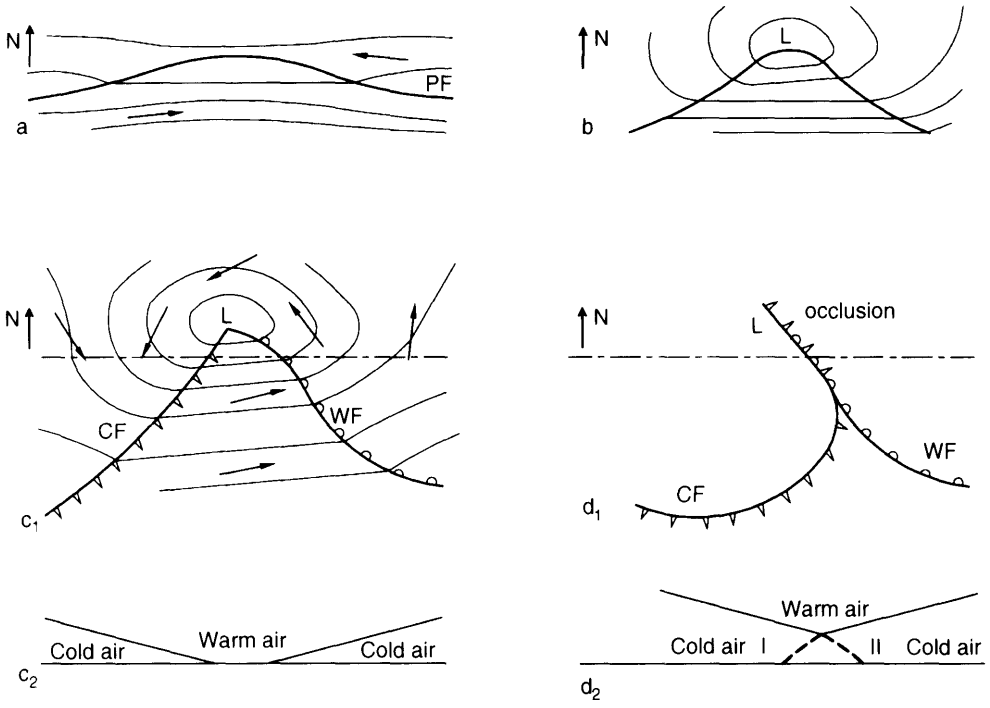

Fig. 2.5 *Development of a cyclone in the Northern Hemisphere. PF: polar front; CF: cold front—advancing cold air; WF: warm front—advancing warm air. Example (a) shows a random bulge on the polar front. This bulge is unstable and grows as shown in (b). In (c) the bulge has developed into a system of fronts, see the vertical section in Figure (c_2). The fronts meet at a low pressure zone, and the wind blows anticlockwise around this zone. In (d) the fronts have collapsed (an occlusion) and the cyclone has disintegrated. (After Jensen (1959)).*

air is above the cold air, and the inclination of the surface of separation is very shallow (1:100 or even less). In the western part of the section, the cold air passes below the warm air. The surface of separation is steeper and is called the cold-front surface. The intersections between the front surfaces and the ground are called the warm front and the cold front, respectively. The entire system in Figure 2.5(c) moves eastwards, with the cold front moving faster than the warm front. The warm section of the original bulge thus becomes narrower and finally the two front surfaces will intersect each other in a line above the ground. This is a "fold up" or "occlusion", see Figure 2.5(d). In summertime, the polar air to the west of the warm sector is colder than the air to the east, and the two masses are separated by a surface like II. In the wintertime, surface I forms the usual occlusion over Northern Europe because the sea is warmer than the continent.

Cyclones

The formation of fronts as described above gives rise to a low-pressure area where the warm front and the cold front meet. As shown in Figure 2.5, the air moves counter clockwise around the area of low pressure. This system is called a cyclone and usually

moves from west to east. The wind velocity in the cyclone is greatest when the low pressure is lowest. The diameter of such a polar cyclone is of the order 500–1000 km. The wind velocity in the cyclone depends partly upon the pressure gradient. Over the North Sea, a pressure gradient of 5 mb per 100 km corresponds to a wind velocity of about 20 m/s (1 mb = 100 Pa). In Europe, cyclones are by far the most important source of high wind velocities.

2.3 GEOSTROPHIC WIND AND GRADIENT WIND

The speed and direction of the wind at high altitudes above ground, say 1 km, is used when evaluating the wind in the atmospheric boundary layer.

Geostrophic wind

The influence of ground surface on wind decreases with increasing height. The wind moves in almost straight lines at heights of approximately 1 km above ground and in areas that are far from high-pressure and low-pressure zones in the weather system considered. Wind speed and direction of the wind depends only on the horizontal pressure gradient and on the Coriolis force originating from the Earth's rotation. This wind is called geostrophic, see Figure 2.6.

The pressure gradient towards a low-pressure zone causes a mass of air to accelerate along a curve, until a state of equilibrium between the pressure gradient and the Coriolis force per unit of air volume is reached. This means that the two forces are of equal magnitude, but in opposite directions, both perpendicular to the wind direction. It follows then that the wind is parallel to the isobars, and the geostrophic wind velocity U_{geo} is

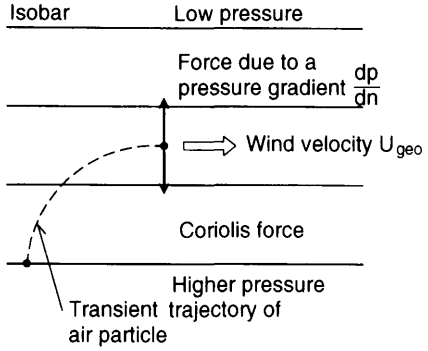

Fig. 2.6 *Geostrophic wind. A particle of air is accelerated towards the low pressure area due to the pressure gradient. However, due to the Coriolis force, its path will be diverted. If the isobars are (almost) rectilinear, a state of equilibrium develops. In this state, the force due to the pressure gradient and the Coriolis force are of the same magnitude but are in opposite directions, and the wind velocity is constant. The Coriolis force is perpendicular to the wind direction and in the Northern Hemisphere to the right. The pressure gradient is orthogonal to the isobars, which are assumed to have such large radii of curvature that the centrifugal force is negligible. (Reproduced by permission of Danish Building Research Institute).*

given by

$$U_{geo} = \frac{1}{\rho f_c} \frac{dp}{dn} \tag{2.3.1}$$

where dp/dn is the pressure gradient at the height of the geostrophic wind, ρ is the air density and f_c is the Coriolis parameter defined by

$$f_c = 2\Omega \sin \lambda \tag{2.3.2}$$

where Ω is the angular velocity of the Earth ($2\pi/24$ hours $= 7.27 \times 10^{-5}$ rad/s), and λ is the latitude. For example, at Greenwich the latitude is $\sim 51°$, giving $f_c = 1.13 \times 10^{-4}$ s^{-1}.

This wind is called geostrophic and U_{geo} is the geostrophic wind velocity corresponding to the pressure gradient. This wind flow is maintained as long as the system of isobars remains the same. It follows from the derivation, that geostrophic wind does not diminish pressure differences and that no energy supply is needed to maintain geostrophic wind.

Geostrophic wind occurs in cases where the radii of curvature of the isobars are so large that the centrifugal force is unimportant. If, however, the radii of curvature are small, i.e. less than a few thousand kilometres, centrifugal force must be taken into account which results in the gradient wind described below.

Gradient wind

Wind follows a curved path in the vicinity of a low-pressure centre or a high-pressure centre. Wind velocity and direction not only depend on the pressure gradient and the Coriolis force but also on the centrifugal force of the curved path. The wind in question is called the gradient wind, see Figure 2.7.

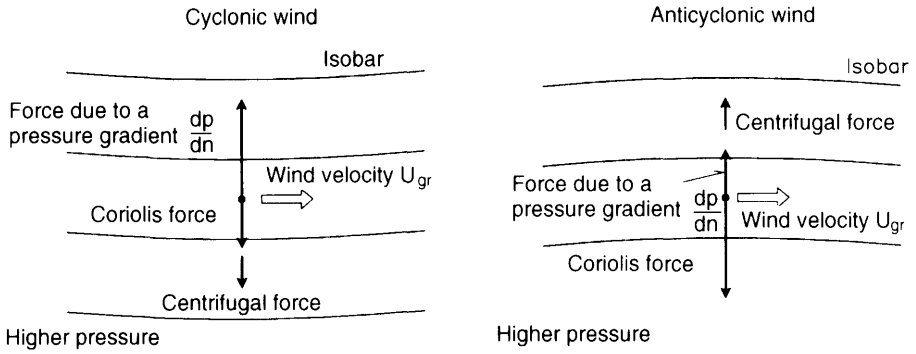

Fig. 2.7 *Gradient wind with constant speed but following a curved path. When cyclonic flow occurs around a low-pressure zone, i.e. anticlockwise in the Northern Hemisphere, the force due to the pressure gradient is equal to the sum of the opposite directed centrifugal force and Coriolis force.*

When anticyclonic flow occurs around a high-pressure zone, i.e. clockwise in the Northern Hemisphere, the Coriolis force is equal to the sum of the opposite directed force due to the pressure gradient and the centrifugal force. (Reproduced by permission of Danish Building Research Institute).

Expressed in polar coordinates, the equation of motion is

$$\pm\frac{U_{gr}^2}{r} + f_c U_{gr} = \frac{1}{\rho}\frac{dp}{dn} \tag{2.3.3}$$

where + and − correspond to cyclonic (i.e. around a low pressure) and anticyclonic (i.e. around a high pressure) winds respectively, see Figure 2.7 showing conditions in the Northern Hemisphere. U_{gr} is the velocity of the gradient wind and r is the radius of curvature of the isobars.

The solution of the equation is

$$U_{gr} = -\frac{f_c r}{2} + \sqrt{\left(\frac{f_c r}{2}\right)^2 + \frac{r}{\rho}\frac{dp}{dn}} \tag{2.3.4}$$

for cyclonic winds, and

$$U_{gr} = +\frac{f_c r}{2} - \sqrt{\left(\frac{f_c r}{2}\right)^2 - \frac{r}{\rho}\frac{dp}{dn}} \tag{2.3.5}$$

for anticyclonic winds.

For anticyclonic winds, the upper limit for U_{gr} is

$$U_{gr} = \frac{f_c r}{2} \tag{2.3.6}$$

Cyclonic winds, which are the most common, have no limits for the magnitude of U_{gr}, and give counter-clockwise flow in the Northern Hemisphere. For cyclonic winds, the geostrophic wind velocity U_{geo} can be expressed using the gradient wind velocity U_{gr} as

$$U_{geo} = U_{gr}\left[1 + \frac{U_{gr}}{f_c r}\right] \tag{2.3.7}$$

from which it follows that $U_{gr} < U_{geo}$. Neither geostrophic wind nor gradient wind is driven by forces along the trajectory of motion, as the flow direction is orthogonal to the forces. This is however an idealization, as friction against lower layers of air has not been taken in account.

The 850 mb "surface"

Atmospheric pressure decreases with height. At a height of approximately 1–2 km it is 850 mb. In meteorology, the 850 mb "surface" is used as reference where the effects of friction are negligible and the winds can be explained by the simple theory of gradient winds.

In the case of very low pressures, the 850 mb "surface" reaches down to approximately 1 km above sea level. It has been found empirically that in strong wind, the maximum gust velocity near the ground is of the same order of magnitude as the wind velocity found at the 850 mb surface.

Wind variation as a result of height

Close to the ground, wind velocity and direction varies as a function of height. This is because the ground tends to reduce wind velocity and this effect spreads upwards. The

effect wears off on reaching the height of the geostrophic wind or gradient wind, i.e. above the atmospheric boundary layer, which is typically approximately 1 km thick.

The equilibrium of forces in the boundary layer is illustrated in Figure 2.8. The state of equilibrium corresponds to a wind direction which crosses the isobars. The wind direction continues to change down through the boundary layer and the wind speed gradually decreases to zero, see Figure 2.9. The turn is typically 20°, but it may vary between approximately 10° and 45° depending on ground roughness and atmospheric stability, see also Section 3.1.

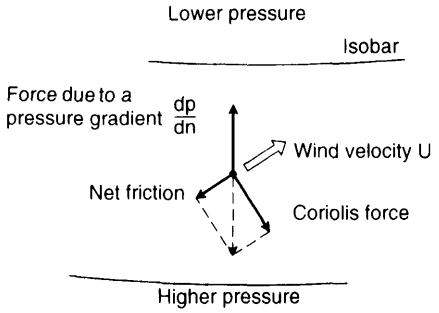

Fig. 2.8 *Equilibrium of forces in the atmospheric boundary layer. There is equilibrium between the force due to the pressure gradient, the Coriolis force and the friction generated. The wind direction is diverted in relation to the isobars. (Reproduced by permission of Danish Building Research Institute).*

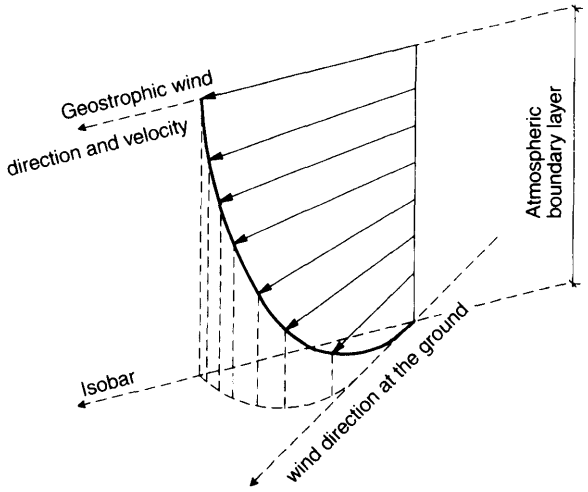

Fig. 2.9 *Wind in the atmospheric boundary layer. Wind speed decreases downwards, as illustrated by the length of the arrows. Furthermore, the direction of the wind is increasingly diverted with respect to the isobars. The figure shows a simplified and exaggerated picture of these directional changes. In reality, the total diversion of wind direction is typically 20° through the boundary layer, which is usually of the order of 1 km high. (Jensen, 1985). (Reproduced by permission of Teknisk Forlag).*

2.4 THERMALLY GENERATED SECONDARY CIRCULATION (TYPHOONS)

Thermally generated secondary circulation occurs when centres of high pressure or low pressure are created when the lower levels of the atmosphere are either heated or cooled.

Monsoons

During the summer, the sea heats up slower than the ground surface, so the air is colder over the sea. As it gets hotter, the air close to the ground rises. This means that at low altitudes, the wind is directed on shore away from the sea to fill the "void" caused by the rising air. During the winter, the opposite happens.

These conditions result in monsoons, which are especially common in Asia and over the Indian Ocean. During the winter, the dry north-easterly monsoon blows from the Asian Continent towards the south-west, and during the summer the humid south-west monsoon blows from the Indian Ocean over south-east Asia. The fertility of this area is mainly due to the rain that accompanies the monsoon. Monsoons often last many days, but generally the wind speeds are moderate.

Tropical storms (hurricanes)

Hurricanes are storms generated over tropical oceans where the water temperature exceeds 26°C. The energy in hurricanes comes from the release of latent heat when vapour condenses.

Near the Equator, at latitudes of between 5° and 20°, warm air is occasionally lifted to high altitudes by upwinds. During certain climatological conditions, the hot, humid

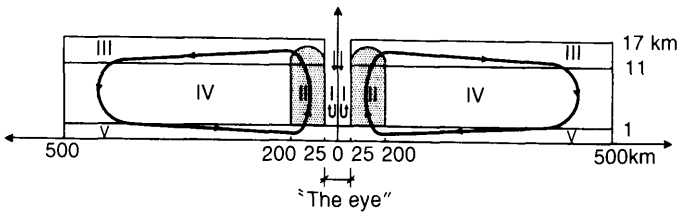

Fig. 2.10 *The structure of a hurricane.*

Region I: The eye of the hurricane is a circular, relatively dry almost calm core, named the eye, about which the gale rages. At the outer limit of the eye, air rises slowly, and it drops correspondingly at the centre.

Region II: Warm humid air rises. The vapour condenses, resulting in the release of large amounts of energy and heavy rain.

Regions III–V: Air is sucked towards the eye along the ground surface. It is transported through region II and moves away from the eye at high altitude (approximately 10 km).

Above water, the airflow moving inwards in region V causes warm humid air to flow into region II, thus generating new energy for the storm. Above land, there is more loss of energy due to the greater friction at the ground surface. The supply of energy as warm, humid air is also reduced, which is why tropical storms usually die out over land after a few days. (Reproduced by permission of Danish Building Research Institute).

air forms a cloud in which vapour condenses and releases latent heat. This can involve extremely large amounts of energy, as the diameter of a hurricane usually measures several hundred kilometers. The amount of energy released by a hurricane in just one hour is of the order of the amount of electrical energy consumed by the USA during a whole week.

Generally, hurricanes rage for several days and cause extensive damage due to their high wind speeds, often about 70–80 m/s. In the USA, on average about 2 billion dollars worth of damage is caused by hurricanes every year. The principal structure of a hurricane is shown in Figure 2.10.

2.5 LOCAL WEATHER SYSTEMS

Small, local weather systems have little influence on the global atmospheric circulation, described in Section 2.2. However, the intensity of these weather systems may, in some cases, be decisive for the design of exposed structures.

Rising and descending winds — the warm foehn or the cold bora

Strong, local storms sometimes form due to varying ground heights. If a mass of air moves from lowlands over a mountainous region, the air cools down while ascending. In the beginning, the temperature drops about 1°C per 100 m increase in ground level. However, when the temperature falls to dew point, water separates into rain or snow, so the drop in temperature slows to typically 0.5°C per 100 m rise. When the highest point is passed, the air flows down again with an increase in temperature of 1°C per 100 m fall, see Figure 2.11.

For example, let the air over a low region have a temperature of 10°C and a dew point of 8°C. When the air meets a mountain, it rises and saturation starts at a height of 200 m. On rising higher, the air produces rain or snow and the temperature drops by 0.5°C per 100 m. If the height of the mountain is 2000 m, the drop in temperature is 2°C for the first 200 m and 9°C for the remaining 1800 m — a total of 11°C. Above the peak, the air temperature is −1°C and the air is saturated with vapour. On reaching the other side of the mountain, the air drops and the temperature rises 1°C per 100 m. If the land continues at the same height, then the air arrives with a temperature of 20°C above the temperature

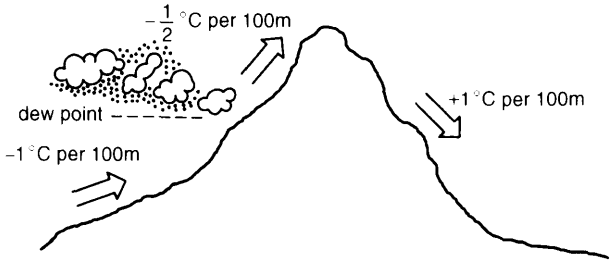

Fig. 2.11 *The foehn wind. Wind coming from a lowland area that is forced upwards along a mountain is cooled 1°C per 100 m rise. If the dew point is passed, water separates from the air and forms rain or snow. As it continues to rise, the air cools 0.5°C per 100 m rise. At the other side of the mountain the air drops, and the temperature rises 1°C per 100 m. This air is very dry. (Reproduced by permission of Danish Building Research Institute).*

at the peak, i.e. 19°C. As the dew point is −1°C, the air is extremely dry. Such warm, dry wind is called a foehn.

Under certain conditions, the air descending down the mountain is not heated sufficiently to cause a warm foehn. Instead, a bora is produced, which is characteristically cold and dry.

Such conditions are found in large ice-covered regions, where the air becomes very cold and therefore has a high density. If ice-covered regions are at relatively high altitudes, like the inland ice in Greenland, so-called drop winds (Piteraq) can be experienced locally in valleys below the rim of the ice. The heavy air quite literally falls down into the valley because of gravitational forces. The wind speed may be very high, 50–60 m/s is not unusual, and this will generally determine the design needed to combat the wind action experienced in Greenland.

Thunderstorms

Thunderstorms may form if there is an upward motion of warm, humid air. Such a motion may occur at fronts.

A schematic sketch of a thunderstorm is shown in Figure 2.12. The condensation of the rising, humid air releases energy, and the accompanying rain initiates the downward motion at the centre. The length scale is about 10 km and the lifetime is of the order of magnitude of 1 hour.

Tornadoes

Severe thunderstorms may develop into tornadoes with very high wind speeds. Tornadoes cause about 100 million dollars' worth of damage every year in the USA.

A tornado is a violent vortex about a vertical or inclining axis. Typically, its diameter is approximately 300 m and it moves with a velocity of 10–30 m/s. The maximum tangential wind speed is 100 m/s. Just below the tornado, which looks like a vertical tube-shaped cloud, a sudden fall in barometric pressure takes place. Therefore, the external surfaces of buildings are subjected to powerful suction. This can become so intense that buildings

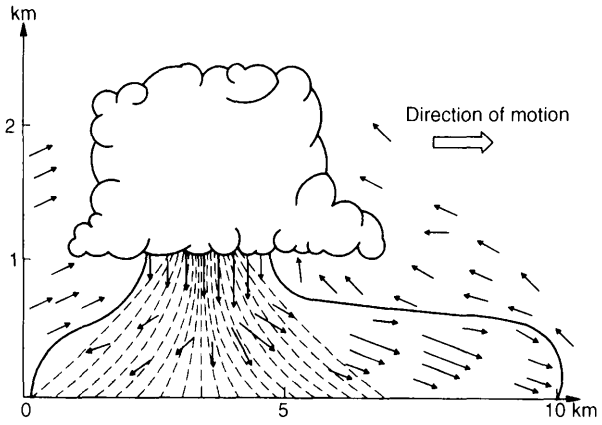

Fig. 2.12 *Cross section of a thunderstorm. (Reproduced by permission of Danish Building Research Institute).*

almost "explode". Airborne debris is another source of damage. By breaking windows or cladding, tornadoes give rise to changes in internal pressure that cause severe destruction of roofs, etc.

Tornadoes are reported to be most frequent and violent in the USA, but they also occur in other regions such as Europe, Japan, Australia and Russia. Some tornadoes have been very destructive, like the one which completely destroyed 321 buildings in St Louis, USA, in May 1896. Cook (1985) provides a great deal of information on damage caused by tornadoes.

Dust devils

In very dry, hot areas, local vortices sometimes form. The phenomenon is initiated by a very high local temperature over a smaller dark surface which is exposed to sunshine. Dust devils can be up to several hundred metres tall and sand or dust is sucked up into the air, hence the name. In contrast to tornadoes, they are not related to thunderstorms. The damage caused by dust devils is not important in the design of structures.

3 The Atmospheric Boundary Layer — Natural Wind

The turbulent nature of wind has been recognized for centuries. One of the early descriptions of the chaotic character of wind was based upon observations of snow-drift. Roger Ascham (1515–68) wrote:

> *And that which was most marvel of all, at one time two drifts of snow flew, the one out of the west into the east, the other out of the north into the east: and I saw two winds by reason of the snow, the one cross over the other, as it had been two highways. And again, I should hear the wind blow in the air, when nothing was stirred at the ground. And when all was still where I rode, not very far from me the snow should be lifted wonderfully. This experience made me more marvel at the nature of the wind, then it made me cunning in the knowledge of the wind.*

Wind flow is turbulent due to the friction caused as it passes over surface terrain. A turbulent wind flow varies in a complex, random way both in space and time. Consequently, it must be described in statistical terms. The momentary velocity is described as the sum of a mean velocity and of fluctuations (the turbulence components) representing the disordered part of the turbulent flow, see Figure 2.3. According to the definition, after a sufficiently long period, say 10 minutes, the mean value of the fluctuations is zero.

As mentioned in Chapter 2, the velocity of the wind increases with the height above terrain in the atmospheric boundary layer. This variation of mean wind velocity is called a wind profile, see Figure 3.12.

To summarize, the wind in the boundary layer may be characterized by a wind profile for the mean wind velocity and the additional turbulence. The wind profile is expounded in Section 3.2 and the turbulence in Section 3.5.

3.1 TURBULENT WIND

This book is about wind load on structures, and in order to avoid unnecessary complications, the following assumptions have been made in the description of the turbulent wind field:

- At geostrophic wind height, where the conditions are independent of surface friction, the flow is assumed horizontally homogeneous. This means that the wind has the same universal speed and direction.
- The wind is stationary. According to international meteorological practice, a 10-minute observation period is applied for calculating mean wind velocities. During this period the wind field may normally be considered stationary, see Appendix A.3.

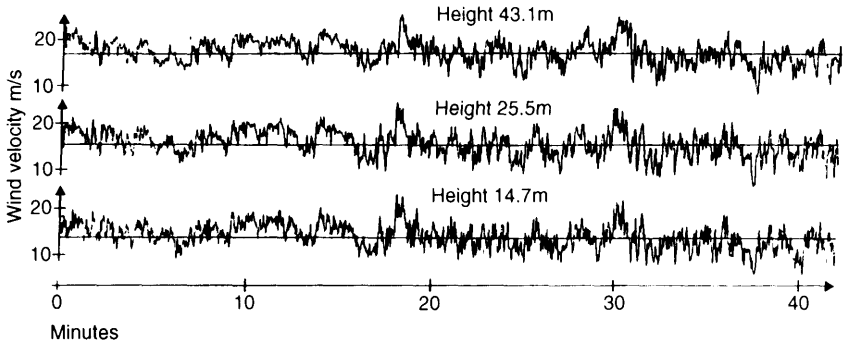

Fig. 3.1 *Wind velocities measured at Stigsnæs, Denmark, at three different heights (after Sigbjörnsson (1974)). The differences of mean wind velocities should be noticed. (Reproduced by permission of R. Sigbjörnsson).*

- The direction of the wind does not change according to height above ground. Due to frictional forces close to the ground, the geostrophical equilibrium of forces shown in Figure 2.6 cannot be maintained, and wind direction will therefore change systematically from ground to geostrophic height, see Section 2.3. However, apart from very high structures and structures which are unusually sensitive to wind direction, an excellent approximation is obtained even though directional changing is not taken into account. Measurements indicate that up to a height of 180 m, direction changes only few degrees (Harris, 1970).

Mathematical description

A Cartesian coordinate system is applied, with the x-axis in the direction of the mean wind velocity, the y-axis horizontal and the z-axis vertical, positive upwards.

The velocities at a given time t are formulated as

in the longitudinal direction	$U(z) + u(x, y, z, t)$	(3.1.1)
in the lateral direction	$v(x, y, z, t)$	(3.1.2)
in the vertical direction	$w(x, y, z, t)$	(3.1.3)

where the mean wind velocity $U(z)$ depends only on the height z above ground. u, v and w describe the fluctuating part of the wind field, and can be treated mathematically as stationary, stochastic processes with a zero mean value. The mean wind velocity $U(z)$ and the turbulence component u in the wind direction are often the most important, as they usually give the main contributions to the wind forces on a structure. v is the horizontal wind velocity perpendicular to the wind direction and w is the vertical wind velocity. A picture of possible wind velocities in the wind direction at a certain time is shown in Figure 3.2.

Thermal conditions

The geostrophical wind velocity at high altitudes above ground is the direct cause of the formation of the atmospheric boundary layer, which is described by the mean wind velocity and turbulence components. The wind conditions in the boundary layer are

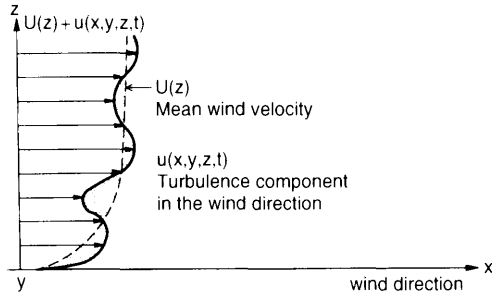

Fig. 3.2 *Simultaneous wind velocities in the wind direction at different heights above the ground. The momentary wind velocities are shown as a solid curve. The wind velocity is composed by a mean wind velocity U and a turbulence component u (velocity fluctuation). The mean wind velocity, indicated by the dotted curve, increases smoothly with the height z. The turbulence component is represented by the difference between the solid and the dotted curve, indicating that u changes between positive and negative values. The horizontal turbulence component v perpendicular to the wind direction and the vertical turbulence component are fluctuating around zero. (Reproduced by permission of Danish Building Research Institute).*

described as being mechanically generated, even though basically they have a thermal origin, see Chapter 2.

In addition to the mechanically generated wind conditions, the thermal state of the atmosphere may significantly influence the actual mean wind velocity and turbulence components. These thermal effects cannot be ignored if the wind velocity is less than approximately 10 m/s (Armitt, 1976). At higher wind velocities, mechanically generated wind conditions are normally by far the most important.

In most cases, as extreme wind velocities are not influenced by the thermal conditions in the atmosphere, the same will apply to the design wind load on structures. However, for slender structures like chimneys, vortex shedding may give rise to the greatest wind load on the structure, see Chapter 7. Vibrations introduced by vortex shedding often occur at moderate wind velocities, and thermal conditions may be important in such cases. For this reason, the Canadian code prescribes a considerable thermal influence on the load due to vortex shedding, see Section 7.4.

Thermal influence on wind conditions

The atmosphere is assumed to be in equilibrium. The pressure p, the density of the air ρ and the temperature T in kelvin (kelvin = Celsius + 273) is given in Figure 3.3, which

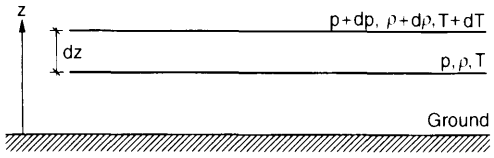

Fig. 3.3 *Vertical section in the atmosphere. (Reproduced by permission of Danish Building Research Institute).*

shows two horizontal planes, separated by the distance dz. The weight per unit of area of the layer with the thickness dz is equal to the increase dp of the pressure, so

$$\frac{dp}{dz} = -\rho g \tag{3.1.4}$$

where g is the acceleration due to gravity. The equation of state of an ideal gas is

$$\frac{p}{\rho} = RT \tag{3.1.5}$$

R is the gas constant, $R = 287.6\ \mathrm{m^2/s^2/K}$.

From (3.1.4) and (3.1.5) it follows that the differential equation is

$$\frac{1}{\rho}\frac{d\rho}{dz} = -\frac{1}{T}\frac{dT}{dz} - \frac{g}{RT} \tag{3.1.6}$$

When the variation of temperature T with height z is known, the air density ρ can be determined. As an example, a constant temperature of T_0 gives the following air density:

$$\rho(z) = \rho(0)\exp\left(-\frac{gz}{RT_0}\right) \tag{3.1.7}$$

Thus, in an atmosphere with a constant, height-independent temperature, the air density decreases exponentially according to height. If a small mass of air in such an atmosphere moves from one level to another, higher, level without any exchange of heat, the mass of air must expand in order to correspond to the decreased density. However, then its temperature also decreases. Therefore, the mass of air cannot be in equilibrium at the new height, but will sink again. Consequently, an atmosphere with a constant temperature is stable.

If the temperature increases with height, it is likewise shown that the atmosphere is even more stable and the air is prevented from mixing. Stable conditions are typically found when the ground surface—and therefore also the lower air layers—are cooled down by radiation in a cloudless sky at night. This phenomenon is called inversion.

However, if the temperature decreases significantly up through the atmosphere, conditions are unstable. A mass of air which is moved upwards will find itself surrounded by heavier air and will probably move even higher. This phenomenon is called convection and gives rise to significant air mixing. Typically, it occurs when the sun heats the ground surface, increasing the temperature in the lower part of the atmosphere in relation to higher layers.

Between the stable and the unstable atmosphere there is a neutral state characterized by equilibrium of the mass of air whatever its position, though only if there is no heat exchange with the surroundings. It follows then, that the neutral state corresponds to a moderate decrease of air temperature with height.

A dry atmosphere is in a neutral state when the temperature decreases upwards at 1°C per 100 m. If the temperature decreases more, the atmosphere becomes unstable, and if it drops at a slower rate or even increases upwards, the atmosphere becomes stable.

The influence of atmospheric stability conditions on air turbulence is illustrated by smoke rising from a chimney, see Figure 3.4. The thermal influence on turbulence, positive or negative, can also be seen in this figure.

Throughout most of the book, it is assumed that there is a neutral stability, i.e. thermal contributions to wind conditions can be disregarded. However, this assumption cannot be used in the case of vortex shedding, see Chapter 7.

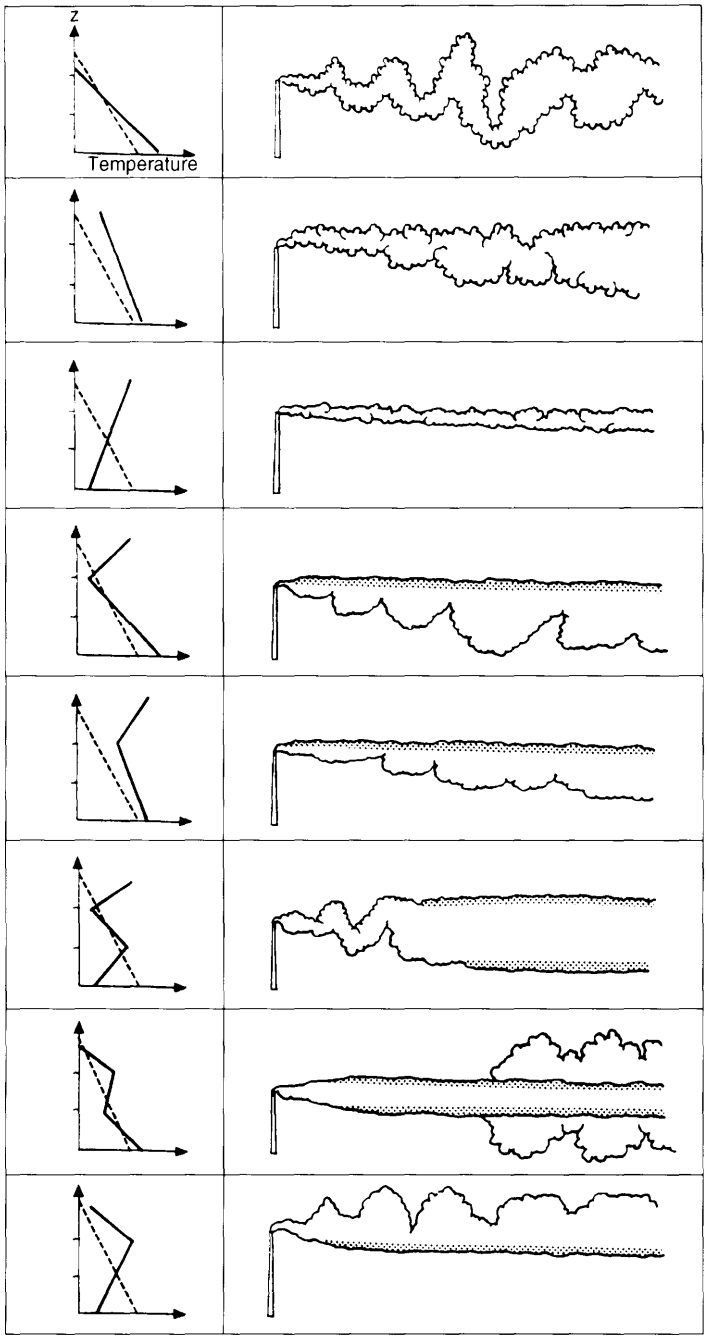

Fig. 3.4 *Thermal influence upon the characteristics of a wisp of smoke. The solid curve to the left indicates the variation of the temperature with the height above the ground. The dotted line corresponds to a temperature decreasing 1°C per 100 m (neutral state). (Reproduced by permission of Danish Building Research Institute).*

3.2 MEAN WIND VELOCITY—WIND PROFILE

Two characteristic length scales apply in the boundary layer. In the lower part of the boundary layer, the dominant length scale is a measure of surface roughness. In the upper part of the boundary layer, close to the free flow regime, the boundary layer height is an important length scale.

In deriving the logarithmic profile shown below, only surface roughness is taken into account, so the profile only applies close to the ground, i.e. up to 50–100 m above terrain. In the so-called corrected logarithmic profile, the height of the boundary layer is also taken into account. At high wind velocities, say more than 20 m/s, the corrected logarithmic profile gives accurate results up to 300 m above ground.

Several codes have introduced a power law profile which is empirical. This is discussed at the end of Section 3.2.

The logarithmic profile

The friction velocity u_* is defined by

$$u_* = \sqrt{\frac{\tau_0}{\rho}} \tag{3.2.1}$$

where τ_0 is the shear stress at the ground surface and ρ is the air density. For extreme winds, typical friction velocities are of the order of magnitude 1–2 m/s. Close to the ground, the velocity gradient $dU(z)/dz$ depends upon τ_0, ρ and the height z above ground. Based upon a dimensional analysis, a differential equation for the mean wind velocities can be formulated, and if there is a long, flat terrain upstream, its solution leads to the following expression for the logarithmic profile

$$U(z) = u_* \frac{1}{\kappa} \ln \frac{z}{z_0} \tag{3.2.2}$$

where κ is von Kármán's constant ($\kappa \sim 0.4$) and z_0 is called the roughness length, see Tables 3.1 and 3.2.

Eurocode 1 uses the logarithmic profile for the mean wind velocity up to 200 m above ground.

Table 3.1 *Roughness lengths z_0 for different terrain categories.*

Roughness length z_0 (m)	Terrain type
10^{-5}	Plane ice
10^{-4}	Open sea without waves
10^{-3}	Coastal areas, on-shore wind
0.01	Open land with little vegetation and few houses, see Figure 3.6
0.05	Agricultural areas with few houses and wind-breaks, see Figure 3.7
0.3	Villages and agricultural areas with lots of wind breaks, see Figure 3.8
1–10	Urban areas

Table 3.2 *Terrain categories and related parameters k_T, z_0, z_{min} and ε from Eurocode 1. ε is a parameter used in an informative Annex of Eurocode 1 to calculate the integral length scale of turbulence $L_u^x(z)$. The exponent α (not included in Eurocode 1) is used in the power law profile, see equation (3.2.9).*

	Terrain category	k_T	z_0[m]	z_{min}[m]	ε	α
I	Rough, open sea, lakes with at least 5 km fetch upwind and smooth flat country without obstacles	0.17	0.01	2	[0.13]	0.12
II	Farmland with boundary hedges, occasional small farm structures, houses or trees	0.19	0.05	4	[0.26]	0.16
III	Suburban or industrial areas and permanent forests	0.22	0.3	8	[0.37]	0.22
IV	Urban areas in which at least 15% of the surface is covered by buildings with an average height exceeding 15 m	0.24	1	16	[0.46]	0.30

The roughness length z_0

Simplified, the roughness length z_0 can be interpreted as the size of a characteristic vortex, which is formed as a result of friction between the air and the ground surface, see Figure 3.5. As indicated by formula (3.2.2), z_0 is the height above ground at which the mean wind velocity is zero.

Roughness length z_0 has been estimated from measurements taken at many locations around the world. A scale of these lengths is shown in Table 3.1.

In Eurocode 1, four terrain categories are introduced. These are shown in Table 3.2, which also introduces a terrain factor k_T. This is proportional to the friction velocity, increasing with surface roughness. The table also shows minimum height z_{min}. Eurocode 1 prescribes a constant velocity below this height.

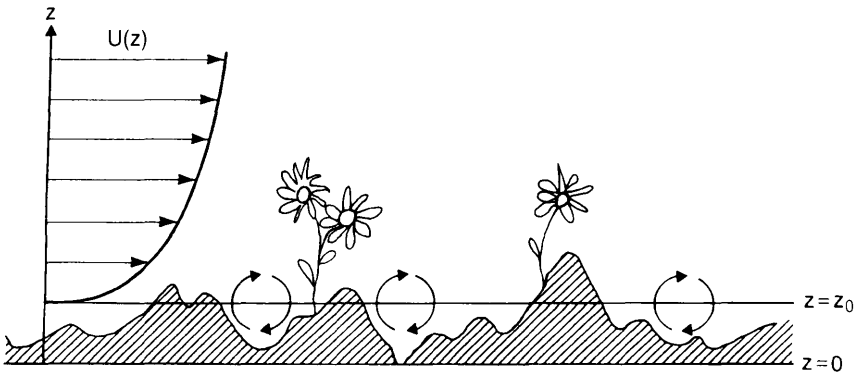

Fig. 3.5 *Simplified illustration of the roughness length z_0. (After Petersen et al. (1980). Reproduced by permission of Risø National Laboratory, Denmark).*

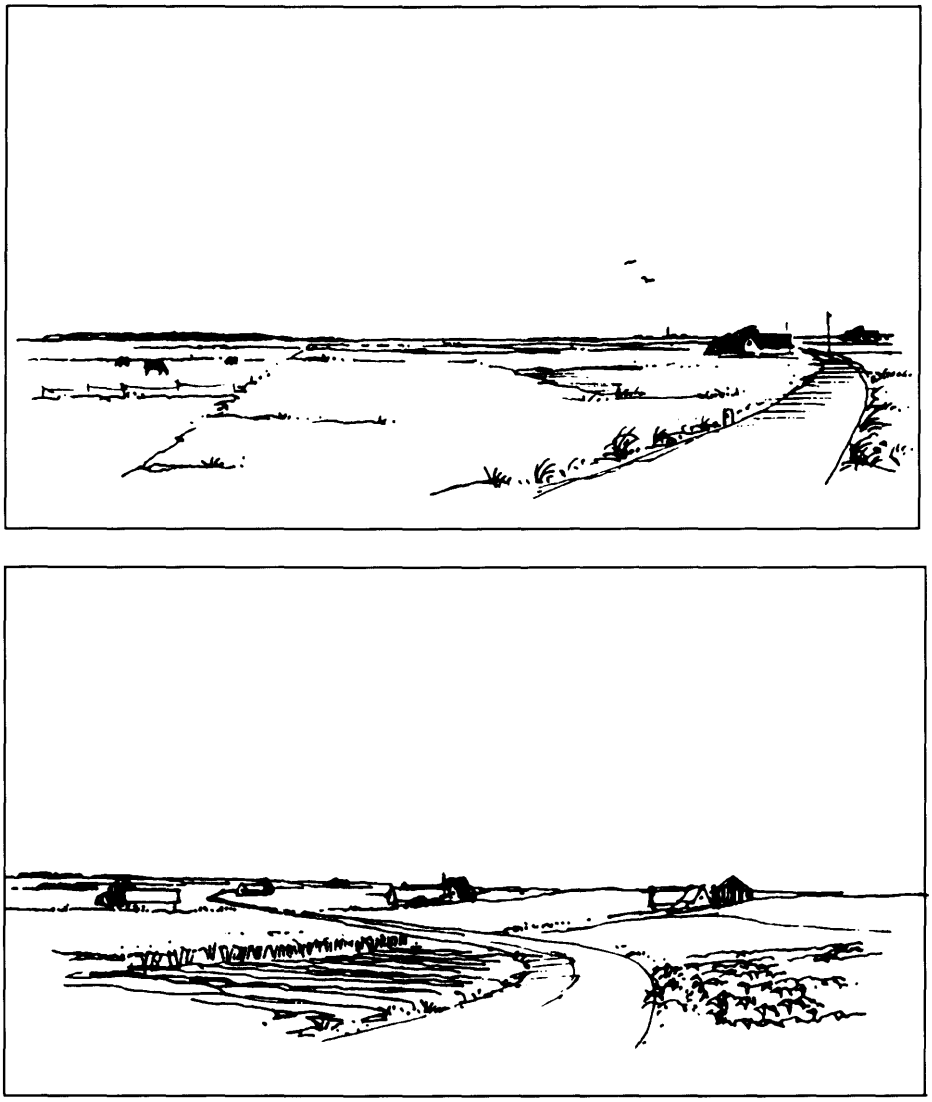

Fig. 3.6 *Examples of terrain with roughness length* $z_0 \approx 0.01$ *m. (After Petersen et al. (1980). Drawn by architect Søren Rasmussen. Reproduced by permission of Risø National Laboratory, Denmark).*

Eurocode 1 states that the mean wind velocity above horizontal terrain varies according to height z above ground as follows:

$$U(z) = U_{\text{bas}} k_T \ln\left(\frac{z}{z_0}\right), \qquad \text{if } z_{\min} \leqslant z \leqslant 200 \text{ m}$$

$$U(z) = U(z_{\min}), \qquad \text{if } z < z_{\min} \tag{3.2.3}$$

where U_{bas} is the reference wind velocity, see Section 3.4. The ratio $U(z)/U_{\text{bas}}$ is shown in Figure 3.9 for the four categories in Eurocode 1.

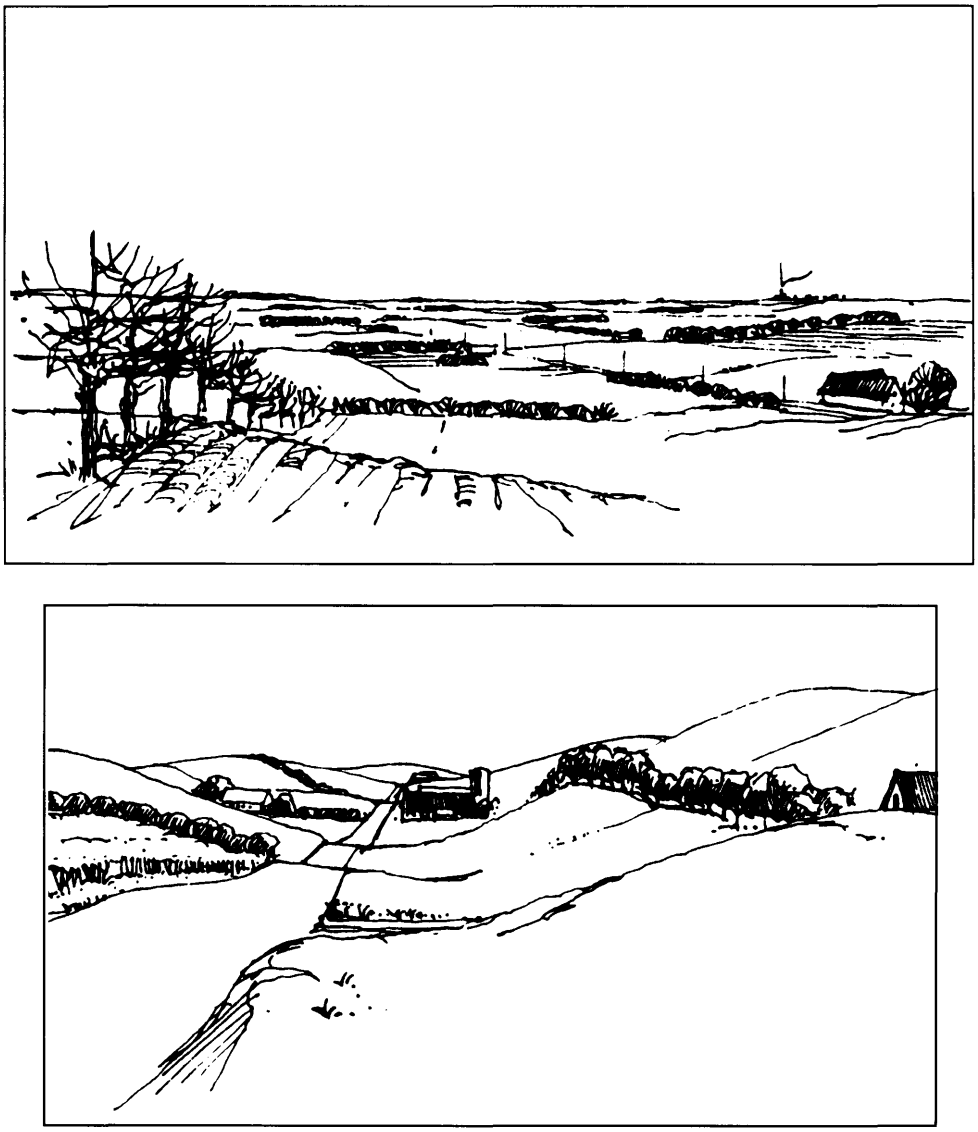

Fig. 3.7 *Examples of terrain with roughness length $z_0 \approx 0.05$ m. (After Petersen et al. (1980). Drawn by architect Søren Rasmussen. Reproduced by permission of Risø National Laboratory, Denmark).*

Theoretical estimation of roughness length

Elements in the terrain which contribute to the surface roughness are called roughness elements. They give rise to increased frictional forces against the flow and thereby also increased wind turbulence. Smooth, long hills are not classed as roughness elements.

If a number of roughness elements are uniformly distributed over a terrain, the following empirical equation can be used to obtain a reasonable approximation (Businger, 1974):

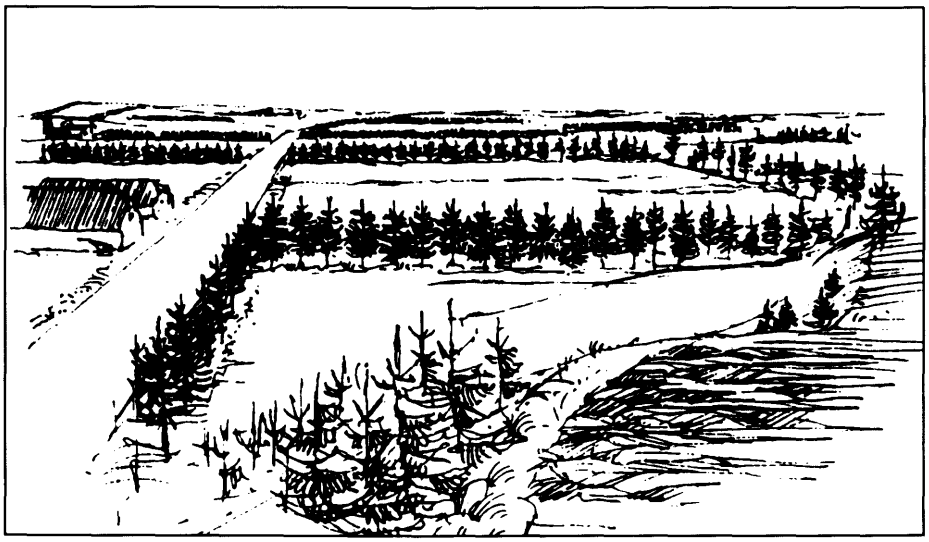

Fig. 3.8 *Example of terrain with roughness length $z_0 \approx 0.3$ m. (After Petersen et al. (1980). Drawn by architect Søren Rasmussen. Reproduced by permission of Risø National Laboratory, Denmark).*

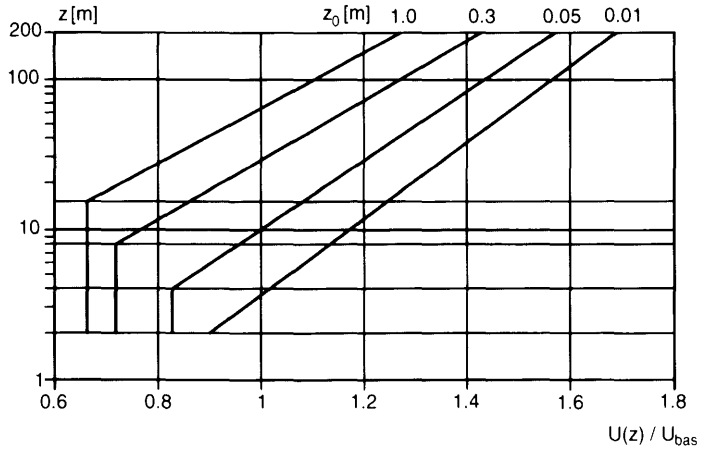

Fig. 3.9 *Variation of mean wind velocity with height according to Eurocode 1.*

$$z_0 = 0.5h\frac{A_r}{A_t} \tag{3.2.4}$$

where h is the roughness element height, A_r is the area of the element normal to the wind direction, and A_t is the ground area per roughness element. To illustrate a simple case, A_r and A_t are shown in Figure 3.10.

As an example, consider an area containing houses 5 m high with facades 20 m long, each with a ground area of 1000 m^2. By applying formula (3.2.4), we find the roughness length for wind normal to the facades is

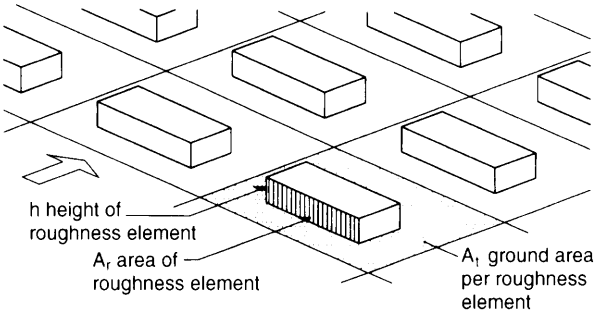

Fig. 3.10 *In a simple case the roughness length z_0 can be calculated from the height of the roughness element, its area perpendicular to the wind and the ground area per roughness element. (Reproduced by permission of Danish Building Research Institute).*

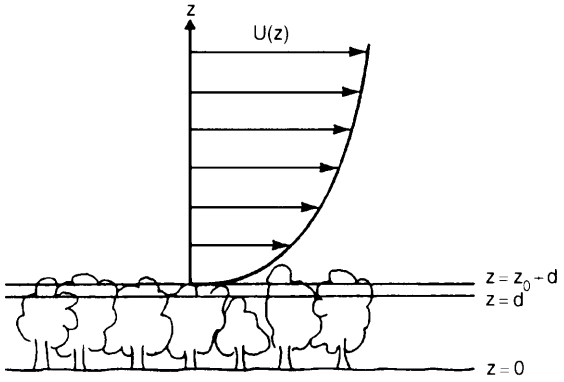

Fig. 3.11 *The wind profile above a wood. The whole flow is lifted, because the roughness elements are very close to each other. (Reproduced by permission of Risø National Laboratory, Denmark).*

$$z_0 = 0.5 \times 5 \times \frac{5 \times 20}{1000} = 0.25 \text{ m}$$

If the area of the roughness element normal to the wind direction, A_r, and the ground area per roughness element, A_t, are of the same order of magnitude, the flow will be raised such that the tops of the roughness elements form a new surface. This is the case in forests, as shown in Figure 3.11.

Mathematically, the change in base level is taken into account by introducing zero displacement d in the logarithmic profile:

$$U(z) = u_* \frac{1}{\kappa} \ln \frac{z - d}{z_0} \tag{3.2.5}$$

Corrected logarithmic profile

The expression (3.2.2) for the logarithmic profile is not valid at very high altitudes above ground. A more precise expression based on the mathematical model developed by Harris

and Deaves (1980) is

$$U(z) = \frac{u_*}{\kappa}\left[\ln\frac{z-d}{z_0} + 5.75a - 1.88a^2 - 1.33a^3 + 0.25a^4\right] \tag{3.2.6}$$

where the actual, effective height, $z - d$, is normalized by the gradient height z_g when calculating the non-dimensional argument a:

$$a = (z - d)/z_g \tag{3.2.7}$$

The gradient height z_g is given by

$$z_g = \frac{u_*}{6f_c} \tag{3.2.8}$$

where f_c is the Coriolis parameter, see formula (2.3.2). The model developed by Harris and Deaves fits experimental data accurately and also covers surface roughness changes. The last three terms of expression (3.2.6) are not significant for heights of up to 300 m above ground.

The power-law profile

The empirical power-law profile is primarily used because of its simplicity, e.g. in the Canadian code NBC 1990. It is expressed as

$$U(z) = U(z_{\text{ref}})\left(\frac{z}{z_{\text{ref}}}\right)^{\alpha} \tag{3.2.9}$$

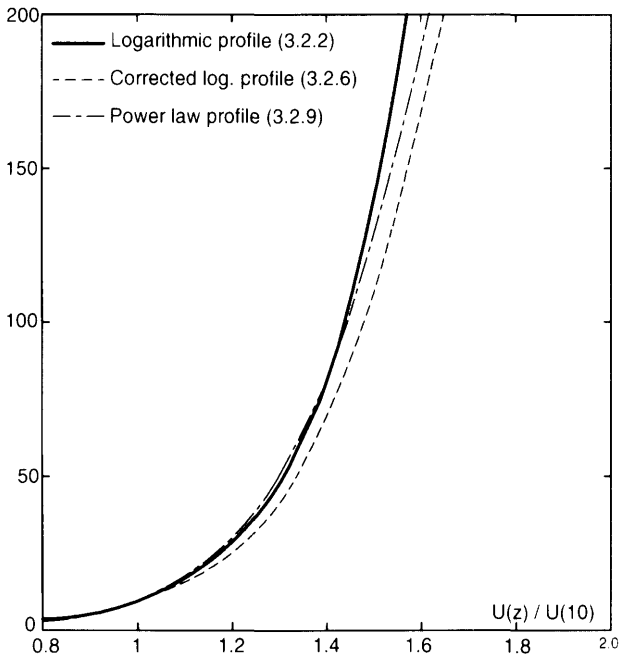

Fig. 3.12 *Comparison of the logarithmic profile, the corrected logarithmic profile and the power-law profile. The roughness length is* $z_0 = 0.05$ *m, the site at* 50° *latitude and in formula (3.2.9) the exponent* $\alpha = 0.16$. *The corrected logarithmic profile is calculated assuming the friction velocity* $u_* = 2.0$ *m/s.*

where z_{ref} is a reference height, usually 10 m. Representative values of the exponent α are included in Table 3.2.

For a site with $z_0 = 0.05$ m, Figure 3.12 shows a comparison of the wind profiles given by formulas (3.2.2), (3.2.6) and (3.2.9).

3.3 INHOMOGENEOUS TERRAIN

The influence of roughness change and topography on mean wind velocity is described below.

Roughness change

When wind flows over a wide area of constant roughness, its profile is determined as described in the Section 3.2. If the wind meets terrain that has another roughness, the wind profile changes, as illustrated in Figure 3.13.

The air moves from one terrain with roughness length z_{01} over a roughness shift to another terrain with roughness length z_{02}. Over the terrain before the roughness shift, and also above a height h_2 after the shift, the wind velocity is determined by the "old" roughness length z_{01} only. After the roughness shift below the height h_1, wind velocity depends only on the "new" roughness length z_{02}. In the region between the heights h_1 and h_2 a gradual transition takes place, and here both roughnesses influence wind velocity. The region from the ground to the height h_2 is called the internal boundary layer. The lower part of this region, up to the height h_1, is called the equilibrium layer.

The height of the internal boundary layer

William P. Elliott formulated the height h_2 of the internal boundary layer as

$$h_2(x) = z_{02}\left[0.75 + 0.03 \ln\left(\frac{z_{01}}{z_{02}}\right)\right]\left(\frac{x}{z_{02}}\right)^{0.8} \qquad (3.3.1)$$

where the distance x is measured from the point where the roughness changes to the point in the wind direction where the height is determined. It follows from the formula that h_2

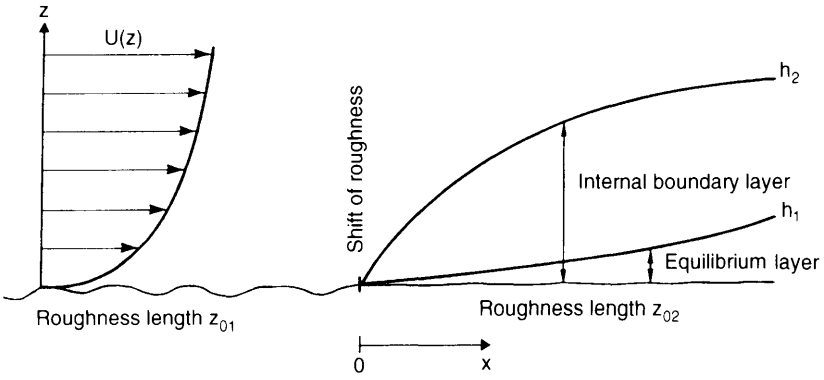

Fig. 3.13 *Height of internal boundary layer and of equilibrium layer after a change of roughness. (Reproduced by permission of Danish Building Research Institute).*

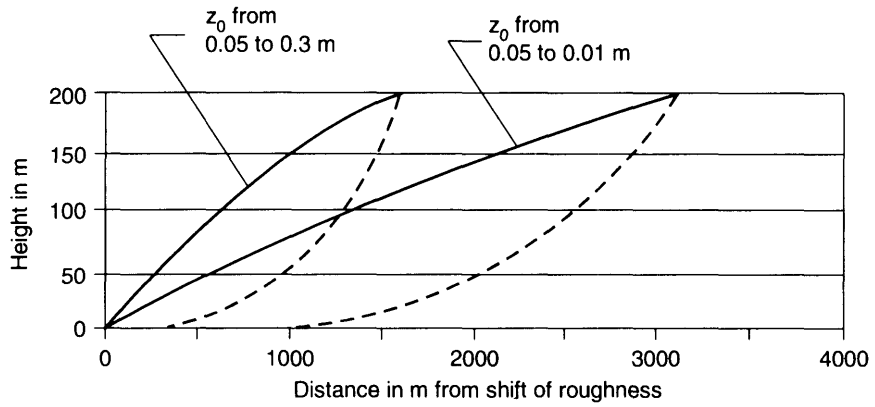

Fig. 3.14 *Height of internal boundary layer after shift of roughness. The dotted curves show the height of the equilibrium layer after Danish Code of Practice. DS410 (1983).*

increases more rapidly after a shift to a rougher terrain than after a shift to a smoother terrain, see Plate (1971). This is illustrated in Figure 3.14.

It should be kept in mind that the roughness of a terrain might change if buildings are erected or demolished, or if other human activity alters the landscape. It may be advisable to consider this at the design stage.

Eurocode 1 deals with the problems of roughness changes by stating that the smoother terrain category in the upwind direction should be used if the structure is less than

- 2 km from the smoother category I
- 1 km from the smoother category II and III

Eurocode 1 also mentions that if doubt exists concerning the category, the worse case scenario should be used. However, these simple rules may be augmented by specific information for each member state, and National Application Documents are likely to incorporate more detailed rules.

Topography

When the wind meets an escarpment or hill, the air flow is forced into a smaller area provided the boundary layer and the gradient height do not change. Therefore, the wind speed and wind pressure increase.

Lemelin *et al.* (1988) deduced some rather simple formulae concerning escarpments and hills with a smoothly curved shape.

In Eurocode 1, formulae are given based on idealized escarpments and hills, which are angular in shape, see Figure 3.15. Eurocode 1 has introduced a topography coefficient c_t related to mean wind speed at the base of the hill or escarpment. c_t is expressed as a function of the slope Φ, the length L of the escarpment or hill measured in the wind direction, the site position x measured from the crest, and height z above ground as

$$c_t = \begin{cases} 1 & \text{for } \Phi < 0.05 \\ 1 + 2s\Phi & \text{for } 0.05 < \Phi < 0.3 \\ 1 + 0.6s & \text{for } \Phi > 0.3 \end{cases} \tag{3.3.2}$$

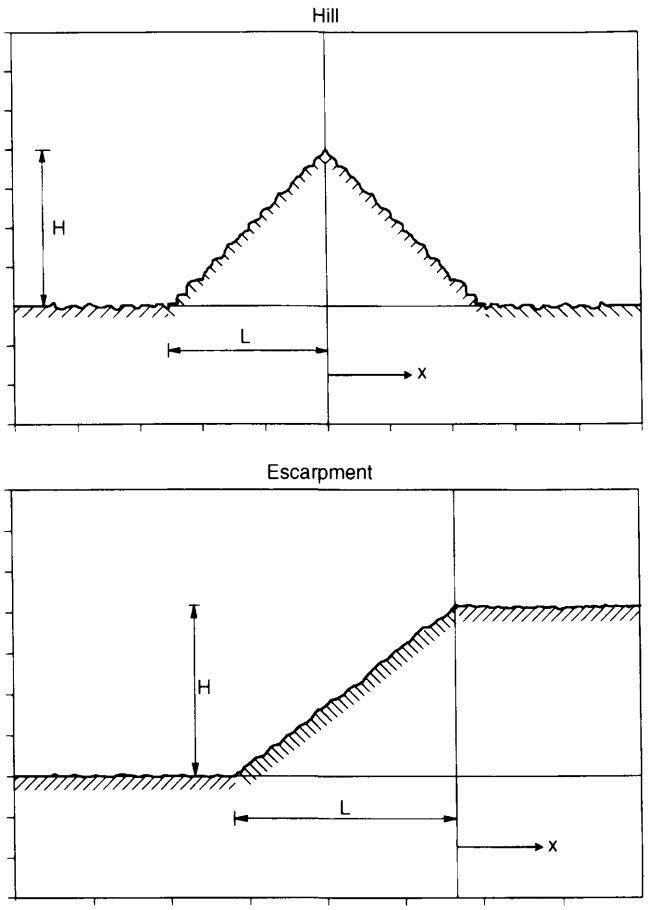

Fig. 3.15 *Hills and escarpments.*

In Eurocode 1, the factor s is presented in diagrams as a function of z/L_e and x/L, where L_e is the effective length of the upwind slope, defined by formula (3.3.3), L_u is the actual length of the upwind or downwind slope (for escarpments the downwind slope is taken as the effective length L_e). x is the horizontal distance from the top of the crest to the site, positive in the wind direction, and z is the vertical distance from the ground level of the site

$$L_e = \begin{cases} L_u & \text{for } 0.05 < \Phi < 0.3 \\ \Phi L_u/0.3 & \text{for } \Phi > 0.3 \end{cases} \tag{3.3.3}$$

The increase in speed should only be considered for locations closer than half the length of the hill slope from the crest or 1.5 times the height of the cliff.

Note: Roughness has no importance in relation to the increase in speed.

3.4 EXTREME WINDS

In the temperate zones of Europe, storms are normally caused by frontal depressions, usually passing in an easterly direction. When one storm mechanism generates the high

winds above a site, the Type 1 extreme-value distribution normally gives a good statistical representation of these extreme winds. In cases with two principal storm mechanisms, a more accurate approach is needed. Gomes and Vickery (1978) suggest separating the high winds according to their storm mechanism and then using the Type 1 distribution for each individual storm mechanism. The statistical description of high winds originating from one storm mechanism only is discussed below.

Usually, the wind load on structures is proportional to velocity pressure q defined as

$$q = \tfrac{1}{2}\rho U^2 \tag{3.4.1}$$

in which ρ is the density of the air and U is the mean wind velocity.

Normally, wind velocity as well as velocity pressure fit a Weibull distribution very well, the wind velocity being nearly Rayleigh with a Weibull shape factor of 2 and the velocity pressure being nearly exponential with a Weibull shape factor of 1. Thus, the annual extreme wind velocity and the annual extreme velocity pressure both fit an extreme value distribution of Type 1, see Appendix A for further statistical details.

The wind load on most structures depends on the velocity pressure, which gives this variable natural preference. The probability distribution function F_q^1, the mean value μ_q^1 and the standard deviation σ_q^1 of the annual extreme velocity pressure are given by

$$F_q^1(q) = \exp\left[-\exp\left(-\frac{q-\alpha_q}{\beta_q}\right)\right] \tag{3.4.2}$$

$$\mu_q^1 = \alpha_q + \gamma\beta_q \tag{3.4.3}$$

$$\sigma_q^1 = \frac{\pi}{\sqrt{6}}\beta_q \tag{3.4.4}$$

where $\gamma = 0.5772$ is Euler's constant, and α_q and β_q are the location parameter (mode) and scale parameter, respectively, that characterize the Type 1 extreme-value distribution. The 50-year extreme velocity pressure also fits an extreme-value distribution of Type 1. The mean value μ_q^{50} and the standard deviation σ_q^{50} are given by

$$\mu_q^{50} = \mu_q^1 + \beta_q \ln(50) \tag{3.4.5}$$

$$\sigma_q^{50} = \sigma_q^1 \tag{3.4.6}$$

The probability density functions of the annual extremes and the 50-year extremes are illustrated in Figure 3.16.

Velocity pressure $q(p)$ which has an annual probability of exceedence equal to $p = 1 - F_q^1(q)$, is given below, see also equation (3.4.2):

$$q(p) = \alpha_q - \beta_q \ln(-\ln(1-p)) \tag{3.4.7}$$

Thus, the ratio between the velocity pressure $q(p)$ and the 50-year velocity pressure q_{50} is given by

$$\frac{q(p)}{q_{50}} = \frac{1 - K_q \ln(-\ln(1-p))}{1 - K_q \ln(-\ln(0.98))} \tag{3.4.8}$$

where $K_q = \beta_q/\alpha_q$. Inserting typical values of α_q and β_q gives $K_q \approx 0.2$. The constant of 0.2 is specified as a representative value in Eurocode 1, which calculates the corresponding

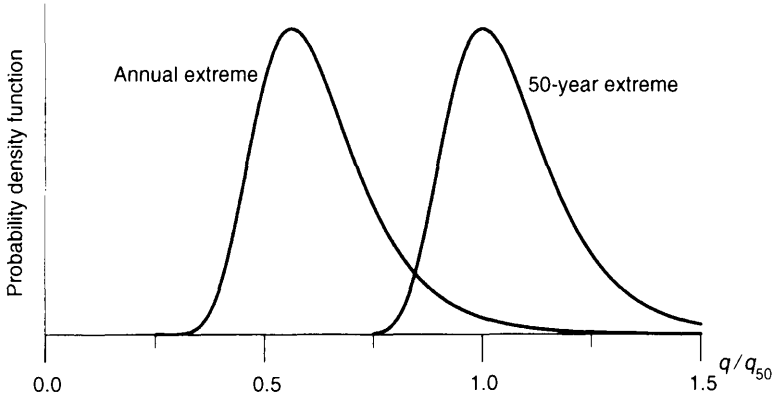

Fig. 3.16 *Probability density function of the annual extreme and the 50-year extreme velocity pressure. The standard deviation of the distributions is identical. Compared to the annual extreme, the 50-year extreme probability density function is shifted towards higher velocity pressures by* β_q ln *(50), see equation (3.4.5).*

ratio of wind velocities, $U(p)/U_{50}$, by taking the square root on both sides of the equality sign in equation (3.4.8). The influence of non-constant air density is neglected.

Definition of reference wind velocity in Eurocode 1

Reference wind velocity U_{bas} is defined as the 10-minute mean wind velocity at 10 m above terrain with the roughness length $z_0 = 0.05$ m and an annual probability of exceedence of 0.02, which corresponds to a return period of 50 years. The reference wind velocity is representative for the climate of the site.

In Eurocode 1, U_{bas} is formulated as

$$U_{bas} = c_{DIR} c_{TEM} c_{ALT} U_{bas,0} \tag{3.4.9}$$

where the symbols mean

c_{DIR} direction factor which takes into account the change of extreme winds with wind direction;

c_{TEM} temporary or seasonal factor, which may be of importance for the wind load on temporary structures or structures during construction;

c_{ALT} altitude factor which takes into account the influence of altitude on extreme winds;

$U_{bas,0}$ basic value of U_{bas}.

Information on a number of European countries is presented in an informative Annex to Eurocode 1. For most countries, the c factors in equation (3.4.9) are specified as 1. In Eurocode 1 different basic values for reference wind speeds $U_{bas,0}$ are presented. These range from 19 m/s in some regions of Sweden to 36 m/s for Greek islands and coastal zones of mainland Greece. The authors are not convinced that all reference wind speeds specified in Eurocode 1 give a correct representation of the wind climate.

The values of $U_{bas,0}$ reflect the knowledge—or perhaps the limits of knowledge—of storms experienced in Europe. This lack of knowledge is reflected in some remarkable changes in the data provided for reference wind speeds at the borders between countries. For instance in the Baltic region, the wind climate is generally homogeneous. However, Southern Sweden prescribes $U_{bas,0} = 24$–26 m/s, Denmark uses 27 m/s and coastal areas of Germany prescribe 32 m/s.

European countries have used different traditions and procedures to estimate extreme winds. Furthermore, the lack of a common understanding between meteorologists and engineers regarding basic physical extreme-wind parameters may also have contributed to the present confusion. Guidelines with clear definitions are needed if more realistic extreme winds are to be established in the future. The note "Guidance for Member States to Provide Wind Data for Incorporation into the Eurocode for Wind Actions", prepared in 1994 by an informal Eurocode 1 *ad hoc* panel on wind action, should be used as the first step towards harmonizing extreme wind estimates across national borders in Europe.

Estimation of reference wind velocity

The term "reference wind velocity" implies expectations for the future. Normally, it is based upon previous data, and as such it contains a hidden assumption that the climate will remain as it is. In other words, a possible greenhouse effect is not taken into account when estimating extreme winds.

Estimates of $U_{bas,0}$ are based on measurements taken during a period of several years. Unfortunately, as systematic collection of wind data from a larger number of positions started only a few decades ago, a considerable element of uncertainty exists and should be recognized.

Every time a storm occurs, the maximum wind is determined. Data from storms during which the maximum wind is above a certain threshold level are used for analysis. This ensures that only storms that generate extreme velocities are considered and that the storm events analysed are mutually independent.

Three basic variables can be used to characterize extreme winds: Wind velocity, wind velocity squared and velocity pressure. As the wind load on most structures depends on the velocity pressure, this variable is naturally to be preferred.

Simulations carried out by (Cook, 1985), indicate that the convergence rate of the velocity squared is much faster than the convergence rate of the wind velocity. However, the velocity pressure and the velocity squared will have similar convergence rates. Consequently, when only a limited number of observations are available, e.g. 10–20 years of data, estimates should be based on the velocity pressure used in load calculations.

Previously, wind velocity was the most typical basic variable when estimating extreme winds. However, the extreme winds specified in the Danish Code of Practice are based on velocity pressures measured by Martin Jensen and Niels Franck from 1959 to 1966. At that time it was considered a pioneering idea to base extreme winds on velocity pressure rather than on wind velocity. The detector used was a large pitot-static tube that rotated thanks to a wind vane. In this way, the pitot tube head faced into the wind at all times. According to Jensen and Franck (1970) the instrumentation time constant gave velocity-pressure averages over 3–5 seconds.

When plotted, Jensen and Franck's data showed that the extreme values of q followed an exponential distribution. It then follows from formula (A.4.18) in Appendix A that the relation between the velocity pressure q and the expected annual number ν of pressures

larger than q is

$$q = C + D \ln \nu \tag{3.4.10}$$

where C and D are parameters which should be based on the recorded data ($C > 0$ and $D < 0$). As the data used by Jensen and Franck were from a period spanning 7 years, the highest value of q corresponds to only $\nu = 1/7$. This means that a remarkable extrapolation is necessary in order to determine the reference value q_{50}, which corresponds to $\nu = 1/50$. However, analyses of wind velocities measured during a 35-year period from 1957 to 1992 show similar reference wind velocities to those obtained using the Jensen and Franck data.

Equation (3.4.10) may be written

$$\frac{q}{q_{50}} = A + B \ln \nu \tag{3.4.11}$$

where A and B are constants. Jensen and Franck's data indicate

$$\frac{q}{q_{50}} = 0.57 - 0.11 \ln \nu \tag{3.4.12}$$

If this result is used for wind speeds, neglecting possible variations in air density, the corresponding relation is:

$$\frac{U}{U_{50}} = \sqrt{0.57 - 0.11 \ln \nu} \tag{3.4.13}$$

A comparison between the Jensen and Franck expression in equation (3.4.12) and the Eurocode specification in equation (3.4.8) is shown in Figure 3.17. This is based on the annual probability of exceedence, p, being equal to

$$p = 1 - \exp(-\nu t_1) \tag{3.4.14}$$

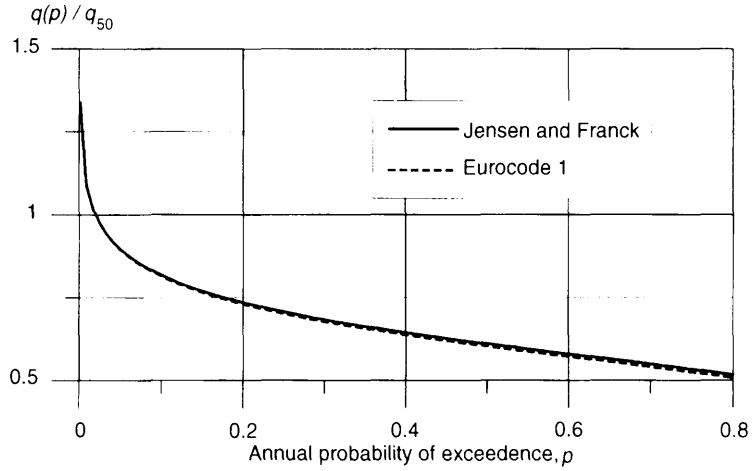

Fig. 3.17 *Comparison between the formula by Jensen and Franck and the specification in Eurocode 1 for relative velocity pressure* q/q_{50}.

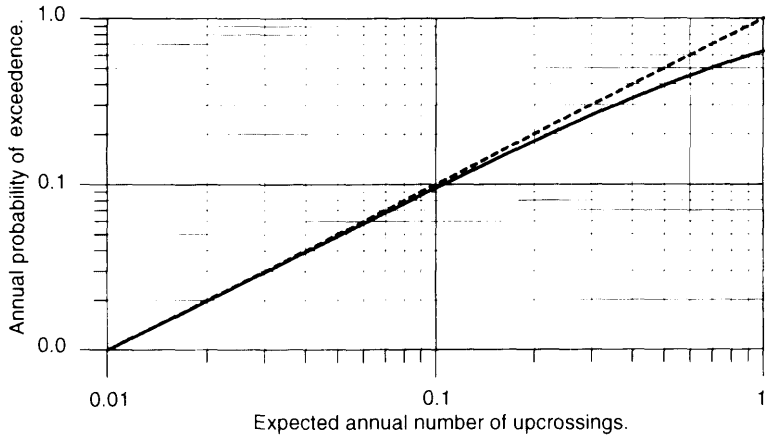

Fig. 3.18 *Annual probability of exceedence, p, as a function of the expected annual number of upcrossings, ν. The dotted line shows that the approximation $p \cong \nu$ is only valid if ν is smaller than approximately 0.1 corresponding to return periods larger than approximately 10 years.*

where $t_1 = 1$ year, see Appendix A.4. The two approaches are seen to give almost identical results for annual probabilities of exceedences shown in the figure. Equation (3.4.14) is illustrated in Figure 3.18 and gives the relation between the expected annual number of up-crossings, ν, and the annual probability of exceedence, p.

3.5 WIND TURBULENCE

The wind in the atmospheric boundary layer, i.e. natural wind, is always turbulent. This means that the flow is chaotic, with random periods varying from fractions of a second to several minutes. In order to describe a turbulent flow, statistical methods must be applied, see Appendix A.

Wind velocity is described by mean velocity U and turbulence components u, v and w, as stated in the formulas (3.1.1)–(3.1.3). The three turbulence components are described below by means of their standard deviation, time scales and integral length scales, power-spectral density functions that define the frequency distribution and normalized co-spectra that specify the spatial correlation.

Eurocode 1 specifications relating to wind turbulence are discussed in Section 3.5.5.

3.5.1 Standard deviation of turbulence components

Assuming homogeneous terrain the flow will be horizontally homogeneous, meaning that its statistical characteristics do not change in a horizontal plane. Standard deviations σ_u, σ_v and σ_w for the turbulence components will therefore only depend on the height z above ground. The three standard deviations are close to zero at geostrophic wind heights, but experimental results, e.g. Davenport (1967), Harris (1970) and Armitt (1976), show that the three standard deviations usually decrease with height very slowly up to the heights of

ordinary structures. Armitt (1976) states that the standard deviations are almost constant up to approximately half the height of the internal boundary layer. Up to a height of about 100–200 m above homogeneous terrain, the standard deviations of the three turbulence components u in the wind direction, v horizontal, perpendicular to u and w vertically, are approximately

$$\sigma_u = Au_* \qquad \sigma_v \approx 0.75\sigma_u \qquad \sigma_w \approx 0.5\sigma_u \tag{3.5.1}$$

where the constant $A \approx 2.5$ if $z_0 = 0.05$ m and $A \approx 1.8$ if $z_0 = 0.3$ m.

The turbulence intensity $I_u(z)$ for the along-wind turbulence component u at height z is defined as:

$$I_u(z) = \frac{\sigma_u(z)}{U(z)} \tag{3.5.2}$$

where $\sigma_u(z)$ is the standard deviation of the turbulence component u and $U(z)$ is the mean wind velocity, both at height z. For flat terrain, the turbulence intensity is approximately given by, see equation (3.2.2) and (3.5.1),

$$I_u(z) = \frac{1}{\ln(z/z_0)} \tag{3.5.3}$$

where z_0 is the roughness length and σ_u/u_* is assumed to be 2.5.

Up to 100–200 m above ground, it is usually reasonable to assume that the turbulence components are distributed normally (see Appendix A) with a zero mean value and standard deviations as given by equation (3.5.1). However, this does not hold for the tails of the distribution, i.e. when the turbulence components are outside a range of ±3 standard deviations. In this case, the assumption of normal distribution may lead to significant errors.

3.5.2 Time scales and integral length scales

In Figure 3.19, the most important autocorrelation function $\rho_u^T(z, \tau)$ is defined as the normalized mean value of the product of the turbulence component u at time t and u at

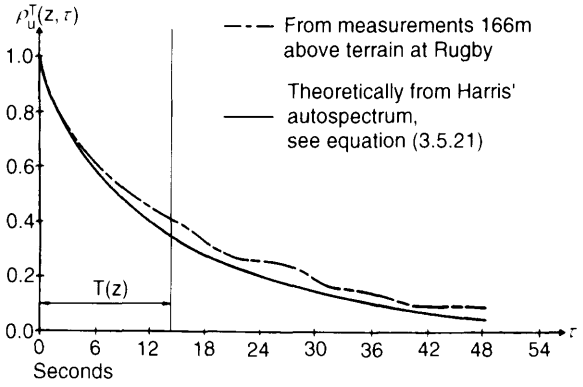

Fig. 3.19 *The autocorrelation function $\rho_u^T(z, \tau)$ (Harris, 1970). The time scale $T(z)$ is also shown. (Reproduced by permission of CIRIA).*

time $t + \tau$, see Appendix A.3:

$$\rho_u^T(z, \tau) = E\{u(x, y, z, t) \cdot u(x, y, z, t + \tau)\}/\sigma_u^2(z) \tag{3.5.4}$$

The function indicates how much information a measurement of the turbulence component $u(x, y, z, t)$ in the mean wind direction will provide about the value of $u(x, y, z, t + \tau)$ measured time τ later, at the same place.

The autocorrelation function depends only on height z above ground and on time difference τ due to the assumption of a horizontally homogeneous flow. u may be said to have a characteristic time of memory, the so-called time scale $T(z)$. Measurements of u taken at time t give a great deal of information about u at a time τ later if $\tau \ll T(z)$, but only little information, if $\tau \gg T(z)$. The formal definition of time scale $T(z)$ is

$$T(z) = \int_0^\infty \rho_u^T(z, \tau)\, d\tau \tag{3.5.5}$$

An example of an autocorrelation function is shown in Figure 3.19. A good approximate description of the autocorrelation function is (τ positive):

$$\rho_u^T(z, \tau) = \exp(-\tau/T(z)) \tag{3.5.6}$$

Integral length scales are a measure of the sizes of the vortices in the wind, or in other words the average size of a gust in a given direction. As an example, L_u^x is the integral length scale for the turbulence component u measured in the longitudinal direction x. Formally, it is defined similarly to the time scale in formula (3.5.5), i.e.:

$$L_u^x = \int_0^\infty \rho_u(z, r_x)\, dr_x \tag{3.5.7}$$

in which $\rho_u(z, r_x)$ is the cross correlation function (see Appendix A.3) between the turbulence component u in two points separated longitudinally by a distance r_x and measured simultaneously.

Taylor's hypothesis of convected "frozen turbulence", see (Batchelor, 1953), is normally considered to be an accurate approximation in natural wind. Using this assumption, temporal variations are obtained via a translation of "frozen turbulence" with the mean wind velocity. According to Taylor's hypothesis, a statistical description of temporal turbulence variations could be based on spatial wind velocity field characteristics and vice versa.

According to Taylor's hypothesis, $\rho_u(z, r_x) = \rho_u^T(z, \tau)$, for $r_x = U(z)\tau$, indicating that the longitudinal integral length scale is equal to the time scale multiplied by the mean wind velocity, $L_u^x(z) = U(z)T(z)$.

In total, 9 integral length scales are defined similarly as shown in equation (3.5.7):

For the longitudinal turbulence component u :	L_u^x	L_u^y	L_u^z
For the lateral turbulence component v :	L_v^x	L_v^y	L_v^z
For the vertical turbulence component w :	L_w^x	L_w^y	L_w^z

Full-scale measurements are used to estimate integral length scales. However, results show extensive scatter originating mainly from the variability of length and degree of

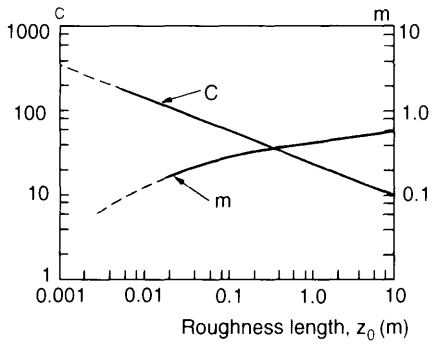

Fig. 3.20 *Values of C and m as functions of surface roughness z_0 (Counihan, 1975). C and m are used to calculate the integral length scale in equation (3.5.8). (Reproduced by permission of Pergamon Press).*

stationarity of the records being analysed. The integral length scales depend on the height z above ground and on the roughness of the terrain, i.e. roughness length z_0. The wind velocity may also influence the integral length scales at a site.

Counihan (1975) has suggested the following purely empirical expression for the longitudinal integral length scale at heights z in the range of 10–240 m:

$$L_u^x = Cz^m \tag{3.5.8}$$

where C and m depend on roughness length z_0 as shown in Figure 3.20, and z and L_u^x are stated in metres. According to Counihan, integral length scales decrease with increasing surface roughness. The opposite variation is specified by ESDU 85020. Integral length scales are discussed further in Section 6.6.1.

The remaining integral length scales are often expressed as a function of longitudinal integral length scale L_u^x. Simultaneous measurements of longitudinal wind velocities in a plane perpendicular to the mean wind direction indicate exponential decaying cross correlation functions given by:

$$\rho_u(r_y) = \exp(-r_y/L_u^y) \tag{3.5.9}$$

$$\rho_u(r_z) = \exp(-r_z/L_u^z) \tag{3.5.10}$$

with integral length scales of $L_u^y \approx 0.3L_u^x$ and $L_u^z \approx 0.2L_u^x$.

3.5.3 Power-spectral density function

The frequency distribution of turbulent along-wind velocity component u is described by the non-dimensional power spectral density function $R_N(z, n)$ defined as:

$$R_N(z, n) = \frac{nS_u(z, n)}{\sigma_u^2(z)} \tag{3.5.11}$$

where n is the frequency in hertz and $S_u(z, n)$ is the power spectrum for the along-wind turbulence component.

Turbulent energy is generated in large eddies (low frequencies) and dissipated in small eddies (high frequencies). In the intermediate region, called the inertial subrange, the

turbulent energy production is balanced by turbulent energy dissipation, and the turbulent energy spectrum is independent of the specific mechanisms of generation and dissipation. Assuming Taylor's hypothesis of "frozen turbulence", and considering frequencies in the inertial subrange, the non-dimensional power spectrum function R_N is given by:

$$R_N(z, n) = A f_L^{-2/3} \tag{3.5.12}$$

where A is a constant depending slightly on height, the non-dimensional frequency $f_L = nL(z)/U(z)$, and $L(z)$ is a height-dependent length scale of the turbulence. Close to the ground, the height z can be used as the turbulent length scale, indicating that $R_N \propto f_z^{-2/3}$, where the non-dimensional frequency $f_z = nz/U(z)$ is known as the Monin similarity coordinate.

The constant A defined in equation (3.5.12) should be based on full-scale spectral density functions measured at different heights, preferably using the integral length scale in the high-frequency behaviour calculated by equation (3.5.12), i.e. $L(z) = L_u^x(z)$. This facilitates the use of the comprehensive data sources on integral length scales published in the literature. According to ESDU 85020, A is a function that decreases slowly with height. For structures with heights of up to 200–300 m, spectral density functions are obtained within approximately 5% accuracy using $A = 0.14$ for all heights assuming $L(z) = L_u^x(z)$.

The turbulent eddies at very low frequencies scale with the boundary layer height. For most structures, these low-frequency fluctuations give no significant response contributions. The spectral density functions considered below do not focus thoroughly on this aspect.

Kaimal spectral density form for the longitudinal turbulence component

A simple and commonly used spectral density with the correct high-frequency behaviour as indicated in equation (3.5.12) was proposed by Kaimal *et al.* (1972) and also quoted by Simiu and Scanlan (1986):

$$R_N(z, n) = \frac{\frac{2}{3}\lambda f_z}{(1 + \lambda f_z)^{5/3}}; \qquad \lambda = 50 \tag{3.5.13}$$

where the non-dimensional parameter λ serves to locate the maximum value of the spectral density obtained for

$$f_z = f_{z,\max} = \frac{3}{2\lambda} \tag{3.5.14}$$

The integral length scale L_u^x obtained using the spectral density function is equal to

$$L_u^x(z) = U(z)T(z) = \frac{U(z)}{4}\frac{S_u(z, 0)}{\sigma_u^2(z)} = \frac{1}{6}\lambda z \tag{3.5.15}$$

Except for low heights of up to approximately 50 m, the integral length scales defined in Section 3.5.2 are not proportional to height z as indicated in equation (3.5.15). For such cases f_z in the spectral density function should be replaced by

$$f_L = nL_u^x(z)/U(z) \tag{3.5.16}$$

and λ changed to 10.2 in order to obtain $A = 0.14$, see equation (3.5.12). This gives the following spectral density expression:

$$R_N(z, n) = \frac{6.8 f_L}{(1 + 10.2 f_L)^{5/3}} \tag{3.5.17}$$

where f_L in equation (3.5.16) should be calculated using the integral length scale L_u^x given in Section 3.5.2. This spectrum is used in Eurocode 1.

This simple spectral form may be used for structures with a fundamental natural frequency of vibration higher than the frequency corresponding to the lower end of the inertial subrange. It gives an accurate representation of the turbulent fluctuations in the frequency range of interest for most structures. For structures with very low natural frequencies, e.g. flexible offshore structures, a more accurate spectral density representation of the low frequency range is called for, see for instance Højstrup *et al.* (1990) for a description of the low-frequency part of the spectrum.

Other proposed spectral density forms for the longitudinal turbulence component

Several other power-spectral density functions have been suggested in the literature; see Figure 3.21 illustrating the different functions.

The non-dimensional von Kármán power-spectral density function can be written as shown below, see (von Kármán, 1948):

$$R_N(z, n) = \frac{4 f_L}{(1 + 70.8 f_L^2)^{5/6}} \tag{3.5.18}$$

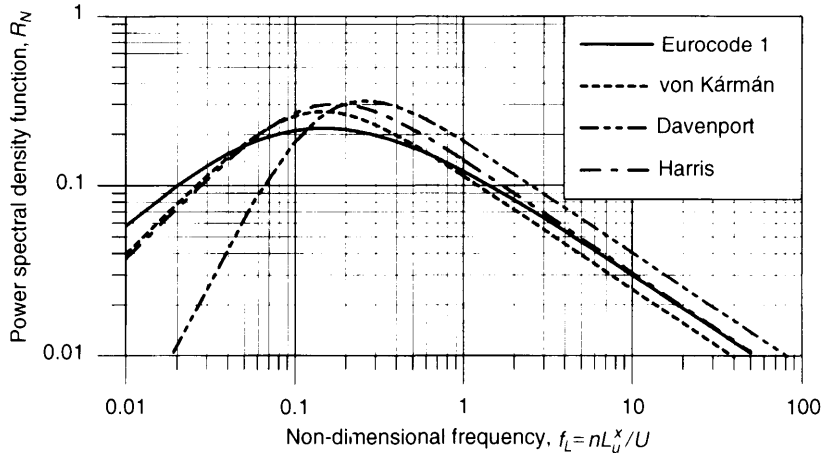

Fig. 3.21 *Power-spectral density functions for the longitudinal turbulence component. The integral length scale L_u^x has been assumed to be 180 m when plotting the spectra suggested by Davenport (3.5.20) and Harris (3.5.21). For $f_L >$ approximately 0.2, the Davenport spectrum gives the largest spectral values. Compared to Eurocode 1 (3.5.17) the von Kármán spectrum (3.5.18) gives slightly lower spectral values for $f_L >$ approximately 1, see also Section 3.5.5.*

where the non-dimensional frequency is given by equation (3.5.16). The maximum value of the spectral density is obtained for

$$f_L = f_{L,\max} = \frac{\sqrt{3/2}}{\sqrt{70.8}} = 0.146 \tag{3.5.19}$$

The von Kármán power spectral density function gives $A = 0.115$, which is slightly less than the value of 0.14 recommended earlier, see equation (3.5.12). Harris (1990) discusses the von Kármán power spectral density function thoroughly, and introduces a systematic modification of the spectrum using a functional series, which uses two terms to give an accurate flow representation.

Davenport (1967) has suggested

$$R_N(z, n) = \frac{2}{3} \frac{f_L^2}{(1 + f_L^2)^{4/3}} \tag{3.5.20}$$

with the non-dimensional frequency $f_L = nL/U(z)$, where $L \approx 1200$ m. Harris (1970) has suggested

$$R_N(z, n) = \frac{2}{3} \frac{f_L}{(2 + f_L^2)^{5/6}} \tag{3.5.21}$$

with the non-dimensional frequency $f_L = nL/U(z)$, where $L \approx 1800$ m.

Power spectra of lateral and vertical turbulence components

The power spectra of the lateral and vertical turbulence components are approximately given by (see Simiu and Scanlan, 1986)

$$\frac{nS_v(z, n)}{u_*^2} = \frac{15 f_z}{(1 + 9.5 f_z)^{5/3}} \tag{3.5.22}$$

$$\frac{nS_w(z, n)}{u_*^2} = \frac{3.36 f_z}{1 + 10 f_z^{5/3}} \tag{3.5.23}$$

Conclusion

As shown in Figure 3.21, several power-spectral density functions have been suggested for the longitudinal turbulence component. Except for structures with very low natural frequencies, such as flexible offshore structures, the spectral values for frequencies in the inertial subrange are the most important. The spectral density expression given in equation (3.5.17) satisfies the inertial subrange criterion specified by ESDU 85020, i.e. $A = 0.14$ and $L(z) = L_u^x(z)$ in equation (3.5.12). Appropriate choices of length scale could also bring the other spectral density functions proposed into agreement with the inertial subrange criterion mentioned.

3.5.4 Correlation between turbulence at two points

The normalized cross-spectrum describes the statistical dependence between the turbulence components at two points at a given frequency n, as mentioned in Appendix A. This dependence is due to the spatial dimension of the vortices in the wind field.

The spatial distribution of the along-wind turbulence component is described by the dimensionless normalized cross-spectrum S_N:

$$S_N = \frac{S_{uu}(P_1, P_2, n)}{\sqrt{S_u(P_1, n) S_u(P_2, n)}} \tag{3.5.24}$$

where S_{uu} is the cross-spectrum of the two longitudinal turbulence components at points P_1 and P_2, respectively, i.e. a complex quantity. S_u is the power spectrum of longitudinal turbulence component in the point specified by the argument of P.

The real part of the normalized cross-spectrum is called the normalized co-spectrum ψ_u and the imaginary part is called the normalized quad-spectrum. The root-coherence function is defined as the absolute value of the normalized cross-spectrum $\sqrt{Coh} = |S_N|$.

The normalized co-spectrum and the root-coherence function are identical, when the phase spectrum is zero. The present description focuses on the normalized co-spectrum, since this is the fundamental function to be used in response calculations.

The normalized co-spectrum ψ_u must decrease with the distance r between the two points considered. This decrease depends on the size of the vortices, and a measure of size is the ratio between the mean wind velocity and the frequency, U/n.

The value of the normalized co-spectrum at zero frequency is of no relevance to the correlation of mean wind velocities, as they are removed from the wind data before the normalized co-spectrum is determined. As mentioned in Section 2.1, the variations of mean wind velocities are expressed by the wind climate component, which is analysed independently of the turbulence in the atmospheric boundary layer.

Exponential format

On a purely empirical basis, Davenport (1962) originally suggested an exponential expression as the normalized co-spectrum and a phase-spectrum of zero:

$$\psi_u(r, n) = \exp(-Crn/U) \tag{3.5.25}$$

where C is a non-dimensional decay constant that determines the spatial extent of the correlation in the turbulence.

For two points with transverse separation (r_y, r_z), Davenport (1977) extended the expression to allow for different normalized co-spectrum decays horizontally and vertically, respectively:

$$\psi_u(r_y, r_z, n) = \exp\left(-\frac{n}{U}\sqrt{(C_y r_y)^2 + (C_z r_z)^2}\right) \tag{3.5.26}$$

where the mean wind velocity used in the exponential expression is the mean value of the wind velocities at the two points considered, $U = \frac{1}{2}(U(z_1) + U(z_2))$, and C_y and C_z are non-dimensional decay constants. When choosing numerical values for the decay constants, due consideration must be given to the fact that surface pressures are better correlated than the turbulence in the undisturbed wind field. Typical values are $C_y = 10$ and $C_z = 10$.

The format of (3.5.25) and (3.5.26) has the advantage of simplicity, but incorporates two inconsistencies:

1. The function is positive for any separations leading to a positive value of the co-spectrum integral over the plane perpendicular to the mean wind velocity. This is in conflict with the definition of the longitudinal turbulence component with a zero mean.
2. The normalized co-spectrum approaches unity for small frequencies, n. This is not true for separations of the same order of magnitude or even larger than the average size of gusts, where the wind structure is characterized by a lack of correlation even at low frequencies. Furthermore, the size of the normalized co-spectrum at large separations and at low frequencies can be quite important in connection with the response of several types of structures. This aspect is demonstrated in Chapter 6 for a cantilevered bridge during construction.

Modified exponential format

Assuming locally isotropic turbulence, Krenk (1995) has derived a simple modified exponential format not encumbered by the two inconsistencies mentioned above. It is based on a generalized form of the von Kármán spectrum given by

$$S_u(n) = \frac{S_0}{(1 + (2\pi nL/U)^2)^\gamma} \tag{3.5.27}$$

where S_0 is a constant, L is a length scale and the parameter γ determines high-frequency behaviour. For $\gamma = 5/6$, the length scale is $L = 1.34L_u^x$, see equation (3.5.18). The normalized co-spectrum determined by Krenk (1995) is as follows:

$$\psi_u(\kappa_1 r) = \frac{2}{\Gamma(\gamma)}\left[\left(\frac{\kappa_1 r}{2}\right)^\gamma K_\gamma(\kappa_1 r) - \left(\frac{\kappa_1 r}{2}\right)^{\gamma+1} K_{1-\gamma}(\kappa_1 r)\right] \tag{3.5.28}$$

where Γ is the gamma function, K_γ and $K_{1-\gamma}$ are modified Bessel functions of the second kind and the modified wave number κ_1 is given by

$$\kappa_1 = \sqrt{\left(\frac{2\pi n}{U}\right)^2 + \left(\frac{1}{L}\right)^2} \tag{3.5.29}$$

For $\gamma = 5/6$ the Bessel-type expression for the normalized co-spectrum in equation (3.5.28) corresponds to that given by Kristensen and Jensen (1979) and Harris (1970). However, Harris (1970) used another argument definition that corresponded with the spectral representation he suggested, see equation (3.5.21) . The normalized co-spectrum form given in equation (3.5.28) with $\gamma = 5/6$ is also suggested by ESDU 86010 using a height-dependent length scale parameter. This is an attempt to include the lack of isotropy in natural wind originating from boundary layer shear flow and blocking caused by the surface.

For $\gamma = 1/2$ the normalized co-spectrum takes the simple form:

$$\psi_u(\kappa_1 r) = (1 - \tfrac{1}{2}\kappa_1 r)\exp(-\kappa_1 r) \tag{3.5.30}$$

which leads directly to the modified exponential format allowing for different horizontal and vertical decay constants of C_y and C_z, see Krenk (1995):

$$\psi_u(r_y, r_z, n) = \left(1 - \frac{1}{2}\frac{n_x}{U}\sqrt{(C_y r_y)^2 + (C_z r_z)^2}\right)\exp\left(-\frac{n_x}{U}\sqrt{(C_y r_y)^2 + (C_z r_z)^2}\right) \tag{3.5.31}$$

where the modified frequency n_x is

$$n_x = \sqrt{n^2 + \left(\frac{U}{2\pi L}\right)^2} \tag{3.5.32}$$

The two inconsistencies mentioned above are removed using this expression in cases involving the normalized co-spectrum. The co-spectrum integral over the plane perpendicular to the mean wind velocity is zero and for frequencies approaching zero, the normalized co-spectrum approaches a value of less than 1 for separations larger than zero.

The modified exponential format and the traditional exponential format are compared with full-scale measurements in Figure 3.22. The implications for structural response are considered thoroughly in Chapter 6.

The isotropic turbulence model used above quite accurately describes the spectra and cross-spectra for high frequencies and small separations compared to the length scale of the turbulence. When low-frequency components and large separations are of primary interest, a more accurate turbulence model should be used. (Mann and Krenk, 1994) and (Mann, 1994) describes a turbulence model in which the effect of shear in natural wind is taken into account by the rapid distortion theory. The influence of surface blocking is also included in the model. Compared to the isotropic model, an eddy-lifetime constant is introduced to give a more accurate second-order, two point statistical description of the air flow. Spectra and cross-spectra calculated by this model match well with full-scale measurements and wind tunnel test results. However, using this model requires numerically complex calculations beyond the scope of the simple representation proposed here.

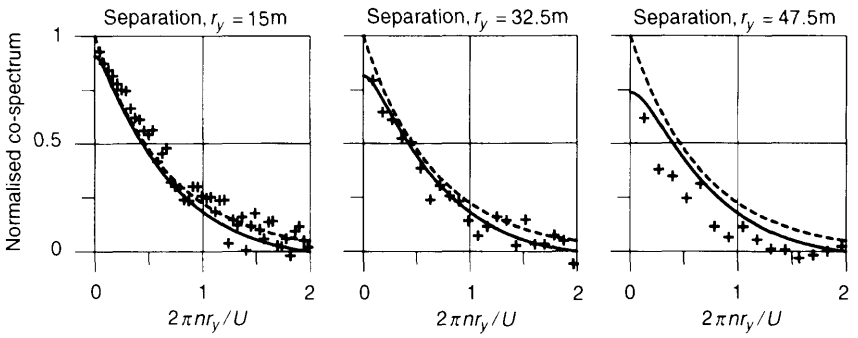

Fig. 3.22 *Normalized co-spectrum as a function of wave number $2\pi n/U$ multiplied by the separation r_y. The full-scale data shown in the figure by + have been measured at lateral separations of 15 m, 32.5 m and 47.5 m, respectively, at a height of 70 m above sea at a mean wind velocity of approximately 22 m/s, see Mann (1994). The solid lines show the modified exponential format given in equation (3.5.31) using $C_y = C_y^M = 2\pi$ and $L = 1.34L_u^x = 240$ m according to the integral length scale given in equation (6.6.2). The dotted lines represent the simple exponential function, see equation (3.5.26), using $C_y = C_y^E = 3\pi$. The modified exponential format is seen to give a better representation of the full-scale data than the simple exponential function, especially when the two points are far apart. (After Hansen and Krenk (1996)). The normalized co-spectra measured were supplied by Risø National Laboratory, Denmark.*

3.5.5 Wind turbulence according to Eurocode 1

The turbulence intensity given in equation (3.5.3) is also specified in Eurocode 1.

The Eurocode non-dimensional power-spectral density function $R_N(z, n)$ has the form indicated in equation (3.5.17):

$$R_N(z, n) = \frac{6.8 f_L}{(1 + 10.2 f_L)^{5/3}} \tag{3.5.33}$$

where $f_L = nL_u^x(z)/U(z)$. It has the correct high-frequency behaviour with $A = 0.14$, see equation (3.5.12), using the integral length scale L_u^x calculating the non-dimensional frequency f_L. The integral length scale L_u^x used in the Eurocode is based on ESDU 74031. Later ESDU updates of turbulent length scales may provide more accurate response estimates.

The normalized co-spectrum ψ_u specified in the Eurocode is based on equation (3.5.26). Decay constants of C_y and C_z are specified to be 11.5, based on a very large number of full-scale measurements, (see Solari, 1993). The value of 11.5 is, apparently, the average value of the measurements, rather than a fractile. The fact that pressures on the structure are better correlated than the longitudinal turbulence in the undisturbed, oncoming air flow has apparently not been taken into account in the choice of decay constants; see Section 6.7 for further discussions.

4 Static Wind Load

For many structures, the wind-induced resonant vibrations are negligible and the fluctuating wind responses can be calculated using procedures applicable for static loads. Since the majority of buildings belong to this category, the so-called static wind load is very important in connection with stress calculations and design.

In 1687, Isaac Newton (1642–1727) discovered that the load on a fixed body in a flow is proportional to the flow velocity squared. This fact is still considered to be correct for sharp-edged bodies, and also for curved structures in certain Reynolds number regions.

In 1738, Daniel Bernoulli published his *Hydrodynamica* with its famous physical interpretation of the equation:

$$p + \tfrac{1}{2}\rho U^2 = \text{constant along a streamline} \tag{4.1}$$

This specifies that the sum of the static pressure p and the velocity pressure $\frac{1}{2}\rho U^2$ is constant along a streamline.

In 1755, Euler was the first to formulate general flow equations as we know them today.

4.1 EXTREME STATIC LOAD

Mean wind velocity is superimposed by wind turbulence varying in space and time, and probabilistic methods are used to describe the wind field. Turbulence gives a fluctuating contribution to the wind load, which depends on structural geometry and on other parameters. Wind loads on structures, therefore, always fluctuate.

The largest wind load occurring during a storm period of say 10 minutes is a sample in a statistical distribution with a mean value which we call the characteristic wind load, see Section 4.6. The characteristic wind load, $F_{\max}$, is expressed by the 10-minute mean wind load F_q plus a peak factor k_p multiplied by the 10-minute standard deviation σ_F:

$$F_{\max} = F_q + k_p \sigma_F \tag{4.1.1}$$

The characteristic structural response, such as stress or deflection, could also be expressed as a mean structural response plus a peak factor multiplied by the standard deviation of the structural response considered. The term "equivalent static load" is defined as the static load that gives a structural response equal to the characteristic response of the structure or structural component due to the actual, fluctuating wind load.

The mean wind load depends on the mean wind velocity. Its variation during a given period is, therefore, relatively slow.

In the simple load model presented in Section 4.4, the load fluctuations are proportional to twice the along-wind turbulence intensity I_u defined in Section 3.5. The standard deviation σ_F may be expressed as

$$\sigma_F = F_q 2I_u \sqrt{k_b} \tag{4.1.2}$$

indicating that the gust factor φ, defined by the ratio between the characteristic wind load F_{max} and the mean wind load F_q, is equal to:

$$\varphi = \frac{F_{max}}{F_q} = 1 + k_p 2I_u \sqrt{k_b} \tag{4.1.3}$$

The background turbulence factor k_b is an integral measure of the load reduction due to a lack of surface pressure correlation for large structures. k_b is equal to 1 for point-like structures. Turbulent eddies with a size larger than, or the same size as, the structure or structural component considered, contribute to k_b. Normally, the effect of eddies that are considerably smaller than the structure is negligible.

In many codes, the extreme responses on finite areas of the structure are estimated using the concept of "equivalent static gust". The time series of either the fluctuating velocity pressure in the undisturbed wind or of the surface pressure measured at a point is filtered using running averaging to remove high-frequency fluctuations lasting for periods shorter than typically 5 to 15 seconds. The cut-off frequency is chosen in accordance with the size of the structural area in question.

"Equivalent static gust" has been widely used in many countries during approximately the last 30 years, e.g. in the United Kingdom, where a great deal of research has been carried out regarding wind load on low-rise structures. The procedure is attractive due to its simple way of dealing with area-averaging of fluctuating wind loads. It seems, however, that the implementation of the procedure needs adjustments in order to improve its accuracy. This is discussed further in Section 4.5.

Cook (1985, 1990) gives a very comprehensive description of the state of the art and includes pressure coefficients for a wide variety of structures.

The procedure for dealing with extreme static loads in Eurocode 1 is discussed in Section 4.8.

4.2 WIND LOAD ON BUILDINGS

When the undisturbed air flow approaches a building, it is forced around and over the building. This creates areas of pressure or suction on the building facades, gables and roof. Pressure and suction refer to air pressures above and below barometric pressure levels, respectively. Pressure is marked by plus and suction is marked by minus in the following figures.

Wind perpendicular to building facades

Wind loads on roofs depend on the roof shape. On a pitched roof with a slope exceeding approximately 35°, there will be pressure on the windward part of the roof and suction on the leeward part of the roof, see Figures 4.1–4.2. For flat roofs and for pitched roofs with a slope of less than 15°, suction affects the whole roof.

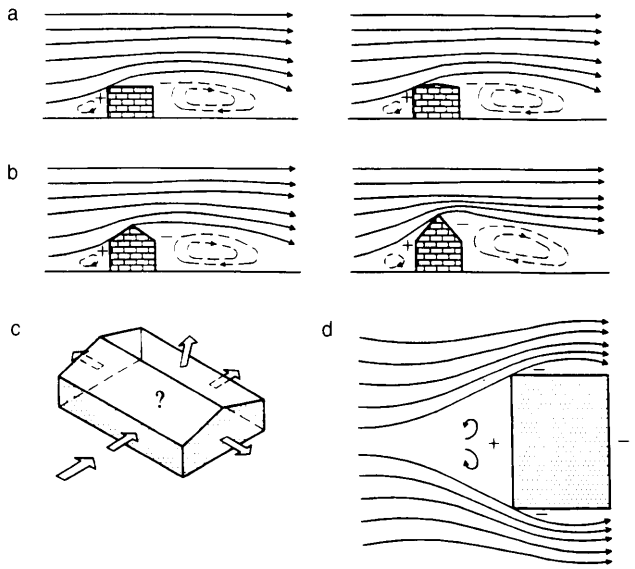

Fig. 4.1 *Wind load on external walls and pitched roof. The direction of the wind is perpendicular to the longitudinal direction of the building. (Reproduced by permission of Danish Building Research Institute) .*

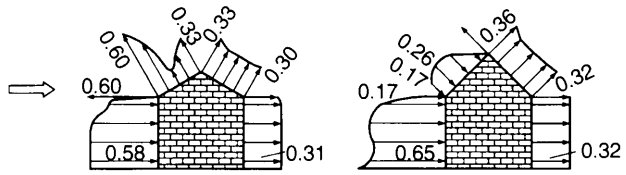

Fig. 4.2 *Distribution of pressure and suction on pitched roofs with 30° and 45° inclinations, respectively (Jensen, 1959).*

For pitched roofs with a slope of between 15° and 30°, suction as well as pressure may occur on the upwind part of the roof. Eurocode 1 includes this by giving two load cases, one specifying suction and one specifying pressure on the upwind part of the roof.

Canopy roofs are subject to vertical, lifting forces below the windward canopy. This load acts with the wind load on the upper roof surfaces.

The flow pattern around a building with a 30° pitched roof is illustrated in Figure 4.3. From a point on the surface in front of the building, the wind field is divided into two parts. One part consists of the approaching, undisturbed wind passing above the roof of the building. The other part includes the vortices generated in front of the building and behind the building. When the roof slope is below 15°, there will also be strong vortices above the windward part of the roof.

Wind parallel with building facades

When the wind flows along building facades, suction will always affect the roof. The greatest suction is obtained close to the upwind gable end.

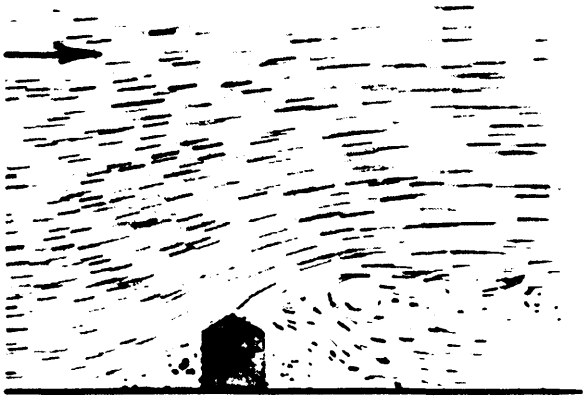

Fig. 4.3 *Streamlines of wind perpendicular to the longitudinal direction of the building (Jensen, 1959).*

Suction on pitched roofs is much greater than the suction on hipped roofs, see Figure 4.4. This effect is very pronounced when considering roof failures in hurricane areas. Failures are often prevented on structures with hipped roofs, whereas many flat roofs and pitched roofs are blown off during strong hurricanes. If this aspect was incorporated into the building traditions of areas prone to severe hurricanes, the number of low-rise structural failures in these areas could be reduced in the future.

Skew wind

When skew wind approaches the building, extreme levels of suction may occur locally on the roof close to the upwind corner of the building, see (Cook, 1990).

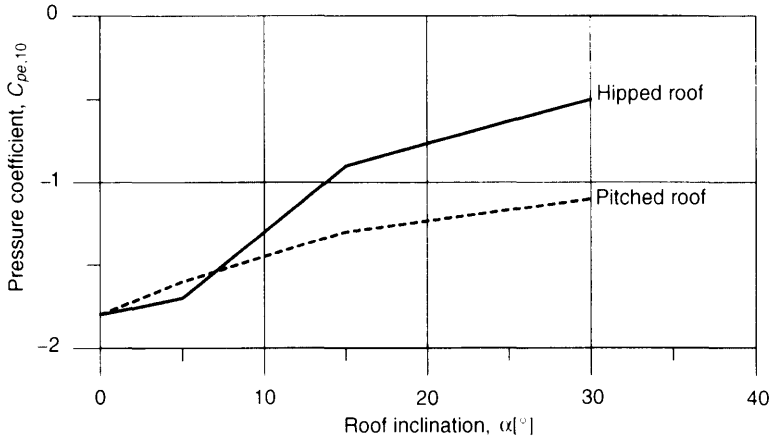

Fig. 4.4 *Suction on pitched roofs and hipped roofs, respectively, based on Eurocode 1. The hipped roof has the same roof inclination at facades and gable ends. The wind direction is along the building and the pressure coefficients shown refer to suction on roof areas of 10 m^2 at the upwind roof corner.*

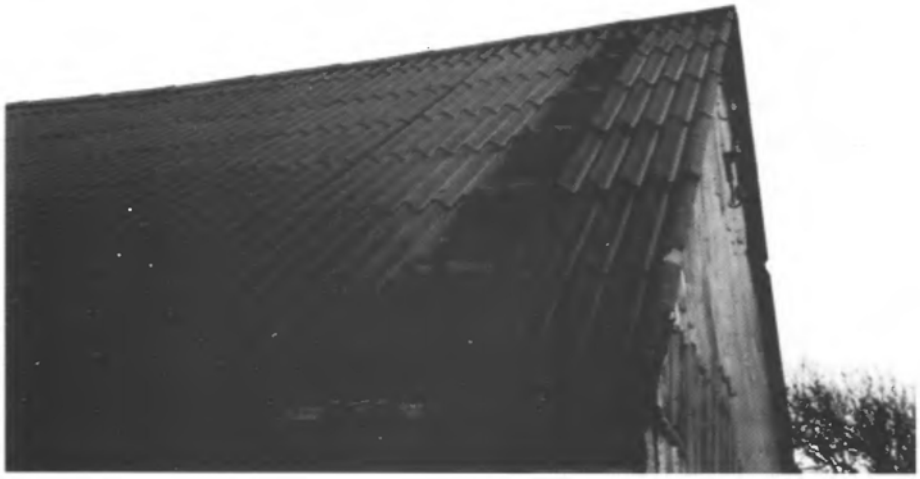

Fig. 4.5 *When the wind blows along the building, the foremost part of the roof is subjected to considerable suction. (Reproduced by permission of Danish Building Research Institute. Photo: H.H. Knutsson).*

Fig. 4.6 *When the wind blows perpendicular to the longitudinal direction of the building, the ridge is prone to a considerable amount of suction. (Reproduced by permission of Danish Building Research Institute. Photo: H.H. Knutsson).*

Fig. 4.7 *When the wind approaches the gable, the roof at the corner is worst hit by suction. (Reproduced by permission of Danish Building Research Institute. Photo: H.H. Knutsson).*

Fig. 4.8 *Suction lifted the roof off entirely and the curtain was sucked out before the roof settled back in position. This could have been avoided if the roof had been properly anchored. (Reproduced by permission of Danish Building Research Institute. Photo: H.H. Knutsson).*

Storm accidents on roofs

Suction effects on roofs are illustrated by photographs taken in Denmark after the storm that occurred in the North Sea region on 24 November 1981, see Figures 4.5–4.8.

4.3 WIND LOAD AT A SURFACE POINT— A MATHEMATICAL DESCRIPTION

Normally, extreme pressure or suction, F, at a point on a structure is calculated using the following expression:

$$F = C_p \tfrac{1}{2}\rho U_d^2 \tag{4.3.1}$$

where the pressure coefficient C_p is defined as the ratio between the extreme pressure or suction on the building surface and the design velocity pressure of the undisturbed, approaching air flow. The design velocity pressure used, $\frac{1}{2}\rho U_d^2$, corresponds to a certain representative reference height above ground, typically the roof height, see Section 4.8. It is an extreme estimate based on the instantaneous velocity pressure $\frac{1}{2}\rho U_{\text{tot}}^2$, see equation (4.4.3), using a characteristic averaging time, depending on the actual surface area considered. Typically, averaging times are of the order of 1–10 seconds, depending on the code considered.

The wind load at a point fluctuates with time due to air turbulence and other effects, see Figure 4.9. This will be considered further in connection with the determination of the total wind load on a structure in Section 4.4.

Normally, pressure coefficient C_p is determined by model tests in a wind tunnel, see Chapter 10. Fluctuating pressures on the structure are measured for different wind directions. The characteristic pressure and suction at each point are determined by a

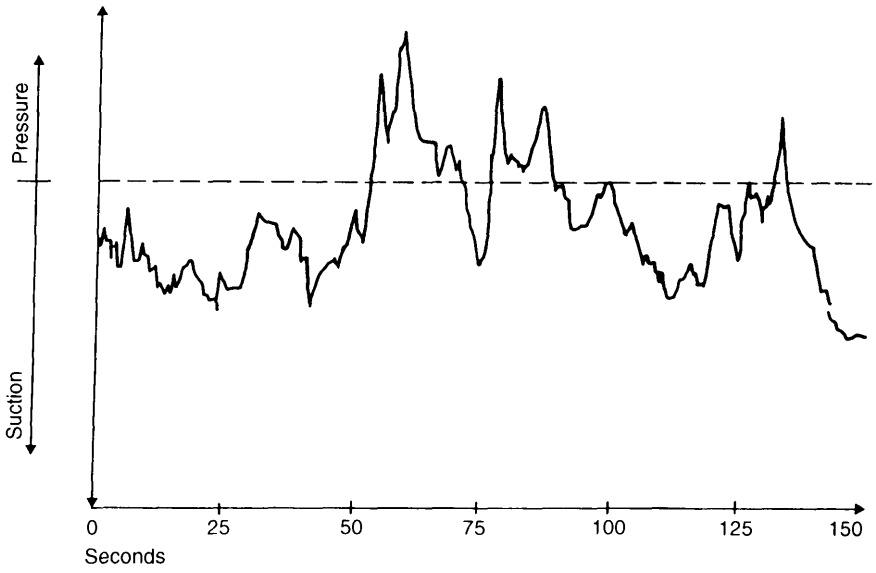

Fig. 4.9 *Wind pressure measured at a point on a structure (Dalgliesh et al., 1967). Suction is dominant. (Reproduced by permission of National Research Council, Canada/Institute for Research in Construction).*

statistical analysis of the fluctuating signals measured. Different statistical methods to determine the characteristic values have been proposed in the literature, see e.g. Cook (1990). Careful consideration must be given as to whether specific wind-tunnel test data published in the literature or in codes are valid in a specific real-life situation.

4.4 TOTAL WIND LOAD ON A STRUCTURE — DAVENPORT'S MODEL

In the early sixties, Davenport (1962) proposed a model for calculating fluctuating wind load on a structure located in the atmospheric boundary layer. The fluctuating wind load calculated is based on a statistical description of the turbulence characteristics of the undisturbed air flow approaching the structure. The turbulence characteristics are combined with aerodynamic admittance functions that convert the air flow properties into wind load on the structure. The model was originally proposed in relation to along-wind vibrations of dynamically sensitive structures, but it is also an important tool for calculating the wind load on static structures. Davenport's model is still widely used, and is described below.

Wind load on a small surface area or point-like structure

A structure can be called small and point-like when its characteristic size is much smaller than the wavelengths of the significant eddies in the natural wind. The characteristic size of a structure may be defined in different ways, for instance as the square root of the wind-exposed area A or as the diagonal dimension of A. Assuming quasistatic aerodynamics, the total wind load on the structure, F_{tot}, is given by:

$$F_{\text{tot}} = C_A A \tfrac{1}{2} \rho U_{\text{tot}}^2 \tag{4.4.1}$$

$$U_{\text{tot}}^2 = (U + u)^2 + v^2 + w^2 \tag{4.4.2}$$

where the shape factor C_A describes the ratio between the wind load per unit of area A and the instantaneous velocity pressure $\frac{1}{2}\rho U_{\text{tot}}^2$, where U_{tot} is the resulting wind velocity. Normally, the mean wind velocity U is much greater than the absolute value of the turbulence components u, v and w. A good approximation is, therefore, expressed by:

$$U_{\text{tot}}^2 = U^2 + 2Uu \tag{4.4.3}$$

Using equation (4.4.3), the standard deviation σ_q of the velocity pressure is calculated to be $q2I_u$, where q is the mean velocity pressure $\frac{1}{2}\rho U^2$ and I_u is the along-wind turbulence intensity defined in Section 3.5. The characteristic velocity pressure, $q_{\max}$, during a time interval is expressed as the mean velocity pressure q plus the peak factor k_p multiplied by the standard deviation of the velocity pressure σ_q, i.e.:

$$q_{\max} = q + k_p \sigma_q = q(1 + k_p 2I_u) \tag{4.4.4}$$

The total wind load, F_{tot}, is found by adding the mean wind load, F_q, and the fluctuating wind load, F_t, with a mean of zero:

$$F_{\text{tot}} = F_q + F_t \tag{4.4.5}$$

$$F_q = C_A A \tfrac{1}{2} \rho U^2 \tag{4.4.6}$$

$$F_t = C_A A \rho U u \tag{4.4.7}$$

The mean wind load, as well as the instantaneous wind load, may be determined by a vector summation of the wind load contributions on the structural surface. However, except for small surface areas, the extreme wind load cannot be calculated by a vector summation of extreme surface pressures, since the extreme values of the individual surface pressures occur at different times.

The power spectrum of the fluctuating wind load F_t is given by the equation below, see Appendix A.3:

$$S_F(n) = (C_A A \rho U)^2 S_u(n) = \frac{4F_q^2}{U^2} S_u(n) \tag{4.4.8}$$

The variance of the fluctuating wind load F_t is calculated by integrating the power spectrum $S_F(n)$ over all frequencies n

$$\sigma_F^2 = \int_0^\infty \frac{4F_q^2}{U^2} S_u(n)\, dn = 4F_q^2 \frac{\sigma_u^2}{U^2} \tag{4.4.9}$$

indicating that

$$\frac{\sigma_F}{F_q} = 2\frac{\sigma_u}{U} = 2I_u \tag{4.4.10}$$

The characteristic wind load, $F_{\max}$, during a time interval is expressed as the mean wind load F_q plus the peak factor k_p multiplied by the standard deviation of σ_F:

$$F_{\max} = F_q + k_p \sigma_F \tag{4.1.1}$$

Thus, the gust factor φ, defined as the ratio between the characteristic wind load $F_{\max}$ and the mean wind load F_q, is equal to

$$\varphi = \frac{F_{\max}}{F_q} = 1 + k_p \frac{\sigma_F}{F_q} = 1 + k_p 2I_u \tag{4.4.11}$$

Equation (4.1.3) indicates that background turbulence factor k_b is equal to 1 for a point-like structure.

For a Gaussian process, the peak factor is typically in the range 3–5. This may often be appropriate for pressures located in the surface boundary layers developed on the upstream parts of the structure; see the description in Section 10.1.2 of boundary layers developed on a circular cylinder. The peak factors for pressures located in the separated regions are often much higher. In the high-suction regions at the windward corners of a structure with rectangular cross sections, peak factors are typically of the order of 6–7. Peak factors as high as approximately 10 have been measured on building roofs.

Wind load on a large structure

For structures that are not point-like, the reduced spatial pressure correlation over the structural surface must be taken into account.

This is illustrated in Figure 4.10 which shows three time-history samples of wind load measured simultaneously on a tall structure with an equilateral triangular cross section. The time history shown at the bottom of the figure is calculated as the spatial average of the three individual loads measured. The high-frequency fluctuations of the spatial

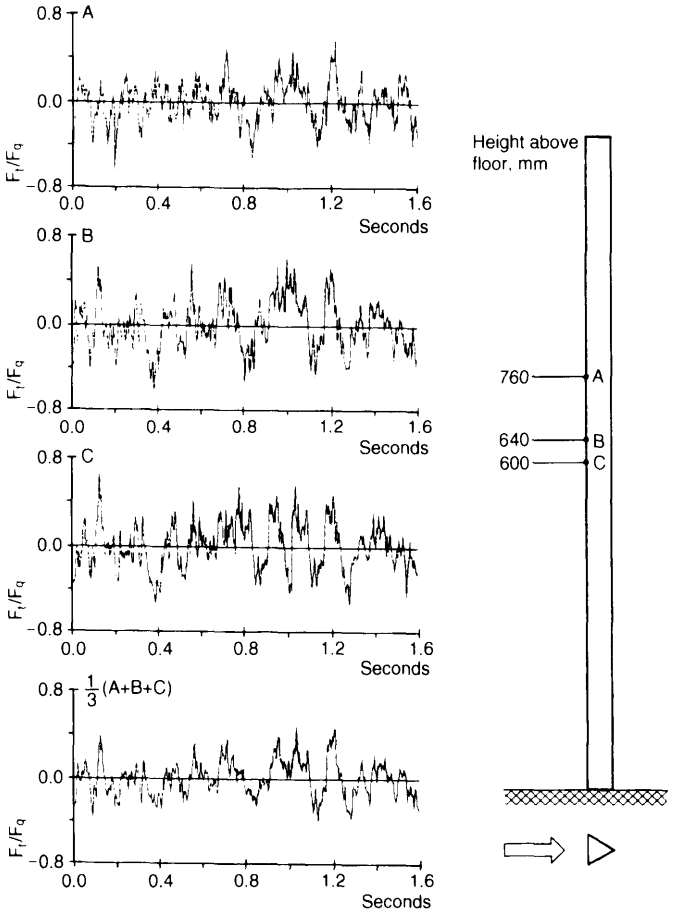

Fig. 4.10 *Wind pressure on the front of a mast with triangular cross section (Gerstoft, 1986). F_t and F_q are the fluctuating and mean wind pressure, respectively, on the windward side at each level. The bottom curve indicates the average of the values in the three upper curves. (Reproduced by permission of P. Gerstoft).*

averaged load are seen to be much smaller than the high-frequency fluctuations of the individual loads.

For a line-like area, the reduced spatial correlations are taken into account by the aerodynamic admittance function, $\chi^2(nl/U)$, in which the argument is the ratio between the length l of the structure and the characteristic eddy size of natural wind, U/n. For a rectangular area with side lengths of l_1 and l_2, respectively, the reduced spatial correlations are taken into account by the aerodynamic admittance function, $\chi^2(nl_1/U, nl_2/U)$, in which the arguments are the ratio between the side lengths of l_1 and l_2, and the characteristic eddy size of natural wind, U/n.

The power spectrum of fluctuating wind load, F_t, acting on an area is

$$S_F(n) = \frac{4F_q^2}{U^2}\chi^2 S_u(n) \tag{4.4.12}$$

where the aerodynamic admittance function χ^2 is equal to

$$\chi^2\left(\frac{nl}{U}\right) = \frac{1}{l}\int_0^l 2\left(1-\frac{r}{l}\right)\psi_p(r, n, U)\,dr \tag{4.4.13}$$

for a line-like area and equal to

$$\chi^2\left(\frac{nl_1}{U}, \frac{nl_2}{U}\right) = \frac{1}{l_1 l_2}\int_0^{l_1}\int_0^{l_2} 4\left(1-\frac{r_1}{l_1}\right)\left(1-\frac{r_2}{l_2}\right)\psi_p(r_1, r_2, n, U)\,dr_1 dr_2 \tag{4.4.14}$$

for a rectangular area. The normalized co-spectrum ψ_p of the surface pressures on the structure is discussed thoroughly in Section 4.5.1.

The aerodynamic admittance functions given above are obtained assuming a uniform weighting of the pressures acting on the areas considered. Other aerodynamic admittance functions are described in Sections 4.5.2 and 4.5.3 in which wind response based on the general response influence function I_R is analysed.

The aerodynamic admittance function for uniform weighting is always less than or equal to 1. Values for various plates and prisms are shown in Figure 4.11, which agrees qualitatively with the data outlined in Figure 4.10.

The variance σ_F^2 of the fluctuating wind load, F_t, is calculated by integrating the power spectrum $S_F(n)$ over the frequency range:

$$\sigma_F^2 = \int_0^\infty \frac{4F_q^2}{U^2}\chi^2\left(\frac{nl_1}{U}, \frac{nl_2}{U}\right) S_u(n)\,dn \tag{4.4.15}$$

Defining the background turbulence contribution k_b as

$$k_b = \int_0^\infty \chi^2\left(\frac{nl_1}{U}, \frac{nl_2}{U}\right)\frac{S_u(n)}{\sigma_u^2}\,dn \tag{4.4.16}$$

gives

$$\frac{\sigma_F}{F_q} = 2I_u\sqrt{k_b} \tag{4.4.17}$$

Thus, the gust factor φ, defined as the ratio between the characteristic wind load $F_{\max}$ and the mean wind load F_q, is equal to:

$$\varphi = \frac{F_{\max}}{F_q} = 1 + k_p 2I_u\sqrt{k_b} \tag{4.4.18}$$

Since the aerodynamic admittance function is less than or equal to 1 for all frequencies, assuming uniform weighting, the background resonance factor k_b will also be lower than or equal to 1.

The size-effect factor c_s is defined by the ratio between the gust factor for a large structure given in equation (4.4.18) and the gust factor for a small structure given in equation (4.4.11), i.e.

$$c_s = \frac{1 + k_p^L 2I_u\sqrt{k_b}}{1 + k_p^S 2I_u} \tag{4.4.19}$$

where the superscripts L and S of the peak factor k_p refer to large and small structures, respectively.

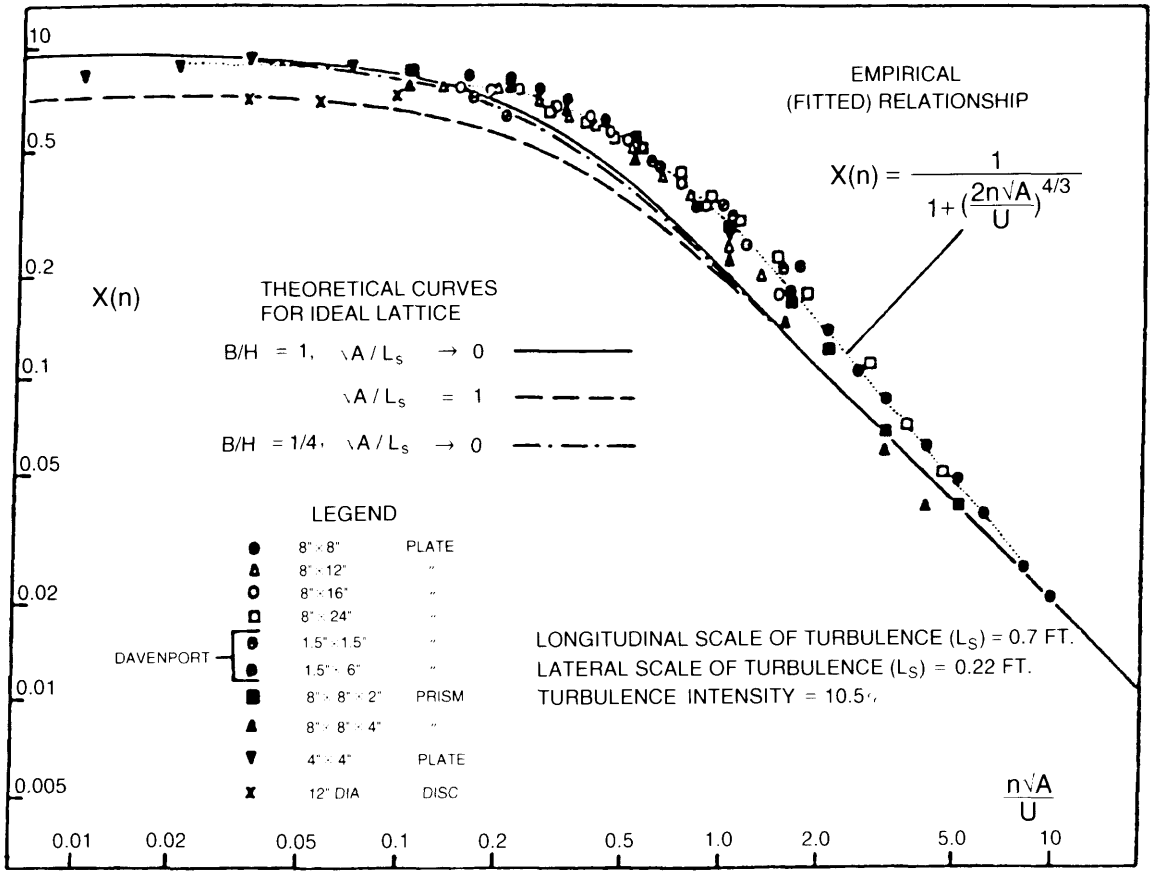

Fig. 4.11 *Experimental and theoretical aerodynamic admittance functions for flat plates and prisms perpendicular to the flow (Davenport, 1977). Note that* $|\chi(n)|$ *and not* $|\chi(n)|^2$ *is shown. (Reproduced by permission of Tapir, Trondheim).*

4.5 AERODYNAMIC ADMITTANCE FUNCTION

Davenport's load model can be used to calculate aerodynamic admittance functions theoretically. Extreme wind responses, such as bending moments, stresses and deflections, are estimated based on a statistical description of the fluctuating load on the structure.

The aerodynamic admittance function depends on the normalized co-spectrum of pressures on a building. The normalized co-spectrum data described in Section 4.5.1 are used as input when calculating wind responses on line-like areas, see Section 4.5.2, and on the rectangular areas considered in Section 4.5.3. The statistical definition of the normalized co-spectrum is given in Section 3.5.4.

The determination of extreme wind responses based on aerodynamic admittance functions is cumbersome and in many situations easier approaches are called for. A popular concept is that of an "equivalent static gust", which is defined as the shortest-duration, hence smallest, gust which fully loads the structure or structural component considered. The basic idea is to estimate extreme wind loads on the basis of air turbulence measured at one point only. The spatial distribution of the load is taken into account by time averaging the air turbulence measured. The load on large structures corresponds to long averaging times, whereas short averaging times are used for small structures.

The "equivalent static gust" concept discussed thoroughly in Sections 4.5.2 and 4.5.3 is used in many codes. A similar discussion was published by Holmes (1995).

4.5.1 Normalized co-spectrum of surface pressures

Full-scale measurements indicate that the normalized co-spectrum, $\psi_p(n, r, U)$, of surface pressures on a building could be described using an exponential decay function:

$$\psi_p(n, r, U) = \exp\left(-C_r \frac{nr}{U}\right) \tag{4.5.1}$$

where n is the frequency, r is the distance between the two points considered, U is the mean wind velocity usually taken at building height, and C_r is a decay constant.

Full-scale measurements on Royex House in London, England, see Newberry *et al.* (1967, 1973), show that a decay constant of $C_r = 4.5$ fits the normalized co-spectrum of pressures on the windward wall in boundary layer turbulence. The decay constant of 4.5 applies to vertical as well as horizontal point separations on the wall.

Full-scale measurements of the turbulence-induced along-wind load per unit of height on a 130 m high, tapered concrete chimney in Denmark show a normalized co-spectrum decay constant of approximately 5–6 for loads per unit of height, vertically separated by up to 47 m corresponding to approximately seven chimney diameters. The decay constants estimated are based on measurements carried out simultaneously at different heights on the upper 2/3 of the concrete chimney. The chimney is located close to the sea and it is exposed to winds with a roughness length of approximately 0.01 m.

The results of the two full-scale experiments are in reasonable agreement and give normalized co-spectrum decay constants of the order of 5. Pressures are, therefore, better correlated than the approaching air turbulence with a co-spectrum decay constant of approximately 10, see Section 3.5. Pressures are also better correlated than normally assumed in gust loading calculations of dynamic sensitive structures such as those considered in Chapter 6.

A normalized co-spectrum decay constant of 4.5 is used in the examples shown in Sections 4.5.2 and 4.5.3. This value was also suggested by Cook (1985) and Lawson (1980).

The exponential normalized co-spectrum decay suggested above results in full correlation at low frequencies, even when the pressure points are considerable distances apart. For very large structures, the lack of correlation at low frequencies may be taken into account using the more accurate, normalized co-spectrum description shown in Section 3.5.

The "equivalent static gust" concept used in many codes corresponds to a moving average filter of the form shown below, see Lawson (1980):

$$\chi_T^2(n, T_l) = \left(\frac{\sin(\pi n T_l)}{\pi n T_l}\right)^2 \tag{4.5.2}$$

where T_l is the averaging time used. Lawson (1980) and Cook (1985) specify that the appropriate moving average time for a structure of characteristic dimension l is given by

$$T_l = C_T l/U \tag{4.5.3}$$

where $C_T = C_r = 4.5$. Appropriate values of C_T are discussed in Sections 4.5.2 and 4.5.3. Aerodynamic admittance functions calculated correctly, as shown in the following equation (4.5.5) and (4.5.8), are compared to the moving average filter in Figures 4.12 and 4.14.

4.5.2 Line-like areas

Responses, such as bending moments and deflections, are calculated as a summation of surface pressures multiplied by response-influence functions. These response-influence functions should be incorporated into the aerodynamic admittance function that corresponds to the response in question.

The wind response at time t, $R(t)$, is calculated as

$$R(t) = \int_0^l I_R(z) F(z, t)\, dz \tag{4.5.4}$$

where $I_R(z)$ is the response-influence function of the point specified by the coordinate z, and $F(z, t)$ is the wind load at point z at time t. $R(t)$ could be a bending moment or a deflection. Assuming that the wind load spectra do not vary along the structure, the aerodynamic admittance function $\chi^2(\phi)$ can be calculated as, see Appendices A and B for further details:

$$\chi^2(\phi) = \frac{\frac{1}{l}\int_0^l k(r)\psi_p(r, n, U)\, dr}{\left(\frac{1}{l}\int_0^l |I_R(z)|\, dz\right)^2} \tag{4.5.5}$$

where the non-dimensional parameter $\phi = C_r n l/U$, i.e. the decay constant C_r multiplied by the reduced frequency $f = nl/U$. The normalized co-influence function $k(r)$ is given by

$$k(r) = \frac{2}{l}\int_0^{l-r} I_R(z) I_R(z + r)\, dz \tag{4.5.6}$$

The absolute value of I_R used in the denominator of equation (4.5.5) facilitates a normalisation that is valid for response-influence functions with constant signs as well as for response-influence functions with changing signs. Response-influence functions with constant signs give aerodynamic admittance functions which are equal to 1 for full pressure correlation occurring at zero frequency according to the exponential decay function in equation (4.5.1).

The normalized co-influence function k and the aerodynamic admittance function χ^2 are shown in Appendix B for different response-influence functions of I_R, e.g. uniform, sinusoidal and cantilever functions. In Appendix B the response-influence function is designated g, which corresponds to the non-dimensional g functions used in Chapter 6.

Line-like areas, where the response-influence functions have constant signs

The aerodynamic admittance function for a one-wave sinusoidal response-influence function is shown in Figure 4.12 as a function of the non-dimensional parameter ϕ. The equivalent moving average filters based on $C_T = C_r$ and $C_T = C_r/3$, respectively, are also shown.

The equivalent moving average filter that uses $C_T = C_r$ was originally suggested by Lawson (1980) and Cook (1985). This filter clearly underestimates the correct aerodynamic admittance functions.

Using $C_T = C_r/3$ gives an aerodynamic admittance function of the correct order of magnitude for the frequencies of interest. The illustrated choice of $C_T = C_r/3$ satisfies that the background turbulence contribution k_b given in equation (4.4.16) using the von Kármán longitudinal power spectrum with an integral length scale of 150 m, see equation (3.5.18), is identical to the k_b value calculated for a sinusoidal response-influence function, assuming a structure length of approximately 25 m. Shorter structures would require larger C_T values of up to approximately $C_r/2$, and longer structures give lower C_T values of approximately $C_r/3.5$.

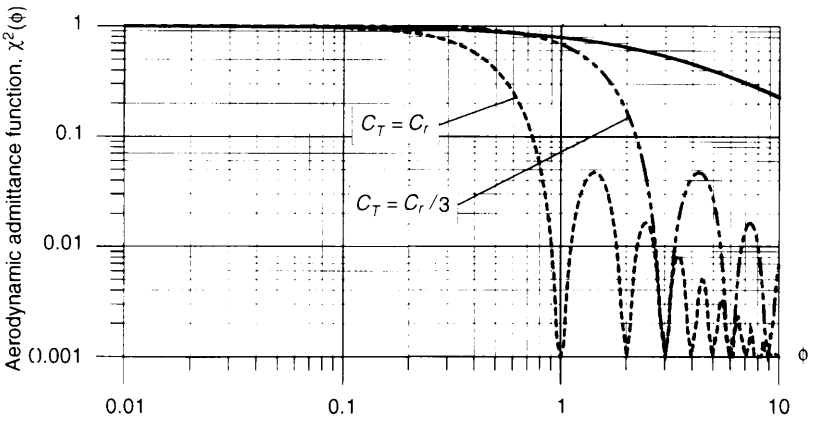

Fig. 4.12 *Aerodynamic admittance function for line-like areas, where the response-influence function, I_R, is one-wave sinusoidal (solid line). The equivalent moving-average aerodynamic admittance functions for two different decay constants, C_T, are also shown (dotted lines). The non-dimensional parameter ϕ is given by $\phi = C_r n l / U$.*

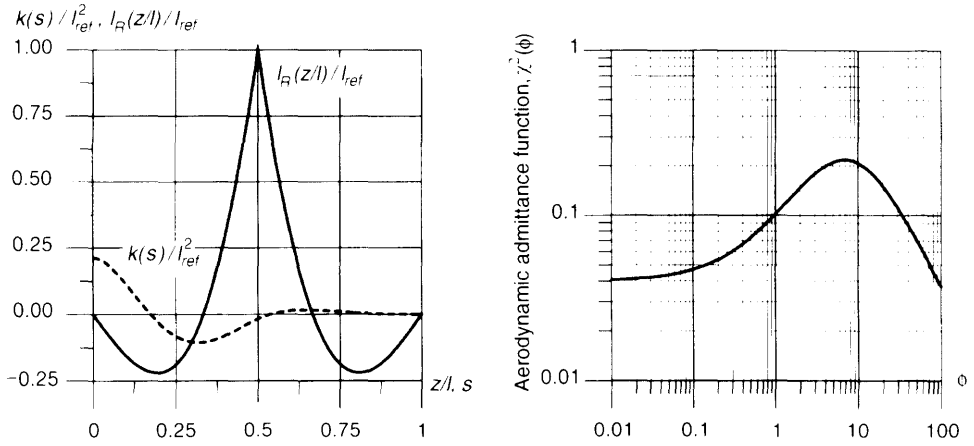

Fig. 4.13 *The figure refers to the bending moment at central midspan of a three-span continuous beam. The left-hand figure shows the normalized bending moment influence function and the normalized co-influence function. The corresponding aerodynamic admittance function is shown in the right-hand figure. The reference bending moment, I_{ref}, used in the normalization on the left-hand figure is $I_{ref} = 0.0583\,l$, in which l is the total beam length. The denominator on the right-hand side of equation (4.5.5) is equal to $0.0567\,I_{ref}^2$.*

Line-like areas, where response–influence functions have changing signs

The bending-moment influence functions of a multi-span continuous beam have changing signs, see Figure 4.13. This is of importance for several types of structures, e.g. roof purlins. The aerodynamic admittance function corresponding to the central midspan bending-moment influence function is shown in Figure 4.13. The aerodynamic admittance function has a maximum for a non-dimensional parameter ϕ of approximately 7. At lower reduced frequencies, the larger pressure correlation reduces the response. The aerodynamic admittance function approaches zero at very high reduced frequencies due to the lack of pressure correlation.

The "equivalent static gust" concept fails when the response–influence function changes sign. For instance, if the wind-induced bending moment has a mean value close to zero, the use of an "equivalent static gust" will give design bending moments which are much lower than the actual wind-induced bending moments. Shear bracing in lattice towers, heavily eiffelated, can also have a mean wind action close to zero. Situations like this are codified using the concept of so-called free actions, i.e. actions which may have any spatial distribution over the structure within given limits, see Eurocode 1, Basis of Design.

4.5.3 Rectangular areas

Only rectangular areas have been considered. The wind response at time t, $R(t)$, is calculated as

$$R(t) = \int_0^{l_1} \int_0^{l_2} I_R(z_1, z_2) F(z_1, z_2, t)\, dz_2 dz_1 \qquad (4.5.7)$$

where $I_R(z_1, z_2)$ is the response-influence function of the point specified by the coordinate (z_1, z_2), $F(z_1, z_2, t)$ is the wind load at point (z_1, z_2) at time t. Assuming that the wind load spectra do not depend on the coordinate (z_1, z_2), the aerodynamic admittance function $\chi^2(\phi_1, \phi_2)$ can be calculated (see Appendices A and B for further details) as

$$\chi^2(\phi_1, \phi_2) = \frac{\dfrac{1}{l_1 l_2}\displaystyle\int_0^{l_1}\int_0^{l_2} k(r_1, r_2)\psi_p(r_1, r_2, n, U)\,dr_2 dr_1}{\left(\dfrac{1}{l_1 l_2}\displaystyle\int_0^{l_1}\int_0^{l_2} |I_R(z_1, z_2)|\,dz_2 dz_1\right)^2} \tag{4.5.8}$$

where $\phi_1 = C_p n l_1/U$, $\phi_2 = C_p n l_2/U$ and the normalized co-influence function $k(r_1, r_2)$ is given by

$$k(r_1, r_2) = \frac{2}{l_1 l_2}\int_0^{l_1 - r_1}\int_0^{l_2 - r_2} I(z_1, z_2, r_1, r_2)\,dz_2 dz_1 \tag{4.5.9}$$

where I is equal to

$$I(z_1, z_2, r_1, r_2) = I_R(z_1, z_2)I_R(z_1 + r_1, z_2 + r_2) + I_R(z_1, z_2 + r_2)I_R(z_1 + r_1, z_2) \tag{4.5.10}$$

The absolute value of I_R used in the denominator of equation (4.5.8) gives a normalization valid for response-influence functions with constant signs as well as for response-influence functions that change signs. Response-influence functions with constant signs give aerodynamic admittance functions which are equal to 1 for full-pressure correlation occurring at zero frequency in accordance with the exponential decay function in equation (4.5.1).

For response-influence functions with constant signs, the aerodynamic admittance function can be approximated by the expressions below, see Section 6.5:

$$\chi^2(\phi_1, \phi_2) = \frac{1}{1 + \sqrt{(G_1\phi_1)^2 + (G_2\phi_2)^2 + \left(\dfrac{2}{\pi}G_1\phi_1 G_2\phi_2\right)^2}} \tag{4.5.11}$$

$$\phi_1 = C_r\frac{n l_1}{U}, \qquad \phi_2 = C_r\frac{n l_2}{U} \tag{4.5.12}$$

For a uniform response-influence function, both constants G_1 and G_2 are equal to 1/2.

The aerodynamic admittance function for a uniform response-influence function is shown in Figure 4.14 as a function of the non-dimensional parameter $\phi = C_r n l/U$, where the effective length chosen is the length of the rectangular diagonal, $l = \sqrt{l_1^2 + l_2^2}$. The equivalent moving-average filters based on $C_T = C_r$ and $C_T = C_r/3$, respectively, are also shown.

The equivalent moving-average filter based on $C_T = C_r$ clearly underestimates the correct aerodynamic admittance functions.

Using $C_T = C_r/3$ gives an aerodynamic admittance function of the correct order of magnitude for the frequencies of interest. The example of $C_T = C_r/3$ shown was estimated in relation to the aerodynamic admittance functions for line-like structures, see Figure 4.12.

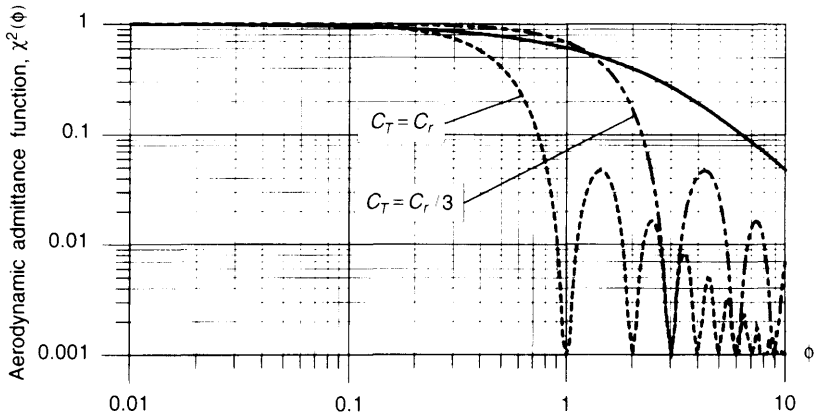

Fig. 4.14 *Aerodynamic admittance functions for a square area with a uniform response-influence function I_R. The equivalent moving-average aerodynamic admittance functions for two different decay constants, C_T, are also shown.*

Conclusion

In conclusion, the "equivalent static gust" concept will give reasonable estimates of extreme wind responses with constant signs. The actual time averaging T_l used for specific structures should be determined as $T_l \approx 1.5l/U$. The averaging time indicated in equation (4.5.3) with $T_l = 4.5l/U$ will underestimate the wind response according to the theoretical basis presented. Whether a more accurate wind-load model would modify the estimated relation of $T_l \approx 1.5l/U$ cannot be ruled out, but equation (4.5.3) with $C_T = 4.5$ is not even close to the present results. The use of $C_T = 4.5$ should be evaluated carefully considering the risk of underestimating the wind response.

The "equivalent static gust" concept does not give accurate results for response-influence functions that change signs.

4.6 PEAK FACTOR FOR A GAUSSIAN PROCESS

As mentioned previously, a wind load fluctuates with time in a very complicated way. This is analysed theoretically using stochastic processes, see Appendix A.3. Of the various concepts used to describe a stochastic process, mean value and standard deviation are two of the most important.

The probability distribution of the largest wind load occurring during a specific period of time, typically taken as 10 minutes, is especially important in connection with designing wind-loaded structures. The normalized stochastic process $Y(t)$ is defined as:

$$Y(t) = \frac{X(t) - \mu_X}{\sigma_X} \tag{4.6.1}$$

where $X(t)$ is the wind load in question with a mean value of μ_X and a standard deviation of σ_X. Assuming that $X(t)$ is a Gaussian process, the mean value $\mu_{Y,\max}$ and the standard deviation $\sigma_{Y,\max}$ of the probability distribution describing the largest value of $Y(t)$ occurring during the time T is asymptotically given (see Cartwright and Longuet-Higgins, 1956) by

$$\mu_{Y,\max} = \sqrt{2\ln(\nu T)} + \frac{\gamma}{\sqrt{2\ln(\nu T)}} \tag{4.6.2}$$

$$\sigma_{Y,\max} = \frac{\pi}{\sqrt{6}} \frac{1}{\sqrt{2\ln(\nu T)}} \tag{4.6.3}$$

where $\gamma = 0.577$ is Euler's constant and ν is the zero-upcrossing frequency determined by

$$\nu = \sqrt{\frac{m_2}{m_0}} \tag{4.6.4}$$

m_0 and m_2 are spectral moments defined as

$$m_j = \int_0^\infty n^j S_Y(n)\, dn \tag{4.6.5}$$

where $S_Y(n)$ is the power spectrum of the process $Y(t)$. νT is the expected number of zero upcrossings during time T.

The mean value $\mu_{X,\max}$ of the largest wind load during time T is determined as the sum of the mean wind load μ_x and the standard deviation σ_x of the wind load, multiplied by a peak factor normally designated as k_p:

$$\mu_{X,\max} = \mu_x + k_p \sigma_x \tag{4.6.6}$$

Comparing equations (4.6.1) and (4.6.6) gives that $k_p = \mu_{Y,\max}$, the latter appears in equation (4.6.2). The peak factor as a function of the expected number of zero upcrossings is shown in Figure 4.15.

The ratio between the rate of zero upcrossings and the rate of local maxima of the normalized process $Y(t)$ is an important parameter which contains information about the regularity of the process, see Madsen *et al.* (1986). This ratio is called the regularity factor α and can be calculated by

$$\alpha = \sqrt{\frac{m_2^2}{m_0 m_4}} \tag{4.6.7}$$

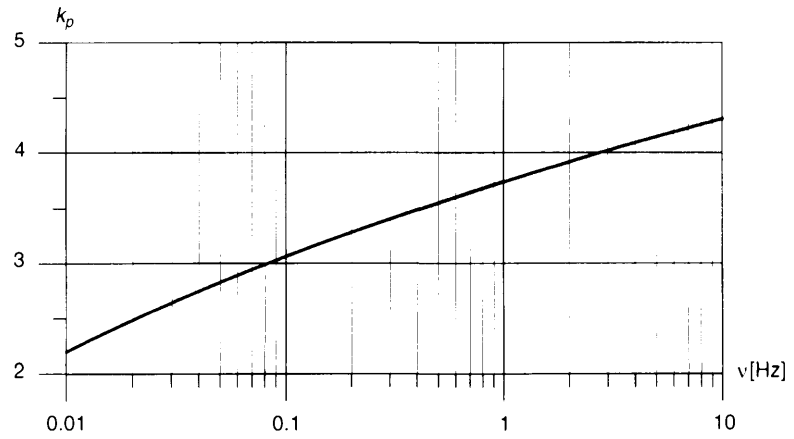

Fig. 4.15 *Peak factor k_p as a function of the expected number of zero upcrossings. T = 600 s.*

Narrow-band process

A stochastic process with $\alpha \approx 1$ is called a narrow-band process. The response of flexible structures vibrating at a natural frequency of n_e is described by a narrow-band process with a zero-upcrossing frequency of $\nu \approx n_e$.

Broad-band process

The power spectrum of the wind load on static structures with high natural frequencies is characterized by the frequency content of the natural wind, modified by the aerodynamic admittance function, see equation (4.4.12). The peak factor in equation (4.4.18) is calculated by inserting the power spectrum of the normalized wind load into equation (4.6.5).

4.7 INTERNAL WIND LOAD

There is no such thing as a completely airtight building. To some extent there will always be leakages around windows and doors, and these will make the internal pressures dependent on the external wind field around the building.

Rooms on the upwind side of the building will experience positive pressures, and rooms in the leeward side will experience suction, i.e. absolute pressures below the barometric pressure. Whether the pressure or suction is dominant inside the building depends on the size and distribution of leakages around the building surfaces. Walls and roofs must be designed to withstand the total load acting, i.e. the external and internal pressures.

Roofs that are almost completely airtight, such as old copper roofs, are often constructed with holes in order to obtain a pressure equalization between external and internal pressures. This reduces the upward wind load on the roof and thereby reduces the risk of structural failure. When the copper roof on Ribe Cathedral in Denmark was replaced around year 1900, the holes found in the old roof were not deemed necessary in the new roof. Consequently, the new roof was blown off in the first storm after the repairs were made. The holes were installed again and there have been no problems since.

Cook (1985) gives a comprehensive description of models used to calculate internal wind load according to different assumptions regarding building geometry, leakages etc.

Just as for external pressures, the codes and literature specify several pressure coefficients for internal wind load. Careful evaluations must always be made to assess whether the published data are representative of the actual situation under consideration.

4.8 STATIC WIND LOAD ACCORDING TO EUROCODE 1

The static wind load specified in Eurocode 1 is divided into wind pressures acting on surfaces and global wind forces.

4.8.1 Wind pressures

Wind pressures acting on external and internal surfaces, respectively, are specified in Eurocode 1.

External pressures

In Eurocode 1, the mean wind velocity at height z, $U(z)$, is defined by multiplying the reference wind velocity U_{bas}, representative for the climate of the site, see Section 3.4,

by coefficients that take into account the effects of terrain roughness and topography as functions of height above ground:

$$U(z) = c_r(z)c_t(z)U_{\text{bas}} \tag{4.8.1}$$

$c_r(z)$ is the roughness coefficient at height z defined by the logarithmic profile:

$$c_r(z) = k_T \ln(z/z_0) \tag{4.8.2}$$

c_r is equal to one at a height of 10 m above reference terrain with a roughness length of 0.05 m and k_T is defined in Section 3.2. The topography coefficient, $c_t(z)$, takes into account the increase of mean wind velocity over hills and escarpments, see Section 3.3. For flat terrain $c_t(z) = 1$, indicating that the mean wind velocity at height z, $U(z)$, is equal to the roughness coefficient multiplied by the reference wind velocity:

$$U(z) = c_r(z)U_{\text{bas}} \tag{4.8.3}$$

The characteristic wind pressure acting on the external surfaces of a structure, F_e, is calculated as

$$F_e = q_{\text{bas}}c_e(z_e)c_{\text{pe}} \tag{4.8.4}$$

where q_{bas} is the reference velocity pressure representative for the climate of the site, see Section 3.4, c_e is the exposure coefficient which takes into account the effects of terrain roughness, topography and height above ground on the mean wind velocity and air turbulence, z_e is the reference height for the external pressure considered and c_{pe} is the external pressure coefficient specified in Eurocode 1. External pressure coefficients are tabulated for areas of 1 and 10 m^2, respectively, and coefficients for intermediate surface areas are found using a logarithmic interpolation based on area. The lack of pressure correlation over surfaces larger than 1 m^2 is thereby taken into account.

The exposure coefficient at height z, $c_e(z)$, is defined as

$$c_e(z) = \frac{q(z)(1 + 2k_pI_u(z))}{q_{\text{bas}}} \tag{4.8.5}$$

where the ratio between the mean velocity pressure at height z, $q(z)$, and the reference velocity pressure, q_{bas}, is given by the equation below, see equation (4.8.1):

$$\frac{q(z)}{q_{\text{bas}}} = c_r^2(z)c_t^2(z) \tag{4.8.6}$$

The exposure coefficient is seen to be the ratio between the characteristic velocity pressure $q_{\max} = q(1 + 2k_pI_u)$, see equation (4.4.4), and the reference velocity pressure q_{bas}. The external pressure coefficient, c_{pe}, could be interpreted as the ratio between the characteristic external wind pressure, F_e, and the characteristic velocity pressure $q_{\max}$.

The characteristic velocity pressure used for static wind load, i.e. the "simple" method stated in Eurocode 1, is arbitrarily based on a peak factor of 3.5. Other peak factor choices would have given alternative specifications of external pressure coefficients and exposure coefficients, but the wind pressure F_e should not, of course, be influenced by the arbitrary peak factor chosen for codification. For more wind-sensitive structures, such as buildings over 200 m high or bridges with spans greater than 200 m, and for all structures

deemed to be dynamically sensitive, as defined by the value of a dynamic coefficient (see Section 4.8.2), this assumption of a peak factor of 3.5 is not adopted in Eurocode 1.

The external pressure coefficients given in Eurocode 1 are based on results obtained in experiments, typically wind-tunnel tests. Extreme pressures and suctions measured in the experiments are normalized as shown in equation (4.8.4) in order to determine the external pressure coefficients specified. Coefficients equal to the ratio between mean pressures/mean suctions and mean velocity pressures are often different from the external pressure coefficients specified in Eurocode 1. The external pressure coefficients c_{pe} give no detailed information on mean pressures and mean suctions on the structure.

For flat roofs, monopitch roofs, duopitch roofs, hipped roofs and multispan roofs, the height of the highest roof point is chosen as the reference height, z_e. For the walls of rectangular buildings, the reference height specified depends on the building aspect ratio h/b. For low buildings where $h < b$, the roof height is chosen as the reference. For taller buildings, the wall is divided into different regions, each with a specific reference height.

Internal pressures

The pressure acting on internal surfaces, F_i, is calculated using an expression similar to equation (4.8.4) valid for external pressures:

$$F_i = q_{bas} c_e(z_i) c_{pi} \tag{4.8.7}$$

where the exposure coefficient is calculated at the reference height, z_i, and c_{pi} is the internal pressure coefficient.

4.8.2 Global wind forces

The global force, F_w, is obtained from the following expression:

$$F_w = q_{bas} c_e(z_e) c_d c_f A_{ref} \tag{4.8.8}$$

where the dynamic coefficient, c_d, accounts for both pressure correlation and dynamic magnification. c_f is the force coefficient and A_{ref} is the reference area, typically the projected area of the structure normal to the wind direction.

The dynamic coefficient c_d is defined as the ratio between the dynamic value of the exposure coefficient representing the gust load on the structure, and the value of the exposure coefficient c_e corresponding to quasistatic gust load at a point at reference height z_{ref}. The dynamic coefficient is calculated using

$$c_d = \frac{1 + 2k_p I_u(z_{ref})\sqrt{k_b + k_r}}{1 + 7I_u(z_{ref})} \tag{4.8.9}$$

where z_{ref} is a representative reference height. The peak factor k_p, the background response factor k_b and the resonant response factor k_r are described further in Chapters 5 and 6. For quasistatic response of a point-like structure, the values $k_p = 3.5$, $k_b = 1$ and $k_r = 0$ are assumed in (4.8.9), so $c_d = 1$ for this case.

Figures are provided in Eurocode 1 that give dynamic coefficients for typical structures. The curves shown are based on a number of assumptions, i.e. a terrain category of I

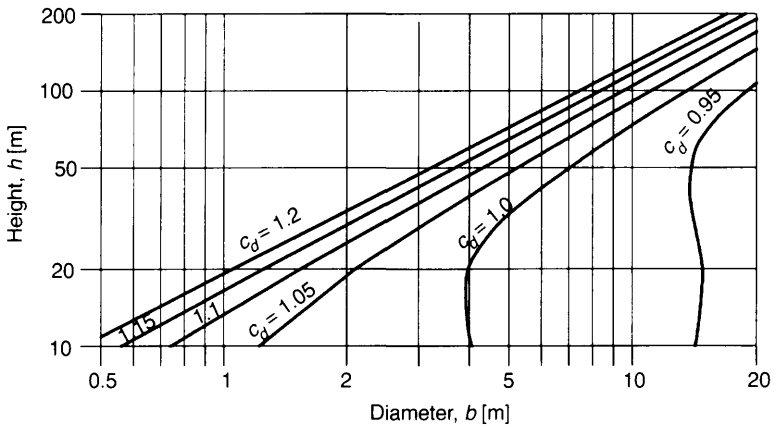

Fig. 4.16 *Dynamic coefficients for unlined, welded steel chimneys based on the detailed procedure specified in Eurocode 1 for dynamic responses. The curves shown for constant dynamic coefficients differ slightly from the ones specified in Eurocode 1. The reason for this discrepancy is not known at present.*

with a roughness length equal to 0.01 m and a reference wind velocity equal to 28 m/s. Figure 4.16 corresponds to the figure in Eurocode 1 for unlined, welded steel chimneys.

The dynamic coefficient of unlined welded steel chimneys is shown in Figure 4.17 as a function of terrain roughness. The dynamic coefficient is approximately 10% lower for terrain category IV with great roughness ($z_0 = 1$ m), compared to terrain category I with low roughness ($z_0 = 0.01$ m). The observed decrease of the dynamic coefficient with increasing roughness occurs because the increase in quasistatic gust load at a point (c_d denominator) is larger than the increase in the exposure coefficient which represents the gust load on the whole structure (c_d numerator).

In Eurocode 1, the dynamic coefficient is used to select a simple procedure suitable for static structures and a detailed procedure specified for structures sensitive to dynamic gust loading. According to Eurocode 1, the detailed procedure should be used when the dynamic coefficient $c_d \geqslant 1.2$, and Eurocode 1 recommends the detailed procedure for $1.0 \leqslant c_d \leqslant 1.2$.

The dynamic coefficient takes into account both the load-reduction effects resulting from lack of pressure correlation over surfaces and the magnification effects due to the frequency content of turbulence close to the fundamental frequency of the structure. A dynamic coefficient of 1 indicates that the load reduction due to lack of pressure correlation is balanced by resonant magnification effects. For large structures, where the lack of pressure correlation is pronounced, the resonant magnification will, therefore, be significant when the dynamic coefficient is equal to 1.

For the static structures considered in this chapter, the dynamic magnification included in the dynamic coefficient, c_d, is negligible.

The concept "mildly dynamic structures" is introduced in Eurocode 1 without an accurate definition. The dynamic coefficient should, however, be less than 1.2 for these structures. Figure 4.18 throws some light on the implications of a dynamic coefficient of 1.15 for an unlined, welded steel chimney. As the chimney increases in size, the background response part, k_b, decreases from lack of pressure correlation, and the resonant

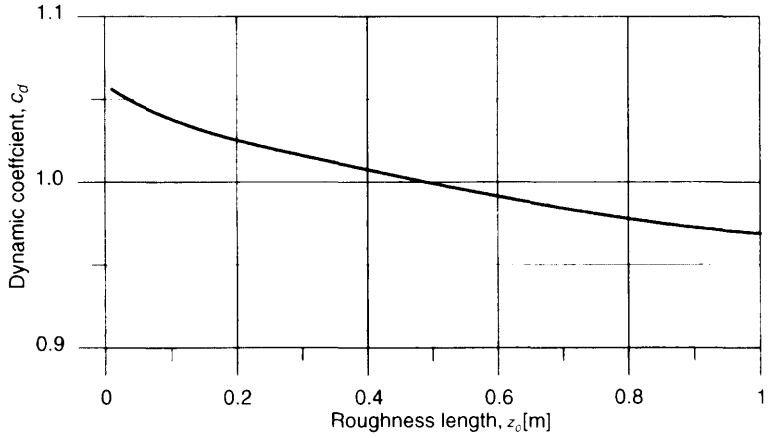

Fig. 4.17 *Dynamic coefficient as a function of terrain roughness. The remaining assumptions used are as specified for unlined welded steel chimneys in Eurocode 1, i.e. a reference wind velocity of* $U_{bas} = 28$ *m/s, structural damping* $\delta_s = 0.015$, *aerodynamic damping equal to 0 and a natural frequency calculated as shown in Eurocode 1. The chimney height is 30 m and its diameter is 3 m.*

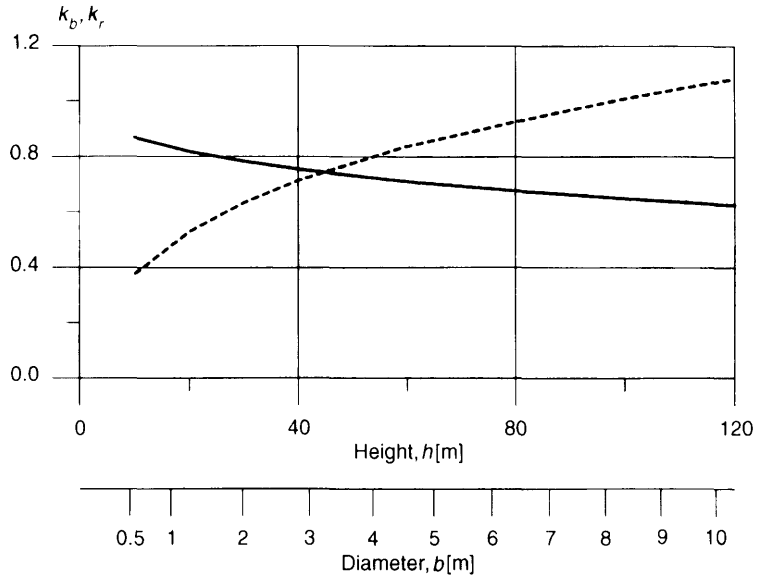

Fig. 4.18 *The background response part* k_b *(solid curve) and the resonant response part* k_r *(dotted curve) were calculated using the detailed procedure prescribed in Eurocode 1 for unlined welded steel chimneys. Each chimney has a dynamic coefficient of 1.15. The response is shown as a function of chimney height h. The corresponding diameter that gives the dynamic coefficient of* $c_d = 1.15$ *assumed is also shown. The response is based on a reference wind velocity of* $U_{bas} = 28$ *m/s, terrain category I,* $\delta_s = 0.015$, *aerodynamic damping equal to 0 and a natural frequency calculated as shown in Eurocode 1.*

response part, k_r, described in Chapters 5 and 6, increases, mainly due to the greater turbulent energy content at lower natural frequencies obtained with taller chimneys. For a mildly dynamic structure, the resonant response can become greater than the background response.

4.8.3 Size-effect factor

The size-effect factor c_s given in equation (4.4.19) is not defined explicitly in Eurocode 1. This factor is, however, indirectly defined as the dynamic coefficient c_d assuming a resonant response factor k_r equal to 0, i.e.

$$c_s = \frac{1 + 2k_p I_u(z_{\text{ref}})\sqrt{k_b}}{1 + 7I_u(z_{\text{ref}})} \tag{4.8.10}$$

The size-effect factor is illustrated in Figure 4.19 as a function of the diagonal dimension of the square area considered. The size-effect factor is approximately equal to 1 for a surface area of 10 m^2. A diagonal dimension of 20 m, corresponding to a square surface area of 200 m^2, gives a size-effect factor of the order of 0.9.

The curves shown in Figure 4.19 can be used to estimate pressure coefficient c_{pe} as a function of the diagonal dimension corresponding to surface areas larger than 10 m^2:

$$c_{pe} = c_s c_{pe,10} \tag{4.8.11}$$

Thus, the lack of surface pressure correlation causes the load per unit of area to decrease with increasing diagonal dimension.

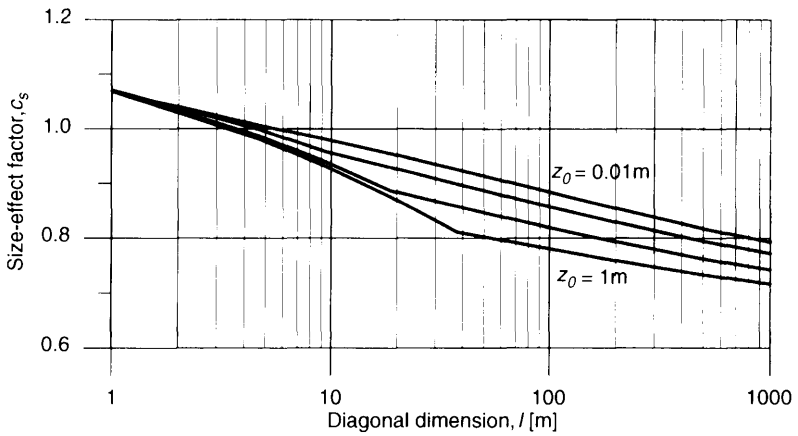

Fig. 4.19 *Size-effect factor as a function of diagonal dimension l of a building with a square frontal area. The building is situated on terrain. The 4 curves shown correspond to terrain categories I–IV specified in Eurocode 1. The minimum height z_{min} indicated in Table 3.2 gives clearly visible curve bends, e.g. at a diagonal dimension of 37.7 m for terrain category IV with z_0 equal to 1 m. The reduction of load per unit of area increases when the terrain becomes rougher.*

5 Along-wind Response, SDOF Structures

Wind turbulence causes a fluctuating load on a structure. This implies that the structure starts to vibrate. If these vibrations are significant, the dynamic response must be calculated.

The number of degrees of freedom a structure has is equal to the number of parameters required to define the positions of all parts of the structure. For many structures, the dynamic along-wind response can be calculated with reasonable accuracy, assuming that the structure has only a single degree of freedom (SDOF). As an example, the structure shown in Figure 5.1 is considered.

Only the along-wind turbulence component u is taken into account, as the other turbulence components are unimportant for the structural vibrations considered.

5.1 EQUIVALENT STATIC LOAD AND DYNAMIC RESPONSE

The concept of characteristic wind load F_{max}, which was introduced in Section 4.1, is frequently used in wind engineering. The gust factor φ is defined as the ratio between F_{max} and the mean wind load F_q. For an SDOF structure, φ is expressed as

$$\varphi = \frac{F_{\max}}{F_q} = 1 + k_p 2I_u \sqrt{k_b + k_r} \tag{5.1.1}$$

k_p is the peak factor, defined as the ratio between the expected maximum of the fluctuating part of the response and the standard deviation of the response, see Sections 4.6 and 5.4. The derivation of the formula is shown in Section 5.2.

I_u is turbulence intensity. $2I_u$ is the ratio between the standard deviation of the fluctuating load and the mean wind load for point-like structures, see Section 5.2.

k_b accounts for contributions from low frequency turbulence. Vortices of at least the same size as the relevant structural part are most important in this respect, as effects from small vortices are smoothed out, integrating the fluctuating wind pressures over the structural surface. The normalization used in formula (5.1.1) is made so that k_b is 1 for point-like structures and less than 1 for large structures, see Sections 5.2 and 5.3.

k_r accounts for contributions from turbulence in resonance with the structure.

Formula (5.1.1) resembles formula (4.1.3). However, the vibrations of the structure at its natural frequency introduces k_r , which did not occur in formula (4.1.3), as this formula was related to a non-vibrating structure.

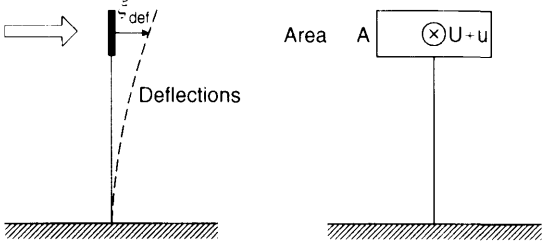

Fig. 5.1 *Structure with a single degree of freedom. (Reproduced by permission of Danish Building Research Institute).*

As in Chapter 4, analyses are performed for a point-like structure and for a large structure.

5.2 WIND LOAD ON POINT-LIKE STRUCTURES

It has been assumed that the structure can be modelled as a mass m supported by an elastic spring with stiffness k acting in parallel with a viscous damper with the damping coefficient c_s. The deflection ξ_{def} follows from

$$m\ddot{\xi}_{def} + c_s\dot{\xi}_{def} + k\xi_{def} = F_{tot} \tag{5.2.1}$$

where F_{tot} is the along-wind load on the structure.

A dot above a letter means differentiation with respect to time. The load F_{tot} is given by

$$F_{tot} = C_D A \tfrac{1}{2}\rho(U + u - \dot{\xi}_{def})^2 \tag{5.2.2}$$

where C_D is the drag coefficient and A is the area of the structure perpendicular to the mean wind direction. The load is determined using the relative wind velocity seen by the structure, i.e. with regard to the velocity $\dot{\xi}_{def}$ of the structure. This is important, as it gives rise to the aerodynamic damping which is often of the same order of magnitude as the structural damping.

Normally, the mean wind velocity U is much larger than the numerical values of the longitudinal turbulence component u and the velocity of the structure $\dot{\xi}_{def}$. Consequently, the following is a good approximation:

$$(U + u - \dot{\xi}_{def})^2 = U^2 + 2Uu - 2U\dot{\xi}_{def} \tag{5.2.3}$$

The total wind load is split into three components: a mean wind load F_q, a fluctuating load F_t caused by the turbulence, and an aerodynamic damping load F_a:

$$F_{tot} = F_q + F_t - F_a \tag{5.2.4}$$

$$F_q = C_D A \tfrac{1}{2}\rho U^2 \tag{5.2.5}$$

$$F_t = C_D A \rho U u \tag{5.2.6}$$

$$F_a = C_D A \rho U \dot{\xi}_{def} = c_a \dot{\xi}_{def} \tag{5.2.7}$$

$$c_a = C_D A \rho U \tag{5.2.8}$$

The aerodynamic damping constant c_a is added to the structural damping constant c_s, giving a total damping constant c:

$$c = c_a + c_s \tag{5.2.9}$$

Mean deflection

The mean deflection μ_ξ is the mean wind load F_q divided by the structural stiffness k,

$$\mu_\xi = \frac{F_q}{k} \tag{5.2.10}$$

and F_q is given by formula (5.2.5).

Structural vibrations

The autospectrum $S_\xi(n)$ for the deflection is determined by

$$S_\xi(n) = |H(n)|^2 S_F(n) \tag{5.2.11}$$

in which $H(n)$ is the frequency response function for the structure and $S_F(n)$ is the autospectrum for the load, see Appendix C.

The autospectrum $S_F(n)$ of the wind load is determined by (4.4.8). Consequently, the variance σ_ξ^2 of deflection ξ_{def} is found by integrating the autospectrum given by (5.2.11)

$$\sigma_\xi^2 = \int_0^\infty S_\xi(n)\,dn = \frac{4F_q^2}{k^2}\frac{\sigma_u^2}{U^2}\int_0^\infty k^2|H(n)|^2\frac{S_u(n)}{\sigma_u^2}\,dn \tag{5.2.12}$$

Inserting the turbulence intensity $I_u = \sigma_u/U$ and using (5.2.10) gives

$$\frac{\sigma_\xi}{\mu_\xi} = 2I_u\sqrt{\int_0^\infty k^2|H(n)|^2\frac{S_u(n)}{\sigma_u^2}\,dn} \tag{5.2.13}$$

Provided that the natural frequency n_e is not very low, it is a good approximation to calculate the integral as the sum $k_b + k_r$ (k_b is the contribution from low frequency turbulence and k_r is the contribution from turbulence in resonance with the structure):

$$k_b = \int_0^\infty k^2|H(n=0)|^2\frac{S_u(n)}{\sigma_u^2}\,dn = 1 \tag{5.2.14}$$

$$k_r = \int_0^\infty k^2|H(n)|^2\frac{S_u(n)}{\sigma_u^2}\,dn = \frac{n_e S_u(n_e)}{\sigma_u^2}\frac{\pi}{4\zeta} \tag{5.2.15}$$

and finally from (5.2.13)

$$\frac{\sigma_\xi}{\mu_\xi} = 2I_u\sqrt{k_b + k_r} \tag{5.2.16}$$

ζ in (5.2.15) is the damping ratio given by

$$\zeta = \frac{c_a + c_s}{2\sqrt{mk}} \tag{5.2.17}$$

5.3 WIND LOAD ON LARGE STRUCTURES

The reduced spatial correlation of wind pressure is important when considering large structures. As shown in Section 4.4, this is done by means of the aerodynamic admittance function. Then factors k_b and k_r are expressed as

$$k_b = \int_0^\infty \chi^2\left(\frac{nl}{U}\right)\frac{S_u(n)}{\sigma_u^2}\,dn \tag{5.3.1}$$

$$k_r = \chi^2\left(\frac{n_e l}{U}\right)\frac{n_e S_u(n_e)}{\sigma_u^2}\frac{\pi}{4\zeta} \tag{5.3.2}$$

in which χ^2 is the aerodynamic admittance function and l is a characteristic length of the wind exposed area. $S_u(n)$ and σ_u are related to the centre of this area.

The aerodynamic admittance function is less than or equal to 1 for all values of its argument, and consequently k_b is also less than or equal to 1.

5.4 GUST RESPONSE FACTOR

The characteristic deflection $\xi_{\max}$ during a certain period of time is expressed as the mean deflection μ_ξ plus the peak factor k_p multiplied by the standard deviation σ_ξ,

$$\xi_{\max} = \mu_\xi + k_p\sigma_\xi \tag{5.4.1}$$

The gust factor is

$$\varphi = \frac{\xi_{\max}}{\mu_\xi} = 1 + k_p\frac{\sigma_\xi}{\mu_\xi} \tag{5.4.2}$$

and using (5.2.16),

$$\varphi = 1 + k_p 2I_u\sqrt{k_b + k_r} \tag{5.4.3}$$

The peak factor is discussed in Section 4.6. Here, however, the zero-upcrossing frequency ν should be taken as a weighted average from background and resonance contributions, and the time $T = 600$ s, as a 10-minute mean value is used to determine the mean wind velocity. Then from (4.6.2)

$$k_p = \sqrt{2\ln(\nu T)} + \frac{0.577}{\sqrt{2\ln(\nu T)}} \tag{5.4.4}$$

$$\nu = \sqrt{\frac{n_0^2 k_b + n_e^2 k_r}{k_b + k_r}} \tag{5.4.5}$$

where n_e is the resonant frequency (Hz) for the along-wind vibrations of the structure and n_0 is the representative frequency (Hz) of the gust loading on rigid structures. The frequency n_0 is determined as

$$n_0 = \sqrt{\frac{\int_0^\infty n^2\chi^2\left(\frac{nl}{U}\right)S_u(n)\,dn}{\int_0^\infty \chi^2\left(\frac{nl}{U}\right)S_u(n)\,dn}} \tag{5.4.6}$$

6 The Along-wind Response of Bluff Bodies

A structure's dynamic along-wind response to a turbulent wind can be estimated theoretically by methods originally proposed by A.G. Davenport in the early 1960s, see Section 4.4. The calculation procedures developed during the preparation of the paper by Hansen and Krenk (1996) are included in the description.

The response calculations described in the present chapter are based on simple line-like and plate-like structures, see Figure 6.1. The theoretical formulations presented lead directly to a simple design procedure which may conveniently be used in design codes to improve their accuracy. The design procedure proposed is based on consistent expressions for plate-like structures and a simplified representation of wind turbulence, see Section 6.6. Section 6.7 deals with dynamic along-wind response of simple structures as described in Eurocode 1.

6.1 ASSUMPTIONS

This procedure assumes that the structure is simple in shape, e.g. as indicated in Figure 6.1. Furthermore, it is assumed that:

1. The wind load is determined from the undisturbed wind field.
2. The structure is assumed to be linear-elastic with viscous damping.
3. The along-wind mode considered is uncoupled from other modes.

Coupling between modes occurs for structures with closely spaced or identical natural frequencies, e.g. certain guyed masts. The response calculations described do not cover mode coupling, but the basic wind load assumptions presented could be used as input for a dynamic analysis that does include mode coupling.

Structures such as guyed masts and transmission lines can have many modes that contribute to the resonant response. If more than one mode gives significant response contributions, the methods described can be used to calculate each single modal response $\sigma_{r,i}$. The total resonant response is given by

$$\sigma_R^2 = \sum_i \sigma_{r,i}^2 \tag{6.1.1}$$

assuming that the cross terms from mode coupling are negligible; see Appendix C for further details.

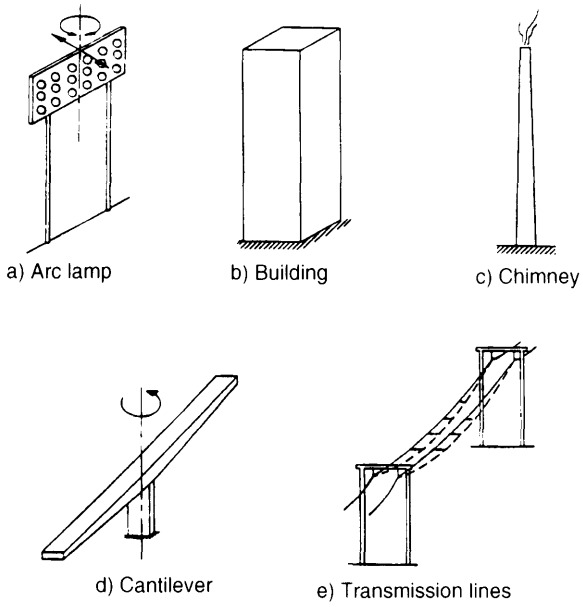

Fig. 6.1 *Structures covered by this procedure (Davenport (1977)). (Reproduced by permission of Tapir, Trondheim).*

Pressure correlation

According to assumption 1 mentioned above, the pressure correlation is assumed to be identical to the correlation of the longitudinal turbulence in the undisturbed wind field. This assumption will lead to an overestimation of the load, due to the lack of correlation between wind load on the structure front face and on the rear face. The load will be underestimated due to the fact that pressures on the structure are better correlated than the longitudinal turbulence in the undisturbed wind field. These two aspects, which to some extent counterbalance each other when predicting loads, are not taken into account due to the rather limited data available. Furthermore, the data show considerable scatter. Comprehensive pressure correlation data covering a variety of structures, such as line-like structures, buildings and bridges, could be used to refine the load model at a later stage.

For rectangular buildings, pressure fluctuations on the building's rear face are much less pronounced than the pressure fluctuations on the front face (see Simiu and Scanlan, 1986). Furthermore, wind-tunnel measurements on buildings indicate that pressures on a building front face are almost uncorrelated with the pressures on the rear face with typical correlation coefficients of the order of 0.1–0.2. The fluctuating wind load on the building front face will, therefore, give the main contributions to the total fluctuating wind load. Neglecting the wind load fluctuations on the rear face completely will not underestimate the total wind load fluctuations on the building significantly. However, if the lack of correlation between pressures on the front face and rear face is taken into account, a more accurate model for calculating the fluctuating wind load on the building's front face is called for. For instance, the fact that pressures on the structure are better correlated than the longitudinal turbulence in the undisturbed wind field should be taken into account.

6.2 JOINT ACCEPTANCE FUNCTIONS AND SIZE REDUCTION FUNCTIONS

In order to systematize the somewhat complicated calculations of dynamic response, we shall introduce two frequency functions; the joint acceptance function and the size reduction function. The joint acceptance function describes the interaction of the actual mode shape and wind load fluctuations on the structure. If the mode shape has constant sign over the structure, the size reduction function is defined as the joint acceptance function normalized to 1 at zero frequency. Therefore, the size reduction function describes the response reduction from the interaction between mode shape and lack of load correlation over the structure as a function of frequency.

The evaluation of response statistics is computationally intensive and involves double integration over the line-like structure and fourfold integration over the plate-like structure when calculating the joint acceptance function. The present chapter uses the integration format described in Appendix B. This means that the joint acceptance function can be found using a single integral for line-like structures and a double integral for plate-like structures. The method is based on normalized co-influence functions, which are straightforward to calculate.

In many codes, the joint acceptance function for plate-like structures is given as a product of joint acceptance functions for two line-like structures. The error introduced by this simplification is discussed and a new simple approximate expression of the joint acceptance function for plate-like structures is given. This new and more accurate expression has the correct asymptotes for low as well as high frequencies based on exponential correlation functions.

6.3 EXTREME STRUCTURAL RESPONSE

The largest structural response occurring during a storm period of say 10 minutes is a sample in a statistical distribution with a mean value which we call the characteristic response, see Section 4.6. The characteristic response, $R_{\max}$, is expressed by the mean structural response, μ_R, plus a peak factor, k_p, multiplied by the standard deviation σ_R of the structural response:

$$R_{\max} = \mu_R + k_p \sigma_R \tag{6.3.1}$$

Structural responses such as bending moments, deflections and stresses are considered. The mean structural response, μ_R, originates from the static wind load on the structure, and is calculated using standard procedures applicable for non-vibrating structures. Background turbulence, i.e. low-frequency turbulence fluctuations, and resonance turbulence, i.e. turbulence in resonance with the natural frequencies of the structure, give contributions to the fluctuating part of the structural response. The standard deviation of the structural response is given by

$$\sigma_R = \sqrt{\sigma_b^2 + \sigma_r^2} \tag{6.3.2}$$

where standard deviations σ_b and σ_r originate from background turbulence and resonance turbulence, respectively. In situations where the fluctuating response can be expressed as functions of the mean response, the following equations are useful in order to systematize the response presentation:

$$\sigma_b = \mu_R 2 I_{u,\mathrm{ref}} \theta_b \sqrt{k_b} \tag{6.3.3}$$

$$\sigma_r = \mu_R 2 I_{u,\mathrm{ref}} \theta_r \sqrt{k_r} \tag{6.3.4}$$

$I_{u,\mathrm{ref}}$ is the turbulence intensity at a reference point with a height z_{ref} above terrain. θ_b and θ_r are factors that incorporate the effect of different influence functions for the mean and fluctuating response, respectively. The background turbulence factor k_b is an integral measure of the load reduction caused by a lack of surface pressure correlation for large structures. The resonance turbulence factor k_r includes the effect of structural amplification, lack of surface pressure correlation and turbulence fluctuations, all at the structure's natural frequency.

The gust factor φ, defined as the ratio between the characteristic structural response $R_{\max}$ and the mean response μ_R, is given by

$$\varphi = 1 + k_p 2 I_{u,\mathrm{ref}} \sqrt{\theta_b^2 k_b + \theta_r^2 k_r} \tag{6.3.5}$$

The gust factor is a useful concept when the mean response is significant, e.g. for buildings, bridges and chimneys. It should not be used when the mean response is negligible, e.g. for the cantilevered bridge considered in Section 6.6.2.

Typically, the bulk of variance in the longitudinal component of turbulence is at frequencies well below the natural frequencies of the structure. This indicates that the background turbulent response can be calculated, assuming that the wind load is quasistatic. This approach is simple and provides accurate response estimates in most situations. Alternatively, the background turbulent response could have been included in the modal analysis. However, this approach is more cumbersome, since often several modes are needed to represent the background turbulent response with sufficient accuracy.

The resonant response is calculated using the principles for vibrating structures outlined in Appendix C.

6.4 RESPONSE OF LINE-LIKE STRUCTURES

The wind load per unit of length, $F(z, t)$, is calculated by

$$F(z, t) = \tfrac{1}{2}\rho(U(z) + u(z, t) - \dot{\xi}_{\mathrm{def}}(z, t))^2 d(z) C(z) \tag{6.4.1}$$

$U(z) + u(z, t)$ is the wind velocity found by adding the mean wind velocity $U(z)$ and the longitudinal turbulence component $u(z, t)$. The wind load depends on the relative wind velocity with respect to the structure, i.e. $U(z) + u(z, t) - \dot{\xi}_{\mathrm{def}}(z, t)$. The quantity $d(z)$ is the width of the structure perpendicular to the wind direction and $C(z)$ is the shape factor.

In most cases mean wind velocity $U(z)$ is much larger than the absolute values of turbulence component $u(z, t)$ and structural velocity $\dot{\xi}_{\mathrm{def}}(z, t)$. The wind load is then given by

$$F(z, t) = F_q(z) + F_t(z, t) - F_a(z, t) \tag{6.4.2}$$

where mean wind load F_q, fluctuating wind load from turbulence F_t, and aerodynamic damping load F_a are given by

$$F_q(z) = \tfrac{1}{2}\rho U(z)^2 d(z) C(z) \tag{6.4.3}$$

$$F_t(z, t) = \rho U(z) u(z, t) d(z) C(z) \tag{6.4.4}$$

$$F_a(z, t) = \rho U(z) \dot{\xi}_{\mathrm{def}}(z, t) d(z) C(z) \tag{6.4.5}$$

The aerodynamic damping load is taken into account using a logarithmic decrement δ describing the total damping and calculated as

$$\delta = \delta_s + \delta_a \tag{6.4.6}$$

where δ_s is the logarithmic decrement corresponding to the structural damping, and δ_a is the logarithmic decrement originating from aerodynamic damping. Making use of the assumption that the deflections of the structure are affine with the non-dimensional mode shape $\xi(z)$, the aerodynamic damping is determined by the following equations:

$$\delta_a = \frac{1}{2} C_{\text{ref}} \frac{U_{\text{red}}}{M_{\text{red}}} \gamma_a \tag{6.4.7}$$

$$U_{\text{red}} = \frac{U_{\text{ref}}}{n_e d_{\text{ref}}} \tag{6.4.8}$$

$$M_{\text{red}} = \frac{m_g/h}{\rho d_{\text{ref}}^2} \tag{6.4.9}$$

$$m_g = \int_0^h m(z) \frac{\xi^2(z)}{\xi_{\text{ref}}^2} dz \tag{6.4.10}$$

$$\gamma_a = \frac{1}{h} \int_0^h \frac{C(z)}{C_{\text{ref}}} \frac{d(z)}{d_{\text{ref}}} \frac{U(z)}{U_{\text{ref}}} \frac{\xi^2(z)}{\xi_{\text{ref}}^2} dz \tag{6.4.11}$$

where C_{ref} is a reference shape factor, U_{red} is a non-dimensional reduced wind velocity, M_{red} is a non-dimensional mass ratio, m is the mass per unit of length, m_g is the normalized, generalized mass of the mode considered and γ_a is a factor that accounts for the actual distribution of shape factor, width, wind velocity and mode shape along the structure. Aerodynamic damping increases with increasing wind velocity and decreasing mass ratio, respectively. Aerodynamic damping gives significant response reductions for light structures such as steel chimneys and lattice towers.

6.4.1 Mean response

The mean response, μ_R, which originates from the mean wind load acting on the structure, is calculated by

$$\mu_R = \int_0^h F_q(z) I_R(z) dz \tag{6.4.12}$$

where $I_R(z)$ is the response-influence function. $I_R(z)$ is equal to the response obtained for a unit, static load applied at height z. For example, $I_R(z) = z$ for the bending moment at $z = 0$. The mean response is given by the following equations, see equation (6.4.3), giving the mean wind load F_q:

$$\mu_R = h d_{\text{ref}} C_{\text{ref}} \tfrac{1}{2} \rho U_{\text{ref}}^2 I_{R,\text{ref}} \gamma_m \tag{6.4.13}$$

$$\gamma_m = \frac{1}{h} \int_0^h g_m(z) dz \tag{6.4.14}$$

$$g_m(z) = \frac{C(z)}{C_{\text{ref}}} \frac{U^2(z)}{U^2_{\text{ref}}} \frac{d(z)}{d_{\text{ref}}} \frac{I_R(z)}{I_{R,\text{ref}}} \tag{6.4.15}$$

g_m is a non-dimensional function describing the variation of the mean wind load and the response-influence function along the structure. γ_m gives the integral effect of the g_m function.

6.4.2 Background turbulent response

The background turbulent response, $R_b(t)$, is calculated by treating the fluctuating wind load caused by turbulence, $F_t(z, t)$, in a quasistatic fashion:

$$R_b(t) = \int_0^h F_t(z, t) I_R(z)\, dz \tag{6.4.16}$$

where $I_R(z)$ is the response-influence function introduced to calculate the mean response. The standard deviation of the background response, σ_b, is given by the following equations:

$$\sigma_b^2 = (h d_{\text{ref}} C_{\text{ref}} \rho U_{\text{ref}} \sigma_{u,\text{ref}})^2 I^2_{R,\text{ref}} J_b^2 \tag{6.4.17}$$

$$J_b^2 = \frac{1}{h^2} \int_0^h \int_0^h \rho_u(r_z) g_b(z_1) g_b(z_2)\, dz_1 dz_2 \tag{6.4.18}$$

$$g_b(z) = \frac{C(z)}{C_{\text{ref}}} \frac{U(z)}{U_{\text{ref}}} \frac{\sigma_u(z)}{\sigma_{u,\text{ref}}} \frac{d(z)}{d_{\text{ref}}} \frac{I_R(z)}{I_{R,\text{ref}}} \tag{6.4.19}$$

The subscript "ref" refers to the function value at the reference point chosen. g_b is a non-dimensional function describing the background turbulent wind-load variation along the structure. $\rho_u(r_z)$ is the correlation coefficient for longitudinal turbulence components separated by r_z vertically. The non-dimensional response variance J_b^2 in equation (6.4.18) is determined by a double integral, which can be calculated as shown in Appendix B, i.e.

$$J_b^2 = \frac{1}{h} \int_0^h k(r_z) \rho_u(r_z)\, dr_z \tag{6.4.20}$$

where the co-influence function $k(r_z)$ is given as

$$k(r_z) = \frac{2}{h} \int_0^{h-r_z} g_b(z) g_b(z + r_z)\, dz \tag{6.4.21}$$

The non-dimensional response variance, J_b^2, and co-influence functions, k, are calculated for different functions of g in Appendix B. The exponential correlation function ρ_u defined in equation (3.5.10) is used in the calculations.

The asymptotic behaviour of J_b^2, using the exponential correlation function, is given by

$$J_b^2 \to k(0)/\phi_z \qquad \text{for } \phi_z = h/L_u^z \to \infty \tag{6.4.22}$$

$$J_b^2 \to \gamma_b^2 \qquad \text{for } \phi_z \to 0 \tag{6.4.23}$$

where the normalization constant γ_b is

$$\gamma_b = \frac{1}{h} \int_0^h g_b(z)\, dz \tag{6.4.24}$$

Table 6.1 *Asymptotic behaviour of the non-dimensional response variance $J_b^2(\phi_z)$, where $\phi_z = h/L_u^z$. It can also be interpreted as joint acceptance function asymptotes replacing $L_u^z = U/(nC_z)$, i.e. $\phi_z = C_z nh/U$, in which C_z is the normalized co-spectrum decay constant introduced in Section 3.5.4, equation (3.5.26). Γ in the last column is used to calculate background turbulence factor k_b in equation (6.4.27).*

Load variation function g	J_b^2 asymptote for $\phi_z \to 0$	J_b^2 asymptote for $\phi_z \to \infty$: $J_b^2 = 1/(J_z\phi_z)$	γ_b (6.4.24) γ_r (6.4.45)	Γ (6.4.27) G (6.5.30)
1	1	$2/\phi_z$	1	$\frac{1}{2}$
z/h	$\frac{1}{4}$	$2/(3\phi_z)$	$\frac{1}{2}$	$\frac{3}{8}$
$(z/h)^2$	$\frac{1}{9}$	$2/(5\phi_z)$	$\frac{1}{3}$	$\frac{5}{18}$
$(z/h)^3$	$\frac{1}{16}$	$2/(7\phi_z)$	$\frac{1}{4}$	$\frac{7}{32}$
$(z/h)^4$	$\frac{1}{25}$	$2/(9\phi_z)$	$\frac{1}{5}$	$\frac{9}{50}$
$\sin(\pi z/h)$	$4/\pi^2$	$1/\phi_z$	$2/\pi$	$4/\pi^2$
$2z/h - 1$	$\phi_z/15$	$2/(3\phi_z)$	0	—

corresponding to J_b for full correlation with $\rho_u = 1$ for all distances of interest. γ_b gives the integral effect of the g_b function.

Table 6.1 shows the asymptotic behaviour of the non-dimensional response variance J_b^2.

g_m and g_b functions with constant sign

When the g_m and g_b functions have constant signs, the background response can be expressed in terms of the mean response using equation (6.3.3) and setting the constants of θ_b and k_b equal to

$$\theta_b = \gamma_b/\gamma_m \tag{6.4.25}$$

$$k_b = J_b^2/\gamma_b^2 \tag{6.4.26}$$

The asymptote of k_b for structural heights approaching infinity is given by $1/(\Gamma\phi_z)$, where $\phi_z = h/L_u^z$ and Γ is a constant dependent on the function $g_b(z)$ (see Table 6.1). An approximation of k_b is given by

$$k_b = \frac{1}{1 + \Gamma\phi_z} \tag{6.4.27}$$

The approximation introduced for k_b is quite accurate in most situations, see Figure 6.2. The factor θ_b is shown in Table 6.2 for some simple functions of $g_b(z)$ and $g_m(z)$.

Table 6.2 *θ_b for different functions of $g_b(z)$ in equation (6.4.19) and $g_m(z)$ in equation (6.4.15).*

$g_m(z)$	$f(z)$	z/h	$(z/h)^2$	$(z/h)^3$
$g_b(z)$	$f(z)$	1	z/h	$(z/h)^2$
θ_b	1	2	$\frac{3}{2}$	$\frac{4}{3}$

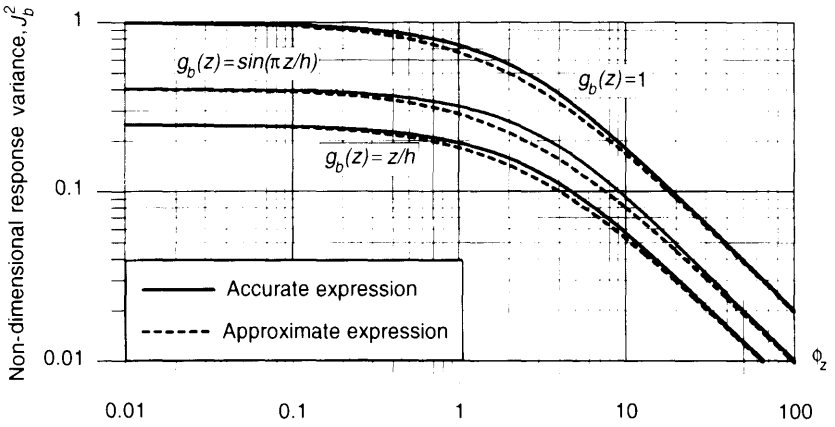

Fig. 6.2 *Non-dimensional response variance J_b^2 as a function of $\phi_z = h/L_u^z$ for $g_b(z) = 1$, $g_b(z) = z/h$, and $g_b(z) = \sin(\pi z/h)$, respectively. The solid lines are in accordance with the accurate expressions derived in Appendix B. The dotted lines correspond to the approximation introduced in equation (6.4.27). The curves shown can also be interpreted as joint acceptance functions replacing $L_u^z = U/(nC_z)$, i.e. $\phi_z = C_z nh/U$, see Section 6.4.3.*

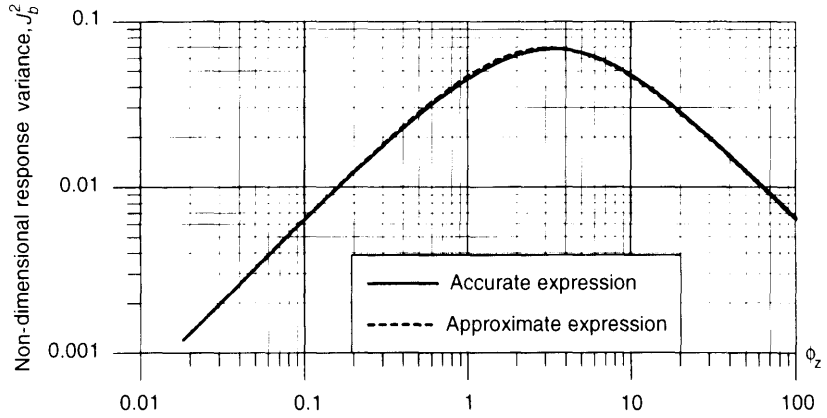

Fig. 6.3 *Non-dimensional response variance J_b^2 as a function of $\phi_z = h/L_u^z$ for $g_b(z) = 2z/h - 1$. The solid line is in accordance with the accurate expression derived in Appendix B. The dotted line corresponds to the approximation introduced in equation (6.4.28). The curves shown can also be interpreted as joint acceptance functions replacing $L_u^z = U/(nC_z)$, i.e. $\phi_z = C_z nh/U$, see Section 6.4.3.*

g_m and g_b functions with changing signs

We shall limit ourselves to the rather simplified variation given by function $g_b(z) = 2z/h - 1$, i.e. a simple linear variation antisymmetrical with respect to the midpoint $z = h/2$. The non-dimensional response variance J_b^2 is shown in Figure 6.3 with the quite accurate approximation:

$$J_b^2(\phi_z) = \frac{2\phi_z}{3\phi_z^2 + 10\phi_z + 30} \tag{6.4.28}$$

where $\phi_z = h/L_u^z$.

6.4.3 Resonant turbulent response

The structural response of the dynamic part of the along-wind loading may be calculated using modal analysis. The response to gusty wind is usually dominated by the fundamental mode, and the corresponding generalized fluctuating load $Q(t)$ is

$$Q(t) = \int_0^h C(z)\rho U(z)u(z, t)\xi(z)d(z)\,dz \tag{6.4.29}$$

where h is the structure height, C is the shape factor, ρ is the air density, u is the along-wind turbulence component, ξ is the non-dimensional mode shape, d is the width of the structure, and z is a coordinate along the structure. The dynamic part of the structural deflection may, as an approximation, be written as $a(t)\xi(z)$, where $a(t)$ is a stochastic amplitude function. The spectral density, $S_a(n)$, of $a(t)$ is proportional to the structural frequency response function squared, $|H(n)|^2$, and to the generalized load spectrum:

$$S_a(n) = (hC_{\text{ref}}\rho U_{\text{ref}}\xi_{\text{ref}}d_{\text{ref}})^2|H(n)|^2|J_z(n)|^2 S_{u,\text{ref}}(n) \tag{6.4.30}$$

where the joint acceptance function $|J_z(n)|^2$, describing the interaction between air flow correlation and structural mode shapes, is calculated by the expression:

$$|J_z(n)|^2 = \frac{1}{h^2}\int_0^h \int_0^h g_r(z_1, n)g_r(z_2, n)\psi_F(r_z, n, U)\,dz_1 dz_2 \tag{6.4.31}$$

The non-dimensional resonant wind-load distribution function $g_r(z, n)$ is defined as

$$g_r(z, n) = \frac{C(z)}{C_{\text{ref}}}\frac{U(z)}{U_{\text{ref}}}\sqrt{\frac{S_u(z, n)}{S_{u,\text{ref}}(n)}}\frac{\xi(z)}{\xi_{\text{ref}}}\frac{d(z)}{d_{\text{ref}}} \tag{6.4.32}$$

where g_r is a non-dimensional function describing the resonant wind load variation along the structure and $\psi_F(r_z, n, U)$ is the normalized co-spectrum for the wind load components at two points with a distance of r_z. In the present load model, ψ_F is equal to the normalized co-spectrum ψ_u for the longitudinal turbulence components described in Section 3.5.4. n is the frequency in hertz and U is the mean wind velocity. The subscript "ref" refers to the function value at the reference point chosen.

The inertia force is proportional to acceleration. The variance of the acceleration at reference height z_{ref}, σ_{acc}^2, is determined as the integral from zero frequency to infinity of the spectral density function in equation (6.4.30) multiplied by $\xi_{\text{ref}}^2(2\pi n)^4$. Using Appendix C.3, the definition of the turbulence intensity I_u in equation (3.5.2) and the non-dimensional power spectral density function R_N defined in equation (3.5.11) give the following expression for σ_{acc}^2:

$$\sigma_{acc}^2 = \xi_{\text{ref}}^2(2\pi n_e)^4\sigma_a^2 = \frac{(2I_{u,\text{ref}})^2}{m_g^2}\left(hC_{\text{ref}}\frac{1}{2}\rho U_{\text{ref}}^2 d_{\text{ref}}\right)^2\frac{\pi^2}{2\delta}R_N(z_{\text{ref}}, n_e)|J_z(n_e)|^2 \tag{6.4.33}$$

where $I_{u,\mathrm{ref}}$ is the turbulence intensity at reference height and the normalized generalized mass m_q is given in equation (6.4.10).

Since the normalized co-spectrum function depends solely on the distance of r_z and not on each of the point coordinates, the joint acceptance function can be calculated (see Appendix B) by

$$|J_z(n)|^2 = \frac{1}{h}\int_0^h k_z(r_z, n)\psi_F(r_z, n, U)\,dr_z \tag{6.4.34}$$

where the normalized co-influence function $k_z(r_z, n)$ is given as

$$k_z(r_z, n) = \frac{2}{h}\int_0^{h-r_z} g_r(z, n)g_r(z + r_z, n)\,dz \tag{6.4.35}$$

The use of equations (6.4.34) and (6.4.35) to calculate the joint acceptance function was originally introduced by Dyrbye and Hansen (1988).

All load pairs with a distance of r_z give a contribution to the joint acceptance function that is equal to $k_z(r_z, n)\psi_F(r_z, n, U)\,dr_z$. Equation (6.4.34) is simply an integral adding joint acceptance function contributions that originate from load pairs, all with a distance of r_z.

The power spectrum S_u given by equations (3.5.17) or (3.5.18) indicates that function g_r, and thereby co-influence function k_z, is independent of the frequency n, except for very low frequencies not important for the resonant turbulent response considered here. Furthermore, the power spectra described in Section 3.5 do not give an accurate representation of the longitudinal turbulence at low frequencies. The frequency dependence of g_r may, therefore, be disregarded without any loss of accuracy.

Examples of normalized co-influence functions are given in Appendix B for different functions of $g_r = g$.

Resonant response R_r, e.g. the bending moment in the structure, is found by applying inertia forces $F_I(z, t)$ to the structure and using the response influence function, $I_R(z)$, introduced when calculating the mean response:

$$R_r(t) = \int_0^h F_I(z, t)I_R(z)\,dz \tag{6.4.36}$$

$$F_I(z, t) = m(z)(2\pi n_c)^2\xi(z)a(t) \tag{6.4.37}$$

Horizontal line-like structure

For a horizontal line-like structure, the joint acceptance function $|J_y(n)|^2$ is given by an expression similar to equation (6.4.34):

$$|J_y(n)|^2 = \frac{1}{b}\int_0^b k_y(r_y, n)\psi_F(r_y, n, U)\,dr_y \tag{6.4.38}$$

where b is the length of the horizontal line-like structure, r_y is the horizontal distance between two points on the structure and k_y is calculated by, see equation (6.4.35) and (6.4.32):

$$k_y(r_y, n) = \frac{2}{b}\int_0^{b-r_y} g_r(y, n)g_r(y + r_y, n)\,dy \tag{6.4.39}$$

$$g_r(y, n) = \frac{C(y)}{C_{\text{ref}}} \frac{U(y)}{U_{\text{ref}}} \sqrt{\frac{S_u(y, n)}{S_{u,\text{ref}}(n)}} \frac{\xi(y)}{\xi_{\text{ref}}} \frac{d(y)}{d_{\text{ref}}} \tag{6.4.40}$$

For flat terrain, the mean wind velocity ratio $U(y)/U_{\text{ref}}$ and power spectrum ratio $S_u(y, n)/S_{u,\text{ref}}(n)$ used in equation (6.4.40) are both equal to 1.

Asymptotic behaviour

For line-like structures, the asymptotes of the joint acceptance function have been described thoroughly by Davenport (1977) using the exponential coherence function given in equation (3.5.25). The similarity between the exponential correlation function and the exponential normalized co-spectrum indicates that the upper frequency limits for horizontal and vertical line-like structures, respectively, are given by

$$|J_y(n)|^2 \to \frac{1}{J_y \phi_y} \tag{6.4.41}$$

$$|J_z(n)|^2 \to \frac{1}{J_z \phi_z} \tag{6.4.42}$$

where $\phi_y = C_y nb/U$ and $\phi_z = C_z nh/U$ and C_y and C_z are the normalized co-spectrum decay constants introduced in Section 3.5.4, equation (3.5.26). The J constants depend on function g_r, see Table 6.1. Thus, for line-like structures of length l, the joint acceptance function is inversely proportional to the non-dimensional frequency $f_l = nl/U$ for high frequencies. Typical joint acceptance functions are shown in Figures 6.2 and 6.3.

The modified exponential coherence function in equation (3.5.31) leads to high-frequency asymptotes equal to half of the asymptotes given in equations (6.4.41) and (6.4.42), see Figure 6.4. Half of this difference in asymptotic behaviour is taken into

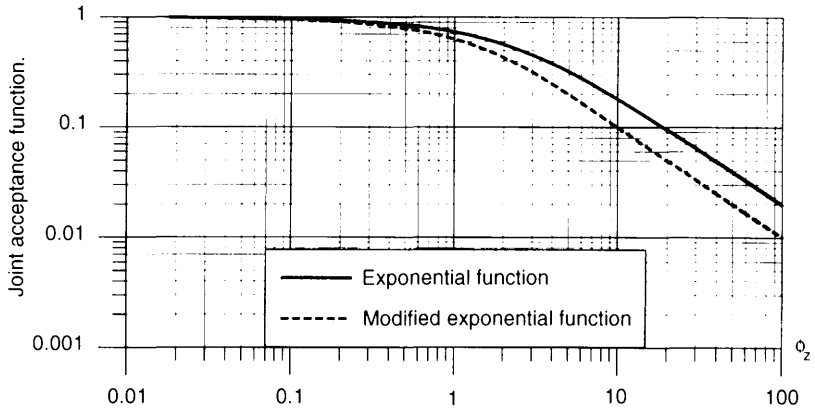

Fig. 6.4 *Joint acceptance functions of $|J^E(\phi)|^2$ and $|J^M(\phi)|^2$ for a constant mode shape ($\xi(z) = 1$) using the exponential coherence function and the modified exponential coherence function, respectively. With these two expressions, the low-frequency behaviour is identical for mode shapes with constant signs. However, $|J^M(\phi)|^2 = \frac{1}{2}|J^E(\phi)|^2$ for frequencies approaching infinity.*

account by different estimates of coherence decay constants in the two expressions, i.e. $C^M \approx \frac{2}{3}C^E$, where the upper index refers to the coherence expression used, see Figure 3.22. Therefore, the modified exponential coherence function leads to resonant response reductions corresponding to a joint acceptance function reduction of approximately 25%.

Modes with constant signs

When the mode shape has a constant sign, the resonant response can be expressed by the mean response using equation (6.3.4) and setting the constants of θ_r and k_r equal to

$$\theta_r = \frac{\gamma_r}{\gamma_m}\frac{1}{m_g}\int_0^h m(z)\frac{\xi(z)}{\xi_{\text{ref}}}\frac{I_R(z)}{I_{R,\text{ref}}}\,dz \tag{6.4.43}$$

$$k_r = \frac{\pi^2}{2\delta}R_N(z_{\text{ref}}, n_e)|J_z(n_e)|^2/\gamma_r^2 \tag{6.4.44}$$

where the normalization constant $\gamma_r = |J_z(0)|$ is given by

$$\gamma_r = \frac{1}{h}\int_0^h g_r(z)\,dz \tag{6.4.45}$$

and m_g is the normalized, generalized mass defined in equation (6.4.10).

Modes with changing signs

For high frequencies corresponding to gusts with wavelengths much smaller than the structure length, the interaction between the wind turbulence and structural modes with changing signs follows the asymptotic behaviour described above. For low frequencies corresponding to gusts with wavelengths of the same size or larger than the structure

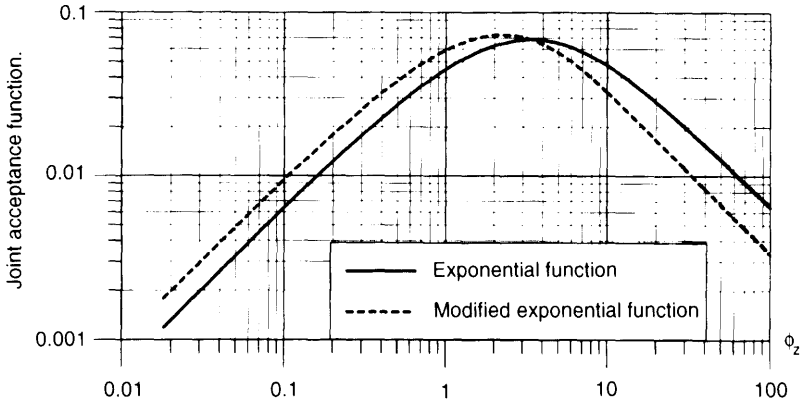

Fig. 6.5 *Joint acceptance functions of $|J^E(\phi)|^2$ and $|J^M(\phi)|^2$ for the linear mode shape changing sign, using the exponential coherence function and the modified exponential coherence function, respectively. $|J^M(\phi)|^2 = \frac{1}{2}|J^E(\phi)|^2$ for frequencies approaching infinity.*

length, the interaction between wind turbulence and structural modes that do not have constant signs is different from the features described for modes with constant signs.

The normalized co-spectrum does not approach unity for low frequencies when the separation is of the same order of magnitude or larger than the turbulent length scale. This fact has a pronounced effect on the wind-induced response, especially for structures with modes that do not have constant signs.

We shall limit ourselves to the rather simplified variation given by function $g_y(y, n) = 2y/b - 1$, i.e. a simple linear variation antisymmetrical with respect to the midpoint $y = b/2$. The joint acceptance functions shown in Figure 6.5 are based on the exponential normalized co-spectrum in equation (3.5.26) and the more accurate modified exponential expression in equation (3.5.31), respectively.

6.5 RESPONSE OF PLATE-LIKE STRUCTURES

The response of plate-like structures is calculated according to the same basic principles as those that applied to line-like structures.

The concept "plate-like" indicates that the lack of correlation along the structural width perpendicular to the mean wind direction is important in the response calculations. This aspect becomes significant when the width is of the same order of magnitude or larger than the wavelength taken at the natural frequency, U/n_e. Therefore, "plate-like" applies to structures such as buildings, chimneys, bridges etc.

6.5.1 Mean response

The mean response, μ_R, which originates from the mean wind load acting on the structure, is calculated by

$$\mu_R = \int_0^h \int_0^b F_q(y, z) I_R(y, z)\, dy dz \tag{6.5.1}$$

where the mean wind load per unit of area $F_q(y, z) = \frac{1}{2}\rho U^2(z) C(y, z)$, and $I_R(y, z)$ is the response–influence function. $I_R(y, z)$ is equal to the response obtained for a unit load acting at point (y, z). A chimney has $I_R(y, z) = z$ for the bending moment at $z = 0$. A bridge with a length b and simply supported at each end has $I_R(y, z) = 1 - y/b$ for the reaction force in the support at $y = 0$.

The mean response is given by the following equations:

$$\mu_R = bhC_{\text{ref}} \tfrac{1}{2}\rho U_{\text{ref}}^2 I_{R,\text{ref}} \gamma_m \tag{6.5.2}$$

$$\gamma_m = \frac{1}{bh} \int_0^h \int_0^b g_m(y, z)\, dy dz \tag{6.5.3}$$

$$g_m(y, z) = \frac{C(y, z)}{C_{\text{ref}}} \frac{U^2(z)}{U_{\text{ref}}^2} \frac{I_R(y, z)}{I_{R,\text{ref}}} \tag{6.5.4}$$

g_m is a non-dimensional function describing the variation of mean wind load and response-influence function over the structure. γ_m gives the integral effect of the g_m function.

6.5.2 Background turbulent response

The background turbulent response, $R_b(t)$, is calculated by treating the fluctuating wind load from turbulence, $F_t(y, z, t) = \rho U(z)u(y, z, t)C(y, z)$, in a quasistatic fashion:

$$R_b(t) = \int_0^h \int_0^b F_t(y, z, t) I_R(y, z)\, dy dz \tag{6.5.5}$$

where $I_R(y, z)$ is the response-influence function introduced when calculating the mean response. The standard deviation of the background response, σ_b, is given by the following equations:

$$\sigma_b^2 = (bhC_{\text{ref}}\rho U_{\text{ref}}\sigma_{u,\text{ref}})^2 I_{R,\text{ref}}^2 J_b^2 \tag{6.5.6}$$

$$J_b^2 = \frac{1}{b^2h^2} \int_0^h \int_0^h \int_0^b \int_0^b \rho_u(r_y, r_z) g_b(y_1, z_1) g_b(y_2, z_2)\, dy_1 dy_2 dz_1 dz_2 \tag{6.5.7}$$

$$g_b(y, z) = \frac{C(y, z)}{C_{\text{ref}}} \frac{U(z)}{U_{\text{ref}}} \frac{\sigma_u(z)}{\sigma_{u,\text{ref}}} \frac{I_R(y, z)}{I_{R,\text{ref}}} \tag{6.5.8}$$

g_b is a non-dimensional function describing the variation of the background turbulent wind load and response-influence function over the structure. $\rho_u(r_y, r_z)$ is the correlation coefficient for longitudinal turbulence components separated r_y horizontally and r_z vertically. The non-dimensional response variance J_b^2 in equation (6.5.7) is determined by the fourfold integral, which can be calculated as shown in Appendix B, i.e.:

$$J_b^2 = \frac{1}{bh} \int_0^h \int_0^b k(r_y, r_z) \rho_u(r_y, r_z)\, dr_y dr_z \tag{6.5.9}$$

where the co-influence function $k(r_y, r_z)$ is given as

$$k(r_y, r_z) = \frac{2}{bh} \int_0^{h-r_z} \int_0^{b-r_y} (g_b(y, z) g_b(y + r_y, z + r_z) + g_b(y, z + r_z) g_b(y + r_y, z))\, dy dz \tag{6.5.10}$$

g_m and g_b functions with constant signs

When the g_m and g_b functions have constant signs, background response can be expressed by the mean response using equation (6.3.3) and setting the constants of θ_b and k_b equal to:

$$\theta_b = \gamma_b/\gamma_m \tag{6.5.11}$$

$$k_b = J_b^2/\gamma_b^2 \tag{6.5.12}$$

where the normalization constant γ_b given by

$$\gamma_b = \frac{1}{bh} \int_0^h \int_0^b g_b(y, z)\, dy dz \tag{6.5.13}$$

is equal to J_b for full correlation with $\rho_u = 1$ for all distances of interest. γ_b gives the integral effect of the g_b function.

Assuming that $g(y,z) = g_y(y)g_z(z)$, background response factor k_b can be approximated by the expressions:

$$k_b = \frac{1}{1 + \sqrt{(\Gamma_y\phi_y)^2 + (\Gamma_z\phi_z)^2 + \left(\frac{2}{\pi}\Gamma_y\phi_y\Gamma_z\phi_z\right)^2}} \tag{6.5.14}$$

$$\phi_y = b/L_u^y \qquad \phi_z = h/L_u^z \tag{6.5.15}$$

where Γ values are obtained for line-like structures, and Γ is given in Table 6.1 for typical g functions. Γ_y is obtained for $g = g_y$, and Γ_z is obtained for $g = g_z$. The asymptotic behaviour that gives the value of $2/\pi$ in the denominator of equation (6.5.14) is explained thoroughly in Section 6.5.3. The background response factor is illustrated in Figure 6.6.

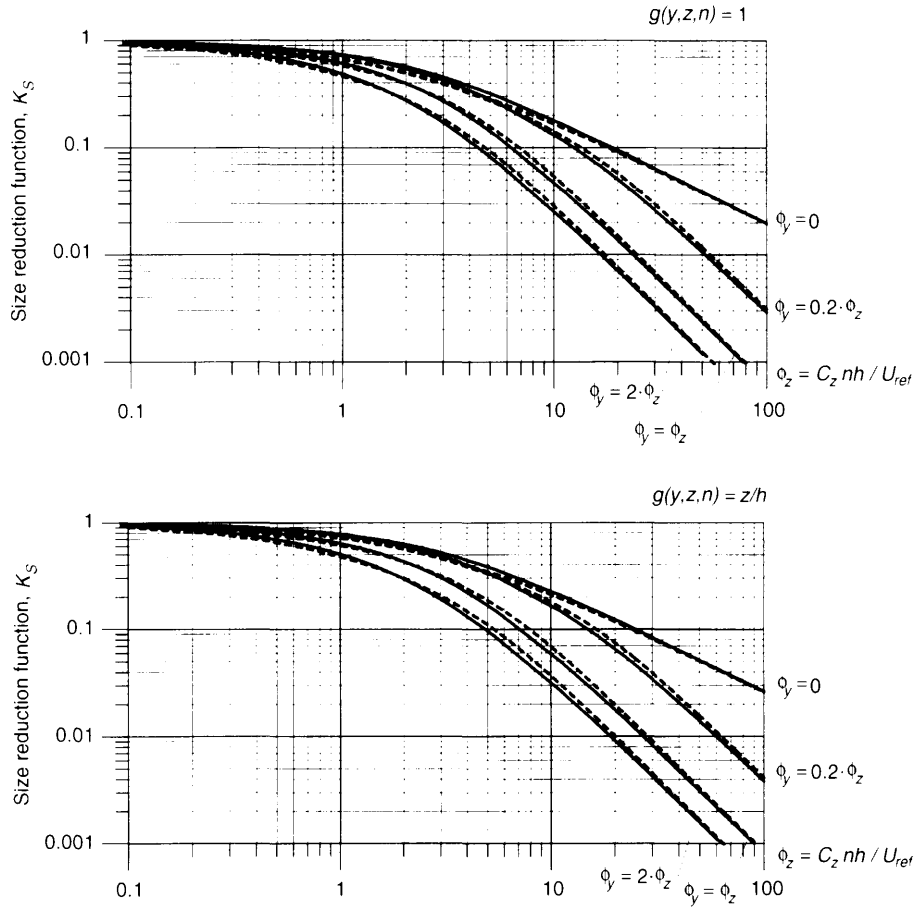

Fig. 6.6 *The solid and dotted lines show the size reduction function given in equations (6.5.29) and (6.5.30), respectively. The curves shown can also be interpreted as the background response factor k_b using $\phi_z = h/L_u^z$ and $\phi_y = b/L_u^y$. (After Hansen and Krenk (1996)).*

6.5.3 Resonant turbulent response

The generalized load in the mode considered is given by

$$Q(t) = \int_0^b \int_0^h C(y, z)\rho U(y, z)u(y, z, t)\xi(y, z)\,dydz \tag{6.5.16}$$

The dynamic part of the structural deflection can be written as $a(t) \cdot \xi(y, z)$, where $a(t)$ is a stochastic amplitude function and $\xi(y, z)$ is a non-dimensional mode shape. The spectral density, $S_a(n)$, of $a(t)$ is given by

$$S_a(n) = (hbC_{\text{ref}}\rho U_{ref}\xi_{\text{ref}})^2|H(n)|^2|J(n)|^2 S_{u,\text{ref}}(n) \tag{6.5.17}$$

where the joint acceptance function $|J(n)|^2$ is found from the expression

$$|J(n)|^2 = \frac{1}{h^2b^2}\int_0^h \int_0^h \int_0^b \int_0^b g(y_1, z_1, n)g(y_2, z_2, n)\psi_F(r_y, r_z, n, U)\,dy_1dy_2dz_1dz_2 \tag{6.5.18}$$

and function $g(y, z, n)$ is defined by

$$g(y, z, n) = \frac{U(y, z)}{U_{\text{ref}}}\sqrt{\frac{S_u(y, z, n)}{S_{u,\text{ref}}(n)}}\frac{C(y, z)}{C_{\text{ref}}}\frac{\xi(y, z)}{\xi_{\text{ref}}} \tag{6.5.19}$$

where $\psi_F(r_y, r_z, n, U)$ is the normalized co-spectrum for the longitudinal turbulence component at two points with a separation r_y horizontally and r_z vertically, n is the frequency in hertz and U is the mean wind velocity. The subscript "ref" refers to the function value at the reference point chosen.

Like the integration procedures used for line-like structures, the joint acceptance function is found as follows, see Appendix B for further details:

$$|J(n)|^2 = \frac{1}{hb}\int_0^h \int_0^b k(r_y, r_z, n)\psi_F(r_y, r_z, n, U)\,dr_ydr_z \tag{6.5.20}$$

where the normalized co-influence function $k(r_y, r_z, n)$ is given by

$$k(r_y, r_z, n) = \frac{2}{hb}\int_0^{h-r_z}\int_0^{b-r_y}(g(y, z, n)g(y + r_y, z + r_z, n) + g(y, z + r_z, n)g(y + r_y, z, n))\,dydz \tag{6.5.21}$$

The normalized co-influence function $k(r_y, r_z, n)$ multiplied by the normalized co-spectrum gives the relative spectral response contribution from all pairs of surface points with separations r_y horizontally and r_z vertically.

All load pairs with a distance of r_y horizontally and r_z vertically give a contribution to the joint acceptance function equal to $k(r_y, r_z, n)\psi_F(r_y, r_z, n, U)\,dr_ydr_z$. Equation (6.5.20) is simply a double integral that adds joint acceptance function contributions originating from load pairs that have distances of (r_y, r_z).

If the function g can be written as

$$g(y, z, n) = g_y(y, n)g_z(z, n) \tag{6.5.22}$$

the normalized co-influence function k is given by

$$k(r_y, r_z, n) = k_y(r_y, n)k_z(r_z, n) \tag{6.5.23}$$

where k_y and k_z are given in equations (6.4.35) and (6.4.39), respectively. The normalized co-influence function given in equation (6.5.21) is expressed in terms of one-dimensional characteristics.

Frequency asymptotes for joint acceptance function

For $n \to 0$ corresponding to large wavelengths in the air flow, the joint acceptance function asymptote is given by

$$|J(n)|^2 \to \frac{1}{hb}\int_0^h \int_0^b k(r_y, r_z, n = 0)\psi_F(r_y, r_z, n = 0)\,dr_y dr_z \tag{6.5.24}$$

For $n \to \infty$ corresponding to small wavelengths in the air flow, the correlation ψ_F is local, i.e. $r_y \approx r_z \approx 0$, and the joint acceptance function asymptote is given by

$$|J(n)|^2 \to k(r_y = 0, r_z = 0, n \to \infty)\frac{1}{hb}\int_0^h \int_0^b \psi_F(r_y, r_z, n \to \infty)\,dr_y dr_z \tag{6.5.25}$$

For high frequencies, the exponential coherence function is used as an approximation of the normalized co-spectrum, see equation (3.5.26). Using this assumption, the upper limit of the joint acceptance function is given by

$$|J(n)|^2 \to k(r_y = 0, r_z = 0, n \to \infty)\frac{\pi/2}{\left(C_y\frac{nb}{U}\right)\left(C_z\frac{nh}{U}\right)} \tag{6.5.26}$$

If the function g is given as a product of the two one-dimensional functions, g_y and g_z, see equation (6.5.22), the asymptote of influence function k is given (see equation (6.5.23)) by

$$k(r_y = 0, r_z = 0, n \to \infty) = k_y(r_y = 0, n \to \infty)k_z(r_z = 0, n \to \infty) \tag{6.5.27}$$

Comparing equation (6.5.26) and (6.5.27) with the asymptotic behaviour of the line-like joint acceptance functions given in equation (6.4.41) and (6.4.42) leads to the following relation:

$$|J(n \to \infty)|^2 = \frac{\pi}{2}|J_y(n \to \infty)|^2|J_z(n \to \infty)|^2 \tag{6.5.28}$$

The factor of $\pi/2$ is the ratio between the plate-like joint acceptance function and the product of the two line-like joint acceptance functions for high frequencies of n. Using products of line-like joint acceptance functions, which is common practice in most building codes, may therefore lead to underestimated response estimates. Normally, this is taken into account using safe estimates of flow parameters, such as normalized co-spectrum decay constants C_y and C_z.

6.5.4 Modes with constant signs

Size reduction function $K_s(n)$ accounts for the interaction between wind turbulence and the structural mode of vibration. For modes with constant signs, the size reduction function approaches its maximum value for low frequencies at which wind turbulence is best correlated over the structure. The correlation, and thereby the size reduction function,

decreases as the frequency increases. The size reduction function is given by

$$K_y(n) = \int_0^h \int_0^b k(r_y, r_z, n)\psi_F(r_y, r_z, n, U)\,dr_y dr_z \Big/ \int_0^h \int_0^b k(r_y, r_z, n = 0)\,dr_y dr_z \tag{6.5.29}$$

where the normalized co-influence function $k(r_y, r_z, n)$ multiplied by the normalized co-spectrum function gives the relative spectral response contribution from all pairs of surface points with separations of r_y horizontally and r_z vertically. The normalized co-influence function k is given by equation (6.5.21).

The size reduction function may be approximated by the expressions:

$$K_y(n) = \frac{1}{1 + \sqrt{(G_y\phi_y)^2 + (G_z\phi_z)^2 + \left(\frac{2}{\pi}G_y\phi_y G_z\phi_z\right)^2}} \tag{6.5.30}$$

$$\phi_y = \frac{C_y bn}{U_{\text{ref}}} \qquad \phi_z = \frac{C_z hn}{U_{\text{ref}}} \tag{6.5.31}$$

where G_y and G_z are determined from the response of equivalent one-dimensional structures with horizontal length b and vertical height h, respectively. The approximation of the size reduction function has the correct asymptotes for frequencies approaching zero and infinity, respectively, see Section 6.5.3.

Some examples of function $g(\cdot)$ and the corresponding coefficient G are given in Table 6.1. In many cases, function g does not depend upon frequency n.

The resonant response can be expressed in terms of the mean response using equation (6.3.4) and setting the constants of θ_r and k_r equal to

$$\theta_r = \frac{\gamma_r}{\gamma_m} \frac{\int_0^h \int_0^b \mu(y, z)\frac{\xi(y, z)}{\xi_{\text{ref}}}\frac{I_R(y, z)}{I_{R,\text{ref}}}\,dydz}{\int_0^h \int_0^b \mu(y, z)\frac{\xi^2(y, z)}{\xi_{\text{ref}}^2}\,dydz} \tag{6.5.32}$$

$$k_r = \frac{\pi^2}{2\delta} R_N(z_{\text{ref}}, n_c)K_y(n_c) \tag{6.5.33}$$

where normalization constant $\gamma_r = |J(0)|$ is given by

$$\gamma_r = \frac{1}{hb}\int_0^h \int_0^b g(y, z)\,dydz \tag{6.5.34}$$

and $\mu(y, z)$ is the structure mass per unit of area.

6.5.5 Modes with changing signs

We shall limit ourselves to the rather simplified variation given by function $g_y(y) = 2y/b - 1$, i.e. a simple linear variation, antisymmetrical with respect to the midpoint $y = b/2$. The height variation is described by $g_z(z) = 1$ and $g_z(z) = z/h$, respectively.

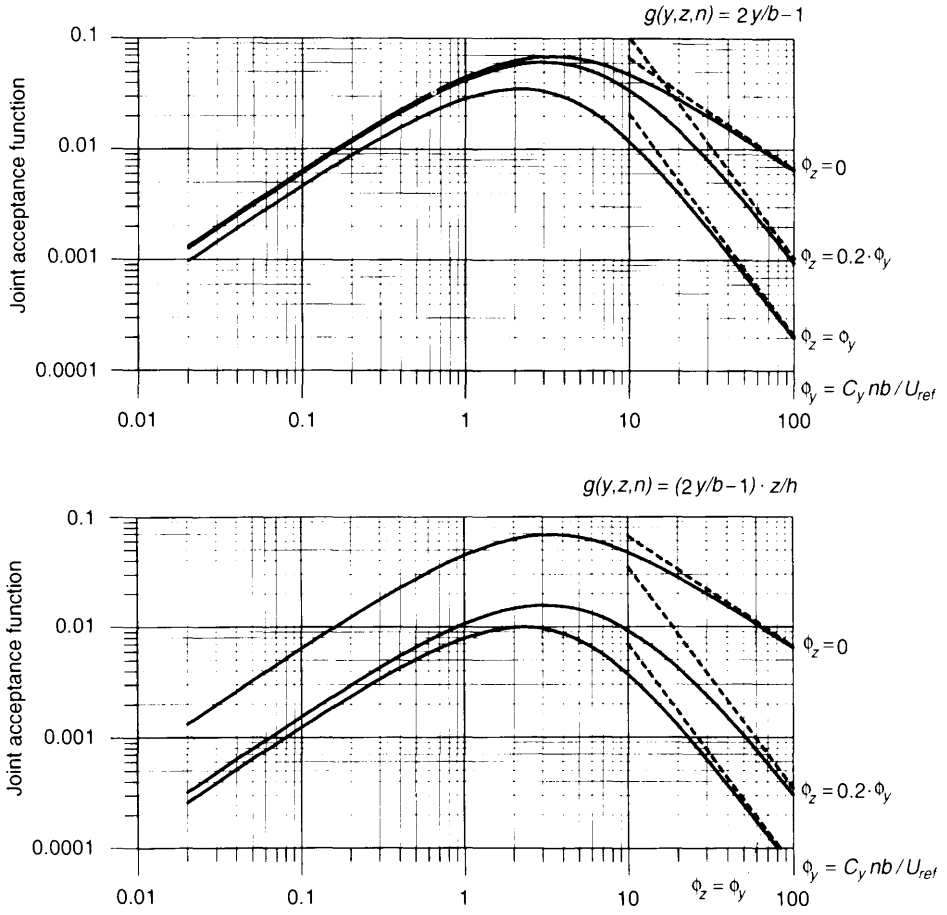

Fig. 6.7 *This figure shows the joint acceptance function given in equation (6.5.20). The curves shown can also be interpreted as the non-dimensional response variance* J_b^2 *using* $\phi_y = b/L_u^y$ *and* $\phi_z = h/L_u^z$. *The dotted lines give the asymptotic behaviour according to equation (6.5.26). (After Hansen and Krenk (1996)).*

6.6 DESIGN PROCEDURES

Now we will look at a design procedure which follows the principles described previously in the chapter. Section 6.6.1 includes examples of a chimney, a bridge and a building to illustrate the procedure proposed, in which the mode shape does not change sign. The special aspects for structures with a mode shape that changes sign are demonstrated in Section 6.6.2, which considers a cantilevered bridge during construction. Section 6.6.3 shows the response calculations for structures with complicated mode shapes not covered by the simple procedures given in Sections 6.6.1–6.6.2.

The algebraic approximations used in the design procedures proposed here are typically accurate within approximately 5%. The uncertainties inherent in the response estimates are, therefore, primarily connected to the accuracy of the input parameters, such as decay constants of the normalized co-spectrum and structural damping.

The design procedures proposed in Sections 6.6.1 and 6.6.2 may conveniently be used in design codes, thereby improving their accuracy.

6.6.1 Design procedure for mode shapes with constant sign

The structures covered by this procedure are shown in Figure 6.8. The design procedure proposed covers structures with heights of up to 200 m that have mode shapes with constant signs. The procedure given is not appropriate for dynamic analysis of guyed masts, continuous bridges, cable-stayed bridges or arch bridges. The height limit of 200 m is due to the simple logarithmic profile used in the design procedure, see Section 3.2.

The structure considered has a vertical dimension h and a horizontal dimension b. If the width varies with height for a vertical line-like structure, the width of b at reference height z_{ref} shown in Figure 6.8 should be chosen. If the structure is horizontal and line-like, the width of h at the centre point should be chosen.

Wind structure

The mean wind velocity at height z above ground, $U(z)$, is assumed to vary according to the logarithmic profile:

$$U(z) = U_{\text{bas}} k_T \ln(z/z_0) \tag{6.6.1}$$

where U_{bas} is the reference wind velocity that specifies the climate of the site, k_T is the terrain factor and z_0 is the roughness length; see Chapter 3 which describes the velocity profile.

Full-scale measurements are used to estimate integral length scales. The results show very wide scatter originating mainly from the variability of length and degree of stationarity of the records being analysed. The integral length scale depends on height z above ground and on terrain roughness. Wind velocity may also influence integral length scales.

Counihan (1975) suggests, that the integral length scale decreases with increasing surface roughness, see Section 3.5.2. The opposite variation is specified by ESDU 85020. The integral length scale depends on surface characteristics on a very long upstream fetch, say of the order of 50 km. Except for offshore structures and structures within a few kilometres of the sea, the integral length scale will typically be influenced in a complicated way by several different terrain categories. At present, there does not seem to be a simple, accurate procedure available in order to determine the integral length scale for terrain with surface roughness changes that occur in most practical design work.

We propose a simple representation of the integral length scale L_u^x, in which the response estimated might be slightly on the safe side in some special cases. This approach is supported by the fact that the response does not depend greatly on the integral length

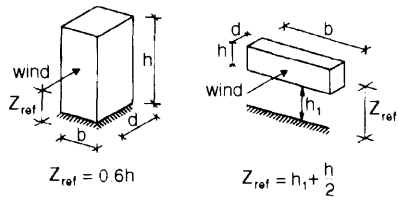

Fig. 6.8 *Structures covered by the design procedure proposed.*

scale. The resonant response depends on the integral length scale to the power of minus one third, i.e. a rather slow decrease for increasing length scale.

The integral length scale used in the design procedure is proposed to be

$$L_u^x = L_{10}\left(\frac{z}{z_{10}}\right)^{0.3} ; 10 \text{ m} \leqslant z \leqslant 200 \text{ m} \tag{6.6.2}$$

where $z_{10} = 10$ m and $L_{10} = 100$ m are independent of surface roughness. The integral length scale at $z = 10$ m is also used for heights lower than 10 m.

The remaining integral length scales used in the design procedure are given by $L_u^y = \frac{1}{3}L_u^x$ and $L_u^z = \frac{1}{4}L_u^x$, see Section 3.5.2. These integral length scales, which are used to calculate the background response, are deliberately slightly overestimated in order to give conservative response estimates.

The design procedure proposed uses the turbulence intensity given in equation (3.5.3), the non-dimensional power spectral density function, $R_N(z, n)$, given in equation (3.5.17) and the exponential normalized co-spectrum given in equation (3.5.26). Decay constants of C_y and C_z are specified to be 10, calculating the resonant response.

Gust factor

The gust factor φ is defined as the ratio between a static wind load which gives the maximum response of the structure during a reference time interval, normally taken as 10 minutes, and the mean wind load which gives the mean response of the structure. The gust factor is calculated as shown below, see equation (6.3.5):

$$\varphi = 1 + k_p 2I_{u,\text{ref}}\sqrt{\theta_b^2 k_b + \theta_r^2 k_r} \tag{6.6.3}$$

A representative reference height is defined in Figure 6.8. The factors of θ_b and θ_r incorporate the effect of different distributions of mean wind load compared to fluctuating wind load. In the design procedure, $\theta_b = 1$ and $\theta_r = 1$, which is a good approximation for the most common structures.

Peak factor k_p

The peak factor k_p is defined as the ratio between the peak and standard deviation of the fluctuating load within reference time interval T. The peak factor is calculated (see Section 4.6) as

$$k_p = \sqrt{2\ln(\nu T)} + \frac{0.5772}{\sqrt{2\ln(\nu T)}} \tag{6.6.4}$$

where ν is the zero-upcrossing frequency and $T = 600$ seconds is the averaging time for the reference wind velocity. The zero-upcrossing frequency ν is calculated from background and resonance contributions as

$$\nu = \sqrt{\frac{n_0^2 k_b + n_e^2 k_r}{k_b + k_r}} \tag{6.6.5}$$

where n_e is the natural frequency (Hz) for the alongwind vibrations of the structure and n_0 is the representative frequency (Hz) of the gust loading on rigid structures. The frequency

n_0 is defined as

$$n_0 = \sqrt{\frac{\int_0^\infty n^2 K_S(n) S_u(n, z_{\text{ref}})\, dn}{\int_0^\infty K_S(n) S_u(n, z_{\text{ref}})\, dn}} \tag{6.6.6}$$

where the size reduction function $K_S(n)$ is given in equation (6.5.30). The frequency n_0 is approximated by

$$n_0 = 0.3 \frac{U(z_{\text{ref}})}{\sqrt{hb}} \sqrt{\frac{\sqrt{hb}}{L_u}}; \qquad n_0 \leq n_e \tag{6.6.7}$$

where $L_u = L_u^x(z_{\text{ref}})$. If equation (6.6.7) gives $n_0 > n_e$, then $n_0 = n_e$ should be used. $\sqrt{hb}$ has been chosen as a characteristic dimension, according to the asymptotic behaviour of the size reduction function for frequencies approaching infinity. The approximation overestimates frequency n_0, and thereby the response, slightly, see Figure 6.9.

Background response

The distribution of the background response is assumed to give $\Gamma_x = \frac{1}{2}$ and $\Gamma_z = \frac{3}{8}$, see Table 6.1. Background response factor k_b takes the excitation from background turbulence into account and is given by equation (6.5.14) using $\Gamma_x \phi_x = \frac{3}{2} b/L_u^x$ and $\Gamma_z \phi_z = \frac{3}{2} h/L_u^x$, i.e.

$$k_b = \frac{1}{1 + \frac{3}{2}\sqrt{\left(\frac{b}{L_u}\right)^2 + \left(\frac{h}{L_u}\right)^2 + \left(\frac{3}{\pi}\frac{b}{L_u}\frac{h}{L_u}\right)^2}} \tag{6.6.8}$$

The background response factor k_b approaches $\frac{2}{9}\pi L_u^2/bh$ for large structures with $h \approx b$.

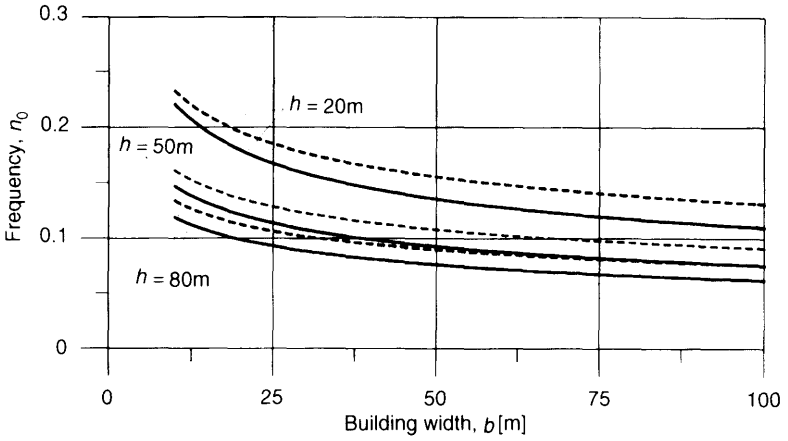

Fig. 6.9 *This figure shows frequency n_0 as a function of building height and width. The solid line corresponds to the accurate expression in equation (6.6.6) and the approximation given in equation (6.6.7) is shown by the dotted line.*

Resonant response

Resonant response factor k_r, which gives the excitation caused by turbulent fluctuations close to the natural frequency n_e of the structure, is defined (see equation (6.5.33)) by

$$k_r = \frac{\pi^2}{2\delta} R_N(z_{\text{ref}}, n_e) K_s(n_e) \tag{6.6.9}$$

where the non-dimensional spectral density $R_N(z_{\text{ref}}, n_e)$ is given in equation (3.5.17), the size reduction function $K_s(n_e)$ is given in equation (6.5.30) and δ is the logarithmic damping decrement of the along-wind vibrations equal to

$$\delta = \delta_s + \delta_a \tag{6.6.10}$$

in which δ_s is structural damping and aerodynamic damping δ_a is

$$\delta_a = \frac{C\rho U(z_{\text{ref}})}{2n_e\mu} \tag{6.6.11}$$

where C is the shape factor, ρ is the air density, $U(z_{\text{ref}})$ is the mean wind velocity at the reference height and μ is the structural mass per unit of area taken at reference height, and for a horizontal line-like structure at the centre point. For line-like structures, the mass per unit of length is equal to μ multiplied by the structure width.

Examples

The design procedure calculations are illustrated for three structures: (1) a 150 m tall concrete chimney, (2) a 100 m long bridge and (3) a 50 m tall, 20 m wide building, see Tables 6.3 and 6.4. Wind load and structural vibrations along the mean wind direction are considered. The natural frequencies and structural damping chosen for the three structures, see rows 7–8 in Table 6.3, are based on experience. They should be estimated accurately for the particular structure in question.

The g functions assumed are as follows:

Structure 1: $g_y = 1$, $g_z = (z/h)^2$.

Structure 2: $g_y = \sin(\pi y/b)$, $g_z = 1$.

Structure 3: $g_y = 1$, $g_z = z/h$.

Table 6.3 *Input parameters specifying the wind climate, terrain and structural characteristics.*

		Struc. 1	Struc. 2	Struc. 3
Wind climate				
1. Reference wind velocity U_{bas} (m/s)		25	25	25
2. Air density ρ (kg/m^3)		1.25	1.25	1.25
Site specifications				
3. Roughness length z_0 (m)	Table 3.2	0.05	0.01	0.3
4. Terrain factor k_T	Table 3.2	0.19	0.17	0.22
Structure specifications				
5. Horizontal dimension b (m)		6	100	20
6. Vertical dimension h (m)		150	5	50
7. Natural frequency n_e (Hz)		0.3	1.0	0.9
8. Logarithmic decrement δ_s		0.06	0.04	0.08
9. Mass per unit of area μ (kg/m^2)		700	1000	500
10. Shape factor C		0.6	1.0	1.2

Table 6.4 *The results calculated were obtained using the design procedure specifications indicated in the table.*

Design parameters		Struc. 1	Struc. 2	Struc. 3
11. Reference height z_{ref} (m)	Figure 6.8	90	50	30
12. Mean wind velocity $U(z_{ref})$ (m/s)	(6.6.1)	35.6	36.2	25.3
13. Turbulence intensity $I_u(z_{ref}) = I_{u,ref}$	(3.5.3)	0.133	0.117	0.217
14. Integral length scale $L_u = L_u^x(z_{ref})$ (m)	(6.6.2)	193	162	139
15. Aerodynamic damping δ_a	(6.6.11)	0.064	0.023	0.042
16. Total damping δ	(6.6.10)	0.124	0.063	0.122
17. Background response frequency n_0 (Hz)	(6.6.7)	0.140	0.180	0.115
18. Background response k_b	(6.6.8)	0.462	0.519	0.631
19. Spectral density function $R_N(z_{ref}, n_e)$	(3.5.17)	0.093	0.050	0.047
20. Mode-shape coefficient G_y	Table 6.1	0.500	0.405	0.500
21. Non-dimensional parameter ϕ_y	(6.5.31)	0.506	27.6	7.11
22. Mode-shape coefficient G_z	Table 6.1	0.278	0.500	0.375
23. Non-dimensional parameter ϕ_z	(6.5.31)	12.6	1.38	17.8
24. Size reduction factor $K_s(n_e)$	(6.5.30)	0.219	0.075	0.056
25. Resonant response k_r	(6.6.9)	0.813	0.299	0.107
26. Zero-upcrossing frequency ν (Hz)	(6.6.5)	0.254	0.622	0.359
27. Peak factor k_p	(6.6.4)	3.35	3.61	3.45
28. Gust factor φ	(6.6.3)	2.01	1.77	2.29

The chimney site is characterized as farmland, the bridge is assumed to be 50 m above sea level and the building is located in suburban terrain.

6.6.2 Design procedure for mode shapes with changing sign

The structure covered by the procedure is shown in Figure 6.10, i.e. a horizontal line-like structure with a simple linear mode shape antisymmetrical about the midpoint. The cantilevered line-like bridge considered has a length of b.

The wind structure is assumed to be as described in Section 6.6.1.

The extreme torsional moment at the top of the support is calculated using the design procedure. The standard gust factor approach cannot be used, since the mean torsional moment is zero. Instead, the gust factor φ is defined as the ratio between the maximum torsional moment occurring during the reference time interval of 10 minutes, and torsional moment μ_R obtained when the mean wind load acts on the left (or right) half of the bridge alone, i.e.:

$$R_{max} = \varphi\mu_R = k_p 2I_u(z_{ref})\sqrt{k_b + k_r}\mu_R \tag{6.6.12}$$

where

$$\mu_R = \tfrac{1}{4}b\tfrac{1}{2}b\,d_{ref}C_{ref}\tfrac{1}{2}\rho U_{ref}^2 \tag{6.6.13}$$

where d_{ref} is the reference width of the bridge deck perpendicular to the mean wind direction.

The effect of background turbulence on the peak factor is assumed to be negligible, indicating that peak factor k_p is determined using equation (6.6.4) with $\nu = n_e$.

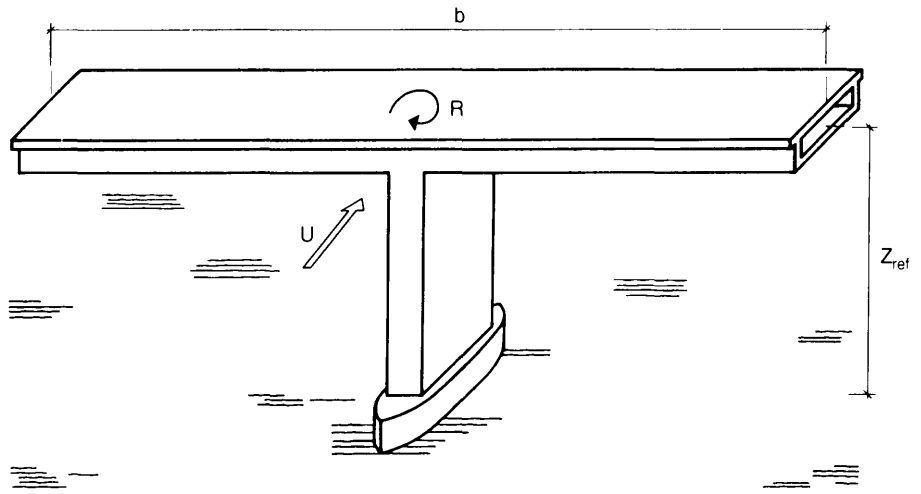

Fig. 6.10 *Cantilevered bridge covered by the design procedure proposed. Wind load and horizontal vibrations along the mean wind direction are considered in this design procedure. (Reproduced by permission of Danish Building Research Institute).*

The standard deviation of the background response, σ_b, is given below, see equation (6.4.17) using $I_{R,\mathrm{ref}} = b/2$:

$$\sigma_b = 2I_{u,\mathrm{ref}}\, 4J_b \mu_R \tag{6.6.14}$$

which shows that the background response factor is equal to

$$k_b = 16J_b^2 \tag{6.6.15}$$

where J_b is determined using equation (6.4.28) with arguments of $\phi_y = b/L_u^y$ and $L_u^y = \frac{1}{3}L_u^x$.

The standard deviation of the resonant response factor, σ_r, which gives the excitation from turbulent fluctuations close to the natural frequency of the structure, is determined by equations (6.4.33), (6.4.36) and (6.4.37). This indicates that the resonant response factor is equal to

$$k_r = 16\frac{\pi^2}{2\delta} R_N(z_{\mathrm{ref}}, n_e)|J_y(n_e)|^2 \tag{6.6.16}$$

where the non-dimensional spectral density $R_N(z_{\mathrm{ref}}, n_e)$ is given in equation (3.5.17) and joint acceptance function $|J_y(n_e)|^2$ is given in equation (6.4.28) using $\phi_y = C_y nb/U_{\mathrm{ref}}$ as an argument. δ is the logarithmic damping decrement of the along-wind vibrations consisting of structural damping and aerodynamic damping. The latter is calculated as shown in equation (6.6.11).

Examples

The design procedure calculations are illustrated for three bridge lengths: 50 m, 150 m and 300 m, see Tables 6.5 and 6.6. The natural frequencies in row 7 of Table 6.5 are based on experience and they refer to the horizontal, torsional vibrations of a cantilevered

Table 6.5 *Input parameters specifying wind climate, terrain and structural characteristics.*

		Bridge 1	Bridge 2	Bridge 3
Wind climate				
1. Reference wind velocity U_{bas} (m/s)		25	25	25
2. Air density ρ (kg/m^3)		1.25	1.25	1.25
Site specifications				
3. Roughness length z_0 (m)	Table 3.2	0.01	0.01	0.01
4. Terrain factor k_T	Table 3.2	0.17	0.17	0.17
Structure specifications				
5. Horizontal dimension b (m)		50	150	300
6. Vertical width d_{ref} (m)		5	5	5
7. Natural frequency n_e (Hz)		2.0	1.0	0.5
8. Logarithmic decrement δ_s		0.05	0.05	0.05
9. Mass per unit of area μ (kg/m^2)		500	500	500
10. Shape factor C		0.6	0.6	0.6

Table 6.6 *The results calculated were obtained using the design procedure specifications indicated in the table.*

Design parameters		Bridge 1	Bridge 2	Bridge 3
11. Reference height z_{ref} (m)	Figure 6.10	50	50	50
12. Mean wind velocity $U(z_{ref})$ (m/s)	(6.6.1)	36.2	36.2	36.2
13. Turbulence intensity $I_u(z_{ref}) = I_{u,ref}$	(3.5.3)	0.117	0.117	0.117
14. Integral length scale $L_u = L_u^x(z_{ref})$ (m)	(6.6.2)	162	162	162
15. Aerodynamic damping δ_a	(6.6.11)	0.014	0.027	0.054
16. Total damping δ	(6.6.10)	0.064	0.077	0.104
17. $\phi_y = b/L_u^y = 3b/L_u$		0.926	2.78	5.55
18. Background response k_b	(6.6.15)	0.708	1.098	0.998
19. Spectral density function $R_N(z_{ref}, n_e)$	(3.5.17)	0.032	0.050	0.077
20. $\phi_y = C_y nb/U_{ref}$	(6.5.31)	27.6	41.4	41.4
21. Joint acceptance function $\lvert J_y(n_e)\rvert^2$	(6.4.28)	0.021	0.015	0.015
22. Resonant response k_r	(6.6.16)	0.853	0.763	0.865
23. Peak factor $k_p(\nu = n_e)$	(6.6.4)	3.92	3.74	3.55
24. Gust factor φ	(6.6.12)	1.15	1.20	1.14

bridge. The natural frequency should be calculated accurately for the particular structure in question.

The bridge is assumed to be 50 m above sea level.

6.6.3 Structures with complicated mode shapes

The calculations will be illustrated by a horizontal, line-like, three-span continuous beam, for which the aerodynamic admittance function was shown in Figure 4.13. The gust factor and the maximum wind-induced bending moment at central midspan are determined.

The height above terrain is 30 m. The beam has a constant mass and stiffness along its length assumed to be 120 m, i.e. each span is 40 m.

The mode shape is a simple sinusoidal function and the natural frequency is assumed to be 1 Hz. The resonant acceleration at central midspan is determined by the procedure outlined in Section 6.4.2. In order to determine the resonant bending moment at central midspan, the ratio between the resonant bending moment and resonant acceleration at central midspan has been calculated to be 405 kNm/(m/s^2) for this particular mode shape assuming a mass of 2500 kg per unit of beam length. This ratio is used in row 26 of Table 6.8 to calculate the resonant bending moment at central midspan.

Table 6.7 *Input parameters specifying wind climate, terrain and structural characteristics.*

Wind climate		
1. Reference wind velocity U_{bas} (m/s)		25
2. Air density ρ (kg/m^3)		1.25
Site specifications		
3. Roughness length z_0 (m)	Table 3.2	0.01
4. Terrain factor k_T	Table 3.2	0.17
Structure specifications		
5. Horizontal length b (m)		120
6. Beam width d_{ref} (m)		5.0
7. Natural frequency n_e (Hz)		1.0
8. Logarithmic decrement δ_s		0.05
9. Mass per unit of area μ (kg/m^2)		500
10. Shape factor C		0.6

Table 6.8 *Design parameters for a three-span beam with a total length of 120 m.*

Design parameters		
11. Reference height z_{ref} (m)		30.0
12. Mean wind velocity $U(z_{ref})$ (m/s)	(6.6.1)	34.0
13. Reference influence number (Nm/N)	Figure 4.13	7.0
14. Integral effect of g_m, i.e. γ_m	(6.4.14)	0.0476
15. Mean bending moment at midspan (kNm)	(6.4.13)	86.7
16. Turbulence intensity $I_u(z_{ref}) = I_{u,ref}$	(3.5.3)	0.125
17. Integral length scale $L_u = L_u^x(z_{ref})$ (m)	(6.6.2)	139
18. $L_u^y = L_u/3$ (m)		46.3
19. Non-dimensional response variance J_b^2	(6.4.20)	0.0095
20. Background bending moment σ_b (kNm)	(6.4.17)	44.4
21. Aerodynamic damping δ_a	(6.6.11)	0.0255
22. Total damping δ	(6.6.10)	0.0755
23. Spectral density function $R_N(z_{ref}, n_e)$	(3.5.17)	0.0533
24. $\phi_y = C_y nb/U_{ref}(C_y = 10)$		35.3
25. Joint acceptance function $\lvert J_y(n_e)\rvert^2$	(6.4.34)	0.0265
26. Resonant bending moment σ_r (kNm)	(6.4.33)	53.4
27. Peak factor $k_p(\nu = n_e)$	(6.6.4)	3.74
28. Maximum bending moment R_{max} (kNm)	(6.3.1)	346
29. Gust factor $\varphi = R_{max}/\mu_R$	(6.3.1), (6.3.2)	3.99

6.7 DISCUSSION OF EUROCODE 1

The dynamic along-wind response of simple structures is specified in an informative Annex of Eurocode 1.

Two papers by Solari (1993) give background information on the calculation procedure used in the Eurocode.

Wind structure

The turbulence intensity given in equation (3.5.3) is also specified in the Eurocode.

The Eurocode's non-dimensional power-spectral density function, $R_N(z, n)$, has the form indicated in equation (3.5.17). The length-scale parameter L_i used in the Eurocode was originally given in ESDU 74031. Later ESDU updates of turbulent length scales may provide more accurate response estimates.

The Eurocode's normalized co-spectrum function is as given in equation (3.5.26). Decay constants of C_y and C_z are specified to be 11.5, based on an extensive number of full-scale measurements of longitudinal turbulence, see Solari (1993a, b). The fact that pressures on the structure are better correlated than the longitudinal turbulence in the undisturbed, oncoming air flow has apparently not been taken into account in the choice of normalized co-spectrum decay constants. However, this is to some extent balanced out by neglecting the lack of correlation between pressures on the front face and rear face of the structure.

Dynamic coefficient

In the Eurocode, dynamic coefficient c_d is defined as the ratio between the dynamic value of the exposure coefficient that represents the gust load on the structure, and the value of exposure coefficient c_e corresponding to the quasistatic gust load at a point. The dynamic coefficient is calculated from

$$c_d = \frac{1 + k_p 2 I_u(z_{\text{ref}}) \sqrt{k_b + k_r}}{1 + 7 I_u(z_{\text{ref}})} \tag{6.7.1}$$

where z_{ref} is a representative reference height. Peak factor k_p, background response factor k_b and resonant response factor k_r are specified in the Eurocode. For quasistatic response of a point-like structure, the values $k_p = 3.5$, $k_b = 1$ and $k_r = 0$ are assumed in (6.7.1), so $c_d = 1$ for this case.

The gust factor is equal to the dynamic coefficient multiplied by reference exposure coefficient c_e which corresponds to quasistatic gust load at a point.

Peak factor k_p

Eurocode 1 uses a complicated approximation of frequency n_0. The characteristic dimension of $b + h$ used in the Eurocode is difficult to interpret physically. However, the Eurocode approximation and the approximation proposed in equation (6.6.7) lead to almost identical results in most situations.

Background response

In the Eurocode, the approximation of background excitation k_b is specified to be

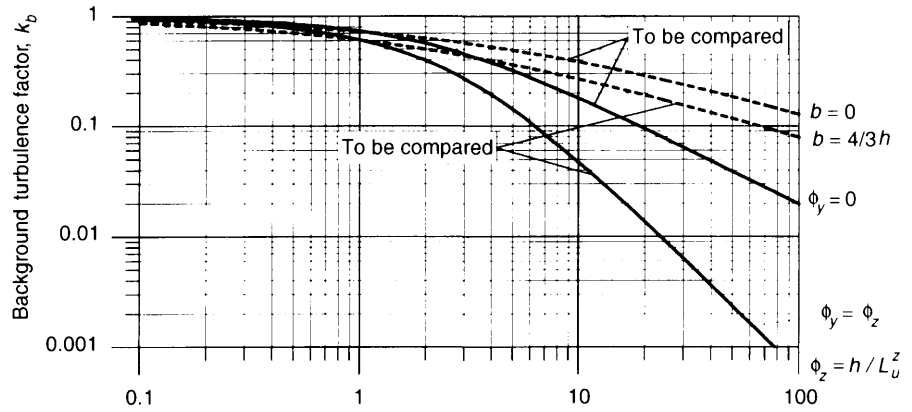

Fig. 6.11 *Background turbulence factor based on the accurate expression given in equation (6.5.12) (solid lines) and on the Eurocode expression in equation (6.7.2) illustrated by dotted lines.*

$$k_b = \frac{1}{1 + 0.9\left(\dfrac{b+h}{L_u}\right)^{0.63}} \tag{6.7.2}$$

where the Eurocode integral length scale L_u was discussed in Section 3.5.5. The characteristic dimension of $b + h$ used in this expression is also difficult to interpret physically.

In Figure 6.11, the Eurocode background turbulence response is compared to the derived background turbulence response in equation (6.5.12) assuming $g_b = 1$, $L_u^z = L_u^x/4$ and $L_u^y = L_u^x/3$. The Eurocode underestimates the background turbulence response for structures with width b or height h below approximately 50 m. For larger structures, the Eurocode overestimates the background turbulence response. Furthermore, the asymptotic behaviour is not reproduced in the simplified expression used in Eurocode 1.

Resonant response

The size reduction function specified in the Eurocode is given by

$$K_s(n) = K_h(n)K_b(n) \tag{6.7.3}$$

where K_h is the size reduction corresponding to a vertical line-like structure and K_b is the size reduction as found for a horizontal line-like structure. The product format used in Eurocode 1 will tend to underestimate the size reduction function by a factor of up to $\pi/2$, see equation (6.5.30).

The product format in equation (6.7.3) leads to an underestimated resonant response. Whether the response obtained using Eurocode 1 is unsafe depends on the accuracy of the method itself and on the choices used for the remaining flow and structural parameters inherent in the calculations.

The Eurocode is more complicated and in the author's opinion less accurate than the design procedure proposed in Section 6.6.1.

7 Cross-wind Vibrations Induced by Vortex Shedding

Vibrations generated by vortex shedding may occur in slender structures such as cables, chimneys, towers or bridge-decks. In rare cases, vortex shedding might induce ovalling vibrations of steel chimneys, i.e. vibrations in which the shape of the cross section varies in time.

The risk of vortex-induced vibrations increases if

- slender structures are in line, separated by a distance of less than approximately 10–15 times the width of the structures;
- a slender structure is affected by the vortices shed by an adjacent large solid structure.

Such phenomena usually call for model tests in a wind tunnel.

Calculation models

Although a great deal of effort has been made during recent decades to improve the analytical models used for predicting vibrations due to vortex shedding, the analytical models available are still rather crude. The cross-wind forcing mechanisms have proved to be so complex that there is no general analytical method available to calculate cross-wind structural response. The main physical parameters involved in the forcing mechanisms have been clarified, but the basic data used in full-scale predictions have not reached a general agreement among researchers.

Some of the most important pioneering research contributions during approximately the last 20 years have come from the University of Western Ontario (UWO) in Canada and the Technical University Aachen (RWTH) in Germany. These two research groups have directed their efforts towards identifying different aspects of vortex-induced vibrations. However, the methods they use to take aeroelastic effects, i.e. motion-dependent forces, into account differ considerably.

The mathematical spectral model proposed by the Canadian research group is used as the basis for the Canadian Code of Practice. It gives accurate results for relatively stiff structures, such as concrete chimneys, in which aeroelastic effects are relatively small or moderate. Flexible structures, such as many steel chimneys, call for accurate modelling of large aeroelastic effects. The mathematical vortex-resonance model suggested by the German research group focuses mainly on these aeroelastic effects. The practical application of the two different approaches is illustrated here by considering the Canadian Code of Practice, see Section 7.4.2, and the Eurocode. The latter is based on the approach suggested by the German research group, see Section 7.5.2. The widely used CICIND

Model Code is mentioned in Section 7.4.3, and a comparison between these codes is presented in Section 7.5.3.

Chimney vibrations calculated using the spectral model depend on the joint acceptance function, which is expressed as a double integral. This integral is calculated in two steps as single integrals by applying the integration format described in Appendix B. This gives a simplified expression for the deflections.

7.1 PHYSICAL BACKGROUND

Vortex-induced vibrations occur when vortices are shed alternately from opposite sides of the structure. This gives rise to a fluctuating load perpendicular to the wind direction, see Figure 7.1. When a vortex is formed on one side of the structure, the wind speed is increased on the other side, and according to Bernoulli's theory, see formula (4.1), this results in reduced pressure. Thus, the structure is subjected to a lateral force away from the side where a vortex is formed. As the vortices are shed alternately first from one side then the other, a harmonically varying lateral load with the same frequency as the frequency of the vortex shedding is formed. In most practical situations the idealized flow pattern described with one vortex shedding frequency is modified due to air turbulence.

In its most simple form a stable street of staggered vortices forms behind the structure, see Figure 7.1. The along-wind velocity, U_1, of the vortices is approximately $0.85U$, where U is the wind velocity in the undisturbed field. This vortex street has been analysed by Th. von Kármán, and is called a von Kármán vortex street.

For a non-vibrating structure the distance l_v between vortices rotating in the same direction must be proportional to the structure width, d, perpendicular to the direction of the wind, since d is the only relevant length. The time between the vortices equals distance l_v divided by velocity U_1 of the vortices. This means that frequency n_s of the lateral load caused by vortex shedding is U_1/l_v, which is proportional to U/d. The factor of proportionality is called the Strouhal number St, so

$$n_s = St\frac{U}{d} \tag{7.1.1}$$

In civil engineering structures, large vibrations may occur if the dominating frequency of vortex shedding n_s is the same as a natural frequency n_e for the structure vibrating in a mode in the crosswind direction. Therefore the critical wind velocity U_{crit} defined by $n_s = n_e$ is

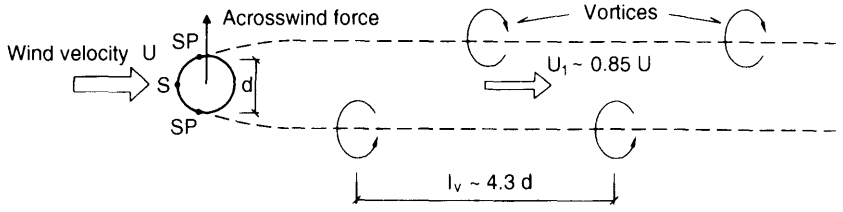

Fig. 7.1 *Principal sketch of vortex street behind a cylinder. S-point of stagnation, i.e. the foremost point of the cylindrical cross section. SP-points of separation where the vortices separate from the structure. (Reproduced by permission of Danish Building Research Institute).*

$$U_{\text{crit}} = \frac{1}{St} n_e d \tag{7.1.2}$$

For many structures, the critical wind velocity for the first mode, i.e. $n_s = n_1$, is of the order of 10 m/s, i.e. frequent wind velocities that give rise to risk of fatigue, see Section 7.6.

Vortex shedding also generates a harmonically varying longitudinal load with a frequency of $2n_s$. However, this load contribution is insignificant for most structures.

The vortex shedding frequency, n_s, given in equation (7.1.1) will be modified by turbulence and structural vibrations. Turbulence modifies the wind velocity, see Section 7.2, and structural vibrations change the effective structure width seen by the wind, see Section 7.3.

Reynolds number Re

For a structure with a circular cross section, the crosswind load is strongly dependent on the Reynolds number $Re = Ud/\nu$; see Section 10.1.2, Reynolds' model law. For high chimneys with circular cross sections, the Reynolds number is usually in the super- or transcritical range for all wind speeds of interest, see Figure 7.2.

The subcritical and transcritical ranges resemble each other, as vortex shedding is regular. Figure 7.3 indicates that aeroelasticity gives rise to a similar regularity, also in the supercritical range.

Strouhal number St

The Strouhal number St is named after the Czech engineer V. Strouhal, who published this relation in 1878. St depends on the shape on the cross section, the surface roughness and the turbulence of the wind.

In Figure 7.3, the Strouhal number is shown to depend on the Reynolds number for a stationary smooth cylinder and for an aeroelastic model chimney. The figure shows that the Strouhal number depends on the motion of the structure (aeroelasticity).

For rectangular cross sections, the Strouhal number depends on the ratio between the structure's depth and width, see Figure 7.4. The Reynolds number is not important for sharp-edged, rectangular cross sections.

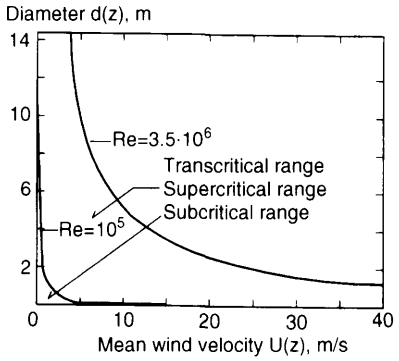

Fig. 7.2 *Diagram for determining the type of flow around structures of circular cross section at a given wind velocity (temperature 5°C). (Reproduced by permission of Danish Building Research Institute).*

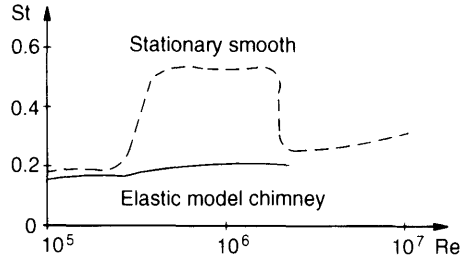

Fig. 7.3 *Strouhal number St as a function of Reynolds number Re (Wooton and Scruton, 1970). (Reproduced by permission of CIRIA).*

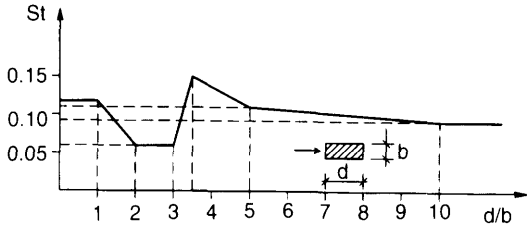

Fig. 7.4 *Strouhal number defined by St = bn_s/U as a function of the ratio between the depth and width of a rectangular section (Eurocode 1).*

Characteristics of cross-wind gross loading

Gross loading which generates crosswind vibrations can generally be classified under the following three headings:

- Net gust load caused by lateral wind fluctuations (gusts). Lateral turbulence is often very important in the design of bridges, see Chapter 8.
- Loads caused by vortex shedding, see Section 7.2. The load occurs whether or not the structure is moving, but may be strongly dependent on the size of the motion. This part of the load is called net vortex shedding load.
- Motion-induced forces, see Section 7.3. Most important is the negative aerodynamic damping generated by vortex shedding.

Mathematically, the gross wind load F per unit of length is determined by:

$$F = F_t + F_v + F_m \tag{7.1.3}$$

in which F_t is the net gust wind load due to air turbulence, F_v is the net vortex shedding wind load and F_m is the motion-induced wind load.

Two turbulence conditions increase the risk of violent vortex shedding structural vibrations:

1. Smooth air flow, for instance that which occurs in the stable atmosphere described in Section 3.1. Structures located close to the sea with no upstream structures generating turbulence are known to be significantly more susceptible to violent vibrations induced

by vortex shedding than structures located in rougher terrain. Topographical features may also increase the risk of smooth air flow.

Negative aerodynamic damping generated by vortex shedding is increased in smooth air flow, see Section 7.3.

2. Increased small-scale turbulence, for instance that occurring in the wake of a slender, nearby structure of similar size.

   Small-scale turbulence increases the lift coefficient induced by vortex shedding as defined in Section 7.2. Small-scale turbulence is discussed thoroughly in Section 10.1.

The influence of smooth air flow and small-scale turbulence on vibrations induced by vortex shedding are described further in the following sections.

7.2 VORTEX SHEDDING ON A NOMINALLY STATIONARY STRUCTURE

The net load caused by vortex shedding can be characterized by four aerodynamic parameters; the lift coefficient, the Strouhal number, the load spectral bandwidth and the spanwise load correlation. All four aerodynamic parameters depend on the cross-sectional shape, the Reynolds number, the turbulence scale and intensity, and the aspect ratio.

The vortex shedding net wind load per unit of length may be written as

$$F_v(z, t) = q(z)\, d(z) C_L(z, t) \tag{7.2.1}$$

where $q(z)$ is the velocity pressure equal to $\frac{1}{2}\rho U^2(z)$, where $U(z)$ is the mean wind velocity at height z, $d(z)$ is the structural width and $C_L(z, t)$ is a non-dimensional, normalized lift force. $C_L(z, t)$ is a stochastic process with a zero mean.

The autospectrum of normalized lift force C_L

Let u' be the part of the turbulence that has large wavelengths compared with the width of the structure. Then u' may be considered as a contribution to a moderately varying mean wind velocity $U + u'$, see Figure 7.5. This wind velocity, used in equation (7.1.1) for the vortex shedding frequency, yields

$$n_s + n_s' = St \frac{U + u'}{d} \tag{7.2.2}$$

which indicates that vortex shedding is within a band of frequencies and not just limited to a single frequency n_s.

u' may also be defined as the part of the turbulence with periods much longer than the natural vibration period of the structure. Using $U + u'$ instead of U reflects the need of a shorter wind velocity averaging time than 10 minutes considering vortex shedding vibrations of structures with natural frequencies of the order of say 1 Hz.

In the atmospheric boundary layer, it is a good approximation to assume that the turbulence u' follows a normal distribution, see Section 3.5.1. Hence it is logical to express the autospectrum $S_{C_L}(z, n)$ of the normalized lift force using the formula (see Vickery and Clark, 1972)

$$\frac{n S_{C_L}(z, n)}{\tilde{C}_L^2(z)} = \frac{n}{\sqrt{\pi} B(z) n_s(z)} \exp\left[-\left[\frac{1 - n/n_s(z)}{B(z)} \right]^2 \right] \tag{7.2.3}$$

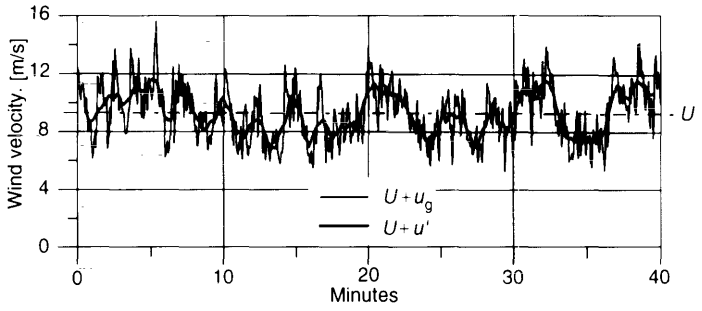

Fig. 7.5 *Principal sketch based on wind measurements at Lammefjord, Denmark (see Courtney and Troen, 1990). A thick line indicates the moderately varying mean wind velocity $U + u'$. U is the mean wind velocity over the measured period of 40 minutes, u' and u_g are the along-wind turbulence component averaged over 63 s and 3 s, respectively. (The wind velocities used in this figure were supplied by Risø National Laboratory, Denmark).*

where the lift coefficient $\tilde{C}_L(z)$ specifies the standard deviation of the normalized lift force C_L.

Spectral bandwidth $B(z)$ is a dimensionless measure of the band of frequencies, within which vortices are shed. If there is no turbulence, the autospectrum contains only contributions close to vortex shedding frequency n_s.

Full-scale data measured for the net wind load on circular cross-sections situated in the atmospheric boundary layer suggest that the spectral bandwidth is approximated by

$$B(z) = 0.1 + 2.0I_u(z) \tag{7.2.4}$$

where $I_u(z)$ is the along-wind turbulence intensity, see Vickery (1995). Small-scale turbulence generated by nearby structures has no pronounced effect on the net wind load spectral bandwidth. Typical spectral bandwidth estimates are approximately 0.25.

The shape of the autospectrum agrees well with experimental results both from the subcritical and the transcritical Reynolds number ranges. A typical example is shown in Figure 7.6.

Vortex shedding frequency n_s increases if the mean wind velocity U increases, and if the structural width d is reduced. Therefore, the velocity profile of the wind, the turbulence of the wind field and a structure width decreasing with height affects the cross-wind net vortex shedding load on the structure as shown in Figure 7.7. The net vortex shedding load occurs within a band of frequencies and not just at a specific frequency.

Large-scale turbulence with characteristic frequencies of up to approximately 0.1 Hz may be interpreted as a slowly varying mean wind velocity. The lift coefficient will not depend greatly on large-scale turbulence, since vortex shedding occurs at much higher frequencies—typically of the order of 1 Hz. Turbulence at scales of the same order as structural width will, on the other hand, be of major importance for the lift coefficient.

The undisturbed air flow approaching high, isolated chimneys will be characterized by a relatively low energy content of small-scale turbulence. This tends to give the vortex shedding load on the chimney rather low lift coefficients. The air in the wake behind a slender, nearby structure will have much more pronounced small-scale turbulence contributions, indicating increased lift coefficients on the chimney. This has been

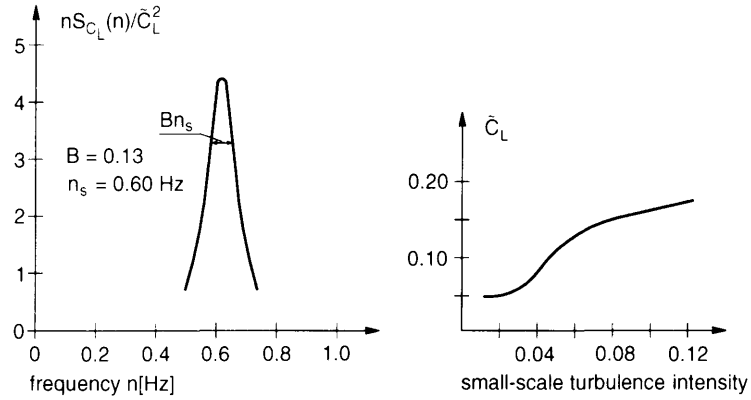

Fig. 7.6 *The left-hand figure shows the non-dimensional autospectrum of the normalized lift force C_L fitted to measured data on a 130 m high, tapered concrete chimney at Stigsnæs, Denmark. The right-hand figure shows the lift coefficient $\tilde{C}_L$ as a function of small-scale turbulence intensity, the latter defined as the turbulence intensity multiplied by the third root of the ratio between cylinder diameter and integral scale of turbulence (Vickery and Daly, 1984). The lift coefficients used to estimate the curve shown have been based on full-scale measurements on chimneys at Reynolds numbers of approximately 10^7. (Reproduced by permission of Elsevier Science Ltd).*

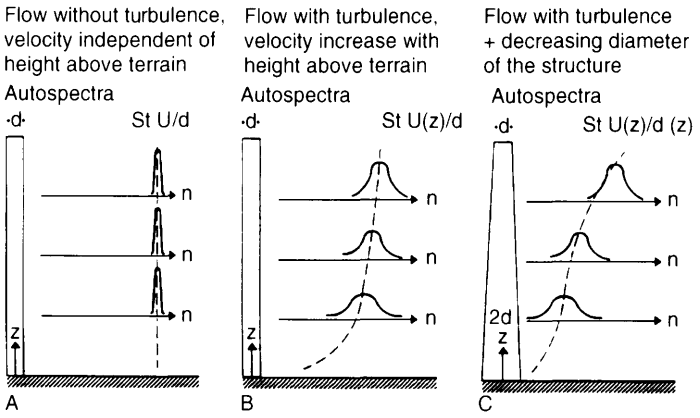

Fig. 7.7 *Principal sketch indicating how height above terrain, turbulence and a decreasing diameter of the structure affects the autospectrum of the crosswind load.*

A. When both the wind velocity and the diameter of the structure are independent of the height above ground, then the frequency of the vortex shedding is also constant. Due to the lack of turbulence the bandwidth of the spectrum is narrow.

B. When the diameter is constant and when the wind velocity increases with the height, then the frequency of the vortex shedding increases with the height. Due to the turbulence the bandwidth is broader than in case A (smooth flow).

C. When diameter decreases and wind velocity increases with height, then again the frequency of the vortex shedding increases with height, but in another and more pronounced way than in the case of constant diameter (case B). (Reproduced by permission of Danish Building Research Institute).

noted in several full-scale observations carried out on concrete chimneys, see Figure 7.16 in Section 7.4.4.

Full-scale pressure measurements on the 130 m high, tapered concrete chimney at Stigsnæs in Denmark showed lift coefficients of the order of 0.05, when the approaching undisturbed wind has turbulence intensities of approximately 10%, see Hansen (1981). In one of the Stigsnæs recordings, however, the approaching wind was influenced by an upstream chimney, which is also 130 m tall. The distance between the two similar chimneys corresponds to approximately 15 chimney diameters. The largest lift coefficient measured in this recording was equal to $\tilde{C}_L = 0.16$, i.e. about 3 times larger than the lift coefficient found for other wind directions. Thus, the lift coefficient depends a great deal on the small-scale turbulence contributions. This fact was originally observed by Vickery (see Vickery and Daly, 1984).

During smooth flow, vortex motions increase, see Section 7.1 and also Section 7.4.2 which discusses the Canadian Code of Practice.

Coherence and phase spectra for normalized lift force C_L

There is evidence from measurements on structures that the coherence and phase spectra for normalized lift force C_L may be approximated by

$$\sqrt{Coh(C_L)} = \exp(-as^2) \tag{7.2.5}$$

$$\Phi(C_L) = bs \tag{7.2.6}$$

where s is a dimensionless distance

$$s = \frac{2(z_1 - z_2)}{d(z_1) + d(z_2)}$$

a and b are constants, approximately $a \sim 0.1$ and b is a constant between 0 and 1 for circular cross-sections. These expressions also apply to frequencies near the peak of the autospectrum.

Full-scale measurements carried out on the 130 m high concrete chimney at Stigsnæs, Denmark, confirm that the expressions for the auto-, coherence, and phase spectra of C_L are reasonable approximations.

A non-dimensional correlation length, i.e. the ratio of correlation length to diameter, is defined as

$$\lambda = \int_0^\infty \sqrt{Coh(C_L)} \cos(\Phi(C_L))\, ds = \frac{\sqrt{\pi}}{2\sqrt{a}} \exp\left(-\frac{b^2}{4a}\right) \tag{7.2.7}$$

Non-dimensional correlation length λ is often found to be near unity or perhaps a little greater.

The exact expressions used to describe the coherence and phase spectra are not important for structural response estimates. The correlation integral effect included in the correlation length is the most important parameter.

7.3 CROSSWIND LOADING CAUSED BY STRUCTURAL MOTION

Structural motion induces a feedback to the air flow generating the crosswind load on the structure. For flexible structures, such as steel chimneys, these motion-induced wind

loads are significant. The concept of aeroelasticity covering these load contributions is described below.

Lock-in

Structural motion interacts with the wind field in such a way that the dominating vortex shedding frequency n_s synchronizes with the structure's natural frequency n_e. This phenomenon, which is shown in Figure 7.8, is called lock-in.

Correlation length

Many experiments have been made in order to determine the influence of structural motions on the correlations of the crosswind loading. The results from one of these investigations is shown in Figure 7.9, indicating that increasing vibration amplitudes cause an increase of correlation length.

Mathematical description of aeroelasticity

The properties of lock-in and motion-dependent correlations are related to aerodynamic cross-wind loading caused by the structural vibrations. In its most simple form, the motion-induced load F_m defined in equation (7.1.3) consists of an inertial load proportional to the accelerations of the structure and an aerodynamic damping proportional to the velocity of the structure:

$$F_m = -h_a \ddot{\xi}_{\text{def}} - c_a \dot{\xi}_{\text{def}} \tag{7.3.1}$$

ξ_{def}, $\dot{\xi}_{\text{def}}$ and $\ddot{\xi}_{\text{def}}$ are the cross-flow deflections, velocities and accelerations, respectively, of the structure. For most civil engineering structures in air, the "added mass of air"

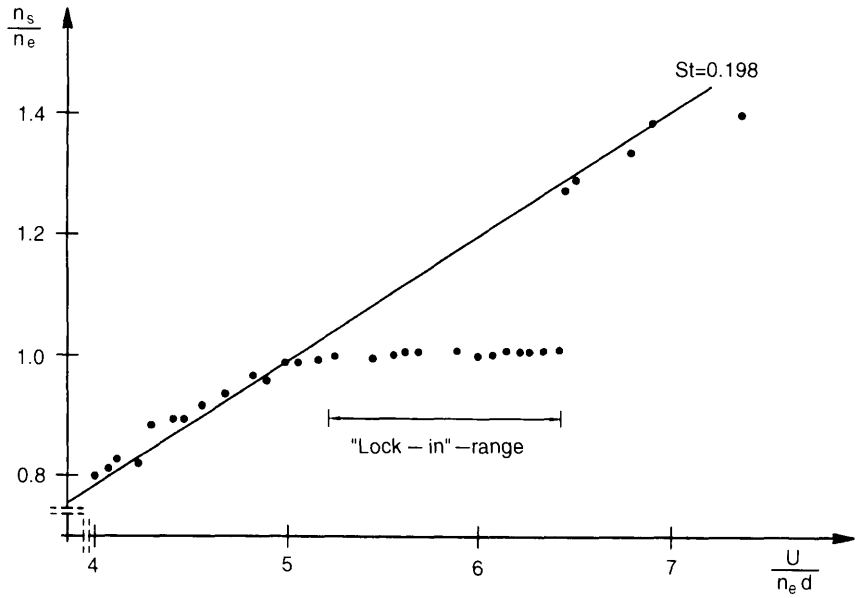

Fig. 7.8 *Experimental investigation of lock-in (after Feng, 1968).*

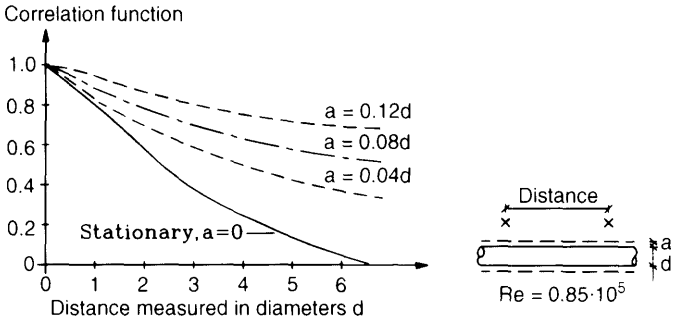

Fig. 7.9 *Influence of the amplitude of motion upon the correlation length estimated by flow measurements (Wooton and Scruton, 1970). Four curves are shown corresponding to four different amplitudes of the structure. The correlation length increases with the amplitude. (Reproduced by permission of CIRIA).*

h_a is small relative to the structural mass, and may thus be disregarded. However, the aerodynamic damping force $c_a\dot{\xi}_{\text{def}}$ will reduce the effective damping of the vibrations when c_a is negative. As this occurs for wind velocities close to the critical wind velocity it is a very essential parameter when calculating the response.

The linear dependence between loading and velocity indicated in equation (7.3.1) is sufficiently accurate for small vibration amplitudes of up to approximately 10–20% of structural width. When the vibration amplitudes are larger, non-linear damping terms become important. Vickery (1981) suggests an aerodynamic damping of the form $a\dot{\xi}_{\text{def}} - b\dot{\xi}^3_{\text{def}}$, where the term $-b\dot{\xi}^3_{\text{def}}$ is a non-linear positive damping that ensures that the response is self-limiting. An equilibrium is attained at an amplitude for which the energy extracted from the flow is equal to the energy dissipated by structural damping.

Structural and aerodynamic damping at small amplitudes

Aerodynamic damping is of primary concern, bearing in mind the risk of violent vortex-induced vibrations. It depends on the ratio between the wind velocity and the critical velocity, the Reynolds number, and scale and intensity of the incoming turbulence.

Aerodynamic damping may be characterized by a dimensionless parameter Sa as

$$Sa = \frac{c_a}{\rho d^2 n_e} \tag{7.3.2}$$

Alternatively, Sa may be expressed in terms of the corresponding logarithmic decrement δ_a of aerodynamic damping, as

$$Sa = \frac{2\delta_a m_e}{\rho d^2} \tag{7.3.3}$$

where m_e is an equivalent mass per unit of length corresponding to the mode considered

$$m_e = \int_0^h m(z)(\xi(z))^2\,dz \Big/ \int_0^h (\xi(z))^2\,dz \tag{7.3.4}$$

$\xi(z)$ is the mode shape, see Appendix C. Aerodynamic parameter Sa is negative for negative aerodynamic damping, which is the situation that leads to significant vortex-induced vibrations.

The Scruton number Sc is defined in a similar way as aerodynamic parameter Sa by

$$Sc = \frac{2\delta_s m_e}{\rho d^2} \tag{7.3.5}$$

where δ_s is the logarithmic decrement of structural damping. The effective structural damping is then proportional to the sum between Scruton number Sc and parameter Sa.

Normally, structural damping increases with vibration amplitude. This structural behaviour is not taken into account in the present formulation using a single Scruton number value characterizing the tendency to obtain large vortex shedding induced vibrations. It might become necessary to specify the structural damping as a function of vibration amplitude in order to establish reliable and accurate models describing vortex shedding induced vibrations.

The variation of aerodynamic damping with wind velocity and Reynolds number is shown in Figure 7.10. The test results shown refer to smooth air flow. The modulating influence of large-scale turbulence can be accounted for by replacing the negative aerodynamic damping in smooth air flow by its average value in turbulent flow using a Gaussian

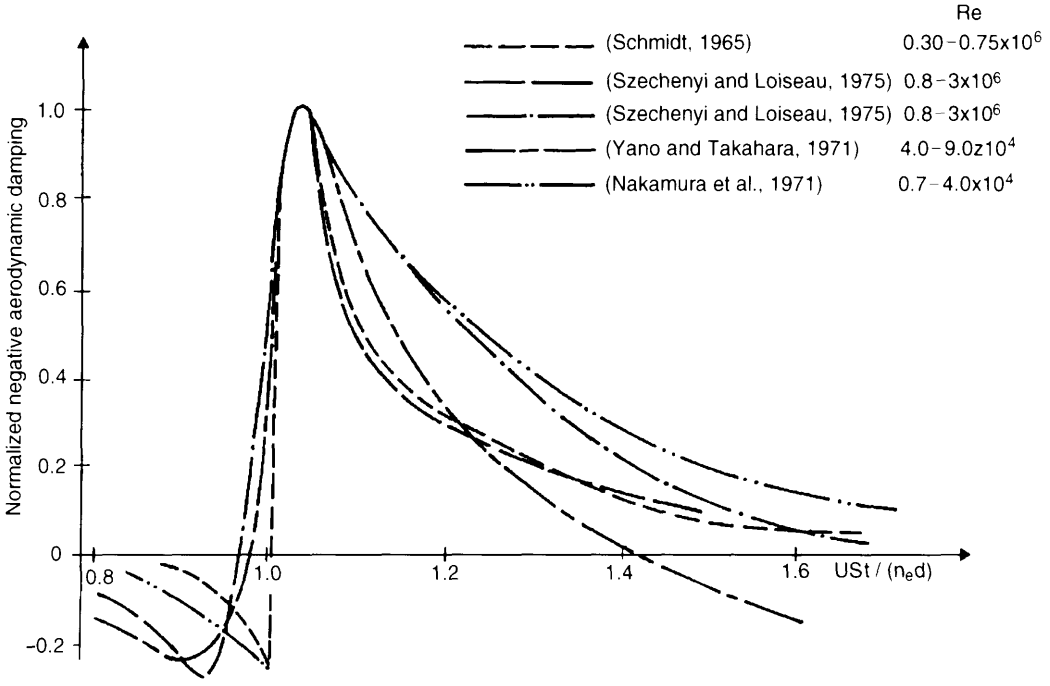

Fig. 7.10 *Variation of the aerodynamic damping with $USt/(n_e d)$ (Vickery, 1978). Positive values in the diagram represent a negative aerodynamic damping. The curves show test results in smooth air flow at five different values of Reynolds number Re, normalized such that the maximum normalized damping value is 1.*

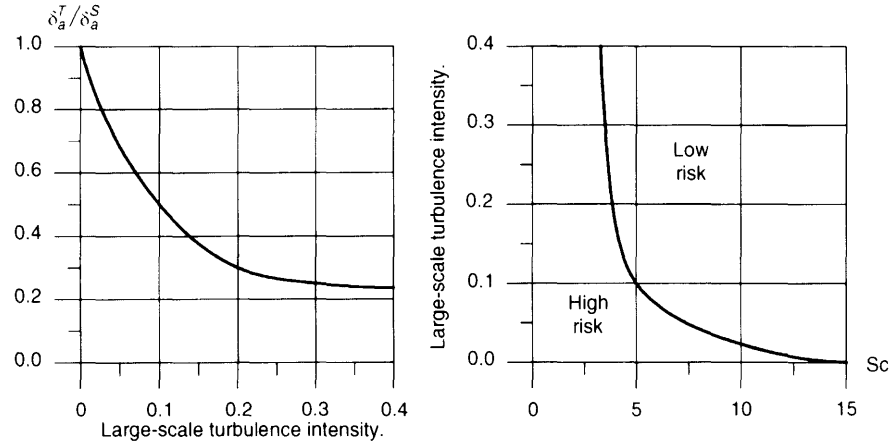

Fig. 7.11 *The left-hand figure shows the ratio between the aerodynamic damping in turbulent flow, δ_a^T, and smooth flow, δ_a^S, as a function of the large-scale turbulence intensity. The increase in large-scale turbulence reduces the risk of significant negative aerodynamic damping, see left-hand figure, and thereby also the risk of violent vortex-induced vibrations, see right-hand figure. The aerodynamic damping, the Scruton number and the large-scale turbulence intensities indicated on the axes should be considered as rough guidelines judging the risk of violent vortex shedding vibrations of circular cylinders.*

probability distribution of the fluctuating wind velocity. So turbulence reduces the most negative aerodynamic damping found in smooth flow, see left-hand Figure 7.11, where the ratio between the most negative aerodynamic damping in turbulent flow, δ_a^T, and smooth flow, δ_a^S, is shown as a function of large-scale turbulence intensity.

The risk of violent vortex-induced vibrations depends on a combination of Scruton number and large-scale turbulence intensity of the incoming wind field. High intensity of large-scale turbulence and/or high Scruton numbers reduce the risk of violent vortex-induced vibrations, see right-hand part of Figure 7.11. Experience shows that there is no risk of lock-in if $Sc >$ approximately 20. If, on the other hand, $Sc < 10$, then the risk of lock-in is very pronounced.

A structure with a given Scruton number may be stable in the kind of turbulent flow normally encountered and unstable in rare cases with low turbulence occurring under stable atmospheric stratification, see Section 3.1. For structures with a medium Scruton number of approximately 5–10, the critical combination of stable stratification, wind direction and critical wind velocity may occur with return periods of say 10–20 years. There are examples of structures which show no signs of significant vibrations during approximately the first 20 years of service and then, due to certain meteorological conditions, violent vortex-induced vibrations start. A given structure may be perfectly stable during its lifetime in one location and unstable at another location where critical meteorological conditions can occur, albeit relatively seldom.

Violent vortex-induced vibrations are unacceptable, not least because spectators complain and cracks form in the critical spots of the steel structure.

The aerodynamic damping parameters for a variety of simple cross sections are shown in Figure 7.12. All data measured were obtained in model studies carried out on moving

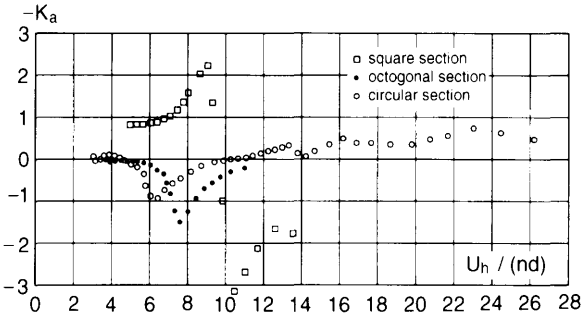

Fig. 7.12 *Aerodynamic damping measured in turbulent shear flow for a circular cylinder, an octagon and a square (Vickery, 1995). The negative value of the aerodynamic damping parameter K_a defined by equation (7.4.11) is shown as a function of U_h/nd, where U_h is the mean wind velocity at the structure top, n is the frequency and d is the structure width.*

prismatic, base-pivoted structures in a simulated atmospheric boundary layer with a turbulence intensity of approximately 8% over the upper part of the models. It is obvious that negative aerodynamic damping, and thereby the risk of large vortex shedding induced vibrations, is most pronounced for structures with sharp-edged cross sections, but these structures are sensitive to the wind direction.

7.4 VORTEX SHEDDING RESPONSE BASED ON THE SPECTRAL MODEL

Vortex shedding response based on the spectral approach is calculated theoretically in Section 7.4.1. The Canadian Code of Practice and the widely used CICIND Model Code, which are both based on the spectral approach, are described in Sections 7.4.2 and 7.4.3, respectively. In Section 7.4.4, the calculated responses are compared with full-scale observations.

The spectral model gives accurate predictions for relatively stiff structures, such as concrete chimneys.

7.4.1 Spectral vortex shedding response

The procedure used to calculate spectral vortex shedding response is based on a modal analysis. Normally, the natural frequencies of chimneys vibrating in a cross-wind direction are well separated, indicating that only the mode, where the wind velocity is equal to the critical wind velocity, contributes to the vortex shedding induced vibrations. The net generalized force $Q(t)$ of the mode considered is

$$Q(t) = \int_0^h F_v(z, t)\xi(z)\,dz \tag{7.4.1}$$

where $F_v(z, t)$ is the net vortex shedding loading per unit of height, see equation (7.2.1), $\xi(z)$ is the mode shape and h is the structural height. n_c is the natural frequency of the mode considered.

The deflection of the chimney can be written as $a(t)\xi(z)$, where the modal displacement $a(t)$ is a stochastic process with the spectral density shown below (subscript "ref" indicates a reference value):

$$S_{aa}(n) = |H(n)|^2 \frac{h^2 (q\, d \tilde{C}_L \xi)^2_{\text{ref}}}{\sqrt{\pi} B_{\text{ref}} n_e} |J(n)|^2 \tag{7.4.2}$$

where $|H(n)|^2$ is the modal frequency response function of the structure and $|J(n)|^2$ is the joint acceptance function given by

$$|J(n)|^2 = \frac{1}{h^2} \int_0^h \int_0^h g(z_1, n) g(z_2, n) \rho(z_1, z_2)\, dz_1 dz_2 \tag{7.4.3}$$

where ρ is the correlation function and function g is defined by the following equation:

$$g(z, n) = \frac{q(z)\, d(z) \tilde{C}_L(z) \xi(z)}{(q\, d \tilde{C}_L \xi)_{\text{ref}}} \sqrt{\frac{B_{\text{ref}}}{B(z)}} \sqrt{\frac{n}{n_s(z)}} \exp\left[\frac{1}{2} \left(\frac{1 - n/n_s(z)}{B(z)} \right)^2 \right] \tag{7.4.4}$$

In most cases, it is sufficiently accurate to assume that the correlation depends only on the distance between the two points considered and not on each of the coordinates. Thus the double integral can be expressed as two single integrals, see Appendix B:

$$|J(n)|^2 = \frac{1}{h} \int_0^h k(r, n) \rho(r)\, dr \tag{7.4.5}$$

$$k(r, n) = \frac{2}{h} \int_0^{h\ r} g(z, n) g(z + r, n)\, dz \tag{7.4.6}$$

where r is the distance between the two points considered.

Corresponding functions g and k are shown in Figure 7.13 below. It is worth nothing that $k(0, n_e)$ = approximately 0.30–0.35 for both structures considered in the figure.

Since the correlation length for the net vortex shedding loading is relatively small (about one diameter), the joint acceptance function is approximately given by

$$|J(n)|^2 = \lambda \frac{d_{\text{ref}}}{h} k(0, n) = 2\lambda \frac{d_{\text{ref}}}{h} \frac{1}{h} \int_0^h (g(z, n))^2\, dz \tag{7.4.7}$$

where λd_{ref} is the correlation length.

Using the white noise approximation described in Appendix C, the standard deviation of deflection y is given by, see equation (7.4.2)

$$\sigma_y(z) = \xi(z) \sqrt{\int_0^\infty S_{aa}(n)\, dn}$$

$$= \frac{\sqrt[4]{\pi}}{\sqrt{2}} \frac{\xi(z)}{m_{\text{ref}} \xi_{\text{ref}}} \frac{\tilde{C}_{L,\text{ref}} \sqrt{\lambda}}{\sqrt{B_{\text{ref}}}} \frac{\sqrt{\frac{1}{h} \int_0^h (g(z, n_e))^2\, dz}}{(2\pi n_e)^2 \gamma_v} \sqrt{\frac{d_{\text{ref}}}{h}} \frac{q_{\text{ref}}\, d_{\text{ref}}}{\sqrt{\delta/(2\pi)}} \tag{7.4.8}$$

where n_e is the natural frequency and γ_v is a non-dimensional factor that takes into account the actual distribution of mass and mode shape along the structure

$$\gamma_v = \frac{1}{h} \int_0^h \frac{m(z) \xi^2(z)}{m_{\text{ref}} \xi^2_{\text{ref}}} dz \tag{7.4.9}$$

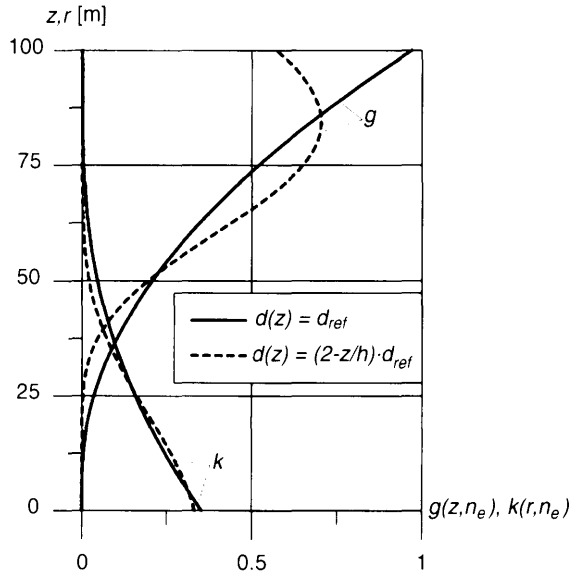

Fig. 7.13 *Corresponding functions of g and k for two 100 m high structures with a constant diameter and a linearly decreasing diameter with height, respectively. The mode shape is assumed to be a parabola, i.e.* $\xi(z) = z^2$ *and the vortex shedding frequency* n_s *is equal to the natural frequency* n_e *at the upper quarter point on the structure, i.e. for* $z/h = 3/4$. *The roughness length is* $z_0 = 0.05$ *m and the spectral bandwidth is* $B = 0.25$. *The lift coefficient is assumed to be independent of height.*

where $m(z)$ is the mass per unit length of the structure. δ is the logarithmic decrement, taking both structural damping δ_s and aerodynamic damping δ_a into account:

$$\delta = \delta_s + \delta_a \tag{7.4.10}$$

$$\delta_a = -2\pi K_a \frac{\rho d_{\text{ref}}^2}{m_e} \tag{7.4.11}$$

where ρ is the air density, d_{ref} is the reference width of the structure and m_e is an equivalent mass per unit length defined in equation (7.3.4). The aerodynamic parameter $K_a = -Sa/4\pi$, where Sa was given in equation (7.3.3), is positive for negative aerodynamic damping. This is the normal sign convention used in the literature.

The maximum bending moment acting on the chimney originates from the inertia forces, which have an amplitude, $F_I(z)$, given as the peak factor k_p multiplied by the standard deviation of the inertia force:

$$F_I(z) = k_p m(z)(2\pi n_e)^2 \sigma_y(z) \tag{7.4.12}$$

Inserting equation (7.4.8) in equation (7.4.12) gives

$$F_I(z) = k_p \frac{\sqrt[4]{\pi}}{\sqrt{2}} \frac{m(z)\xi(z)}{m_{\text{ref}}\xi_{\text{ref}}} \frac{1}{\gamma_v} \frac{\tilde{C}_{L,\text{ref}}\sqrt{\lambda}}{\sqrt{B_{\text{ref}}}} \sqrt{\frac{1}{h}\int_0^h (g(z, n_e))^2 \, dz} \sqrt{\frac{d_{\text{ref}}}{h}} \frac{q_{\text{ref}} d_{\text{ref}}}{\sqrt{\delta/(2\pi)}} \tag{7.4.13}$$

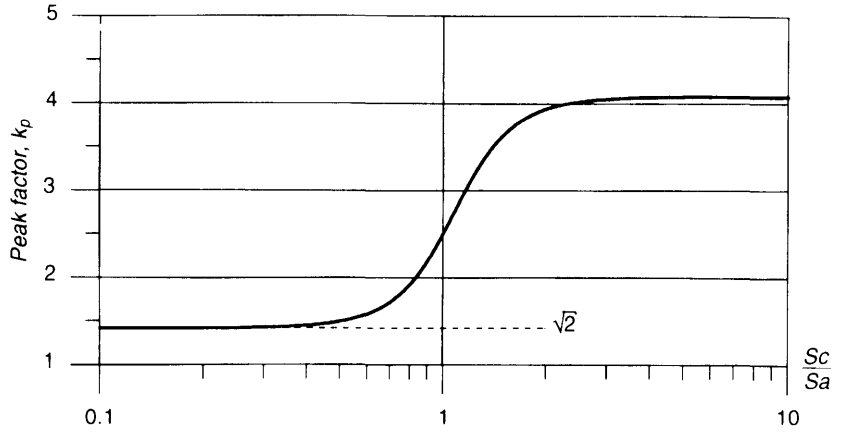

Fig. 7.14 *Peak factor as a function of the ratio of structural to aerodynamic damping. The curve shown follows the specification used in the CICIND model code.*

An equivalent static load used in design should yield a bending moment similar to the bending moments originating from the maximum inertia force given in equation (7.4.13).

The peak factor k_p depends on the type of vibration. For the stochastic type of response, the peak factor reaches approximately 4.0, and for the single harmonic type of response with constant amplitude the peak factor is equal to $\sqrt{2}$. Typically the response type caused by vortex shedding corresponds to peak factors somewhere between the two extremes mentioned. The peak factor is illustrated in Figure 7.14 as a function of the ratio of structural damping to aerodynamic damping. The peak factor shown in Figure 7.14 corresponds to the CICIND Model Code which specifies the following (see Ruscheweyh and Sedlacek, 1988):

$$k_p = \sqrt{2}(1 + 1.2\tan^{-1}(0.75(Sc/Sa)^4)) \tag{7.4.14}$$

7.4.2 The Canadian code NBC 1990

The dependence of the Strouhal number St on the Reynolds number Re is taken into account. For a circular cylinder the code states

$$St = \begin{cases} \frac{1}{6} & \text{if } Re < 2 \times 10^5 \\ \frac{1}{5} & \text{if } Re > 2.5 \times 10^5 \end{cases} \tag{7.4.15}$$

and St varies approximately linearly between the two mentioned values of Re.

Let U_h denote the value of the wind speed at the top of the chimney when the frequency of vortex shedding at the top equals the natural frequency n_e of the chimney. Then

$$U_h = \frac{n_e d}{St} \tag{7.4.16}$$

where d is the diameter at the top of the chimney. The Reynolds number is

$$Re = \frac{U_h d}{\nu} \tag{7.4.17}$$

where the kinematic viscosity is $\nu = 1.5 \times 10^{-5}$ m^2/s, corresponding to a temperature of approximately 19°C.

Combining formulas (7.4.15), (7.4.16) and (7.4.17) leads to the rule

$$U_h = \begin{cases} 6n_c d & \text{for } n_c d^2 \leqslant 0.5 \text{ m}^2/\text{s} \\ 5n_c d & \text{for } n_c d^2 \geqslant 0.75 \text{ m}^2/\text{s} \end{cases} \tag{7.4.18}$$

In the range between these limits, the code uses an interpolation formula

$$U_h = \left(3n_c d + \frac{1.5 \text{ m}^2/\text{s}}{d}\right) \text{ for } 0.5 \text{ m}^2/\text{s} < n_c d^2 \leqslant 0.75 \text{ m}^2/\text{s} \tag{7.4.19}$$

The dynamic effects of vortex shedding are determined as the effects of an equivalent static force F_L per unit of length acting over the top one-third of the structure. F_L is given by

$$F_L = C_1 \frac{1}{\sqrt{\zeta_s - C_2 \dfrac{\rho d^2}{m}}} \sqrt{\frac{d}{h}} q_h d \tag{7.4.20}$$

where the following notations are used:

C_1, C_2	non-dimensional parameters
m	average mass per meter over the top one-third of the chimney
q_h	velocity pressure corresponding to U_h
ζ_s	damping ratio of the structure

If the diameter variation exceeds 10%, then the effective static load should be applied only to that part of the structure over which the diameter is within 10% of the average for that part.

Alternatively, the dynamic effects of vortex shedding can be specified by the maximum top amplitude $y_{\max}$ calculated as below, see the ISO TC98 proposal: "Wind loads on structures" based on the Canadian code:

$$\frac{y_{\max}}{d} = C_3 \frac{\rho d^2/m}{\sqrt{\zeta_s - C_2 \dfrac{\rho d^2}{m}}} \sqrt{\frac{d}{h}} \tag{7.4.21}$$

where $C_3 = 1$ corresponds to equation (7.4.22) and $C_3 = 2$ corresponds to equation (7.4.24).

In most cases, NBC 1990 specifies the parameters C_1 and C_2 to be

$$C_1 = \begin{cases} 3 & \text{if } h > 16d \\ 0.75\sqrt{h/d} & \text{if } h < 16d \end{cases} \tag{7.4.22}$$

$$C_2 = 0.6 \tag{7.4.23}$$

If $\zeta_s < C_2 \rho d^2/m$, then vibrations with an amplitude of up to 1 diameter may occur. For such cases, the NBC 1990 refers to a more complete treatment (Vickery and Basu, 1983).

If the velocity U_h is low, then turbulence levels may be very low, due to temperature gradients, and vortex-induced motions are significantly increased. Thus, if $U_h < 10$ m/s and if $h > 12d$, then

$$C_1 = 6 \tag{7.4.24}$$

$$C_2 = 1.2 \tag{7.4.25}$$

These rules also apply to tapered structures, provided the variation of the diameter along the top third is less than one tenth of the average diameter of the top third.

By comparing equation (7.4.11) and equation (7.4.13) with equation (7.4.20) it is seen that $C_2 = K_a$ and

$$C_1 = k_p \frac{\sqrt{\pi}}{\sqrt{2}} \frac{18}{5} \left[\frac{1}{h} \int_0^h \frac{m(z)\xi(z)}{m_h \xi_h} \frac{z}{h} \, dz \right] \frac{1}{\gamma_s} \frac{\tilde{C}_{L,h}\sqrt{\lambda}}{\sqrt{B_h}} \sqrt{\frac{1}{h} \int_0^h (g(z, n_c))^2 \, dz} \tag{7.4.26}$$

gives that the bending moment at the chimney foundation is identical when calculated using $F_I(z)$ in equation (7.4.13) and F_L in equation (7.4.20) over the top third. The chimney height is used as the reference height.

Assuming a constant mass per unit of height, $C_1 = 3$, $k_p = 4$, $\xi(z) = z^2$, $B(z) = 0.25$, $\lambda = 1$ and $k(0, n_c) = 0.35$ (see equation (7.4.6)) gives $\tilde{C}_{L,h} = 0.21$, which is in good agreement with the largest lift coefficients shown in Figure 7.6.

7.4.3 The CICIND model code

The CICIND model code is based on the spectral model using a large number of full-scale observations to estimate the relevant parameters, see Daly (1986). The self-limiting vibration amplitude due to the non-linear damping term is also accounted for.

In the CICIND model code for steel chimneys, May 1988, the following procedure is given for chimneys with circular cross-sections.

The Strouhal number is $St = 0.2$, and the critical wind speed is

$$U_{\text{crit}} = \frac{n_c d}{St} \tag{7.4.27}$$

If the chimney has a constant cross section, then Scruton number Sc is

$$Sc = \frac{2\delta_s m}{\rho d^2} \tag{7.4.28}$$

where the same symbols are used as before. According to the CICIND code, $\rho = 1.25$ kg/m^3.

If $Sc > 15$, crosswind oscillations will be so small that no action against vortex shedding is required.

If $Sc < 5$, the crosswind oscillations may be violent and stabilizers or damping devices are mandatory.

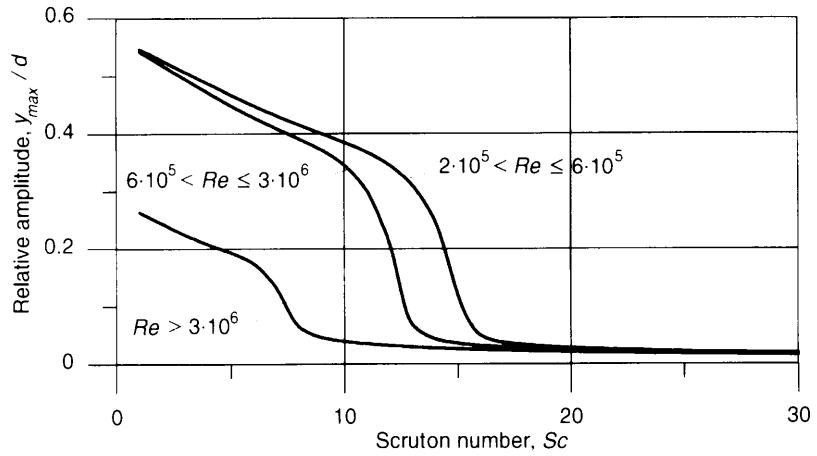

Fig. 7.15 *Relative amplitude as a function of Scruton number according to the CICIND model code.*

If $5 < Sc < 15$, the designer is permitted to use the structure if response calculations confirm that it will not suffer from fatigue damage.

The Scruton number limits indicated above are primarily based on deflection response criteria. The stress response and the accumulated fatigue damage should always be determined as a part of the structural design.

Using test results and approximative assumptions, the curves shown in Figure 7.15 have been established. They show the relative top amplitude as a function of the Scruton number. Each curve corresponds to a certain flow regime characterized by the Reynolds number. The supercritical range mentioned in Section 7.1 is divided up into two Reynolds number regimes in the CICIND model code, see Figure 7.15.

7.4.4 Comparison of predicted and observed responses—concrete chimneys

Vickery and Basu (1984) compared theoretical predictions based on the spectral model with full-scale experiments on several concrete chimneys. They found that the spectral model gave reasonable predictions of the concrete structures concerning vortex shedding. Their comprehensive investigations are supplemented here by full-scale data from two sites with 130 m and 150 m tall, tapered concrete chimneys, respectively. At both sites a similar chimney is located at a distance of approximately 15 diameters from the chimney in question.

The measurements on the chimneys at both sites indicate much larger vibrations in cross-wind directions, when the neighbouring chimney is located upstream, see Figure 7.16. This is due to the increase in small-scale turbulence produced by the upstream chimney. The predictions based on the spectral model are seen to be in good agreement with the full-scale measurements considered here. The predictions based on the Canadian code also shown in Figure 7.16 are in good agreement with the response observed on the two chimneys in question.

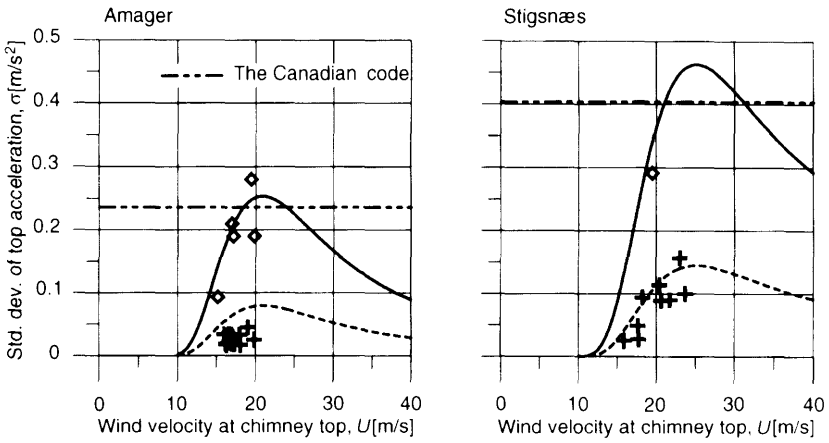

Fig. 7.16 *Standard deviation of the top acceleration as a function of mean wind velocity for a 150 m (Amager) and a 130 m (Stigsnæs) high tapered concrete chimney. The theoretical prediction is based on a Strouhal number of St = 0.2, a spectral bandwidth B = 0.25, a correlation length λ = 1.0, and an aerodynamic mass-damping parameter K_a = 0.5. The solid lines correspond to a lift coefficient of $\tilde{C}_L$ = 0.16 found to be representative for the wind direction with a similar chimney located approximately 15 diameters upstream. Predictions for all other wind directions are shown by the dotted lines based on $\tilde{C}_L$ = 0.05. The Canadian code is shown as reference assuming a peak factor of 4.0.*

7.5 VORTEX SHEDDING RESPONSE BASED ON THE VORTEX RESONANCE MODEL

Vortex shedding responses based on the vortex resonance model are calculated theoretically in Section 7.5.1. As described in Section 7.5.2, Eurocode 1 is based on the vortex resonance model. In Section 7.5.3 the calculated responses based on code specifications are compared with full-scale observations.

The vortex resonance model seeks to include large aeroelastic effects that occur with flexible structures, such as many steel chimneys, by a single harmonic gross load.

7.5.1 Vortex resonance response

The modal force $Q(t)$ of the mode considered is

$$Q(t) = \int_0^h F(z,t)\xi(z)\,dz \tag{7.5.1}$$

where the vortex resonance model specifies the cross-wind loading per unit of height due to vortex shedding, $F(z,t)$, as (see Ruscheweyh, 1982)

$$F(z,t) = q(z)d(z)c_F(z)\sin(2\pi n_s t + \gamma(z)\pi) \tag{7.5.2}$$

where $q(z)$ is velocity pressure, $d(z)$ is width, $c_F(z)$ is a non-dimensional shape factor describing the load amplitude and n_s is the vortex shedding frequency. $\gamma(z)$ is a factor

equal to 0 or 1 facilitating that the load has the same sign as the mode shape in all points along the structure. For modes with constant sign $\gamma(z) = 0$. The shape factor, $c_F(z)$, depends on vibration amplitude, air turbulence, the Reynolds number, the Strouhal number, cross section and aspect ratio.

Maximum deflection amplitude y_{max} is calculated by

$$y_{max} = \frac{F_e}{(2\pi n_e)^2 m_e} \frac{\pi}{\delta_s} \tag{7.5.3}$$

where δ_s is the logarithmic decrement describing the structural damping. The equivalent mass m_e per unit of length is given in equation (7.3.4) and the equivalent load F_e is given by

$$F_e = \xi_{max} \int_0^h q(z) d(z) c_F(z) \xi(z)\, dz \Big/ \int_0^h \xi^2(z)\, dz \tag{7.5.4}$$

where ξ_{max} is the maximum mode shape amplitude.

The maximum deflection amplitude is obtained when the load frequency n_s is equal to the natural frequency n_e:

$$\frac{y_{max}}{d_{ref}} = \xi_{max} \frac{\int_0^h \frac{q(z)}{q_{ref}} \frac{d(z)}{d_{ref}} c_F(z) \xi(z)\, dz}{4\pi \int_0^h \xi^2(z)\, dz} \frac{1}{Sc} \frac{1}{St^2} \tag{7.5.5}$$

where the Scruton number Sc is calculated as shown in equation (7.3.5) using the reference diameter $d = d_{ref}$, and St is the Strouhal number defined by equation (7.1.1) using $U = U_{ref}$ and $d = d_{ref}$.

The load amplitude fluctuates in time and the limited load correlation described by the correlation length indicates that maximum loads do not occur simultaneously along the structure. Ruscheweyh (1982) takes the effect of limited correlation into account by integrating the maximum load amplitude over length L', where $L'/2$ is the correlation length equal to the integral of the correlation function from zero to infinity, see Figure 7.17. The maximum load amplitudes are taken near the points with maximum mode deflections. This is because of aeroelastic effects and in order to obtain the wind action that gives the largest response.

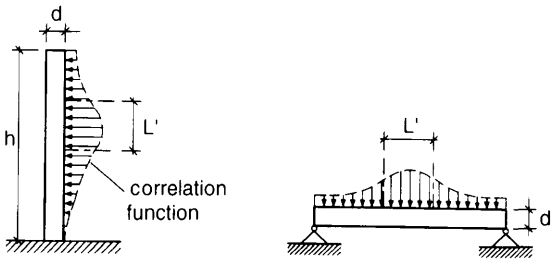

Fig. 7.17 *Definition of correlation length according to Ruscheweyh (1982). The correlation length is equal to L'/2, where the length L' is shown in the figure for a cantilevered beam (left hand) and a simply supported beam (right hand). (Reproduced by permission of Bauverlag GmbH).*

The variation of velocity pressure and structure width over heights of the order of the correlation length will normally be insignificant. Further assuming that the mode has a constant sign, the integral in the numerator of equation (7.5.5) can be approximated as

$$\int_0^h c_F(z)\xi(z)\,dz = c_{\text{lat}}k_p \int^{L'} \xi(z)\,dz \tag{7.5.6}$$

where k_p is the peak factor, c_{lat} is the standard deviation of the load, and the integral on the right-hand site of the equation is taken over the length L'. The maximum load has been set equal to the standard deviation multiplied by the peak factor.

Ruscheweyh takes the peak factor into account by integrating the mode shape over a so-called effective correlation length L_c defined by

$$\int^{L_c} \xi(z)\,dz = k_p \int^{L'} \xi(z)\,dz \tag{7.5.7}$$

Thus, the effective correlation length incorporates the influence of load correlation as well as the peak factor.

Inserting equations (7.5.6) and (7.5.7) in equation (7.5.3) shows that the maximum deflection amplitude is given by

$$\frac{y_{\max}}{d_{\text{ref}}} = K_\xi K_w c_{\text{lat}} \frac{1}{Sc}\frac{1}{St^2} \tag{7.5.8}$$

where constants K_ξ and K_w are defined as shown in Eurocode 1:

$$K_\xi = \xi_{\max} \frac{\int_0^h \xi(z)\,dz}{4\pi \int_0^h \xi^2(z)\,dz} \tag{7.5.9}$$

$$K_w = \frac{\int^{L_c} \xi(z)\,dz}{\int_0^h \xi(z)\,dz} \tag{7.5.10}$$

For modes that have no constant sign, the load is assumed to act in the same direction as the mode deflection. This is taken into account by modifying the definitions of K_ξ in equation (7.5.9) and K_w in equation (7.5.10), see Eurocode 1.

7.5.2 Eurocode 1

Eurocode 1 states that chimneys need not be checked for vortex shedding if their height is less than 8 diameters. For other chimneys, the following method is described in an informative Annex.

The Strouhal number is taken as $St = 0.2$ for a circular cylinder, and the critical wind velocity U_{crit} follows as

$$U_{\text{crit}} = \frac{n_e d}{St} \tag{7.5.11}$$

where n_e is the fundamental frequency of the structure and d is the diameter at the centre of the fully correlated loading length, see Eurocode 1.

The Reynolds number Re will be calculated from the velocity U_{crit}:

$$Re = \frac{dU_{\text{crit}}}{\nu} \tag{7.5.12}$$

where kinematic viscosity $\nu = 1.5 \times 10^{-5}$ m^2/s corresponding to an air temperature of approximately 19°C.

The basic value $c_{\text{lat},0}$ of the aerodynamic exciting force coefficient for circular cylinders is defined as

$$c_{\text{lat},0} = \begin{cases} 0.7 \text{ for } Re \leqslant 3 \times 10^5 \\ 0.2 \text{ for } 5 \times 10^5 \leqslant Re \leqslant 4 \times 10^6 \\ 0.3 \text{ for } Re \geqslant 10^7 \end{cases} \tag{7.5.13}$$

In each of the intervals $3 \times 10^5 < Re < 5 \times 10^5$ and $4 \times 10^6 < Re < 10^7$, it is assumed that $c_{\text{lat},0}$ varies linearly with $\ln(Re)$.

In most cases, the lift coefficient $c_{\text{lat}} = c_{\text{lat},0}$. However, c_{lat} is reduced for high winds with return periods of the order of 50 years. Eurocode 1 assumes that high winds have a limited duration and are not able to excite the structure to its stationary response amplitude within its action time.

The next step in the calculations is a determination of a maximum amplitude $y_{\max}$ using equation (7.5.8) and an effective correlation length $L_e = L_j$, given by

$$\frac{L_j}{d} = \begin{cases} 6 \text{ for } \frac{y_{\max}}{d} \leqslant 0.1 \\ 12 \text{ for } \frac{y_{\max}}{d} \geqslant 0.6 \end{cases} \tag{7.5.14}$$

In the interval $0.1 < y_{\max}/d < 0.6$, it is assumed that L_j/d is a linear function of $y_{\max}/d$.

For a cantilever structure with an assumed mode shape of $\xi(z) = z^2$

$$K_\xi = 0.13 \tag{7.5.15}$$

$$K_w = \begin{cases} \frac{L_j}{h}\left[3 - 3\frac{L_j}{h} + \left(\frac{L_j}{h}\right)^2\right] & \text{if } \frac{L_j}{h} \leqslant 0.263 \\ 0.6 & \text{if } \frac{L_j}{h} > 0.263 \end{cases} \tag{7.5.16}$$

Rules for determining δ_s to be used in the Scruton number, see equation (7.3.5), are given in an Annex of Eurocode 1. An example is presented in Section 7.8.

Equations (7.5.8) and (7.5.14)–(7.5.16) are solved by an iterative procedure. Then the lift coefficient c_{lat} should be checked to see if it needs correcting. The mean wind velocity U_m at the centre of the fully correlated loading length is determined. If $U_{\text{crit}} \leqslant 0.83U_m$, no corrections are necessary. If $U_{\text{crit}} > 1.25U_m$ vortex shedding will not be taken into account. If U_{crit} is between these limits, c_{lat} is reduced to

$$c_{\text{lat}} = \left(3 - 2.4\frac{U_{\text{crit}}}{U_m}\right) c_{\text{lat},0} \tag{7.5.17}$$

7.5.3 Comparison between predicted and observed response—steel structures

Predictions based on the Canadian code, Eurocode 1 and the CICIND model code are compared in Figure 7.18. The figure shows the relative chimney top amplitude, y_{max}/d, as a function of the Scruton number. Large differences in predicted amplitudes are observed, especially for low Scruton numbers. The Canadian code does not give useful predictions for Scruton numbers below approximately 10, i.e. Scruton numbers encountered for many steel structures constructed in practice. The CICIND model code applies to all Scruton numbers, but it gives much larger response predictions than Eurocode 1, especially for low Scruton numbers.

Ruscheweyh and Sedlacek (1988) compared vortex shedding specifications according to ISO TC98, CICIND and DIN 4133 with results from full-scale experiments on steel chimneys. They concluded that predictions based on ISO TC98, which is similar to the Canadian code, and on CICIND, overestimate the response from vortex shedding and that predictions based on DIN 4133 coincide with full-scale response measured in the whole range of relevant Scruton numbers. Since DIN 4133 and Eurocode 1 give identical specifications for the structures considered here, their conclusion holds for Eurocode 1 as well.

The full-scale measurements analysed below have been selected in order to investigate whether Eurocode 1 may sometimes underestimate the response induced by vortex shedding. In Figure 7.19 full-scale vibrations of 8 steel chimneys and 1 distillation column are compared with the theoretical predictions based on Eurocode 1. Six of the nine structures have Scruton numbers below approximately 10, making them susceptible to vortex shedding vibrations. The main structural data are given in Table 7.1.

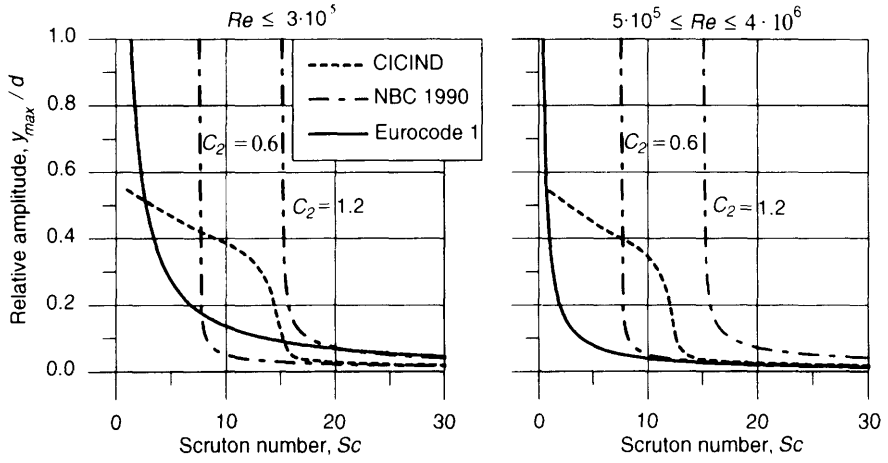

Fig. 7.18 *Relative amplitude as a function of Scruton number as specified by the CICIND model code, the Canadian code and Eurocode 1. In agreement with the Reynolds number limits given in Eurocode 1, the left-hand figure refers to Reynolds number Re below* 3×10^5 *and the right-hand figure to* $5 \times 10^5 \leq Re \leq 4 \times 10^6$. *For all curves the Strouhal number* $St = 0.2$, *the slenderness ratio* $h/d = 20$ *and* $m/(\rho d^2) = 100$.

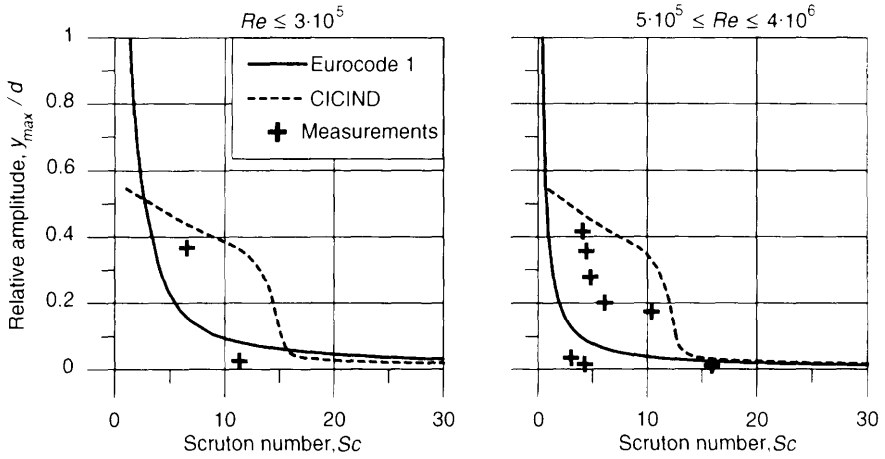

Fig. 7.19 *Comparison between relative amplitudes measured full-scale and relative amplitudes predicted using the CICIND model code and Eurocode 1. In agreement with the Reynolds number limits given in Eurocode 1, the left-hand figure refers to Reynolds number Re below* 3×10^5 *and the right-hand figure to* $5 \times 10^5 \leq Re \leq 4 \times 10^6$. *According to the full-scale structures considered, see Table 7.1, the slenderness ratio h/d is chosen to be 36.8 in the left-hand figure and 20.0 in the right-hand figure.*

Danish steel chimneys

Full-scale measurements on the four Danish steel chimneys mentioned in columns 1–4 in Table 7.1 were carried out in the late 1970s (see Frandsen, 1979). They were part of a research project that primarily aimed to improve the prediction accuracy regarding the vortex shedding response of steel chimneys. None of chimneys used in the project had experienced unacceptable vibrations during service. Natural frequencies and structural damping were determined by ambient vibration tests and wind-induced vibration amplitudes were measured.

According to the measurements carried out in the late 1970s, Eurocode 1 does not underestimate the response, see Table 7.1. However, at least three Danish steel chimneys have experienced unacceptable large vibrations in December 1995, see columns 4–6 in Table 7.1. All three chimneys were constructed in the 1970s, and no serious vibrations were reported until the large vibrations occurred in December 1995, i.e. approximately 20 years after construction. It is worth noting that one of the three chimneys in question was used in the full-scale experiment carried out in the 1970s.

The large vibrations were observed during periods of cold weather with temperatures of approximately $-5°C$ to $-10°C$. They occurred in the morning and in the evening, indicating that the air flow is characterized by extremely low turbulence levels due to stable stratification of the atmosphere. For the chimney in Thyborøn, see Column 4 in Table 7.1, the vibrations caused a 1 m long crack in the shell at the smoke pipe inlet. A tuned mass damper has now been installed at the top of the chimney.

The observations indicate that chimneys are susceptible to large vortex shedding induced vibrations, especially in cold weather with low turbulence levels. The risk of smooth air flow at the critical wind velocities should be carefully considered in the

Table 7.1 *The first six chimneys described, see columns 1–6, are all situated in Denmark (see Frandsen, 1979) describing full-scale measurements carried out on the first four chimneys in columns 1–4. Chimneys A and B in columns 7–8 are situated in Poland and they are described by Ciesielski et al. (1992). The full-scale measurements on the 80 m steel distillation column in column 9 were published in Basu (1983). Rows 1–6 give the main structural data. Derived Eurocode 1 parameters are shown in rows 7–14. The last two rows give the maximum amplitude predicted by Eurocode 1 and as measured or observed at full-scale. Key: M: measured, O: observed, EC1: Eurocode 1.*

		1	2	3	4	5	6	7	8	9
	Equation	Nykøbing	Skjern	Brovst	Thyborøn M/EC1	Odense	Herning	Chimney A	Chimney B	Distil. column
1. Height h (m)	—	50	45	54	64	75	56	26	30	80
2. Diameter d (m)	—	2.20	1.10	2.20	2.80	2.4	1.8	1.25	0.816	3.96
3. Slenderness ratio h/d	—	22.7	40.9	24.5	22.9	31.3	31.1	20.8	36.8	20.2
4. Top shell thickness (mm)	—	6	5	8	8	5	6	5	5	not informed
5. Natural freq. n_e (Hz)	—	0.92 (M)	0.63 (M)	0.61 (M)	0.58/0.60	0.37 (EC1)	0.49 (EC1)	1.88 (Calc.)	1.06 (M)	0.53 (M)
6. Log. decrement δ_S	—	0.014 (M)	0.034 (M)	0.059 (M)	0.014/0.03	0.03 (EC1)	0.025 (EC1)	0.03 (M)	0.02 (M)	0.02 (M)
7. Scruton number Sc	(7.3.5)	4.27	11.3	15.9	3.03/4.42*	4.08	4.77	6.1	6.5	10.4
8. Crit. velocity U_{crit} (m/s)	(7.5.12)	10.1	3.5	6.7	8.1/8.4	4.4	4.4	11.8	4.3	10.5
9. $Re \times 10^5$	(7.5.13)	14.8	2.5	9.8	15.1/15.7	7.08	5.26	9.8	2.4	27.7
10. $c_{lat} = c_{lat,0}$	(7.5.14)	0.2	0.7	0.2	0.2/0.2	0.2	0.2	0.2	0.7	0.2
11. Eff. correlation length	(7.5.15)	6	6	6	6.35/6	6	6	6	6.7	6
12. K_ξ	(7.5.16)	0.13	0.13	0.13	0.13/0.13	0.13	0.13	0.13	0.13	0.13
13. K_w	(7.5.17)	0.6	0.379	0.569	0.6/0.599	0.472	0.474	0.6	0.454	0.6
14. Eurocode 1 y_{max} (mm)	(7.5.9)	201	84	51	361/247	181	116	80	130	149
15. Measured/observed y_{max} (mm)	—	35 (M)	28 (M)	26 (M)	98 (M) >1000 (O)	>1000 (O)	> 500 (O)	250 (O)	300 (O)	690 (M)

* The difference in Scruton number is due to differences in structural damping and assumed mode shape.

design. The large air density in cold weather with a barometric pressure above normal standard should also be taken into account calculating the Scruton number.

Polish steel chimneys, see Ciesielski et al. (1992)

The Polish steel chimneys did experience large vibrations just after construction. Cracks in the shell of chimney B, see Table 7.1, were observed in the corner of a burned-gas outlet shortly after the chimney was constructed.

The vibration amplitudes indicated in Table 7.1 are based on visual comparison with a reference non-vibrating object, e.g. a building. The structural damping given was measured and interpreted as independent of the size of the motion.

The vibrations of the Polish chimneys, which were observed during the winter season, are approximately three times larger than those predicted using Eurocode 1.

80 m steel distillation column, see Basu (1983)

Over a period of some months, large peak amplitudes of 0.38 m and 0.69 m were measured. The natural frequency and structural damping were determined by ambient vibration tests.

The vibrations measured are approximately 3–4 times larger than those predicted using Eurocode 1.

Full-scale results — conclusion

According to the results shown in Table 7.1, under special conditions, e.g. certain meteorological situations with cold and smooth air flow over a relatively long period of time, say of approximately 1 hour, some slender steel structures may experience larger vibrations than predicted by Eurocode 1. Furthermore, the low temperatures may increase the risk of brittle fracture due to low ductility steel.

The vibration amplitude and structural damping of the 80 m steel distillation column are based on actual measurements that are expected to be reliable. The Polish and some of the Danish vibration amplitudes are based on observations, which might overestimate the actual vibration amplitudes. However, the uncertainties related to observations are not expected to be able to explain the large discrepancies, where responses observed are of the order of 5 times larger than the vibration amplitudes calculated using Eurocode 1.

In conclusion, Eurocode 1 sometimes overestimates and sometimes underestimates the response caused by vortex shedding. There seems to be a need for adjustments of the calculation procedure specified and in the basic parameters used to estimate the response. The meteorological situations that lead to larger vibration amplitudes than predicted using Eurocode 1 should be clarified. The present models describing the phenomenon of vortex shedding might still be too crude to establish the level of clarification needed. If so, a more conservative approach than Eurocode 1 is asked for when designing steel structures against vortex shedding.

The CICIND model code can be used for all Scruton numbers and does not underestimate the response induced by vortex shedding on the structures considered here.

7.6 DESIGN

As vibrations from vortex shedding occur at moderate wind speeds, structures may undergo a considerable number of stress variations. Thus, the risk of fatigue must be taken into account at the design stage.

Information about the probability of critical wind speeds, i.e. wind speeds which cause structural vibrations, is needed in order to perform a fatigue analysis.

Even if a fatigue analysis is not explicitly demanded in the code which is applied, the risk of fatigue should be kept in mind, especially with regard to slender steel chimneys.

Information about the probability of wind speeds is given in the *European Wind Atlas* (Troen and Petersen, 1989). The probability has been found to follow a Weibull distribution, see Appendix A.1. The probability P that a mean wind speed U at a certain time is in a range between U_a and U_b is expressed as

$$P = \exp\left[-\left(\frac{U_a}{A}\right)^C\right] - \exp\left[-\left(\frac{U_b}{A}\right)^C\right] \tag{7.6.1}$$

where scale parameter A and shape parameter C in the Weibull distribution are given in tables in the wind atlas for a large number of locations in the 12 countries that formed the EEC in 1989. For each location, parameters are given for four roughness classes at five different heights, and corresponding to twelve sectors of 30°. Data giving a total for all sectors are also presented.

A chimney may be located at a site where the roughness varies according to wind direction. If h_i is the probability for direction no. i, (7.6.1) should be replaced by

$$P = \sum_{i=1}^{12} h_i \left\{\exp\left[-\left(\frac{U_a}{A_i}\right)^{C_i}\right] - \exp\left[-\left(\frac{U_b}{A_i}\right)^{C_i}\right]\right\} \tag{7.6.2}$$

The interval $U_a \leqslant U \leqslant U_b$ is not obvious, but should be related to the lock-in phenomenon. Ruscheweyh (1982) shows a lock-in range for both sides of the critical wind speed, whereas Simiu and Scanlan (1986) have U_{crit} as a lower limit to be $U_a \equiv U_{crit}$ and the upper limit to be U_b = approximately $1.3U_{crit}$. Accurate estimates of the upper limit depend on the Scruton number used.

The expected number of cycles N during a period of T years is

$$N = 365 \times 24 \times 60 \times 60 \times Tn_cP = 3.15 \times 10^7 Tn_cP \tag{7.6.3}$$

where n_c is the natural frequency of the mode considered. P follows from formula (7.6.1) or (7.6.2).

7.7 REDUCTION OF VORTEX-INDUCED VIBRATIONS

As demonstrated in Section 7.8, steel chimneys may be subjected to considerable motion caused by vortex shedding. Therefore it may be necessary to reduce such vibrations using aerodynamic or mechanical provisions.

Aerodynamic measures

Many kinds of aerodynamic devices for removing or diminishing the risk of vibrations induced by vortex shedding have been suggested, (see Zdravkovich, 1981). They all aim to change the air flow around the structure in order to remove the cause of the rhythmic formation of vortices.

Helical strakes on the top third of the chimney, as shown in Figure 7.20, are a widely used device. Often three strakes are used with a pitch of one revolution in three diameters

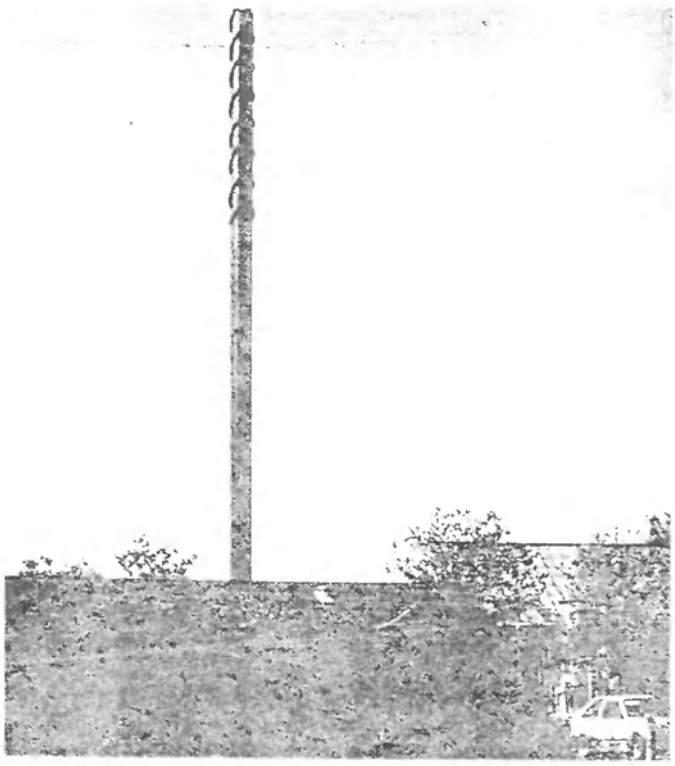

Fig. 7.20 *Chimney with helical strake. (Reproduced by permission of Danish Building Research Institute. Photo: H.H. Knutsson).*

and with a height of approximately 10% of the chimney diameter. Helical strakes should not be used for Scruton numbers below approximately 5.

Spirals increase along-wind loading. Both Eurocode 1 and CICIND introduce a shape factor of 1.4 for along-wind loading, which is to be calculated with an area corresponding to the same area as without the strakes. The shape factor should only be applied in the zone containing strakes.

Tuned mass dampers (TMD)

Introducing mechanical damping in the structure is another effective way of reducing the vibrational response to vortex shedding. A frequently applied method is to suspend a mass in a spring–damper system at the top of the chimney. The mass should be about 0.01–0.02 times the total mass of the chimney, and the natural frequency of this device should be close to the natural frequency of the structure.

Total damping should be used when calculating the amplitude of the induced vibrations. When a steel chimney is provided with a TMD, the order of magnitude of the logarithmic decrement is typically $\delta_s \sim 0.1$. The principles for calculating responses when TMDs are applied are described in many textbooks on structural dynamics (see e.g. Smith, 1988). Many papers on vibrations and dampers were presented at the 8th International Conference on Wind Engineering in 1991, see *Journ. of Wind Engineering* **43**, 1881–2071. Several examples of TMDs are shown by Ruscheweyh (1982).

7.8 EXAMPLE: A STEEL CHIMNEY 60 METRES TALL

In order to demonstrate the application of the theories in the preceding section, the cross-wind loading induced by vortex shedding will now be calculated for a steel chimney with one liner. Steel rather than concrete has been chosen because of its greater sensitivity to vortex shedding. In the example, Eurocode 1, the Canadian NBC 1990 and the CICIND model code are applied.

For damping, coefficient of fluctuating lift etc., the values in the codes are used without further comments. In order to simplify the calculations and make it easier for the reader to verify the results, a constant thickness of the shell is assumed, although this is unrealistic. The foundation at ground level is assumed to be perfectly stiff. This means that the chimney may be considered to be a clamped-free beam.

The influence of a TMD will be investigated.

In this example, only the vortex shedding is analysed.

Data on the chimney

- Location: In the UK, in a flat, rural area in East Anglia, i.e. farmland with very few buildings and trees.
- Lifetime: $T = 50$ years
- Height: $h = 60$ m
- External diameter: $d = 3$ m
- Thickness of shell: $t_1 = 10$ mm
- Moment of inertia: $I = 0.1050$ m^4
- Steel grade: S355, cf. Eurocode 3.
- Young's modulus: $E = 2.1 \times 10^5$ MPa
- Steel density: $\rho_S = 7850$ kg/m^3
- Mass of shell: 740 kg/m
- Mass of liner etc.: 260 kg/m
- Total mass: $m = 1000$ kg/m

The first two natural frequencies are calculated as $n_1 = 0.73$ Hz and $n_2 = 4.57$ Hz. Data from the *European Wind Atlas* (Troen and Petersen, 1989) will be used to estimate the risk of fatigue. Data from Coltishall, 14 km NNE of Norwich is deemed to be best suited to the purpose. According to the description, the roughness class is no. 1 with the roughness length $z_0 = 0.01$ m. At the height of 50 m above ground, the scale parameter is $A = 7.6$ and the shape parameter is $C = 2.25$. No distinction is made for different wind directions.

Eurocode 1

As $h/d = 20 > 8$, vortex shedding will be dealt with.

The Strouhal number $St = 0.2$, and the critical wind velocity is

$$U_{\text{crit}} = \frac{dn_1}{St} = \frac{3.0 \times 0.73}{0.2} = 10.9 \text{ m/s}$$

Corresponding to the second mode, the value becomes

$$\frac{dn_2}{St} = \frac{3.0 \times 4.57}{0.2} = 69 \text{ m/s}$$

According to Eurocode 1, the terrain category is between I and II. Here we shall assume category I, but it should be kept in mind that future changes in the surroundings may alter the category at a later date. From this category, the roughness length $z_0 = 0.01$ m and the terrain factor $k_T = 0.17$. According to the wind map of the UK, $U_{\text{bas}} = 25$ m/s.

Assuming the effective correlation length to be about 20 m, the mean wind velocity for the 50-year wind should be determined at a height of 50 m:

$$U_m = 25 \times 0.17 \times \ln(50/0.01) = 36 \text{ m/s}.$$

Thus $U_{\text{crit}} < 0.83U_m$, and as $69 > 1.25 \times 36$, only the response in the first mode will be considered.

According to Eurocode 1, the logarithmic decrement should be taken as $\delta_s = 0.025$, the value given for welded steel stacks with 1 liner. The air density, according to Eurocode 1, is $\rho = 1.25$ kg/m^3. Then the Scruton number is found using (7.3.5) to be

$$Sc = \frac{2 \times 0.025 \times 1000}{1.25 \times 3.0^2} = 4.4$$

At the critical wind velocity, Reynolds number is

$$Re = \frac{3.0 \times 10.9}{1.5 \times 10^{-5}} = 2.2 \times 10^6$$

so, from (7.5.13) $c_{\text{lat},0} = 0.2$, and as $U_{\text{crit}} < 0.83U_m$, $c_{\text{lat}} = 0.2$.

Equations (7.5.8) and (7.5.14)–(7.5.16) are solved by iteration, starting by assuming the effective correlation length $L_j = 6d$. Iteration leads to the effective correlation length 18 m and the maximum amplitude $y_{\max} = 0.266$ m.

For vibrations in the fundamental mode, the moment amplitude at foundation level then becomes ~5.73 MN m.

The corresponding maximum bending stresses are

$$\sigma_{\max} = \pm\frac{5.73 \times 1.5}{0.1050} = \pm 82 \text{ MPa}$$

which is an unacceptably high value.

A tuned mass damper will be used at the top of the chimney. It should be fixed with some spring devices leading to a natural frequency close to 0.73 Hz. We shall assume an increase in damping that leads to a logarithmic decrement $\delta_s = 0.1$ and thus $Sc = 17.8$. The correlation length remains 18 m, and the top amplitude reduces to 0.066 m. The moment amplitude at the bottom becomes 1.42 MNm and the stress amplitude 20.2 MPa.

According to Eurocode 1, the number of stress cycles N is given by

$$N = 6.3 \times 10^7 T n_1 \varepsilon_0 \left(\frac{U_{\text{crit}}}{U_0}\right)^2 e^{-(U_{\text{crit}}/U_0)^2}$$

Equation (7.6.3) has been used with a probability P given by

$$P = 2\varepsilon_0 \left(\frac{U_{\text{crit}}}{U_0}\right)^2 e^{-\left(\frac{U_{\text{crit}}}{U_0}\right)^2}$$

Bandwidth factor ε_0 and the velocity U_0 equal to $\sqrt{2}$ times the modal value of the probability distribution of the wind velocity are specified in Eurocode 1 to be

$$\varepsilon_0 = 0.3$$

$$U_0 = \tfrac{1}{5} U_{m.Li}$$

where $U_{m.Li}$ is the mean wind velocity at the centre of the effective correlation length, i.e. 51 m above ground,

$$U_{m.Li} = 25 \times 0.17 \times \ln(51/0.01) = 36.3 \text{ m/s},$$

$$U_0 = 7.26 \text{ m/s}$$

$$N = 6.3 \times 10^7 \times 50 \times 0.73 \times 0.3 \left[\frac{10.9}{7.26}\right]^2 \exp\left[-\left[\frac{10.9}{7.26}\right]^2\right]$$

$$= 1.63 \times 10^8.$$

The fatigue check is not specifically demanded in Eurocode 1, but according to Eurocode 3 the fatigue stress range $\Delta\sigma_R = 29$ MPa, as $N > 10^8$ and transverse butt welds are foreseen.

Assuming the steel temperature is less than 200°C, the partial safety factor for accessible joints, where local failure leads rapidly to failure of the structure is, according to Eurocode 3, $\gamma_R = 1.25$ (boxed value). Then the stress range $\Delta\sigma$ shall satisfy the condition

$$\Delta\sigma < \frac{29}{1.25} = 23 \text{ MPa}$$

As the calculated stress range is $\Delta\sigma = 40$ MPa, the chimney with the assumed TMD is not acceptable.

In order to obtain a satisfactory structure, the damping should be larger. If the logarithmic damping decrement is increased to $\delta_s = 0.2$, then the Scruton number will be $Sc = 35.6$. The moment amplitude drops to 0.71 MN m at the bottom, and the stress amplitude becomes 10.1 MPa. Then the stress variation is $\Delta\sigma = 20 < 23$ MPa, meaning that the structure is acceptable.

The Canadian code NBC 1990

Formula (7.4.18) gives $U_h = 5 n_1 d$, as $n_1 d^2 = 0.73 \times 3^2 > 0.75$ m^2/s. Then $U_h = 5 \times 0.73 \times 3.0 = 11.0$ m/s. The aspect ratio is $h/d = 60/3 = 20$, and as $U_h > 10$ m/s, the parameters C_1 and C_2 in formula (7.4.22) and (7.4.23) are $C_1 = 3$ and $C_2 = 0.6$:

$$C_2 \frac{\rho d^2}{m} = 0.6 \frac{1.20 \times 3^2}{1000} = 0.0065$$

The structure's damping ratio ζ_s is only indicated in the supplement to National Building Code of Canada, 1990. However, it is likely to be $\zeta_s < 0.0065$, so extensive motions may be expected, amplitudes of about 1 diameter, according to the code, i.e. 3.0 m. This means that some precautions are necessary, and a TMD is assumed, leading to a logarithmic decrement of 0.1—corresponding to a damping ratio $\zeta_s = 0.1/(2\pi) = 0.016$.

Using formula (7.4.20) gives

$$F_L = 3 \times \frac{1}{\sqrt{0.016 - 0.0065}} \times \sqrt{\frac{3}{60}} \times \frac{1}{2} \times 1.2 \times 11.0^2 \times 3.10^{-3} = 1.50 \text{ kN/m}$$

If F_L is applied as a static load on the top third of the chimney, the bending moment at the bottom is

$$M = 1.50 \times 20 \times 50 \text{ kN m} = 1.50 \text{ MN m}$$

and the maximum bending stresses are

$$\sigma_{max} = \frac{1.50 \times 1.5}{0.1050} = 21.4 \text{ MPa}$$

CICIND model code

The damping ratio for a steel chimney with a liner on a stiff foundation is presented as $\zeta_s = 0.006$, from which

$$Sc = \frac{4\pi \times 0.006 \times 1000}{1.25 \times 3.0^2} = 6.7$$

As $5 < Sc < 15$, the top amplitude should be checked. And as $U_{crit} = 10.9$ m/s, the Reynolds number is

$$Re = \frac{10.9 \times 3.0}{1.5 \times 10^{-5}} = 2.2 \times 10^6 < 3 \times 10^6$$

Using Figure 7.15, it is obvious that the response is very sensitive to the Scruton number, and the top amplitude is approximately 0.4 diameter, i.e. 1.2 m. The bending moment at the bottom is 26 MN m, and the maximum bending stress σ_{max} = 369 MPa, which must be reduced.

If a tuned mass damper is used, giving rise to a logarithmic decrement $\delta_s = 0.1$, then $Sc = 2 \times 0.1 \times 1000/(1.25 \times 3.0^2) = 17.8$, and from Figure 7.15 follows that $y_{max} = 0.032d = 0.096$ m. This corresponds to a bending moment $M = 2.1$ MN m at the bottom, and the maximum bending stress is $\sigma_{max} = 30$ MPa.

Comparison between the codes

The results of the calculations according to the three different codes are briefly summarized in Table 7.2. Using the structure without a damper or other device is not possible in any

Table 7.2 *Results of calculations. Comparison of the codes.*

Code	EC1	NBC	CICIND
No TMD:			
δ_s	0.025	—	0.038
y_{max} (m)	0.27	~ 3.0	1.2
σ_{max} (MPa)	82	—	369
TMD, δ_s	0.1	0.1	0.1
y_{max} (m)	0.066	—	0.096
σ_{max} (MPa)	20.2	21.4	30
TMD, δ_s	0.2	0.2	0.2
y_{max} (m)	0.033	—	—
σ_{max} (MPa)	10	13.1	—

of the cases. The application of a tuned mass damper is effective in reducing the vibration amplitude and the bending stresses in the chimney. It is obvious from the example that the method used in Eurocode 1 leads to lower stresses than the methods in the Canadian code and the CICIND model code.

8 Wind Load on Bridges

This chapter focuses on wind-induced vibrations of cable-supported bridges induced by fluctuating wind load on the bridge deck. The large flexibility of cable-supported bridges indicates that bridge movements are of primary interest, i.e. deflections, accelerations etc. The induced stresses in the structure should also be considered carefully during the design.

The total wind load on a bridge deck, F_{tot}, is found by adding the time-averaged mean wind load, F_q, the fluctuating wind load due to air turbulence (buffeting), F_t, and the motion-induced wind load, F_m, i.e.

$$F_{\text{tot}} = F_q + F_t + F_m \tag{8.1}$$

The motion-induced wind load plays an important role for cable-supported bridges. The bridge vibration frequencies and the aerodynamic damping terms depend strongly on the wind velocity. In the mathematical formulation presented, clear distinctions are made between still-air and in-wind bridge characteristics.

Flutter occurs at the critical flutter wind velocity defined as the wind velocity at which the energy input from the motion-induced wind load is equal to the energy dissipated by structural damping. At the critical flutter wind velocity the dominating term in equation (8.1) is the motion-induced wind load. The critical flutter wind velocity found assuming zero mean wind load and zero buffeting wind load is a mathematical abstraction often used as a guideline for judging the aerodynamic behaviour of the bridge, see Section 8.2.4 considering critical flutter wind velocities in a pure torsional motion and Section 8.4 analysing coupled flutter vibrations.

Many modes are involved in structural bridge vibrations. Vibrations occur as a coupling of a vertical bending mode and a torsional mode, both with significant bridge-deck movements. Furthermore, the modes that give coupled vibrations have their largest deflections at the same part of the bridge-deck structure. The first symmetrical vertical bending mode may couple with the first symmetrical torsional mode of the bridge. Having said this, the first symmetrical bending mode is not likely to couple with the first antisymmetrical torsional mode, since the largest vertical deflections are found where the torsional vibrations are small. The influence of coupling between vertical and torsional modes is analysed in more detail in Section 8.3 considering buffeting vibrations and in Section 8.4 analysing coupled flutter-induced vibrations.

The bridge will also be subject to horizontal deflections. However, in most situations the vertical deflection/vertical load and angular rotation/torsional moment are not coupled strongly to the horizontal bridge deflections. This uncoupling is assumed in the following formulation.

For suspension bridges with very long spans of above 1–2 km, for example, horizontal deflections will be significant. Mode shapes, where horizontal, vertical and torsional deflections couple, may also become important. In such situations, the present formulation should be expanded by additional motion-induced load terms, see for instance Jain *et al.* (1995) in which 18 different aerodynamic derivatives are introduced: 3 load components, combined with 3 deflection and 3 velocity terms ($18 = 3 \times (3 + 3)$).

Aerodynamic characteristics

The aerodynamic characteristics of a bridge deck have a significant influence on the vibrations encountered. Streamlined bridge decks improve aerodynamic stability, changing the critical flutter conditions to higher wind velocities. Typically, the aerodynamic bridge-deck data used in analyses are based on wind-tunnel test results or numerical flow simulations.

Structures with limited torsional stiffness, such as suspension bridges and cable-stayed bridges, are susceptible to flutter vibrations. Increasing the torsional stiffness improves stability. This is possibly the most important reason for using closed, box-shaped cross sections in long-span suspension bridges such as the Severn Bridge, Humber Bridge and the Great Belt Bridge.

Wind screens and safety barriers on bridge decks significantly alter the aerodynamic characteristics and typically reduce the critical flutter wind velocities. In cold areas, iced-up wind screens may reduce the critical flutter wind velocities even further. Rail and road traffic may also influence the aerodynamic behaviour of a bridge, so the effect of screens, safety barriers and traffic should be considered carefully during the design of flutter-susceptible bridges.

The mathematical model presented is useful when calculating the wind-induced vibrations of a bridge deck. The structural characteristics are combined with aerodynamic data described by aerodynamic derivatives, see Section 8.2.3. The structural data used include modal masses, natural frequencies and damping ratios of the vertical and torsional modes coupling in the flutter vibrations.

The principles outlined in the following are explained using a flat plate as an example. Flat-plate aerodynamics are often used as a guideline during the preliminary design of flutter-sensitive bridges, see e.g. Selberg and Hjorth-Hansen (1966).

Content of Chapter 8

The analysis presented in this chapter supplements the extensive description of wind load on bridges given in the literature, see e.g. Simiu and Scanlan (1986). The mathematical formulation outlined is basically the same. Some additional aspects are, however, included in this text:

1. A detailed analysis of suspension bridges during construction. The example used explains the main features of flutter-induced vibrations using a physical approach that is easy to comprehend. The description given adds to the sparse information published about wind loads on suspension bridges during construction.
2. Emphasis will be placed on the importance of choosing an accurate scaled mass and mass moment of inertia in full-scale predictions based on section-model tests. A detailed description of the principles used in section-model tests is given by Hjorth-Hansen (1992).

3. A thorough discussion of the aerodynamic admittance functions defined as the ratio between load spectra and wind velocity spectra.
4. The coherence of the aerodynamic forces is stronger than that of the turbulence fluctuations in the oncoming, undisturbed air flow. Results obtained in recent wind-tunnel tests are used to quantify the importance of this aspect.
5. The buffeting response calculations presented include the influence of coupling between vertical and torsional bridge modes. Mode coupling is investigated in detail for a streamlined bridge section.

The mean wind load including the static stability of a bridge deck is analysed in Section 8.1. The motion-induced wind load is described thoroughly in Section 8.2 using aerodynamic derivatives. Buffeting vibrations are discussed in Section 8.3, in which aerodynamic admittance functions are introduced. Flutter vibrations initiated mainly by the motion-induced wind load is analysed theoretically in Section 8.4, and Section 8.5 describes flutter vibrations of suspension bridges during construction.

Where vortex shedding vibrations of bridge decks are concerned, reference is made to the literature, see e.g. Simiu and Scanlan (1986).

A number of comments on the Eurocode 1 clauses are given in Section 8.6.

8.1 MEAN WIND LOAD ON BRIDGE DECKS

The mean wind load on the bridge deck is described by drag (F_q^D), lift (F_q^L) and moment (F_q^M) loads per unit of length as follows:

$$F_q^D(y) = \tfrac{1}{2}\rho U^2(y) h C_D(\alpha(y)) \tag{8.1.1}$$

$$F_q^L(y) = \tfrac{1}{2}\rho U^2(y) b C_L(\alpha(y)) \tag{8.1.2}$$

$$F_q^M(y) = \tfrac{1}{2}\rho U^2(y) b^2 C_M(\alpha(y)) \tag{8.1.3}$$

in which $U(y)$ is the mean wind velocity as a function of the coordinate y along the bridge deck, and C_D, C_L and C_M are non-dimensional shape factors depending on the angle of incidence $\alpha(y)$. The positive directions of loads and angle of incidence are shown in Figure 8.1. Typical shape-factors determined for streamlined box girder sections are shown in Figure 8.2.

Flat plate approximation

It is assumed that the mean wind velocity, U, and the angle of incidence, α, are constant along the flat plate.

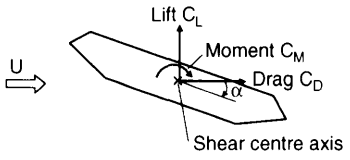

Fig. 8.1 *Definition of positive directions of loads and angle of incidence. The moment acts with respect to the shear center axis.*

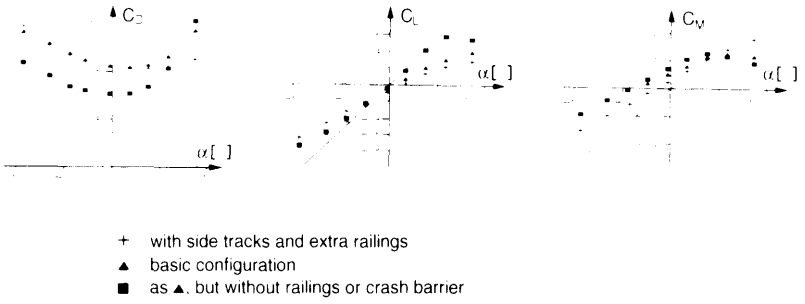

Fig. 8.2 *Shape factors for streamlined box girder sections (Hjorth-Hansen, 1993). The theoretical flat plate slopes of the aerodynamic lift and moment coefficients are also shown.*

Several authors have theoretically calculated the aerodynamic lift, F_q^L, and moment, F_q^M, acting on a stationary, thin, flat plate per unit of length, see e.g. Joukowski (1916):

$$F_q^L(\alpha) = \tfrac{1}{2}\rho U^2 b \frac{dC_L}{d\alpha}\alpha \qquad \frac{dC_L}{d\alpha} = 2\pi \tag{8.1.4}$$

$$F_q^M(\alpha) = \tfrac{1}{2}\rho U^2 b^2 \frac{dC_M}{d\alpha}\alpha \qquad \frac{dC_M}{d\alpha} = \pi/2 \tag{8.1.5}$$

where b is the plate width, and $dC_L/d\alpha$ and $dC_M/d\alpha$ are the slope of aerodynamic lift and moment, respectively. Equations (8.1.4) and (8.1.5) are valid for small angles of attack. The width as the main structural dimension is logical, bearing in mind that the

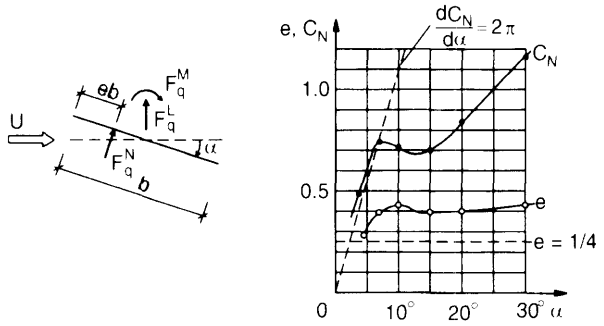

Fig. 8.3 *Wind load on a stationary, flat plate. The dotted lines in the right-hand figure show the nondimensional coefficient for the force perpendicular to the flat plate, $C_N = F_q^N/(\frac{1}{2}\rho U^2 b)$, and the non-dimensional eccentricity factor e based on theoretical calculations assuming small angles of attack. The solid lines in the right-hand figure show C_N and e based on wind-tunnel test results in small turbulent flow (Jensen and Franck, 1965). The flat plate tested has a thickness of 3.5% of the plate width and is located at a distance from the wind tunnel floor equal to the plate width. The sudden drop in lift force at an angle of attack of approximately 7° is due to flow separation occurring at angles of attack larger than approximately 7°. Flow separation has not been taken into account in the theoretical calculations presented. (Reproduced by permission of N. Franck).*

aerodynamic lift and moment originate from pressures and suctions acting on the top and bottom of the flat plate. The total effect can be described as a force, F_q^N, per unit of length acting in the so-called aerodynamic centre, see Figure 8.3. According to the theoretical calculations this is located in the foremost quarter point of the plate width.

Static stability

It is assumed that the mean wind velocity, U, and the slope of the aerodynamic moment, $dC_M/d\alpha$, are constant along the bridge deck.

The aerodynamic moment tends to increase the angle of attack, giving an apparent reduction in torsional stiffness. The structural modal torsional stiffness, k_α, in still air will be equal to the aerodynamic modal torsional stiffness $k_M = dF_q^M/d\alpha$ for the wind velocity, U_{div}, given by, see equation (8.1.3):

$$U_{\text{div}} = \sqrt{\frac{2k_\alpha}{\frac{dC_M}{d\alpha}\rho b^2}} \tag{8.1.6}$$

The wind velocity U_{div} is called the divergence velocity. If the gust wind velocity acting over the bridge span exceeds the divergence velocity, the structure will collapse due to excessive twist, because any angle of incidence, however small, will increase without limit. An adequate safety margin against divergence should always be ensured.

The structural modal torsional stiffness, k_α, in still air is equal to

$$k_\alpha = (2\pi n_\alpha)^2 I_e \tag{8.1.7}$$

in which n_α is the torsional natural frequency in still air and I_e is the equivalent mass moment of inertia introduced in equation (8.2.11). Inserting this expression of k_α in equation (8.1.3), and using the flat plate approximation of $dC_M/d\alpha = \pi/2$, the non-dimensional reduced divergence velocity, $U_{\text{div}}/n_\xi b$, is found to be

$$\frac{U_{\text{div}}}{n_\xi b} = 4\sqrt{\pi\gamma_I}\frac{n_\alpha}{n_\xi} \tag{8.1.8}$$

in which n_ξ is the vertical natural frequency in still air and γ_I is the non-dimensional mass moment of inertia ratio, $\gamma_I = I_e/(\rho b^4)$. The normalization used for the divergence velocity facilitates a direct comparison between the reduced divergence velocity and the reduced critical flutter wind velocities, $U_c/(n_\xi b)$, calculated in Section 8.4, see Figure 8.17.

Typically, the flat plate approximation used in equation (8.1.8) will underestimate the divergence velocity, since most cross sections have lower aerodynamic moment slopes than the flat plate, see Figure 8.2.

8.2 MOTION-INDUCED WIND LOAD

Originally, this mathematical model was formulated in the aeronautical field of application. The formulation was transported into the bridge community by R.H. Scanlan and has been described in several papers and textbooks, see e.g. (Simiu and Scanlan, 1986).

The cross section shown in Figure 8.4 has a mass m per unit of length and the mass moment of inertia per unit of length is designated I. The structure is assumed to have

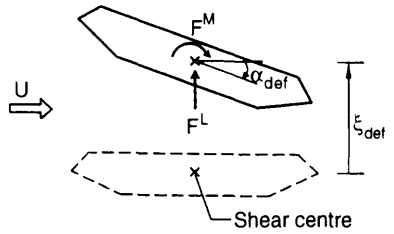

Fig. 8.4 *Definition of wind load and deflections.*

a vertical deflection, $\xi_{\text{def}}(y, t)$, and an angular rotation equal to $\alpha_{\text{def}}(y, t)$, both functions of the coordinate y along the bridge deck and time t. The natural vibrations of the two modes in still air are assumed to be mutually independent.

8.2.1 Bridge-deck sections

Assuming harmonic vibrations at a frequency n, and using the notation by Scanlan (1992), the motion-induced wind load on the structure with constant mode shapes is given by (see Scanlan 1992)

$$F_m^L = \tfrac{1}{2}\rho U^2 b \left[KH_1^*(K)\frac{\dot{\xi}_{\text{def}}}{U} + KH_2^*(K)\frac{b\dot{\alpha}_{\text{def}}}{U} + K^2 H_3^*(K)\alpha_{\text{def}} + K^2 H_4^*(K)\frac{\xi_{\text{def}}}{b} \right] \quad (8.2.1)$$

$$F_m^M = \tfrac{1}{2}\rho U^2 b^2 \left[KA_1^*(K)\frac{\dot{\xi}_{\text{def}}}{U} + KA_2^*(K)\frac{b\dot{\alpha}_{\text{def}}}{U} + K^2 A_3^*(K)\alpha_{\text{def}} + K^2 A_4^*(K)\frac{\xi_{\text{def}}}{b} \right] \quad (8.2.2)$$

and the reduced non-dimensional frequency K is defined as

$$K = \frac{b\omega}{U} = \frac{b(2\pi n)}{U} \quad (8.2.3)$$

where b is the deck width of the structure, U is the wind velocity, ω is the angular frequency of the oscillation and n is the frequency in hertz. The non-dimensional coefficients H_i^* and A_i^* $(i = 1, 2, 3, 4)$ are called aerodynamic derivatives; H_1^* and A_2^* are the aerodynamic damping in the vertical and torsional motion, respectively.

It is worth noting that the notation used gives aerodynamic derivatives twice the magnitude of the aerodynamic derivatives defined by Simiu and Scanlan (1986). Furthermore, H_2^*, H_3^*, A_1^* and A_4^* have opposite signs due to the present sign convention, in which the lift force and vertical deflection are both positive upwards. The notation used here is identical to the one used by Jacobsen (1995).

The motion-induced wind load on the structure is proportional to velocity pressure $\frac{1}{2}\rho U^2$. The vertical wind load is proportional to bridge-deck width b and the torsional moment is proportional to the width squared, b^2. The width as the main structural dimension was also used for the aerodynamic lift and moment on a stationary, thin, flat plate, see Section 8.1.

The wind load depends in a complicated way on angular rotation α_{def} and vertical and angular velocities $\dot{\xi}_{def}$ and $\dot{\alpha}_{def}$, respectively, as given by the aerodynamic derivatives. The H_4^* and A_4^* terms proportional to ξ_{def} originate from 90° out-of-phase load terms proportional to $\dot{\xi}_{def}$ and 180° out-of-phase load terms proportional to acceleration $\ddot{\xi}_{def}$. The quantities α_{def}, $\dot{\xi}_{def}/U$ and $b\dot{\alpha}_{def}/U$ are non-dimensional, effective angles of attack.

The Fourier transforms $\Phi_m^L(\omega)$ of F_m^L and $\Phi_m^M(\omega)$ of F_m^M are given by

$$\Phi_m^L(\omega) = F_{L\xi}(\omega)\Xi_{def}(\omega) + F_{L\alpha}(\omega)A_{def}(\omega) \tag{8.2.4}$$

$$\Phi_m^M(\omega) = F_{M\xi}(\omega)\Xi_{def}(\omega) + F_{M\alpha}(\omega)A_{def}(\omega) \tag{8.2.5}$$

where $\Xi_{def}(\omega)$ and $A_{def}(\omega)$ are the Fourier transforms of $\xi_{def}(t)$ and $\alpha_{def}(t)$, respectively, and

$$F_{L\xi}(\omega) = \tfrac{1}{2}\rho\omega^2 b^2(H_4^* + iH_1^*) \qquad F_{L\alpha}(\omega) = \tfrac{1}{2}\rho\omega^2 b^3(H_3^* + iH_2^*) \tag{8.2.6}$$

$$F_{M\xi}(\omega) = \tfrac{1}{2}\rho\omega^2 b^3(A_4^* + iA_1^*) \qquad F_{M\alpha}(\omega) = \tfrac{1}{2}\rho\omega^2 b^4(A_3^* + iA_2^*) \tag{8.2.7}$$

In order to satisfy system causality, the 4 F functions in equation (8.2.6) and (8.2.7) should all have real inverse Fourier transforms, which are zero for negative arguments. This may be used to check the validity of aerodynamic derivatives determined experimentally.

8.2.2 Modal loads

Vertical and torsional modes that couple in the flutter vibrations are described by

$$\xi_{def}(y, t) = \xi(y)p(t) \tag{8.2.8}$$

$$\alpha_{def}(y, t) = \alpha(y)q(t) \tag{8.2.9}$$

in which $\xi(y)$ and $\alpha(y)$ are the vertical and torsional modes that couple to produce flutter vibrations.

The modal mass is defined in Appendix C. The equivalent mass, m_e, and equivalent mass moment of inertia, I_e, are defined by the respective modal masses normalized by the square of the mode shape integrated over the bridge deck length, i.e.

$$m_e = \int^S m(y)\xi^2(y)\,dy \Big/ \int^D \xi^2(y)\,dy \tag{8.2.10}$$

$$I_e = \int^S I(y)\alpha^2(y)\,dy \Big/ \int^D \alpha^2(y)\,dy \tag{8.2.11}$$

The integrals in the numerators are the modal mass and modal mass moment of inertia taking the whole structure including bridge deck, cables and pylons into account. The integrals in the denominators are the squares of the mode shapes integrated over the bridge deck length where the motion-induced force acts. The equivalent masses defined above are similar to the equivalent mass defined in Chapter 7 in connection with vortex shedding induced vibrations.

ζ_ξ, ζ_α are structural damping ratios to critical in still air, and ω_ξ, ω_α are the natural angular frequencies in still air defined by

$$\omega_\xi = 2\pi n_\xi \tag{8.2.12}$$

$$\omega_\alpha = 2\pi n_\alpha \tag{8.2.13}$$

where n_ξ, n_α are the natural frequencies in still air, expressed in hertz, in the vertical and torsional degrees of freedom, respectively.

Assuming linear elasticity and viscous damping, the differential equations for vertical and torsional motion are given by

$$m_e(\ddot{p} + 2\zeta_\xi\omega_\xi\dot{p} + \omega_\xi^2 p) = F^L_{m,\text{modal}} + F^L_{t,\text{modal}} \Big/ \int^D \xi^2(y)\,dy \tag{8.2.14}$$

$$I_e(\ddot{q} + 2\zeta_\alpha\omega_\alpha\dot{q} + \omega_\alpha^2 q) = F^M_{m,\text{modal}} + F^M_{t,\text{modal}} \Big/ \int^D \alpha^2(y)\,dy \tag{8.2.15}$$

in which the motion-induced modal wind load on the bridge deck is described by modal loads normalized by the square of the mode shape integrated over the bridge deck length:

$$F^L_{m,\text{modal}} = \tfrac{1}{2}\rho U^2 b \times \left[KH_1^*(K)\frac{\dot{p}}{U} + KC_\xi H_2^*(K)\frac{b\dot{q}}{U} + K^2 C_\xi H_3^*(K)q + K^2 H_4^*(K)\frac{p}{b}\right] \tag{8.2.16}$$

$$F^M_{m,\text{modal}} = \tfrac{1}{2}\rho U^2 b^2 \times \left[KC_\alpha A_1^*(K)\frac{\dot{p}}{U} + KA_2^*(K)\frac{b\dot{q}}{U} + K^2 A_3^*(K)q + K^2 C_\alpha A_4^*(K)\frac{p}{b}\right] \tag{8.2.17}$$

$F^L_{t,\text{modal}}$ and $F^M_{t,\text{modal}}$ are modal loads due to air turbulence defined by

$$F^L_{t,\text{modal}}(t) = \int^S F_t^L(y,t)\xi(y)\,dy \tag{8.2.18}$$

$$F^M_{t,\text{modal}}(t) = \int^S F_t^M(y,t)\alpha(y)\,dy \tag{8.2.19}$$

in which t is the time.

The non-dimensional coefficients C_ξ and C_α are given by

$$C_\xi = \int^D \xi(y)\alpha(y)\,dy \Big/ \int^D \xi^2(y)\,dy \tag{8.2.20}$$

$$C_\alpha = \int^D \xi(y)\alpha(y)\,dy \Big/ \int^D \alpha^2(y)\,dy \tag{8.2.21}$$

Mode coupling depends on the product $C_\xi C_\alpha$ of the non-dimensional coefficients. When the vertical and torsional mode shapes are equal, e.g. for section models with constant mode shapes, $C_\xi C_\alpha = 1$ indicating possible mode coupling. Mode shapes not likely to couple give $C_\xi C_\alpha$ close to zero. For instance, mode coupling is impossible combining a symmetrical bending mode and an antisymmetrical torsional mode giving $C_\xi = C_\alpha = 0$.

8.2.3 Aerodynamic derivatives

Normally, aerodynamic derivatives are given as functions of the non-dimensional reduced velocity U_r defined by

$$U_r = \frac{U}{nb} \tag{8.2.22}$$

Aerodynamic derivatives depend on the external shape of the bridge deck and can be determined using wind-tunnel tests. Since they describe the fluctuating forces on a vibrating bridge deck, the aerodynamic derivatives should be obtained using a vibrating model in the tests. The bridge-deck section is suspended in a dynamic test rig that simulates the relevant bridge-vibration characteristics, typically the vertical and torsional bridge modes. Unequal full-scale vertical and torsional mode shapes are handled as if they were identical in the section model test. The wind-tunnel tests can be carried out using one of several procedures:

1. Vibration tests where the bridge deck is given an initial vertical and torsional displacement. The aerodynamic derivatives are based on the transient behaviour that occurs when the bridge deck is released.
2. A forced oscillation technique that involves forcing the model through a prescribed motion and measuring the aerodynamic forces on the model. The aerodynamic forces may be determined using pressure measurements at a number of pressure taps on the model.
3. Buffeting tests, where bridge-deck behaviour is analysed for different wind velocities in the tunnel. The behaviour observed in the simulated natural wind is analysed in accordance with the theoretical models presented in equations (8.2.14) and (8.2.15).

Examples of aerodynamic derivatives are shown in Figure 8.5, where flat plate data have been included for reference. It is worth noting that the aerodynamic derivatives measured on the Great Belt Bridge by procedure 1 and 2 above differ considerably. Of special importance is the large discrepancies measured for the aerodynamic damping in torsion, A_2^*. The bridge response calculated depends strongly on this parameter. Aerodynamic derivatives obtained by numerical flow simulations with the Great Belt Bridge are also shown in Figure 8.5, see Walther (1994).

The following aerodynamic derivatives can be calculated for flat plates, see e.g. Theodorsen (1934):

$$
\begin{aligned}
H_1^*(K) &= -\frac{\pi F(k)}{k} & A_1^*(K) &= -\frac{\pi F(k)}{4k} \\
H_2^*(K) &= \frac{\pi}{4k}\left[1 + F(k) + \frac{2G(k)}{k}\right] & A_2^*(K) &= -\frac{\pi}{16k}\left[1 - F(k) - \frac{2G(k)}{k}\right] \\
H_3^*(K) &= \frac{\pi}{2k^2}\left[F(k) - \frac{kG(k)}{2}\right] & A_3^*(K) &= \frac{\pi}{8k^2}\left[F(k) - \frac{kG(k)}{2}\right] \\
H_4^*(K) &= \frac{\pi}{2}\left[1 + \frac{2G(k)}{k}\right] & A_4^*(K) &= \frac{\pi}{4}\frac{G(k)}{k}
\end{aligned}
\tag{8.2.23}
$$

where F and G are the real and imaginary parts of the Theodorsen circulatory function, see Figure 8.6, and k is based on the half chord, i.e. $k = K/2$. F and G are given by

$$
F(k) = \frac{J_1(J_1 + Y_0) + Y_1(Y_1 - J_0)}{(J_1 + Y_0)^2 + (Y_1 - J_0)^2} \tag{8.2.24}
$$

$$
G(k) = -\frac{J_1 J_0 + Y_1 Y_0}{(J_1 + Y_0)^2 + (Y_1 - J_0)^2} \tag{8.2.25}
$$

where J_i and Y_i are Bessel functions of the first and second kind, respectively, of order i.

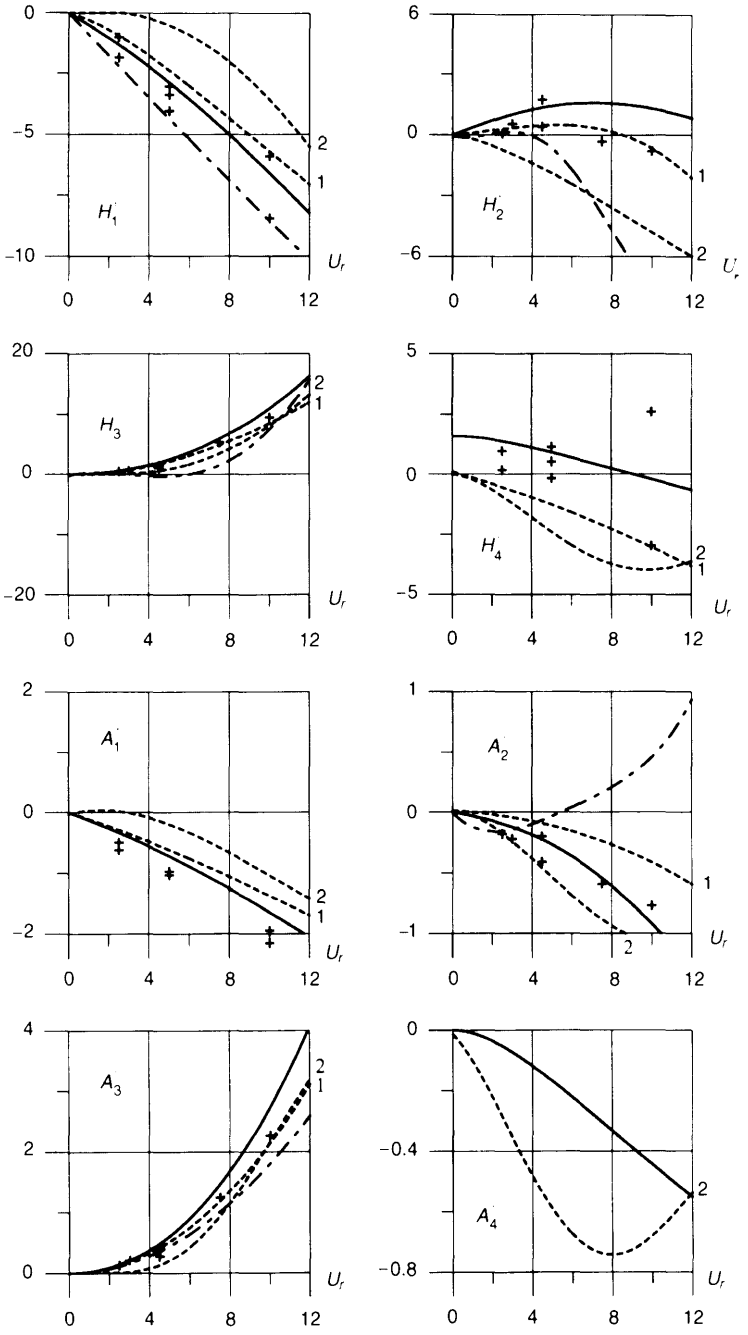

Fig. 8.5 *Aerodynamic derivatives. The solid lines correspond to the theoretical expression for a flat plate (8.2.23). 1 and 2 refer to data for the Great Belt Bridge (a streamlined box-girder section) obtained by procedure 1 and 2, respectively, mentioned above. + refer to numerical flow simulations also for the Great Belt Bridge (see Walther, 1994). — · — correspond to a truss-supported bridge girder. The numerical flow simulation data are used by permission of J.H. Walther.*

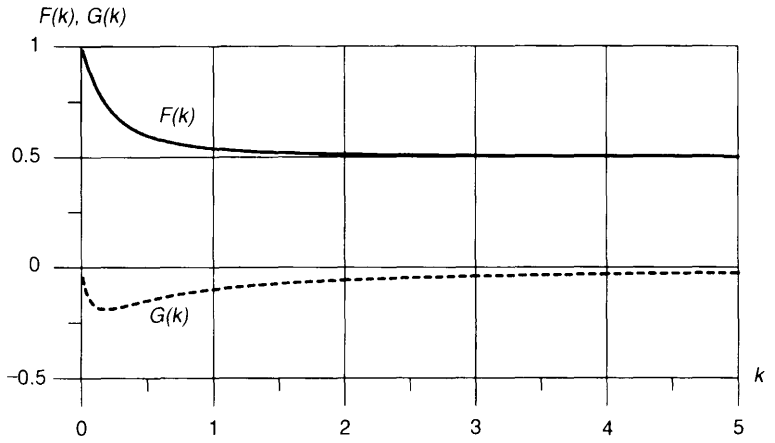

Fig. 8.6 *Theodorsen circulatory function* $C(k) = F(k) + iG(k)$.

At present, it is not clear whether all eight aerodynamic derivatives for bridge decks may be expressed by universal functions such as the F and G functions for flat plates.

8.2.4 Natural frequencies and damping ratios in wind

Vertical and torsional natural frequencies in wind depend on the stiffness modifications caused by the aerodynamic wind load terms proportional to the aerodynamic derivatives H_4^* and A_3^*, respectively, see equations (8.2.16) and (8.2.17). Since aerodynamic derivatives depend on $U/(nb)$, the actual vibration frequency n should, in principle, be estimated iteratively. In most situations, however, quite accurate results are obtained using approximations, in which iterative calculations are avoided, see equations (8.2.28) and (8.2.32) below. If not, iterative calculations should be carried out in order to obtain correct correspondence between vibration frequencies and the function parameters used to calculate aerodynamic derivatives H_4^* and A_3^*.

Pure vertical bending

Pure vertical bending is obtained if $H_2^* = 0$ and $H_3^* = 0$. The apparent stiffness $k_{\xi,\text{wind}}$ of the structure in wind is given by (see equations (8.2.14) and (8.2.16))

$$k_{\xi,\text{wind}} = k_\xi - \tfrac{1}{2}\rho U^2 K^2 H_4^*(K) \tag{8.2.26}$$

in which the structural stiffness per unit of length is $k_\xi = m_e\omega_\xi^2$ and m_e is the equivalent mass per unit of length. Negative H_4^* values increase the apparent stiffness and thereby also increase the natural vibration frequency $n_{\xi,\text{wind}}$ of the structure in wind, i.e. $n_{\xi,\text{wind}} > n_\xi$:

$$n_{\xi,\text{wind}} = n_\xi\sqrt{1 - \frac{\rho b^2}{2m_e}\frac{n_{\xi,\text{wind}}^2}{n_\xi^2}H_4^*\left(\frac{U}{n_{\xi,\text{wind}}b}\right)} \approx n_\xi\sqrt{1 - \frac{\rho b^2}{2m_e}H_4^*\left(\frac{U}{n_\xi b}\right)} \tag{8.2.27}$$

where the approximation used above:

$$\frac{n_{\xi,\text{wind}}^2}{n_\xi^2} H_4^*\left(\frac{U}{n_{\xi,\text{wind}} b}\right) \approx H_4^*\left(\frac{U}{n_\xi b}\right) \tag{8.2.28}$$

is typically quite accurate.

The observed damping ratio with wind, $\zeta_{\xi,\text{wind}}$, is the sum of structural damping ζ_ξ corrected for the change of natural frequency and aerodynamic damping ζ_ξ^a:

$$\zeta_{\xi,\text{wind}} = \frac{n_\xi}{n_{\xi,\text{wind}}}\zeta_\xi + \zeta_\xi^a = \frac{n_\xi}{n_{\xi,\text{wind}}}\zeta_\xi^a - \frac{\rho b^2}{4m_e} H_1^*\left(\frac{U}{n_{\xi,\text{wind}} b}\right) \tag{8.2.29}$$

For bridge decks normally used for long span bridges, aerodynamic damping in pure vertical bending vibrations is positive due to the negative values of H_1^*, see Figure 8.5.

Pure torsional motion

Pure torsional motion is obtained when $A_1^* = 0$ and $A_4^* = 0$. The apparent stiffness $k_{\alpha,\text{wind}}$ of the structure in wind is given by (see equations (8.2.15) and (8.2.17)):

$$k_{\alpha,\text{wind}} = k_\alpha - \tfrac{1}{2}\rho U^2 b^2 K^2 A_3^*(K) \tag{8.2.30}$$

where the structural stiffness per unit of length is $k_\alpha = I_e \omega_\alpha^2$ and I_e is the equivalent mass moment of inertia per unit of length. Positive A_3^* values reduce this apparent stiffness and thereby also reduce the natural frequency $n_{\alpha,\text{wind}}$ of the structure in wind, i.e. $n_{\alpha,\text{wind}} < n_\alpha$:

$$n_{\alpha,\text{wind}} = n_\alpha \sqrt{1 - \frac{\rho b^4}{2I_e}\frac{n_{\alpha,\text{wind}}^2}{n_\alpha^2} A_3^*\left(\frac{U}{n_{\alpha,\text{wind}} b}\right)} \approx n_\alpha \sqrt{1 - \frac{\rho b^4}{2I_e} A_3^*\left(\frac{U}{n_\alpha b}\right)} \tag{8.2.31}$$

where the approximation used above:

$$\frac{n_{\alpha,\text{wind}}^2}{n_\alpha^2} A_3^*\left(\frac{U}{n_{\alpha,\text{wind}} b}\right) \approx A_3^*\left(\frac{U}{n_\alpha b}\right) \tag{8.2.32}$$

is typically quite accurate.

The observed damping ratio in wind, $\zeta_{\alpha,\text{wind}}$, is the sum of structural damping ζ_α corrected for the change of natural frequency and aerodynamic damping ζ_α^a:

$$\zeta_{\alpha,\text{wind}} = \frac{n_\alpha}{n_{\alpha,\text{wind}}}\zeta_\alpha + \zeta_\alpha^a = \frac{n_\alpha}{n_{\alpha,\text{wind}}}\zeta_\alpha - \frac{\rho b^4}{4I_e} A_2^*\left(\frac{U}{n_{\alpha,\text{wind}} b}\right) \tag{8.2.33}$$

For streamlined bridge decks, aerodynamic damping in pure torsional vibrations is positive due to the negative values of A_2^*, see Figure 8.5. However, non-streamlined bridge decks may have positive values of A_2^* causing negative aerodynamic damping and thereby increasing the risk of aerodynamic instabilities due to flutter. When the total damping $\zeta_{\alpha,\text{wind}}$ is negative, vibrations will increase in amplitude until the structure collapses. The critical flutter wind velocity, U_c, is found when the total damping is zero:

$$A_2^*\left(\frac{U_c}{n_{\alpha,\text{wind}} b}\right) = \frac{4I_e}{\rho b^4}\zeta_\alpha \frac{n_\alpha}{n_{\alpha,\text{wind}}} = 4\gamma_I \zeta_\alpha \frac{n_\alpha}{n_{\alpha,\text{wind}}} \tag{8.2.34}$$

in which the non-dimensional mass moment of inertia ratio, $\gamma_I = I_e/\rho b^4$, is introduced. When γ_I and the structural damping ratio ζ_α are increased, the critical flutter wind velocity, U_c, also increases.

8.3 BUFFETING VIBRATIONS

Motion-induced wind loads were represented in Section 8.2 using aerodynamic derivatives. In the most simple formulation, all cross terms (H_2^*, H_3^*, A_1^*, A_4^*) are assumed negligible in the buffeting calculation. This assumption may be justified in buffeting response predictions when the wind velocity is considerably smaller than velocities in the vicinity of any coupled instabilities. Thus, motion-induced forces can be transferred to the left-hand side of the motion equations, and perceived as changes in the structural damping and stiffness characteristics. The response calculations follow the general principles set out in Chapter 6 using damping and stiffness characteristics that include the motion-induced wind load on the bridge deck.

The present section analyses the coupled buffeting vibrations occurring in vertical and torsional modes. The tendency of two modes to couple depends on the frequency separation in still air and on the similarities between the two mode shapes in question. Bridge buffeting calculations that include the influence of coupling are considerably more lengthy than the uncoupled response calculations presented in Chapter 6. Furthermore, the complexity is enhanced by the fact that both the longitudinal and vertical turbulence components contribute to the bridge deflections, whereas the longitudinal turbulence component was the only one considered in Chapter 6.

The buffeting response calculations presented take into account that mean wind velocities and turbulence characteristics may vary along the bridge deck, e.g. due to topographical effects. This is of interest for many cable-supported bridge sites.

Lateral bridge deflections, which are assumed to be uncoupled from other vibrational modes, are determined using the theory outlined in Chapter 6.

Coupled buffeting vibrations

The coupled buffeting vibrations are calculated by spectral analysis. The motion-induced wind loads given in equations (8.2.16) and (8.2.17) are transferred to the left-hand side of the equations of motion (8.2.14) and (8.2.15). Taking the Fourier transform on both sides gives the following well-known matrix equation for vibration systems with two degrees of freedom (∗: transposed and complex conjugated matrix):

$$\begin{bmatrix} S_{pp} & S_{pq} \\ S_{qp} & S_{qq} \end{bmatrix} = \bar{A}^{-1} \begin{bmatrix} S_{LL} & S_{LM} \\ S_{ML} & S_{MM} \end{bmatrix} (\bar{A}^{-1})^* \tag{8.3.1}$$

in which spectra and cross-spectra of p and q, defined by equations (8.2.8) and (8.2.9), are the matrix elements on the left-hand side, spectra and cross-spectra of $F^L_{t,\text{modal}}$ and $F^M_{t,\text{modal}}$, defined by equations (8.2.18) and (8.2.19), are the elements in the second matrix on the right-hand side, and the stiffness matrix $\bar{A}$ is given by

$$\bar{A} = \begin{bmatrix} a_{11} m_e \omega_\xi^2 \int^D \xi^2(y)\,dy & a_{12} m_e \omega_\xi^2 b \int^D \xi^2(y)\,dy \\ a_{21} I_e \omega_\xi^2 \frac{1}{b} \int^D \alpha^2(y)\,dy & a_{22} I_e \omega_\xi^2 \int^D \alpha^2(y)\,dy \end{bmatrix} \tag{8.3.2}$$

The spectra of the vertical deflection ξ_{def} and of the angular rotation α_{def} are equal to the spectra S_{pp} and S_{qq} multiplied by their respective mode shapes squared.

The elements a_{jk} are given by

$$a_{11} = -\Omega^2 + 2i\zeta_\xi \Omega + 1 - \frac{\Omega^2}{2\gamma_m}(H_4^* + iH_1^*) \tag{8.3.3}$$

$$a_{12} = -\frac{\Omega^2}{2\gamma_m} C_\xi (H_3^* + iH_2^*) \tag{8.3.4}$$

$$a_{21} = -\frac{\Omega^2}{2\gamma_I} C_\alpha (A_4^* + iA_1^*) \tag{8.3.5}$$

$$a_{22} = -\Omega^2 + 2i\zeta_\alpha \gamma_\omega \Omega + \gamma_\omega^2 - \frac{\Omega^2}{2\gamma_I}(A_3^* + iA_2^*) \tag{8.3.6}$$

in which

$$\Omega = \omega/\omega_\xi \tag{8.3.7}$$

$$\gamma_\omega = \omega_\alpha/\omega_\xi \quad \gamma_m = m_e/\rho b^2 \quad \gamma_I = I_e/\rho b^4 \tag{8.3.8}$$

Thus, $\bar{A}$ becomes a diagonal matrix when the coefficients C_ξ and C_α defined in equations (8.2.20) and (8.2.21) are both equal to zero. The two mode shapes considered will be uncoupled and response calculations follow the principles outlined in Chapter 6.

Wind load spectra

The right-hand sides of the motion equations are given by the fluctuating buffeting lift, F_t^L, and moment, F_t^M, per unit of length as follows:

$$\begin{bmatrix} F_t^L \\ F_t^M \end{bmatrix} = \tfrac{1}{2}\rho U^2 b \begin{bmatrix} 2C_L & \dfrac{dC_L}{d\alpha} + C_D h/b \\ 2C_M b & \dfrac{dC_M}{d\alpha} b \end{bmatrix} \begin{bmatrix} u/U \\ w/U \end{bmatrix} \tag{8.3.9}$$

All shape factors and shape-factor derivatives shall be taken at an angle of attack equal to $\alpha_q(y)$ corresponding to the mean wind load acting on the bridge. Normally, the most important coefficients in equation (8.3.9) are the derivatives of the lift coefficient and moment coefficient used in combination with the vertical turbulence component. The vertical turbulence component is, therefore, of primary interest when calculating the buffeting response of bridges.

Using the theory outlined in Appendix C, the spectra of the modal loading components associated with the modal displacement functions, see equations (8.2.18) and (8.2.19), are given by

$$\begin{bmatrix} S_{LL}(n) \\ S_{MM}(n) \\ S_{LM}(n) \end{bmatrix} = \left(\tfrac{1}{2}\rho U_{\text{ref}} b l\right)^2$$

$$\begin{bmatrix} \xi_{\text{ref}}^2 (2C_L)^2 |J_{LL}^u(n)|^2 & \xi_{\text{ref}}^2 \left(\dfrac{dC_L}{d\alpha} + C_D \dfrac{h}{b}\right)^2 |J_{LL}^w(n)|^2 \\ \alpha_{\text{ref}}^2 (2C_M b)^2 |J_{MM}^u(n)|^2 & \alpha_{\text{ref}}^2 \left(\dfrac{dC_M}{d\alpha} b\right)^2 |J_{MM}^w(n)|^2 \\ \xi_{\text{ref}} \alpha_{\text{ref}} 4C_L C_M b |J_{LM}^u(n)|^2 & \xi_{\text{ref}} \alpha_{\text{ref}} \left(\dfrac{dC_L}{d\alpha} + C_D \dfrac{h}{b}\right) \dfrac{dC_M}{d\alpha} b |J_{LM}^w(n)|^2 \end{bmatrix} \begin{bmatrix} S_{u,\text{ref}}(n) \\ S_{w,\text{ref}}(n) \end{bmatrix} \tag{8.3.10}$$

where l is the bridge deck length, and the joint acceptance functions for modal loading components are ($X, Y = L, M$; $j = u, w$):

$$|J_{XY}^j(n)|^2 = |\chi_{XY}^j(n)|^2 \frac{1}{l^2} \int_0^l \int_0^l g_X^j(y_1) g_Y^j(y_2) \psi_j(r_y, n)\, dy_1 dy_2 \tag{8.3.11}$$

where the so-called cross-sectional aerodynamic admittance functions of frequency n, $|\chi^j_{XY}(n)|^2$, take into account the load correlation at a certain bridge-deck cross-section, and ψ_j is the normalized co-spectrum for lateral separations with distances of r_y. The g functions are given by

$$g^u_L(y) = \frac{\xi(y)}{\xi_{\text{ref}}} \frac{C_L(y)}{C_{L,\text{ref}}} \frac{U(y)}{U_{\text{ref}}} \sqrt{\frac{S_u(y,n)}{S_{u,\text{ref}}(n)}} \tag{8.3.12}$$

$$g^w_L(y) = \frac{\xi(y)}{\xi_{\text{ref}}} \frac{dC_L(y)/d\alpha + C_D(y)h/b}{(dC_L/d\alpha + C_D h/b)_{\text{ref}}} \frac{U(y)}{U_{\text{ref}}} \sqrt{\frac{S_w(y,n)}{S_{w,\text{ref}}(n)}} \tag{8.3.13}$$

$$g^u_M(y) = \frac{\alpha(y)}{\alpha_{\text{ref}}} \frac{C_M(y)}{C_{M,\text{ref}}} \frac{U(y)}{U_{\text{ref}}} \sqrt{\frac{S_u(y,n)}{S_{u,\text{ref}}(n)}} \tag{8.3.14}$$

$$g^w_M(y) = \frac{\alpha(y)}{\alpha_{\text{ref}}} \frac{dC_M(y)/d\alpha}{(dC_M/d\alpha)_{\text{ref}}} \frac{U(y)}{U_{\text{ref}}} \sqrt{\frac{S_w(y,n)}{S_{w,\text{ref}}(n)}} \tag{8.3.15}$$

All cross-spectra between the longitudinal turbulence component u and the vertical turbulence component w have been assumed to be negligible, and all phase spectra are assumed equal to zero. This assumption does not influence response predictions significantly, since the main response contributions normally originate from the vertical turbulence component.

The ratios between the wind velocity spectra used to calculate the g functions above are assumed to be independent of the frequency, see Chapter 6 for further discussions on this topic.

The double integral in equation (8.3.11) is conveniently calculated by two single integrals as shown in Chapter 6 and Appendix B. The double integral approximations introduced in Chapter 6 may also turn out to be useful here.

Buffeting response

The bridge buffeting vibrations increase as the mean wind velocity increases. Typically, this increase is described by the mean wind velocity raised to a power considerably larger than 2. This is mainly due to the aeroelasticity introduced by motion-induced forces that give natural frequencies and critical damping ratios dependent on the mean wind velocity.

The influence of mode coupling is described in Figures 8.7–8.9, illustrating the typical buffeting behaviour of cable supported bridges with a streamlined box-girder section. The aerodynamic derivatives used here correspond approximately to the data given in Figure 8.5 for the Great Belt Bridge. The vertical wind spectrum assumed is in accordance with equation (3.5.23), and the normalized co-spectrum of vertical turbulence components with lateral separations follows an exponential expression, see equation (3.5.25), with a decay constant equal to 8. The critical flutter wind velocity of the bridge considered is equal to approximately 90 m/s.

The influence of wind direction is shown in Figure 8.10. The bridge is most sensitive to winds perpendicular to the bridge axis.

The aerodynamic admittance functions and the correlation of forces described by the normalized co-spectrum are discussed below. The information available in the literature is rather sparse, see Jacobsen (1995), Davenport *et al.* (1992) and Larose (1992) however.

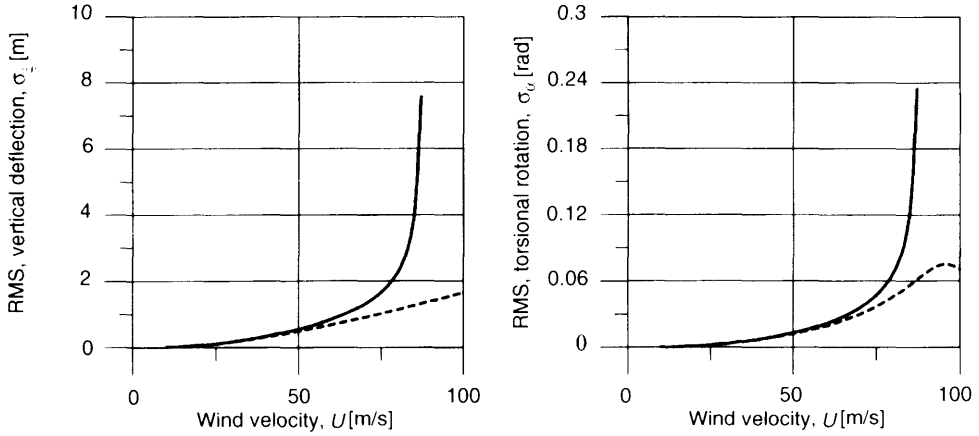

Fig. 8.7 *Bridge buffeting response as a function of mean wind velocity. Mode coupling is included in the solid lines, not in the dotted lines. Mode coupling is seen to become important for mean wind velocities larger than approximately 60% of the critical flutter wind velocity. The response increases rapidly for wind velocities close to the critical flutter wind velocity.*

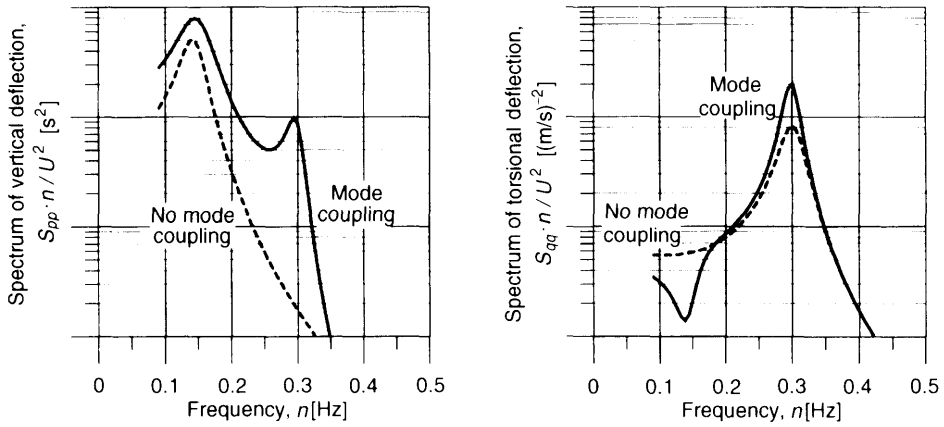

Fig. 8.8 *Response spectra at 70 m/s, i.e. a mean wind velocity of approximately 80% of the critical flutter wind velocity. The influence of mode coupling is most significant for the vertical response, less significant for the torsional response. Two spectral peaks are seen to occur for the coupled vertical response.*

On-going research projects focus on aerodynamic admittance functions and correlation of forces on bridge-decks. Increasing information on these aspects will, therefore, be available in the years to come.

Aerodynamic admittance functions

The relationship between fluctuating wind velocity and fluctuating wind load acting on a structure is commonly referred to as "aerodynamic admittance". Generally, this relation

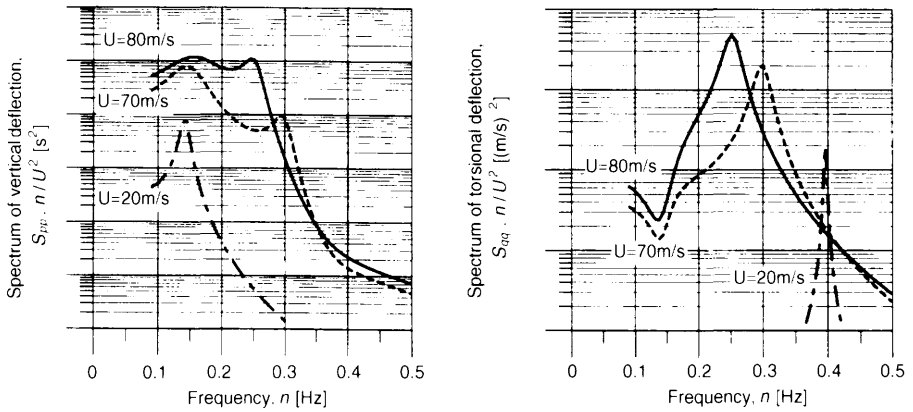

Fig. 8.9 *Response spectra at three mean wind velocities. In the curves shown, the response spectra have been normalized by the mean wind velocity squared. Mode coupling has been included in all spectra shown. The torsional vibration frequency gradually decreases as the wind velocity increases. Except for wind velocities very close to the critical fluttter wind velocity, the vertical vibration frequency does not depend strongly on wind velocity. The vertical and torsional vibration frequencies become identical at wind velocities close to the critical flutter wind velocity.*

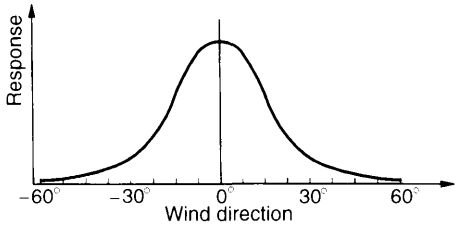

Fig. 8.10 *Bridge buffeting response as a function of wind direction.*

is based on coefficients determined experimentally, since the flow around a structure in turbulent wind is too complex to be dealt with analytically.

The cross-sectional admittance functions for bridge decks take into account the change of power spectral density function due to the "non-line-like" shape of the bridge deck. The influence of the pressure correlation around the deck periphery is included in the cross-sectional admittance functions.

At very low frequencies, the wavelengths of the air flow will be much larger than the bridge deck width. The aerodynamic admittance functions should, therefore, approach unity for low frequencies. At higher frequencies corresponding to smaller wavelengths, the aerodynamic admittance functions are expected to decline.

The aerodynamic admittance functions can be measured on motionless wind-tunnel models using different approaches, see Jacobsen (1995). One method is based on simultaneous measurements of cross-sectional surface pressures and the approaching incoming wind turbulence.

The observed form of aerodynamic admittance functions for the streamlined box-girder bridge-deck section used for the Great Belt Bridge is shown in Figure 8.11. The vertical

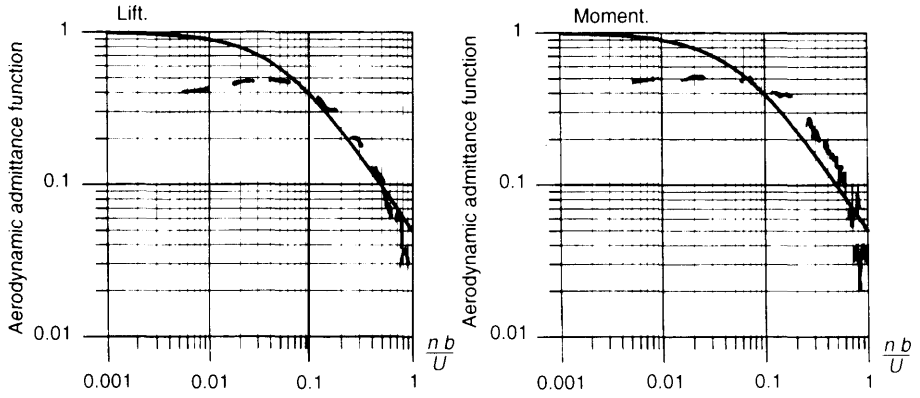

Fig. 8.11 *Aerodynamic admittance functions between the vertical turbulence component and the wind load. The so-called Sears function calculated for thin, symmetrical airfoils is shown for reference as a solid line, see equation (8.3.16). The aerodynamic admittance function shown by the dotted line has been determined using a wind-tunnel test with a streamlined box-girder bridge section (Davenport et al. 1992). (Reproduced by permission of A.A. Balkema, Rotterdam).*

and longitudinal turbulence wind components were measured using hot-wire anemometers located upwind of the model.

The Sears function, see Sears (1941), is shown for reference in Figure 8.11. It seems to fit the aerodynamic admittance function measured over the frequency region typically of interest for cable-supported bridges. The Sears function is derived theoretically as the aerodynamic admittance function of a thin, symmetrical airfoil and is given by

$$\chi^2_{\text{Sears}}(n) = \frac{J_0(x)K_1(ix) + iJ_1(x)K_0(ix)}{K_1(ix) + K_0(ix)} \tag{8.3.16}$$

in which the non-dimensional parameter $x = nc\pi/U$. c is the chord length, J_0 and J_1 are Bessel functions of the first kind, and K_0 and K_1 are modified Bessel functions of the second kind. The Sears function may be approximated by a somewhat simpler expression suggested by Liepmann (1952):

$$\chi^2_{\text{Sears}}(n) \approx \frac{1}{1 + 2\pi^2(nc/U)} \tag{8.3.17}$$

Correlation of forces

Several wind-tunnel tests and full-scale experiments have shown that the correlation of aerodynamic forces is stronger than that of the turbulence fluctuations in the incoming air flow; see Chapter 4 which discusses this aspect in connection with static load on structures.

For a streamlined box-girder bridge section, wind-induced forces on the deck have been measured simultaneously at different span-wise separations using pressure transducers located inside the deck-section model. The mean and fluctuating lift and moment forces were determined, including the correlation of forces along the bridge deck, see Figure 8.12. These tests have shown that the load on a bridge deck is better correlated than the undisturbed incoming air flow.

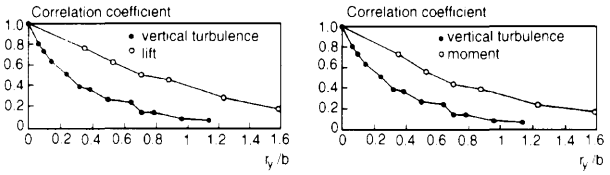

Fig. 8.12 *Span-wise zero-lag correlation of vertical turbulence fluctuations, and lift and moment acting on a streamlined box-girder bridge section (Jakobsen, 1995). Vertical turbulence has been used for comparison, since this velocity component gives the major part of the fluctuating load observed on the bridge section. (Reproduced by permission of J.B. Jakobsen).*

8.4 COUPLED FLUTTER VIBRATIONS

For a single degree of freedom system, the mechanism for aerodynamic instability is negative aerodynamic damping; see Chapter 7 and the critical flutter wind velocity determined in equation (8.2.34) for a pure torsional motion. Coupled flutter, on the other hand, can occur even if all diagonal aerodynamic damping terms are positive (H_1^* and A_2^*). It arises because of the coupling of two vibrational modes.

The flutter vibrations discussed below include the aeroelastic phenomenon in which angular rotation and vertical translation of the structure combine as an unstable oscillation. Coupling of the two modes gives the characteristic aeroelastic behaviour of flutter-susceptible engineering structures such as suspension bridges and cable-stayed bridges.

Coupled flutter vibrations can occur when the torsional natural frequency exceeds the vertical natural frequency, both referring to still air.

The wind-load terms described by aerodynamic derivatives H_4^* and A_3^* will tend to increase vertical stiffness and reduce torsional stiffness, respectively. The apparent frequency separation, $n_{\alpha,\text{wind}} - n_{\xi,\text{wind}}$ in wind is thereby reduced by the motion-induced wind load on the structure. Flutter occurs at a wind velocity that has a motion-induced wind load at which the vertical and torsional vibration couple at a certain oscillation frequency n of between n_ξ and n_α, both in still air.

The risk of flutter-induced vibrations is significant when the torsional natural frequency n_α is only slightly larger than the vertical natural frequency n_ξ in still air; see Figure 8.16, in which the influence of frequency ratio is considered in detail.

During a coupled flutter oscillation, the vertical and torsional motions occur together with a phase difference. The phase difference is essential for the energy transfer from air flow to the structure, see Figure 8.13 below.

If the structure is given an initial disturbance, its motion will either decay or diverge. The divergent flutter behaviour is established when energy transfer from the air flow to the structure exceeds the energy dissipated by structural damping. The critical flutter condition occurs at a wind velocity at which the energy input is equal to the energy dissipated. This wind velocity is called the critical flutter wind velocity.

Energy input and energy dissipation

Assuming constant mode shapes, the energy input per meter over a vibration period is given by the equation

$$E_{\text{input}} = \int_{\text{period}} F_m^L \dot{\xi}_{\text{def}}\, dt + \int_{\text{period}} F_m^M \dot{\alpha}_{\text{def}}\, dt = \tfrac{1}{2}\pi\rho U^2 K^2 \xi_0 b\alpha_0 (E_{\text{vel}} + E_{\text{def}}) \qquad (8.4.1)$$

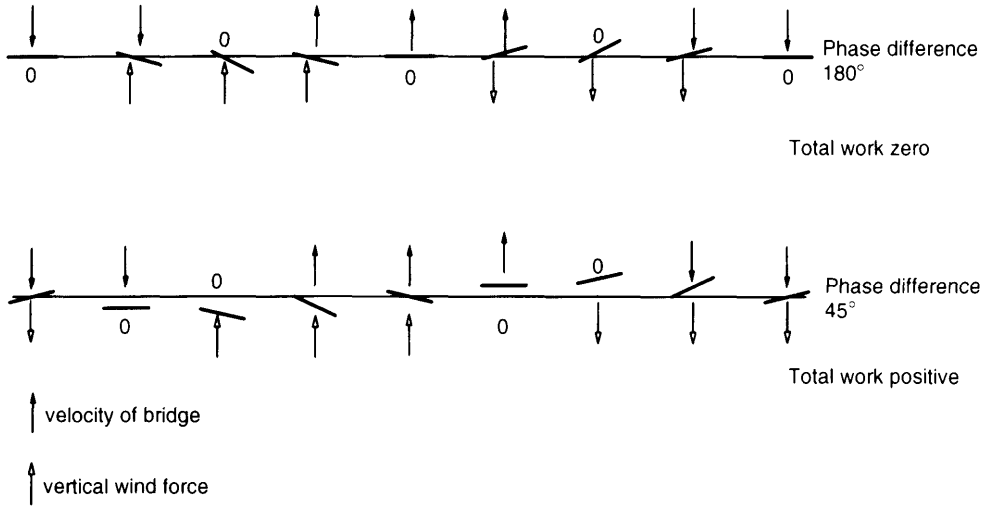

Fig. 8.13 *Coupled vibrations with a phase difference of* 180° *and* 45°, *respectively. Typical flutter vibrations observed for streamlined box girder sections resemble the vibration pattern shown in the upper figure. This corresponds to the fact that the critical flutter wind velocity often does not depend strongly on structural damping for these types of deck sections.*

in which ξ_0 and α_0 are vibration amplitudes, and the normalized velocity-related energy, E_{vel}, and the normalized deflection-related energy, E_{def}, are defined as

$$E_{\text{vel}} = (H_2^*(K) + A_1^*(K))\cos(\theta) + \left(H_1^*(K)\frac{\xi_0}{b\alpha_0} + A_2^*(K)\frac{b\alpha_0}{\xi_0}\right) \tag{8.4.2}$$

$$E_{\text{def}} = (-H_3^*(K) + A_4^*(K))\sin(\theta) \tag{8.4.3}$$

where θ is the phase angle, which the torsional displacement lags behind the vertical displacement. Terms $-H_3^*$ and A_4^* feed energy into the structural vibrations, whereas the aerodynamic damping terms H_1^* and A_2^* extract energy where streamlined box-girder deck sections are concerned.

The energy dissipated per meter due to mechanical damping is equal to

$$\begin{aligned} E_{\text{dis}} &= \int_{\text{period}} 2m_e\zeta_\xi\omega_\xi(\dot{\xi}_{\text{def}})^2\,dt + \int_{\text{period}} 2I_e\zeta_\alpha\omega_\alpha(\dot{\alpha}_{\text{def}})^2\,dt \\ &= 2\pi(m_e\zeta_\xi\omega_\xi\omega\xi_0^2 + I_e\zeta_\alpha\omega_\alpha\omega\alpha_0^2) \end{aligned} \tag{8.4.4}$$

The input and dissipation energies are illustrated in Figure 8.14 below. In the example considered, structural damping increases the flutter wind velocity from approximately 32 m/s to approximately 37 m/s.

Solving flutter equations

Assuming that ξ and α are proportional to $e^{i\omega t}$, the solution obtained will, in general, be of the form $\omega = \omega_1 + i\omega_2$, and will therefore represent either a decaying ($\omega_2 > 0$) or a

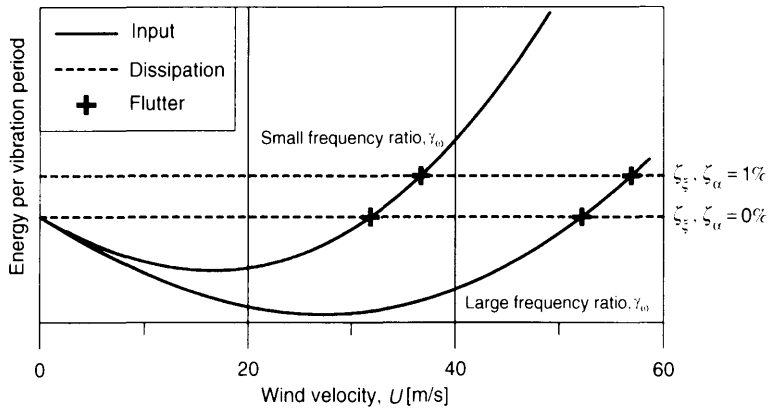

Fig. 8.14 *The input (solid line) and dissipated (dotted line) energy per vibration period are shown as a function of wind velocity, assuming flat-plate aerodynamic derivatives and a fixed ratio of $b\alpha_0/\xi_0$ determined for the critical flutter wind velocity. The energy input is shown for a small and a larger frequency ratio of $\gamma_\omega = \omega_\alpha/\omega_\xi$. For low wind velocities, the energy input is negative, giving a stable structure. The energy input exceeds the energy dissipation when the wind velocity is above the critical flutter wind velocity, giving unstable vibrations. The two sets of curves shown cross each other for a wind velocity equal to the critical flutter wind velocity marked by +.*

divergent ($\omega_2 < 0$) oscillation. The critical flutter wind velocity U_c is found for the value K_c of K, where the solution is purely imaginary ($\omega = \omega_1$, $\omega_2 = 0$):

$$U_c = \frac{b\omega}{K_c} \tag{8.4.5}$$

The oscillation frequency n in hertz is equal to $\omega/(2\pi)$. This procedure has been described thoroughly by Simiu and Scanlan (1986) for the case in which H_4^* and A_4^* are both equal to 0. The expressions given in Appendix D include all the aerodynamic derivatives.

The absolute critical flutter vibration amplitudes ξ_0 and α_0 are indefinite. However, the ratio $b\alpha_0/\xi_0$ and the phase angle between the vertical and torsional deflection can be determined using the flutter equations.

Influence of wind direction and wind inclination

The flutter wind velocities shown above are determined on the assumption that the wind direction is perpendicular to the bridge axis. In skew winds, flutter wind velocities are often increased considerably.

The influence of wind direction not being perpendicular to the bridge axis has been investigated by a number of researchers using wind-tunnel tests (see e.g. Davenport, 1982). Rough estimates of flutter wind velocities for different wind directions could be based on the so-called cosine rule, which uses the projection of the wind velocity on the axis perpendicular to the bridge as a reference wind velocity.

The influence of wind inclination with horizontal is not important for streamlined box-girder sections, see Figure 8.15. However, truss-supported bridge decks may give considerably lower critical flutter wind velocities for inclined wind compared to horizontal wind.

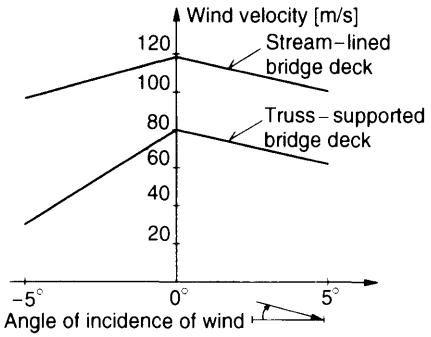

Fig. 8.15 *Critical flutter wind velocities as a function of wind inclination with horizontal (Ostenfeld et al. 1970).*

Flat plate approximations

The principles outlined in the following are explained using a flat plate as an example. Flat-plate aerodynamics is often used as a guideline during the preliminary design of flutter-sensitive bridges. It is straightforward to calculate critical flutter wind velocities for flat plates using the mass, natural frequencies and damping ratios of the actual bridge. The critical flutter wind velocity of the actual bridge, U_c, can be calculated by multiplying the critical flutter wind velocity for the flat plate with a positive constant β describing the aerodynamic characteristics of the bridge deck geometry. β values for different bridge decks are given in Table 8.1. As shown, velocity ratio β approaches unity for streamlined bridge sections.

The reduced critical flutter wind velocity, $U_c/(n_\xi b)$, for a flat plate depends on the aerodynamic derivatives, on the damping ratios ζ_ξ and ζ_α in still air, and on the non-dimensional frequency ratio γ_ω in still air, mass ratio γ_m and mass moment of inertia ratio γ_I given by

$$\gamma_\omega = \omega_\alpha/\omega_\xi \quad \gamma_m = m_e/(\rho b^2) \quad \gamma_I = I_e/(\rho b^4) \tag{8.4.6}$$

The reduced critical flutter wind velocities illustrated in Figure 8.16 are based on flat-plate aerodynamic derivatives. Closed box-girder sections have critical flutter wind velocities which are approximately 10% lower than the velocities based on flat-plate

Table 8.1 *Typical ratios β between the critical flutter wind velocity of actual bridge decks and the critical flutter wind velocity of a flat plate with the same mass, natural frequencies and damping ratios. The flutter vibrations are assumed to be a coupling of two vibrational modes.*

Bridge-deck section		β
Flate plate		1
Streamlined box-girder section	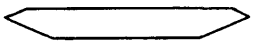	approximately 0.8–0.9
Non-streamlined box-girder section	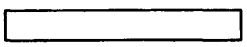	approximately 0.4–0.6
Truss-stiffened girder	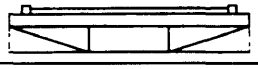	approximately 0.6–0.8

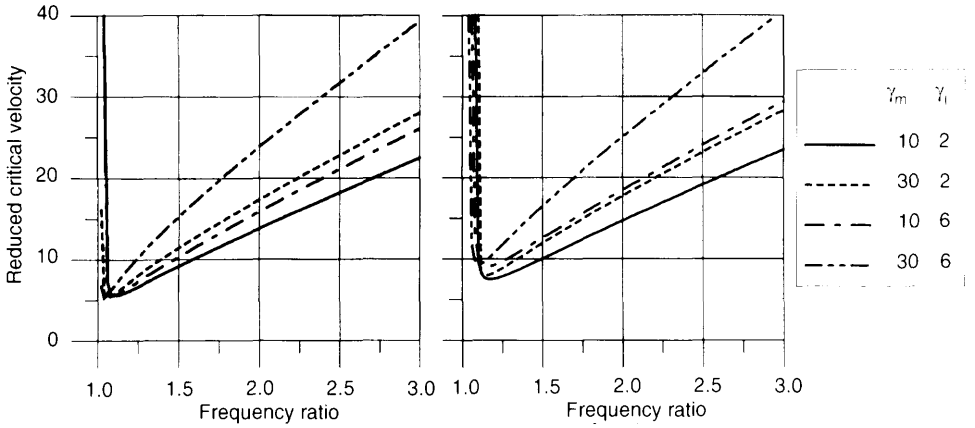

Fig. 8.16 *Reduced critical flutter wind velocity, $U_c/(n_\xi b)$, for a flat plate as a function of the frequency ratio $\gamma_\omega = \omega_\alpha/\omega_\xi$ in still air for 4 different combinations of mass ratios $\gamma_m = m_e/(\rho b^2)$ and $\gamma_I = I_e/(\rho b^4)$. The curves are based on damping ratios of 0% (left) and 1% (right), respectively, and it has been assumed that $C_\xi = 1$ and $C_\alpha = 1$.*

aerodynamics. Compared to the flat plate data, truss-stiffened girders normally experience larger flutter velocity reductions than closed box-girder sections.

The critical flutter wind velocity increases as the frequency ratio increases ($\gamma_\omega >$ approximately 1.1). The minimum critical flutter wind velocity is found for frequency ratios γ_ω of approximately 1.1 dependent on structural damping. As the frequency ratio γ_ω approaches unity, the critical flutter wind velocity approaches infinity, see Figure 8.16.

The critical flutter wind velocity increases with increasing bridge mass and bridge mass moment of inertia. This is considered thoroughly in Section 8.5.

The influence of damping is only significant for small frequency ratios.

A large frequency ratio of γ_ω may be obtained using closed box girders with significant torsional rigidity, see for instance the Humber Bridge and the Great Belt Bridge. For very long span suspension bridges, the torsional rigidity of the closed box-girder section may, however, become too small. Instead, large critical flutter wind velocities may be obtained using a design in which the torsional and vertical natural frequencies are deliberately made identical. The torsional deck rigidity should be low and the deck-mass distribution should give the same cable stiffness in vertical and torsional vibrations. To the authors' knowledge, this principle has not yet been used in practice in the design of suspension bridges.

The torsional rigidity must not be reduced to a level giving static divergence, see Section 8.1 and Figure 8.17 below comparing static divergence wind velocities with critical flutter wind velocities for a flat plate.

Design criteria

Typically, large bridges have decks that are high above the ground or sea surface, indicating that the design-wind velocities at bridge-deck levels are much higher than the design-wind velocities at lower heights of say 10 m. Furthermore, the low surface roughness of the sea will also tend to give high design-wind velocities for many bridges.

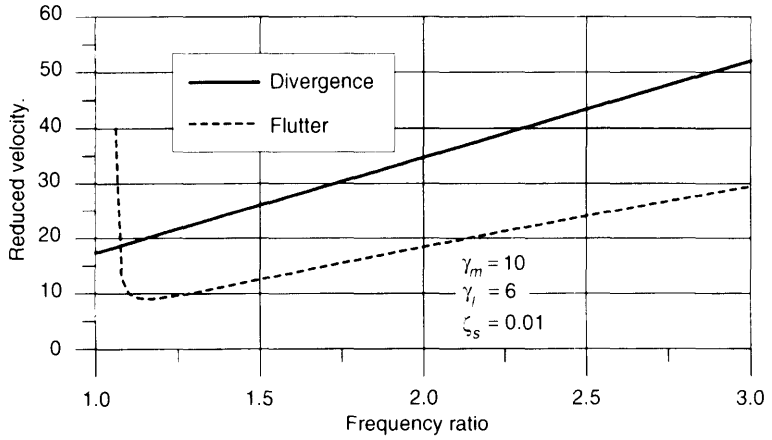

Fig. 8.17 *Reduced divergence wind velocity, $U_{div}/n_\xi b$, and critical flutter wind velocity, $U_c/n_\xi b$, for a flat plate as a function of frequency ratio γ_m in still air. The structural damping ratio is assumed to be 0.01.*

The critical flutter wind velocity calculated should be much larger than the characteristic wind velocity of the site. In most neutral climatic zones, i.e. not typhoon zones, a yearly probability of failure of 10^{-7}, which is often used for long-span bridges, will be obtained for a critical flutter wind velocity approximately 50% larger than the characteristic 10 minute mean velocity at bridge-deck height.

8.5 FLUTTER VIBRATIONS OF SUSPENSION BRIDGES DURING CONSTRUCTION

Suspension bridge flutter vibrations in service have been investigated in many textbooks and papers. The information available on suspension bridges during construction is much sparser. See Brancaleoni (1992), Larsen and Jacobsen (1992) and Jensen and Petersen (1994), however.

Typically, truss-stiffened girders do not display any severe flutter behaviour during construction. The erection of the traffic decks, which give the bridge cross section the flutter sensitive shape, may be postponed until the bridge is sufficiently stiff to prevent any flutter vibrations.

Of course, this construction principle is not possible for closed box girders using prefabricated girder sections. Neighbouring box-girder sections are only hinged by preliminary welds during construction because the bridge geometry continuously changes as the main cable curve changes. The lack of the bridge deck's torsional rigidity and the fact that the bridge deck lacks continuity from pylon to pylon, means that the critical flutter wind velocity during construction is normally much lower than that of the completed bridge, see Figure 8.23.

Some important and interesting aspects of bridge-flutter calculations relate to suspension bridges at the beginning of the construction stage. It is, for instance, very important to distinguish between actual masses and modal masses when calculating realistic flutter wind velocities. The presentation given below, therefore, concentrates on these aspects.

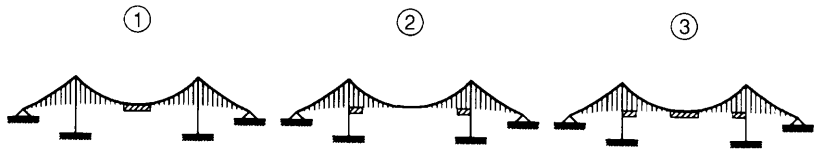

Fig. 8.18 *Three different erection-sequence strategies for suspension bridges.*

Erection sequence strategies

Different erection sequences may be used, see Figure 8.18:

1. Starting from midspan. This strategy, which is most commonly used in practice, relies on the increase in torsional rigidity originating from the increased cable stiffness during construction. The minimum critical flutter wind velocity is obtained at the beginning of the construction stage in a coupled vibration of the symmetrical vertical and torsional modes. In these symmetrical modal vibrations of the relatively short deck lengths erected, bridge-deck rigidity gives no significant contributions to the total stiffness of the structure, which mainly originates from the cables.
2. Starting from the two pylons simultaneously. This strategy ensures that the torsional bridge-deck rigidity may become active in increasing the bridge flutter wind velocity at the beginning of the construction stage. However, the positive influence of bridge-deck rigidity decreases during the construction stage and critical flutter wind velocities may become lower than the minimum critical flutter velocities obtained using the first erection sequence strategy that starts from midspan.
3. Starting from the two pylons and at midspan simultaneously. This strategy combines the positive effects of starting from midspan and starting from the two pylons simultaneously. Furthermore, the increased dead load on the cables close to the pylons will increase the effective stiffness of the main cables for a given midspan deck length erected. This leads to higher torsional frequencies and thereby higher critical flutter wind velocities during construction. One disadvantage is the increased number of bridge-deck lifting positions the contractor must use. Typically, this increases construction costs considerably.

The critical flutter wind velocities obtained during the different erection sequences depend on the actual vertical and torsional natural frequencies obtained, especially frequency separation. Modal masses in the bending and torsional modes are also important.

Kinetic energy connected with cable vibrations should also be considered when selecting the most appropriate erection sequence. The midspan erection sequence may lead to relatively large cable movements during the beginning of the construction period. The energy input from wind load on the small bridge-deck length converts primarily into kinetic energy in the cables. This will have a stabilizing effect on the bridge and will significantly increase critical flutter wind velocities.

The midspan erection sequence (1 above) has been assumed below.

Natural vibrations—midspan erection sequence

Flutter vibrations could occur as a coupling of anti-symmetrical and symmetrical vertical and torsional mode shapes. For anti-symmetrical mode shapes, torsional frequencies are

very high because of the high torsional rigidity of the bridge deck erected. The lowest flutter wind velocities are obtained by combining the lowest symmetrical pure vertical and pure torsional modes. Consequently, only symmetric in-plane cable vibrations are analysed below.

For short deck lengths, the deck mode shapes are close to being constant along the deck erected. Therefore, large deck displacements will not produce any significant stresses in the structure.

Natural vibrations in early erection stages can be determined using a simplified description of the main cable with a distributed load which acts symmetrically on the midspan and represents the mass of the bridge deck.

The basic principles will be explained considering a suspension bridge with the following characteristics:

Main span length:	1500 m
Deck mass:	10 t/m
Deck-mass moment of inertia:	1000 t m^2/m
Main-cable mass:	3 t/m (each cable)
Distance between cable planes:	30 m
Initial cable sag:	150 m

The natural frequencies of the lowest symmetrical pure vertical and pure torsional modes obtained during the early erection stages depend on pylon stiffness. Longitudinal and torsional pylon stiffness are important for both the vertical modes and torsional modes, respectively. The influence of pylon stiffness depends on the actual suspension bridge design, e.g. whether concrete or steel pylons have been chosen. Figure 8.19 shows a typical evolution of natural frequencies obtained during early erection stages, but the actual values should only be considered as a rough guideline for the behaviour of an actual suspension bridge.

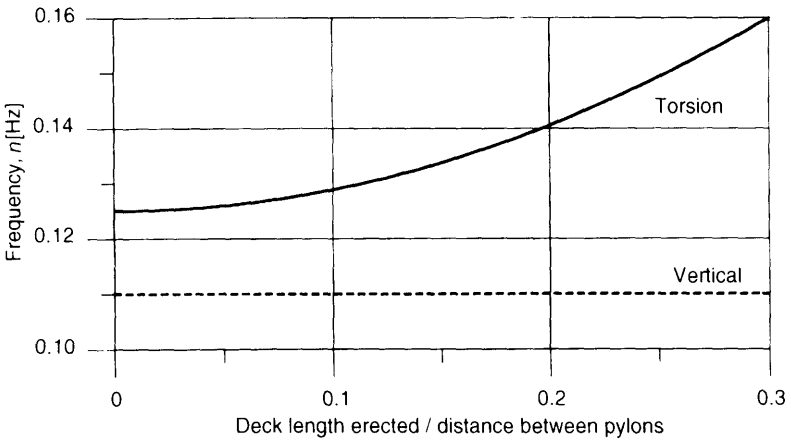

Fig. 8.19 *The natural frequencies as a function of deck length erected. The torsional natural frequency is greater than the vertical natural frequency even when only the cable is in position with no deck erected. This is due to the different influence of pylon stiffness in the two modes considered.*

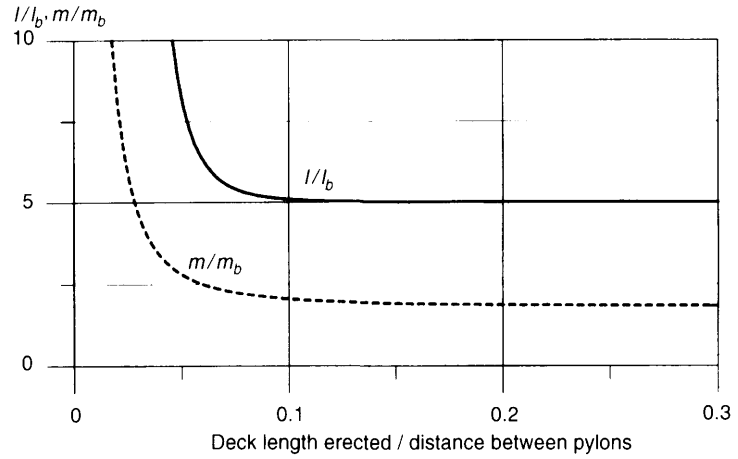

Fig. 8.20 *The solid line shows the ratio between the bridge (cable and deck) modal-mass moment of inertia per unit of deck length erected, I, and the modal-mass moment of inertia per unit of deck length erected, I_b, of the bridge deck alone. The dotted line indicates the equivalent ratio, m/m_b, based on modal masses for vertical bridge vibrations.*

The vertical frequency is seen to be almost unaffected by the deck length erected as cable stiffness increases proportionally to the increase in mass loading. The torsional frequency increases gradually as more deck is erected because torsional mass loading is smaller than the mass loading that gives cable stiffness.

At the very start of deck erection, the vertical and torsional frequencies will be almost equal, provided that the pylon-top flexibility is similar for the two modes considered. This may lead to large critical flutter velocities, as shown in Figure 8.16.

The modal masses during the early erection stages are shown in Figure 8.20. The calculations have been carried out assuming infinitely stiff pylons and the influence of bridge deck stiffness and cable movements in the side spans have been neglected. This simplified approach will often be a good approximation in the early erection stages considered.

In the early erection stages, large cable masses per unit of deck length erected participate in the vibrations, see Figure 8.21. It is obvious that cable masses contribute considerably to the bridge modal mass. This tends to significantly increase the critical flutter wind velocity. However, small frequency separations for short deck lengths erected, see Figure 8.16, will have an opposite effect, i.e. they will decrease the critical flutter wind velocities.

Influence of bridge deck-end effect

For short deck lengths erected at the beginning of the construction sequence, bridge deck-end effects will tend to increase the critical flutter wind velocity. End effects depend on the aspect ratio defined as the deck length erected divided by the width of the bridge deck.

The influence of bridge deck-end effects has been analysed for elliptic wings with aspect ratios of 3 and 6, respectively, see Jones (1939). In a specific example with a streamlined, closed box-girder section, the elliptical wing data were, however, not sufficient to fully explain the end effects measured on a wind-tunnel section model. This might be due

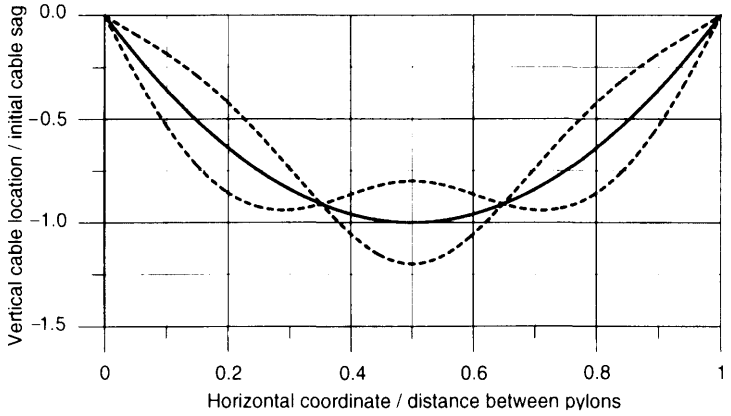

Fig. 8.21 *The vertical cable movements in torsion when 20% of bridge deck is erected. The solid line refers to static cable displacements. The dotted line shows the cable displacements in the symmetrical mode. The lack of deck stiffness assumed in this approach is obvious when considering the cable movements close to midspan. However, the overall cable behaviour is not significantly influenced by this assumption.*

to the actual shape of the wing ends with a gradually decreasing width towards the ends. Since bridge decks have a constant width that gives an abrupt change of cross section, end effects are expected to be more pronounced for bridge decks.

Lift-force coefficient data for airfoils with different aspect ratios also give some indications of the order of magnitude of end effects. According to Von Mises (1945), the end effects on the static lift force can be described by

$$\frac{C_{L,3D}}{C_{L,2D}} = \frac{1}{1 + 2b/l} \tag{8.5.1}$$

in which l is the deck length and b is the deck width. This relation is illustrated in Figure 8.22.

As a first rough estimate critical flutter wind velocities for relatively short deck lengths erected could be calculated by reducing all aerodynamic derivatives according to the reduction of lift-force coefficients shown in Figure 8.22. For a specific streamlined, closed box-girder section, this procedure agreed reasonably with the end effects measured on a wind tunnel section model with an aspect ratio of 8.

In conclusion, bridge deck-end effects will increase the critical flutter wind velocity for suspension bridges during construction. If accurate end-correction effects are called for, wind-tunnel tests simulating the actual geometric configurations of interest should be carried out. The wind-tunnel models used should also simulate the actual bridge modal masses accurately.

Critical flutter velocities—midspan erection sequence

At the beginning of the construction stage, large flutter wind velocities occur because of the significant amount of moving cable mass per unit deck length erected. For short deck lengths erected, the disturbed air flow around bridge deck ends increases the flutter wind velocity even further (see Figure 8.23).

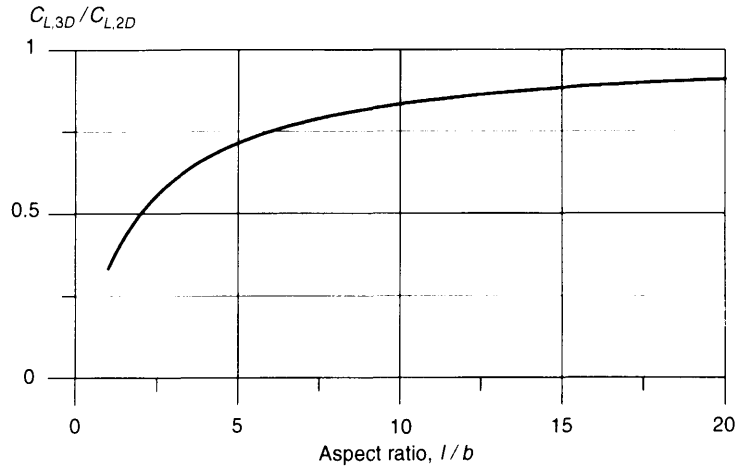

Fig. 8.22 *Shows the lift-force coefficient for airfoils as a function of aspect ratio (Von Mises, 1945). The lift-force coefficients shown have been normalized by the lift-force coefficient obtained for infinite aspect ratio, i.e. two-dimensional flow with no end effects.*

This is a coupled vibration of the lowest symmetrical pure bending and pure torsional bridge mode. For longer deck lengths erected, the critical flutter wind velocity increases during the construction stage. This is due to the increased separation of torsional and vertical natural frequency of the structure erected.

The wind loads on the main cables give significant contributions to aerodynamic damping. Since this is not included in the aerodynamic derivatives describing the wind load on the deck, the structural damping used when estimating critical flutter wind velocities should also include the aerodynamic damping of the cables.

For the suspension bridge example considered, the critical flutter wind velocity is underestimated by approximately 40% using actual masses and no deck-end effects in the early erection stages, when the bridge is most sensitive to flutter vibrations. The influence of using modal masses instead of actual masses is less pronounced when the bridge span is smaller than the 1500 m main span considered here. For longer bridge spans, the importance of choosing modal masses in the calculations will be crucial in order to estimate realistic critical flutter wind velocities.

Provisional measures during construction

If the critical flutter wind velocities during construction do not meet the requirements, different provisional measures may be used to improve bridge stability.

Critical flutter wind velocities during early critical erection stages could be increased using additional masses located symmetrically and outside the two cable planes. Coupled flutter vibrations do not occur when the torsional natural frequency is lower than the vertical natural frequency.

Additional masses located to the windward side of the bridge's centre line can also improve flutter conditions. The principle is to move the bridge mass centre upwind in order to improve the aerodynamic characteristics of the bridge deck. It has been used in practice in connection with the construction of the Humber Bridge (see Brancaleoni,

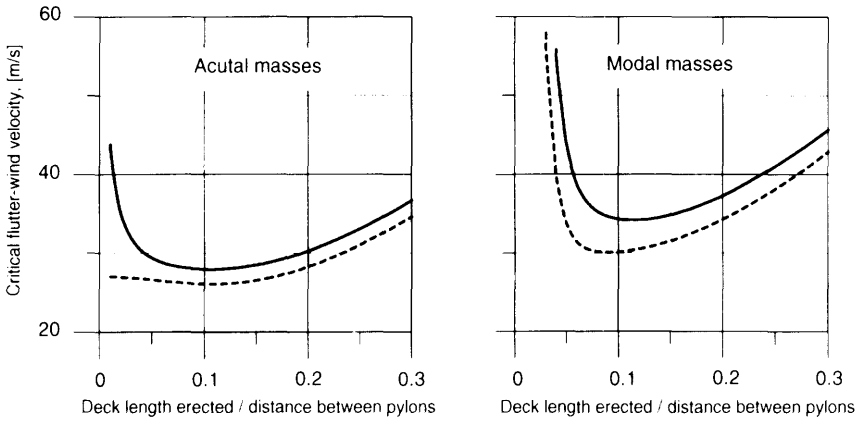

Fig. 8.23 *Critical flutter wind velocity of a box-girder suspension bridge during construction using actual masses and modal masses, respectively, in the calculations. Actual mass corresponds to bridge deck mass plus main cable mass, i.e. 16 t/m in the example considered. The solid lines include deck-end effects which are not taken into account by the dotted lines. Damping ratios to critical of 1% have been assumed in the calculations shown. The lowest critical flutter wind velocities are found when approximately 10% of the deck is erected.*

1992). Water was used to provide the additional mass. If high wind has been forecast, the water on the leeward side of the bridge centre line should be released.

Of course, the safety margin against divergence should also be checked for suspension bridges during construction.

8.6 EUROCODE 1 CLAUSES ON BRIDGES

Eurocode 1 specifies lift-force coefficients which for wide bridge sections should correspond to lift forces on flat plates. For the flat-plate limit, the lift-force coefficient is specified to be ± 0.9 when the wind inclination is $\pm$ 10°. This agrees well with the flat-plate data based on wind tunnel test results given in Section 8.1.

The divergence velocity derived in Section 8.1 is found in Eurocode 1. The influence of plate thickness is also specified in Eurocode 1.

According to Eurocode 1, a bridge will not be prone to flutter vibrations when the lowest torsional natural frequency is larger than 2 times the lowest vertical natural frequency. Eurocode 1 does not indicate whether the natural frequencies are to be calculated in still air or in wind. Independent of the interpretation, the guideline will probably be valid for the bridges covered by Eurocode 1, i.e. highway and railway bridges up to 200 m span and footbridges up to 30 m span. Cable-supported bridges are not covered by Eurocode 1.

Cable-supported bridges with long spans, of say 1–2 km, may be susceptible to flutter-induced vibrations even if the lowest torsional natural frequency is larger than two times the lowest vertical natural frequency, both taken in still air. The reduced critical flutter wind velocity is relatively high, see Figure 8.16, but long suspended spans give low natural frequencies and thereby also low critical flutter wind velocities which may be too small in areas exposed to wind.

9 Galloping

Galloping refers to structural vibrations in a direction almost perpendicular to the wind direction, if these vibrations are mainly due to negative aerodynamic damping.

One possible mechanism is illustrated in Figure 9.1. The total wind load consists of contributions from the time-averaged mean wind load F_q, contributions F_t from turbulence, and contributions F_m from the motion of the structure. These contributions cannot be considered as mutually independent. In particular, the values of F_m are usually significantly influenced by the turbulence, an influence that may be favourable or unfavourable. Figure 9.1 shows that an upwards motion may give rise to such changes in the suctions that the resultant of forces, F_y, perpendicular to the wind velocity in the free field has the same direction as the velocity $\dot{\xi}_{\text{def}}$, of the structure.

The forces are shown in Figure 9.2, with components F_x and F_y. It is convenient to use components F_D in the direction of the relative wind velocity U_r and F_L perpendicular to F_D, where F_D is drag and F_L is lift.

If the influence of turbulence is neglected, then the drag and lift forces are expressed as

$$F_D = \tfrac{1}{2}\rho U_r^2 d C_D \tag{9.1}$$

$$F_L = \tfrac{1}{2}\rho U_r^2 d C_L \tag{9.2}$$

d is the structural width, C_D and C_L are the drag and lift coefficients, respectively. C_D and C_L depend on the geometry of the structure, on the wind direction and generally also on the turbulence of the wind (see Figure 10.6). C_D and C_L can be determined by wind-tunnel tests.

The velocity of the structure implies that the wind direction, relative to the structure, varies. The wind direction is characterized by an angle α shown in Figure 9.2.

Positive values of $\dot{\xi}_{\text{def}}$ correspond to negative values of α, and α is determined by

$$\tan\alpha = -\dot{\xi}_{\text{def}}/U \tag{9.3}$$

It follows from Figure 9.2 that the force F_y is expressed as

$$F_y = F_D \sin\alpha + F_L \cos\alpha \tag{9.4}$$

This force is expressed in terms of the wind velocity U as

$$F_y = \tfrac{1}{2}\rho U^2 d C_y \tag{9.5}$$

C_y is a shape factor, and it follows from Figure 9.2 and from formulas (9.1)–(9.5) that

$$C_y = (C_L + C_D \tan\alpha)\frac{1}{\cos\alpha} \tag{9.6}$$

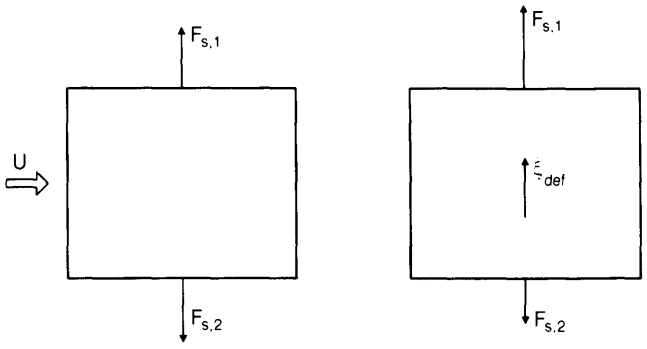

Fig. 9.1 *Cross section of a prismatic structure. On the left, the structure is supposed to be stationary, and if the wind is perpendicular to the left side, then on average, the suctions $F_{s,1}$ and $F_{s,2}$ are equal. On the right, the structure is supposed to vibrate perpendicular to the wind direction positive upwards. Relative to the structure, the wind velocity is the vector sum of the wind velocity U in the free field minus the structural velocity $\dot{\xi}_{def}$. For certain cross-sections and under some circumstances, this may cause $F_{s,1} > F_{s,2}$, which is equivalent to a negative aerodynamic damping.*

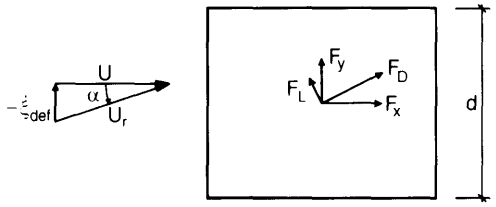

Fig. 9.2 *Cross section of a prismatic structure moving downwards. The arrows indicate positive directions for the wind force on the structure per unit of length. It may be described either by components F_x and F_y along the sides of the prism, or as drag and lift components F_D and F_L parallel to the relative wind velocity and perpendicular to it. The angle α between U and U_r is positive when the structural velocity $\dot{\xi}_{def}$ is negative.*

Referring to the case shown in Figure 9.1 and 9.2, C_L and consequently C_y are 0 if $\alpha = 0$. Then a Taylor's expansion shows that

$$F_y = \tfrac{1}{2}\rho U^2 d \left.\frac{dC_y}{d\alpha}\right|_{\alpha=0} \alpha \tag{9.7}$$

From formulas (9.3) and (9.6)

$$F_y = -\tfrac{1}{2}\rho U \dot{\xi}_{def} d \left.\left(\frac{dC_L}{d\alpha} + C_D\right)\right|_{\alpha=0} \tag{9.8}$$

As an approximation, it is assumed that the structural motions vary along the structure as a mode shape, i.e.

$$\xi_{def} = \xi(z)a(t) \tag{9.9}$$

where $\xi(z)$ is the mode shape function and $a(t)$ is an amplitude function of time t. The differential equation for determining $a(t)$ takes the form

$$a(t)\frac{d^2}{dz^2}\left(EI(z)\frac{d^2\xi(z)}{dz^2}\right) + c\dot{a}(t)\xi(z) + \mu(z)\xi(z)\ddot{a}(t) = F_y \tag{9.10}$$

This equation is multiplied by $\xi(z)$ and integrated over the height h of the structure. Then dividing by $\int_0^h(\xi(z))^2dz$, we arrive at the equation (see Appendix C)

$$m_e(\ddot{a}(t) + 2\zeta_s\omega_e\dot{a}(t) + \omega_e^2 a(t)) = -\tfrac{1}{2}\rho U d\left(\frac{dC_L}{d\alpha} + C_D\right)\Big|_{\alpha=0}\dot{a}(t) \tag{9.11}$$

where m_e is the equivalent mass per unit of length

$$m_e = \int_0^h \mu(z)(\xi(z))^2\,dz \Big/ \int_0^h (\xi(z))^2\,dz \tag{9.12}$$

ω_e is the angular, natural frequency and ζ_s is the damping ratio of structural damping. As the loading term on the right-hand side of equation (9.11) is proportional to $\dot{a}(t)$, it can be combined with the damping term on the left-hand side of equation (9.11) to give an overall damping F_d of

$$F_d = \left(2m_e\zeta_s\omega_e + \tfrac{1}{2}\rho U d\left(\frac{dC_L}{d\alpha} + C_D\right)\Big|_{\alpha=0}\right)\dot{a}(t) \tag{9.13}$$

The second term is the aerodynamic damping. A necessary condition for the occurrence of galloping is that the aerodynamic damping is negative. This leads to the so-called Den Hartog criterion:

$$\left(\frac{dC_L}{d\alpha} + C_D\right)\Big|_{\alpha=0} < 0 \tag{9.14}$$

For galloping to occur, the overall damping must also be negative. It follows from equation (9.13) that this is the case only if the wind velocity U is greater than a critical velocity

$$U_c = -\frac{4m_e\zeta_s\omega_e}{\rho d}\frac{1}{\left(\dfrac{dC_L}{d\alpha} + C_D\right)\Big|_{\alpha=0}} \tag{9.15}$$

The value of $dC_L/d\alpha + C_D$ depends not only on the shape of the cross section but also on the mean wind direction. In November 1972, a pylon for the cable-stayed bridge, Lodemann Brücke, was ruined due to galloping. Later wind-tunnel tests with a model of the hexagonal cross section of the pylon showed that C_D and C_L varied with the wind direction in a way that explained the galloping (see Mahrenholz and Bardowicks, 1979).

It follows from (9.15) that the wind velocity necessary to cause galloping increases with the damping and mass of the structure. Thus galloping is more likely in steel structures than in corresponding concrete structures.

10 Wind-tunnel Testing

Describing the wind flow over a smooth landscape is straightforward. Meteorological observations provide a further basis for estimating the magnitude of the extreme velocities in such winds. However, a theoretical calculation of the wind load on a structure based on this knowledge is very difficult. The fundamental equations that describe the mechanics of air flows are very complicated, and there are many parameters in the boundary conditions for the system of equations. This is particularly true of the boundary conditions that describe the geometry of the structure and its surroundings.

In spite of the evolution of computers, numerical calculations of wind load on structures in turbulent flow will only be obtained accurately in very few cases. Today, to a certain degree the design wind load must be based on measurements. However, the increase in computer power during the decades to come is expected to make numerical calculations of wind load more common in the future.

The most accurate measurements for determining wind loads will be on full-scale structures. However, in order to obtain more general insight we need to study the effects of all the important parameters. As this would be impossible in practice, the most appropriate method for determining wind load is using model tests in a wind tunnel. Full-scale tests are normally only carried out in connection with research projects to verify the methods of simulation that are applied in model tests in the wind tunnel.

The validation of wind-tunnel tests using full-scale measurements has been carried out for several structures during the years. The most comprehensive validation of pressure measurements is probably the many model and full-scale tests carried out on the Texas Tech University experimental building, see e.g. Cochran and Cermak (1992). Tunnel-to-tunnel differences in pressure measurements on low-rise structures have been investigated in the Aylesbury experiment, see Sill *et al.* (1992).

Model tests are used partly for systematic investigations, which form the basis for the rules in different codes, and partly as a tool for determining the wind load on special structures, which are not covered by the codes. For these reasons, the following subsections aim to provide a more in-depth description of model laws and wind-tunnel technique.

Of course, the model laws presented should be followed as closely as possible. However, in most practical situations discrepancies have to be accepted, indicating that the conversion of model-scale results to full-scale predictions should be assessed carefully. The interpretation of model-scale data should focus on the basic physical mechanisms generating the wind load in question.

10.1 MODEL LAWS

A model law describes a condition for model testing and for the interpretation of test results with regard to the prototype.

Formally, model laws are formulated either by introducing a number of crucial non-dimensional parameters, or by considering a system of equations which are known to give a good description of the relevant phenomena. In wind engineering, the number of parameters is so large that it is impossible to satisfy all the conditions simultaneously. Therefore it becomes necessary to disregard parameters that are of minor importance for the actual case in question. In this way a basis is created for formulating different model laws that separately give realistic results within a certain range of validity.

In wind-tunnel tests, models are geometrically similar to the real structures in a predetermined length scale. The wind flow around the model should be similar to the wind around the prototype. This is achieved when the forces acting on a mass of air are modelled in the same mutual ratio as in full scale. These forces are

- inertia forces
- gravitational forces
- viscous forces.

Each of these forces occurs in any flow, but usually their relative importance varies a great deal. The model conditions can only be fulfilled if the three above-mentioned forces are not acting simultaneously. In the mechanics of flows, two model laws are often used:

- Froude's model law, which accounts for inertia and gravitational forces but disregards viscous forces.
- Reynolds' model law, which accounts for inertia and viscous forces but disregards gravitational forces.

In order to achieve realistic results from model tests in a wind tunnel, the flow in the atmospheric boundary layer should be simulated. Chapter 3 describes how the flow in the atmospheric boundary layer is influenced by the roughness of the terrain. If the terrain roughness in the wind tunnel is modelled similarly to the full scale conditions and if Reynolds' law is respected, then the lower part of the atmospheric boundary layer is correctly simulated in the model test. However, as the flow around bodies with sharp edges is almost independent of Reynolds number, see Figure 10.1, terrain roughness is the completely dominating parameter. The demand for correct scaling of terrain roughness was first formulated in the mid 1950s by Martin Jensen, and is now called Martin Jensen's model law. The remaining part of this section deals with the model laws from Froude, Reynolds and Jensen in this order.

It is convenient to introduce a parameter scale λ_p of any parameter p as

$$\lambda_p = p_{\text{model}} / p_{\text{prototype}} \tag{10.1.1}$$

and the first one to be chosen is in most cases the length scale

$$\lambda_l = l_{\text{model}} / l_{\text{prototype}} \tag{10.1.2}$$

In order to scale wind turbulence described by the spectra and co-spectra introduced in Section 3.5, see e.g. equations (3.5.12) and (3.5.26), the scaling of wind velocities is

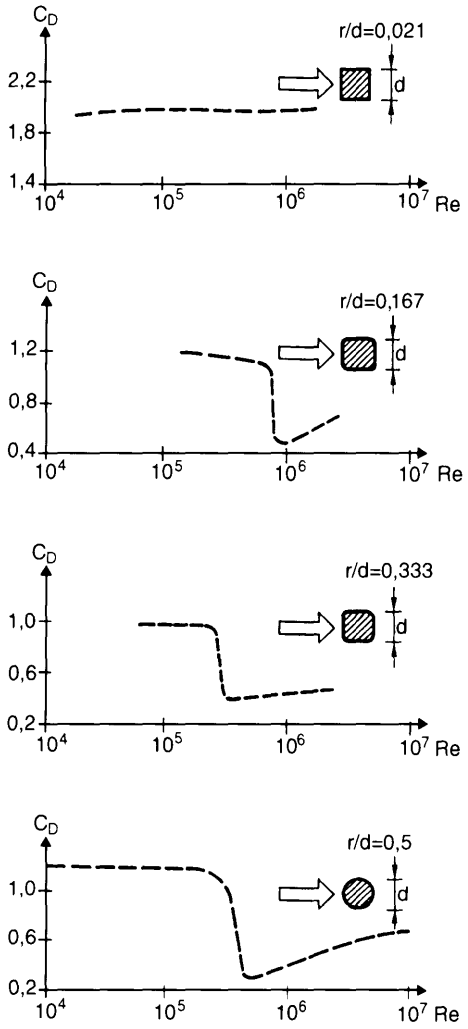

Fig. 10.1 *Dependence of the drag coefficient C_D upon Reynolds number Re and the radius r of curvature at the edges (Scruton and Rogers, 1971).*

expressed by

$$(nl/U)_{\text{model}} = (nl/U)_{\text{prototype}} \tag{10.1.3}$$

in which n is the frequency, l a characteristic length and U the wind velocity. This scaling also follows from the similarity requirement of a model scale Strouhal number equal to the full-scale value.

Equation (10.1.3) gives the time scale λ_T as follows:

$$\lambda_T = 1/\lambda_n = \lambda_l/\lambda_U \tag{10.1.4}$$

Time scale λ_T is inversely proportional to frequency scale λ_n and is given as the ratio between length scale λ_l and wind velocity scale λ_U.

10.1.1 Froude's model law

The Froude number, Fr, is defined as the ratio between the inertia forces of the flow to the gravity forces acting on the structure:

$$Fr = \text{inertia forces of flow/gravity forces on structure} = c(\rho l^3 a)/\rho_s l^3 g \qquad (10.1.5)$$

in which c is a constant, a is the acceleration of the air, l is a characteristic length, g is the acceleration of gravity, ρ is air density and ρ_s is the structure density.

If U is the wind velocity, then the acceleration, a, is proportional to U^2/l, which follows from the dimensions. Since the ratio ρ/ρ_s is assumed to be taken into account in the mass scaling used in the model test, the Froude number may be presented as

$$Fr = U^2/gl \qquad (10.1.6)$$

Froude's model law, which was published in about 1870, neglects the importance of viscous forces.

For aeroelastic structures with the property that wind-induced vibrations are influenced by gravity, it is important to satisfy Froude's model law. This means that the Froude number should be the same for the model as for the prototype. Examples of such structures are transmission lines, suspension bridges, cable-stayed bridges and guy cables for masts.

The Froude number is not significant in relation to wind-induced vibrations of high-rise buildings. The permanent load is gravitational, but is taken directly to the foundations and does not interact with the wind-induced vibrations of the building.

In order to fulfil Froude's model law, the velocity scale λ_U must correspond to the square root of the length scale λ_l

$$\lambda_U = \sqrt{\lambda_l} \qquad (10.1.7)$$

A typical length scale for aeroelastic model studies of suspension bridges and cable-stayed bridges is 1:200. Thus, the wind speed in the tunnel should be about 15 times lower than in full scale, i.e. about 2–3 m/s.

In aeroelastic model studies, the significant natural frequencies should be scaled in accordance with the Froude frequency scaling of $\lambda_n = \lambda_U/\lambda_l = 1/\sqrt{\lambda_l}$. However, since it will be impossible to construct an aeroelastic model satisfying this criterion literally for all natural frequencies of interest, the conversion of model-scale results to full-scale predictions should always be evaluated carefully.

10.1.2 Reynolds' model law

The Reynolds number Re is defined as the ratio between the inertia forces and the viscous forces acting on the flow

$$Re = \text{inertia force/viscous force} = \rho l^3 a/l^2 \tau \qquad (10.1.8)$$

where τ is the shear stress. Reynolds' model law, which was published in 1883, disregards gravitational forces (Reynolds, 1883).

Dimensional methods lead to

$$a \sim U^2/l \qquad (10.1.9)$$

$$\tau \sim \mu \frac{\partial U}{\partial l} \sim \mu U/l \qquad (10.1.10)$$

where μ is the dynamic air viscosity. The kinematic viscosity, ν, is defined as

$$\nu = \mu/\rho \tag{10.1.11}$$

Based on these expressions, the following formulation is generally used for Reynolds number:

$$Re = Ul/\nu \tag{10.1.12}$$

If the viscous forces are decisive for the flow around a structure, Reynolds' model law is important.

Small values of Reynolds number mean that the viscous forces are large compared with the inertia force acting on a mass of air. This indicates that any particle acceleration will soon be damped by viscous forces, and therefore the flow is laminar.

Large Reynolds numbers mean that the viscous forces are small compared with the inertia forces. Therefore, a generated turbulence in the flow is not well damped, and the flow remains turbulent.

The importance of Reynolds number is illustrated by the following description of the flow near the surface of a circular cylinder. Generally, cylinder diameter d is chosen to be the characteristic length, i.e.

$$Re = Ud/\nu \tag{10.1.13}$$

The flow around the cylinder is illustrated in Figure 10.2. The position of the separation points, and thus the width of the vortex street, depends on the Reynolds number. In the literature, e.g. Walshe (1972) and Roshko (1961), the different ranges of Reynolds number are described as:

Subcritical: approx. $300 < Re <$ approx. 10^5	The boundary-layer flow at the cylinder surface is laminar, and the points of separation are about 80° from the point of stagnation. Vortices are shed from alternate sides of the cylinder within a relatively narrow frequency band. Thus, the autospectrum of the lateral load has a characteristic maximum at the predominant frequency of vortex shedding.
Supercritical: approx. $10^5 < Re <$ approx. 3.5×10^6	The points of separation are on the leeward side and the wake has become much narrower. This range gives the transition to the transcritical range. The lateral load is aperiodic and random, and the autospectrum has no characteristic maximum.
Transcritical: approx. $3.5 \times 10^6 < Re$	The boundary-layer flow at the cylinder surface is turbulent, and the points of separation are about 115° from the point of stagnation. The wake is narrower than in the subcritical range but wider than in the supercritical range. Vortices are shed from alternate sides of the structure within a relatively narrow frequency band, thus resembling the subcritical range.

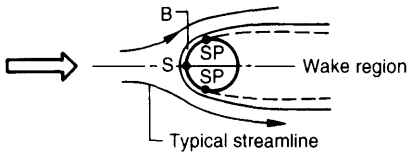

Fig. 10.2 *Flow around a circular cylinder. S: stagnation point; SP: separation point; B: boundary layer at the surface. (Reproduced by permission of Danish Building Research Institute).*

The value of the critical Reynolds number, i.e. the limit between the subcritical range and the supercritical range, depends both on the free-stream turbulence in the natural wind and on the surface roughness of the structure.

The description presented here explains that the drag coefficient, C_D, depends on the Reynolds number, see Figure 10.1. The conditions for the circular cross section are compared with a prismatic body with sharp or rounded edges. C_D is independent of the Reynolds number if the edges are sharp, but strongly dependent even if the edges are only slightly rounded.

For prismatic structures with sharp edges, the points of separation are at the edges, which explains that C_D is independent of *Re*. On curved surfaces the separation points are strongly dependent on Reynolds number, so the flow around the structure as a whole varies with *Re*.

Consequently, the wind load on structures with curved surfaces depends upon the Reynolds number, and Reynolds' model law is relevant for wind-tunnel tests with such structures.

Usually, atmospheric pressure exists in a boundary-layer wind tunnel, and the kinematic viscosity, ν, has the same value in the model test as in full scale. In order to obtain the same value of *Re* in the model test as in full scale, the velocity scale should be the reciprocal of the length scale, i.e.

$$\lambda_U = 1/\lambda_l \tag{10.1.14}$$

Even for a rather large length scale such as $\lambda_l = 1{:}100$ this leads to a velocity of some kilometres per second, which is out of the question. Normally, we have to accept that Reynolds' model law cannot be fulfilled in a boundary layer wind tunnel. When testing structures with curved surfaces, scale effects must be accepted and their importance should be estimated.

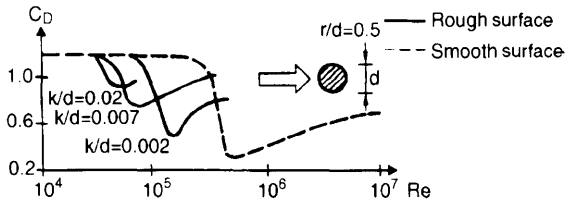

Fig. 10.3 *The dependence of drag coefficient C_D of a cyclinder upon Reynolds number Re and surface roughness characterized by the grain size, k (Scruton and Rogers, 1971).*

When simulating flow features corresponding to high Reynolds numbers a frequently applied measure is to make the curved surfaces rough, as this creates a turbulent boundary layer along the surface. The importance of surface roughness for the drag coefficient of the cylinder is shown in Figure 10.3.

It should be emphasized that although the roughness at best may reduce the scale effects, it cannot eliminate them.

10.1.3 Jensen's model law

Martin Jensen formulated the condition for realistic model tests:

- The flow in the wind tunnel should be turbulent in the same way as the flow in the natural wind.

This demand is fulfilled with good approximation in boundary-layer wind tunnels (see Section 10.2). Typical vortex structures and vortex sizes in natural wind can be represented in a wind tunnel in the same scale as that used for the structure. It is particularly important that vortices controlling the pattern of air flow around the structure are modelled correctly, see the discussion on small-scale turbulence later in this section.

Wind turbulence follows from the roughness of the terrain. If the terrain surrounding the structure is built in the wind tunnel to the same scale as the structure, then Jensen's model law is satisfied. Mathematically this is expressed as

$$\left(\frac{h}{z_0}\right)_{\text{model}} = \left(\frac{h}{z_0}\right)_{\text{prototype}} \tag{10.1.15}$$

where h is the height of the structure and z_0 is the roughness length of the surrounding terrain.

Verifying the fulfillment of the model law in a specific test requires only an experimental determination of the velocity profile — and thus of the roughness length, z_0 — in the wind tunnel. If the model law is fulfilled, the velocity profile in the lower part of the boundary layer, in which the surface roughness is the dominating length scale, will be simulated satisfactorily. Turbulence characteristics of the simulated flow should also be demonstrated.

Although Jensen's model law seems obvious nowadays, it led to a complete break with the common practice when it was put forward (Jensen, 1958). The importance of this law is illustrated in Figure 10.4.

Like other non-dimensional parameters such as Reynolds number and Strouhal number, Jensen number has been introduced as

$$Je = h/z_0 \tag{10.1.16}$$

where h is the height of the structure and z_0 is the roughness length of the surrounding terrain.

When Jensen's model law is satisfied, the turbulent vortex structures and hence the spectra of the natural wind as presented in Section 3.5 will be simulated with reasonable accuracy in the wind tunnel. However, the low-frequency turbulent fluctuations that scale with the boundary layer height will not be represented automatically using Jensen's model law. This dilemma is discussed further below, see the discussions related to Figure 10.7.

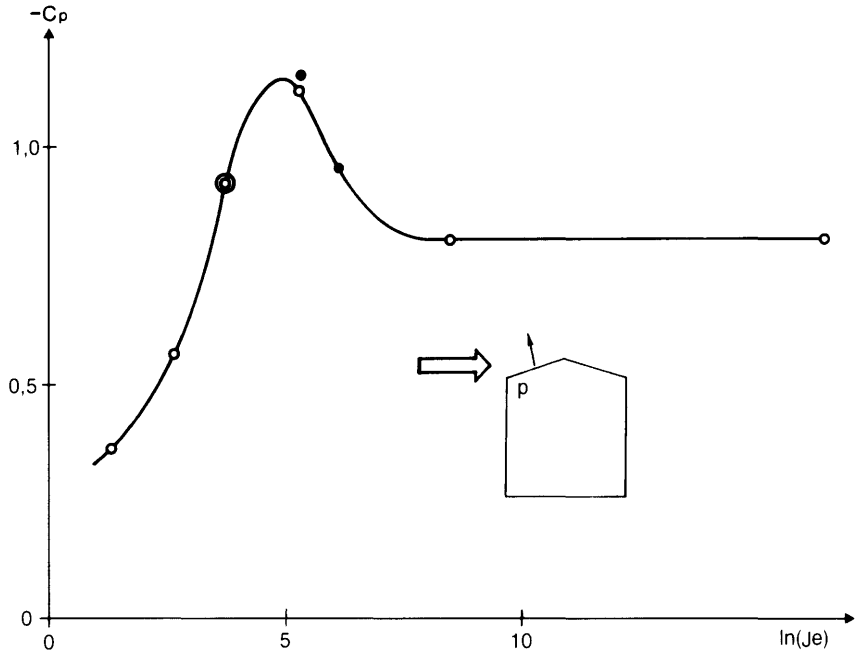

Fig. 10.4 *The pressure coefficient as a function of Jensen number Je defined in equation (10.1.16) (Jensen and Franck, 1965). (Reproduced by permission of N. Franck).*

Small-scale turbulence

The free-stream turbulence controls the pressure fluctuations on the upstream face of a structure. It also determines the shear layer behaviour, see Figure 10.5. The shear layer behaviour is crucial for the flow around the structure and thereby for the mean and fluctuating pressures acting on the structure. Increasing the free-stream turbulence increases the rate of entrainment of wake fluid into the more turbulent shear layers, which in turn changes the pressures acting on the structure. Gartshore (1973) showed that free-stream turbulence affects the drag and lift on rectangular sections, see Figure 10.6.

The shear layer behaviour is mainly determined by the small-scale turbulence components in the free stream, i.e. turbulent components with scales of the order of the shear layer width. Melbourne (1975) introduced the small-scale spectral density parameter, S, as the normalized spectral density of the longitudinal velocity component at a wavelength U/n with an order of magnitude lower than the typical frontal body dimension defined

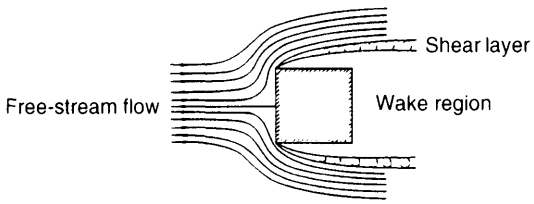

Fig. 10.5 *Time-average pattern of the flow past a square cylinder.*

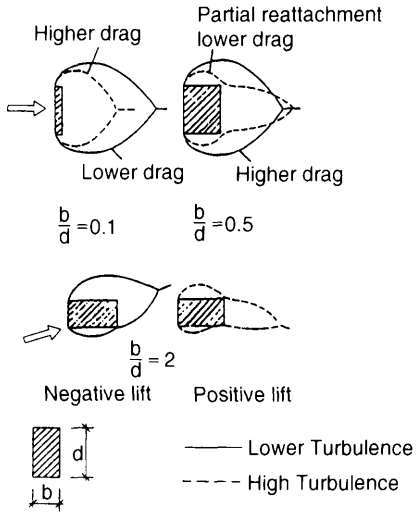

Fig. 10.6 *Increased free-stream turbulence increases the rate of entrainment of wake fluid into the more turbulent shear layer, see Gartshore (1973).*

as the square root of the frontal area A. The spectral density of the longitudinal velocity component is normalized by the mean wind velocity U squared giving a small-scale spectral density parameter defined as

$$S = \frac{nS_u(n)}{U^2} \qquad \frac{U}{n} = 0.1\sqrt{A} \tag{10.1.17}$$

where n is the frequency in hertz. For a surface-mounted prism, whose plan dimension b is smaller than its height h, Tieleman (1995) suggested using the prism width as a typical body dimension for defining the small-scale spectral density parameter. For a low-rise structure with $h < b$, Tieleman suggested using the prism height. These length-scale choices seem logical, when considering the mechanisms that generate shear layers.

Melbourne (1975) showed the dominating role of small-scale turbulence on shear-layer behaviour and on the magnitude of the low pressures under reattaching shear layers. An increase in small-scale turbulence in the approaching air flow increases the magnitude of high negative suction occurring near the leading edge under a reattaching shear layer. The exact role of small-scale turbulence is, however, not clear at present, see the overview given by Melbourne (1995).

Air-flow scaling alternatives

The observations described above should be taken into account when choosing the appropriate scaling for model studies of loads on bluff bodies in turbulent flow. It is most important that the main physical features that generate the load on the structure are simulated in the wind tunnel, and that the generation of wind load at model scale and full scale follows the same basic load mechanism. The actual flow scaling chosen in a specific test should not only be based on the scaling effects on the test results itself, but rather on the accuracy obtained for the test results corrected mathematically for scaling effects.

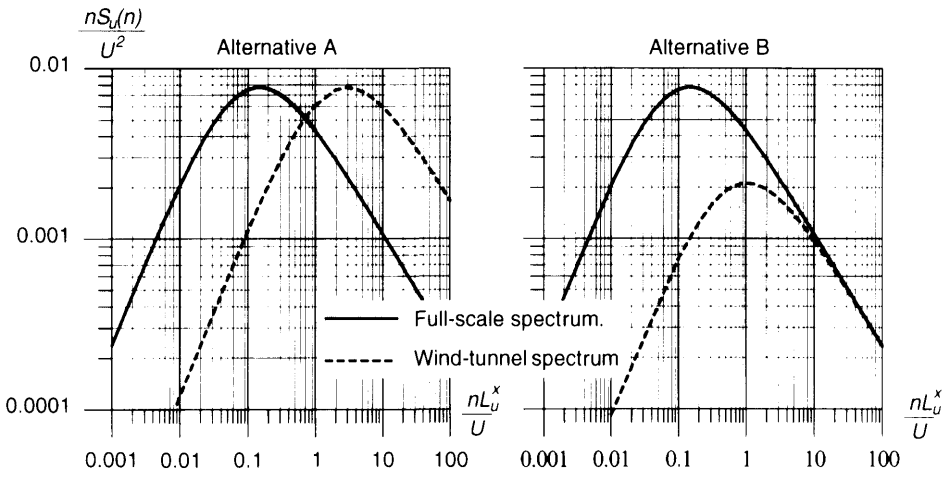

Fig. 10.7 *In the left-hand figure the spectrum of the longitudinal wind velocity component is shifted to the right when compared to the full-scale spectrum. The turbulence intensity is simulated correctly, but the low-frequency fluctuations in the wind tunnel are underestimated, and the small-scale turbulence is overestimated. In the right-hand figure, the turbulence intensity has deliberately been reduced in the wind tunnel in order to obtain the correct scaling of small-scale turbulence and thereby of shear layer behaviour.*

Using model scales larger than flow scales underestimates the low-frequency velocity fluctuations. The small-scale spectral density parameter is then too large, see scaling alternative A in Figure 10.7. This is probably the most common situation in wind-tunnel tests carried out in practice, and it is a natural consequence originating from the restrictions imposed on the flow by the wind tunnel's walls and roof. The effects of the underestimated low-frequency velocity fluctuations and turbulent integral length scales may often be corrected for mathematically. However, the shear layer influence on the load is not represented satisfactorily in the model due to the overestimated small-scale turbulence. Consequently, a mathematical scaling correction of measured data to full-scale conditions will often be difficult or impossible.

Scaling alternative B shown in Figure 10.7 may provide a more accurate full-scale load prediction. The influence of small-scale turbulence is reproduced using this scaling principle with $S_{\text{model}} = S_{\text{prototype}}$, in which the small-scale spectral density parameter, S, is defined in equation (10.1.17). Just as in alternative A described above, the influence of the underestimated low-frequency fluctuations may often be corrected mathematically. Scaling alternative B may, therefore, provide the most accurate load predictions in many situations.

10.2 WIND-TUNNEL TECHNIQUE

Boundary-layer wind tunnels and procedures used in wind-tunnel model studies are described briefly below.

Boundary-layer wind tunnels

Before Martin Jensen's model law was published in the mid 1950s, the wind tunnels used were often aeronautical tunnels with short working sections. They were converted for use in civil engineering applications by adding passive devices, such as grids, in the test section entrance in order to generate turbulence. However, turbulence generated in these tunnels does not meet the basic similarity requirements necessary to obtain realistic test results for structures situated in the atmospheric boundary layer.

Martin Jensen's model law changed wind-tunnel practice fundamentally. Boundary-layer wind tunnels with long working sections have been constructed since the model law was published in the mid 1950s. The long working section, typically of the order of 20–30 m, facilitates a natural grown boundary layer according to the Martin Jensen model law.

One of the first large boundary layer wind tunnels was designed by Professor A.G. Davenport. It was constructed and commissioned in November 1965 at the University of Western Ontario in Canada. Today, boundary-layer wind tunnels have been constructed in most parts of the world. One example is shown in Figure 10.8.

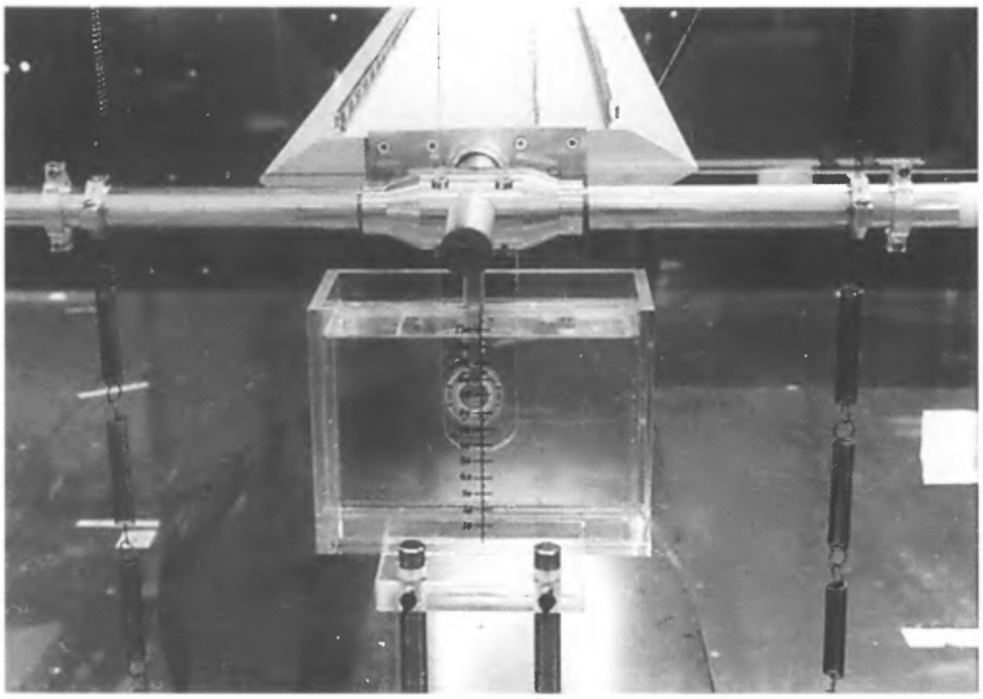

Fig. 10.8 *The boundary-layer wind tunnel at the Norwegian University of Science and Technology. A typical bridge section model suspended by springs is shown in the figure. The springs to the left and right outside the tunnel are used to simulate the stiffness of the bridge modes investigated in the test. The model mass and mass moment of inertia are scaled down from the modal characteristics of the full-scale bridge. The basin with liquid outside the tunnel in the front is used to simulate full-scale structural damping by having a moving part of the wind-tunnel model submerged in the liquid. (Reproduced by permission of Erik Hjorth-Hansen).*

Procedures used in wind-tunnel model studies

Procedures used in wind-tunnel model studies vary widely depending on particular objectives and available resources. However, a number of commonly used tests have emerged, e.g.:

- Topographic model tests used to determine the wind conditions in the flow over complex terrains. Typical scales are of the order of 1:2000 to 1:5000.

  Topographic model tests may be used to assess wind energy potentials of particular sites and to estimate wind velocity distributions along bridges located in a complex terrain. Typically, this type of test is used to connect wind conditions of the site with wind velocities measured full scale at a measuring station.

  Length scales of the order of 1:5000 give very low Reynolds numbers in the wind-tunnel test. The atmospheric boundary layer simulated at these low Reynolds numbers may possess a significant scaling distortion, making the test results obtained difficult to interpret. Sometimes the roughness of the model surface is increased deliberately in order to obtain an improved boundary layer simulation and to avoid a so-called aerodynamically smooth surface in the tests.

- Tests of local pressures using scaled static models with pressure taps. Typical scales are of the order of 1:100 to 1:500.

  Mean and fluctuating pressures are often measured by connecting the pressure taps on the model with pressure transducers using thin vinyl tubing. The distortion of pressure fluctuations caused by the long tubes may be corrected using Fourier transform techniques. Alternatively, tubes giving low distortion up to high frequencies of several hundred hertz may be used in the tests, see e.g. the tubing system developed by Gerstoft and Hansen (1987).

  The fluctuating pressures measured in the wind tunnel are used to calculate the characteristic pressure and suction at each point of the structure.

- Tests of area wind loads using pressure models. Typical scales are of the order of 1:100 to 1:500.

  Simultaneous measurement of several fluctuating pressures facilitate that the fluctuating area wind load can be determined by adding linear combinations of the pressures measured. Each pressure is weighed according to its influence on the actual loading in question. Pressures measured along a simply supported model beam, for instance, could be used to estimate reaction forces and bending moments. The response is estimated by appropriate linear pressure combinations based on the influence functions related to the response considered.

- Direct measurements of overall wind loads. Typical scales are of the order of 1:100 to 1:500.

  The model is fixed to a base balance measuring the overall wind load acting on the model. Some balances measure all six load components, i.e. three forces and three moments, other balances measure only some of the load components.

  Specially designed high-frequency base balances may be used to measure the fluctuating overall wind load on the model without significant distortion from natural model vibrations. The models used in these tests should have a natural frequency in excess of the most significant wind-loading frequencies. Light and stiff models are asked for, e.g. models constructed by foam.

- Section model tests as shown in Figure 10.8. Typical scales are of the order of 1:50 to 1:100. Section model tests are used to determine the aerodynamic data outlined in Chapter 8, see e.g. the aerodynamic derivatives described in Section 8.2.3 and the flutter vibrations analysed in Section 8.4.
- Aeroelastic tests using dynamically scaled models of buildings, bridges etc. Typical scales are of the order of 1:100 to 1:300.

  In aeroelastic tests the model movements should be affine with the movements of the full-scale structure, and the natural frequencies and structural damping should be simulated in the test. The construction of aeroelastic models is often time consuming due the demand of accurate scaling of the many significant modes contributing to the wind-induced structural behaviour.

Thus, a large variety of wind-tunnel test procedures are used to determine wind actions on structures. In a particular situation the best choice of test depends on the type of design data required and the intended use of mathematical models for converting model-scale data to full-scale predictions.

Appendix A Random Variables and Stochastic Processes

Within the field of engineering there are many phenomena which cannot be predicted deterministically either in time or in space. However, if a phenomenon has been measured/recorded on many occasions during sufficiently long intervals of time, then certain statistical properties of the phenomenon can be deduced. Statistical properties may also be based on mathematical modelling of the phenomenon.

The phenomenon itself is then described as a stochastic process, and any measured sample during a time period is called a realization of the stochastic process.

Expected values of the process itself, or combinations of the process at different times or positions, can be derived from measurements or mathematical modelling. If these expected values are time-independent, and if correlations between values at different times only depend on time differences, then the process is called stationary. In wind engineering it is common practice to describe wind velocity as a stationary, stochastic process. The assumption of stationarity is not quite correct, but the errors are not important and the calculations are significantly simplified as a result.

Some of the concepts frequently used with random variables and stochastic processes are defined below.

A.1 ONE RANDOM VARIABLE

In this Appendix, random variables are indicated by capital letters. The probability density function $f_X(x)$ is introduced, corresponding to one random variable X. The meaning of this function follows from the fact that the probability of $x_1 \leqslant X \leqslant x_2$ is given by the expression

$$P\{x_1 \leqslant X \leqslant x_2\} = \int_{x_1}^{x_2} f_X(x)\,dx \tag{A.1.1}$$

where the symbol $P\{\ \}$ means probability.

The concept of probability is defined in such a way that the probability of a certain event is 1, hence

$$\int_{-\infty}^{\infty} f_X(x)\,dx = 1 \tag{A.1.2}$$

Furthermore, as probability is non-negative,

$$f_X(x) \geqslant 0 \text{ for all } x \tag{A.1.3}$$

The notation for the mean value of a random variable X is μ_X or $E\{x\}$ and is determined by

$$\mu_X = \int_{-\infty}^{\infty} x f_X(x)\,dx \tag{A.1.4}$$

The variance σ_X^2 of random variable X is defined as

$$\sigma_X^2 = E\{(X-\mu_X)^2\} = \int_{-\infty}^{\infty} (x-\mu_X)^2 f_X(x)\,dx \tag{A.1.5}$$

By definition, $\sigma_X \geqslant 0$, and σ_X is called the standard deviation of the random variable X. If $\mu_X > 0$, the coefficient of variation V_X can be defined as

$$V_X = \frac{\sigma_X}{\mu_X} \tag{A.1.6}$$

Gaussian distribution

It is often a good approximation to assume that a random variable has a Gaussian distribution, cf. Figure A.1. The probability density function is then given by mean value μ_X and standard deviation σ_X, and is calculated by the formula

$$f_X(x) = \frac{1}{\sqrt{2\pi}\sigma_X} \exp\left(-\frac{1}{2}\left(\frac{x-\mu_X}{\sigma_X}\right)^2\right) \tag{A.1.7}$$

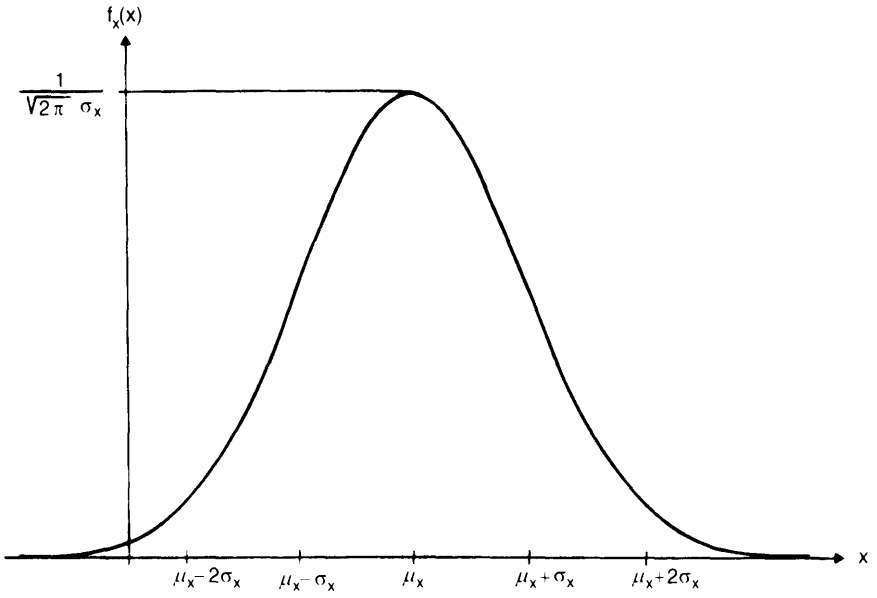

Fig. A.1 *Probability density function for a Gaussian distribution. μ_X may be interpreted as the x coordinate of the centre of gravity of the area between $f_X(x)$ and the X-axis. (Reproduced by permission of Danish Building Research Institute).*

Weibull distribution

The Weibull distribution is also commonly used in wind engineering. With this distribution, random variable X can only take positive values. This distribution is characterized by two parameters—the scale parameter A and the shape parameter C. Both parameters are positive.

The Weibull probability density function $f_X(x)$ is given as

$$f_X(x) = C\frac{x^{C-1}}{A^C}\exp\left(-\left(\frac{x}{A}\right)^C\right) \tag{A.1.8}$$

Using (A.1.4) and (A.1.5), mean value μ_X and variance σ_X^2 are

$$\mu_X = A\Gamma\left(1+\frac{1}{C}\right) \tag{A.1.9}$$

$$\sigma_X^2 = A^2\left(\Gamma\left(1+\frac{2}{C}\right) - \Gamma^2\left(1+\frac{1}{C}\right)\right) \tag{A.1.10}$$

in which the gamma function $\Gamma(x)$ is defined by the integral

$$\Gamma(x) = \int_0^\infty t^{x-1}e^{-t}\,dt \tag{A.1.11}$$

The gamma function is a differentiable function that satisfies the condition

$$\Gamma(x+1) = x\Gamma(x) \tag{A.1.12}$$

For positive integer values n of x, the gamma function satisfies the condition

$$\Gamma(n) = (n-1)! \tag{A.1.13}$$

Another useful value is

$$\Gamma\left(\tfrac{1}{2}\right) = \sqrt{\pi} \tag{A.1.14}$$

If the random variable X is Weibull distributed, then the coefficient of variation V_X, defined by (A.1.6), takes the value

$$V_X = \frac{1}{\Gamma\left(1+\frac{1}{C}\right)}\sqrt{\Gamma\left(1+\frac{2}{C}\right) - \Gamma^2\left(1+\frac{1}{C}\right)} \tag{A.1.15}$$

Note that V_X depends only upon parameter C.

The values in Table A.1 have been calculated for some special values of C:

Table A.1 *The Weibull distribution.*

C	μ_X/A	σ_X^2/A^2	V_X
1/2	2	20	$\sqrt{5}$
1	1	1	1
2	$\sqrt{\pi}/2$	$1-\pi/4$	$\sqrt{(4-\pi)/\pi}$

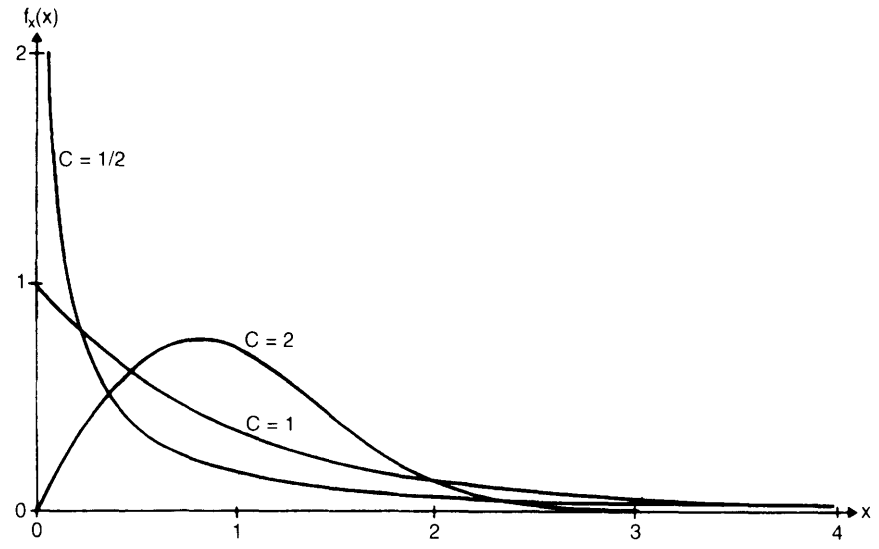

Fig. A.2 *Weibull distributions with $E\{X\} = 1$. (Reproduced by permission of Danish Building Research Institute).*

Expressions (A.1.12) and (A.1.14) are used to calculate μ_X for $C = 2$. Some examples of Weibull distributions are shown in Figure A.2. The Weibull distribution with a shape factor $C = 2$ is called a Rayleigh distribution, and with a shape factor $C = 1$, it is called an exponential distribution.

A.2 TWO RANDOM VARIABLES

The probability density function $f_{XY}(x, y)$ for a combined event of the two random variables X and Y can be defined, and its meaning is derived from

$$P\{x_1 \leqslant X \leqslant x_2 \wedge y_1 \leqslant Y \leqslant y_2\} = \int_{x_1}^{x_2} \int_{y_1}^{y_2} f_{XY}(x, y)\, dy dx \tag{A.2.1}$$

in which the symbol $\wedge$ denotes 'and'. The probability of a certain event is 1, giving

$$\int_{-\infty}^{\infty} \int_{-\infty}^{\infty} f_{XY}(x, y)\, dy dx = 1 \tag{A.2.2}$$

If only one of the random variables, X, is considered, then the probability density function is found to be

$$f_X(x) = \int_{-\infty}^{\infty} f_{XY}(x, y)\, dy \tag{A.2.3}$$

and it follows from (A.2.2) that the condition (A.1.2) has been satisfied.

If random variable Y is known to take a certain value y_0, then the corresponding probability density function for X is called conditional, and

$$\int_{-\infty}^{\infty} f_X(x|Y = y_0)\, dx = 1 \tag{A.2.4}$$

Consequently

$$f_X(x|Y = y_0) = f_{XY}(x, y_0) \Big/ \left(\int_{-\infty}^{\infty} f_{XY}(x, y_0)\, dx \right) \tag{A.2.5}$$

If and only if the random variables X and Y are independent, then

$$f_{XY}(x, y) = f_X(x) f_Y(y) \tag{A.2.6}$$

Gaussian distribution

Gaussian random variables are of particular importance. In this case the combined probability density function is

$$f_{XY}(x, y) = \frac{1}{2\pi\sigma_X\sigma_Y} \frac{1}{\sqrt{1 - \rho_{XY}^2}} \exp(-g_{XY}(x, y)) \tag{A.2.7}$$

in which ρ_{XY} is the correlation coefficient describing the mutual dependence between the two random variables, and $g_{XY}(x, y)$ is defined by

$$g_{XY}(x, y) = \frac{1}{2(1 - \rho_{XY}^2)} \left[\frac{(x - \mu_X)^2}{\sigma_X^2} + \frac{(y - \mu_Y)^2}{\sigma_Y^2} - 2\rho_{XY} \frac{(x - \mu_X)}{\sigma_X} \frac{(y - \mu_Y)}{\sigma_Y} \right] \tag{A.2.8}$$

From (A.2.3) it follows that $f_X(x)$ is given by (A.1.7), meaning that X follows a Gaussian distribution with the mean value μ_X and the standard deviation σ_X.

The correlation coefficient ρ_{XY} is introduced in formula (A.2.7). The value of ρ_{XY} must be between -1 and $+1$, and its importance is most easily explained by the conditional probability density function determined by (A.2.5). The conditional distribution is Gaussian, with a mean value of μ_X^c and a standard deviation of σ_X^c given by

$$\mu_X^c = \mu_X + \rho_{XY} \frac{\sigma_X}{\sigma_Y} (y_0 - \mu_Y) \tag{A.2.9}$$

$$\sigma_X^c = \sigma_X \sqrt{1 - \rho_{XY}^2} \tag{A.2.10}$$

From (A.2.10) it follows that standard deviation σ_X^c takes values of between 0 and σ_X. If $\rho_{XY} = 0$, then $\mu_X^c = \mu_X$ and $\sigma_X^c = \sigma_X$, and the known value of Y has no influence on the value of X. In this special case, X and Y are said to be uncorrelated or statistically independent. If $\rho_{XY} = 1$, then $\sigma_X^c = 0$, and the value of X is uniquely determined by the known value of Y. In this case, X and Y are called fully correlated.

Covariance

In cases where two random variables are involved, it is convenient to define the concept of covariance, Cov$\{X, Y\}$, This is defined as

$$\text{Cov}\{X, Y\} = E\{(X - \mu_X)(Y - \mu_Y)\} \tag{A.2.11}$$

which is calculated as

$$\text{Cov}\{X, Y\} = \int_{-\infty}^{\infty} \int_{-\infty}^{\infty} (x - \mu_X)(y - \mu_Y) f_{XY}(x, y)\, dy dx \tag{A.2.12}$$

and generally the correlation coefficient ρ_{XY} can be defined as

$$\rho_{XY} = \frac{1}{\sigma_X \sigma_Y} \operatorname{Cov}\{X, Y\} \tag{A.2.13}$$

which is in agreement with the introduction of ρ_{XY} in cases where a Gaussian distribution is involved.

A.3 STOCHASTIC PROCESSES

Mean value

For stationary and ergodic processes (which covers the processes included in this book) denoted by $X(t)$, mean value μ_X can be determined as an average during a long time interval T, by the mathematical formulation

$$\mu_X = E\{X(t)\} = \lim_{T \to \infty} \frac{1}{T} \int_{t_1}^{t_1+T} X(t)\, dt \tag{A.3.1}$$

The stationarity implies that μ_X is independent of time. The limit should be interpreted as a need for an integration period of sufficient length.

Variance

The variance σ_X^2 of the process $X(t)$ is defined as

$$\sigma_X^2 = E\{(X(t) - \mu_X)^2\} \tag{A.3.2}$$

At this point, it is useful to review some simple rules about mean values. The mean value of a sum is the sum of the mean values. Let $X(t)$ and $Y(t)$ be stationary processes, then

$$E\{X(t) + Y(t)\} = E\{X(t)\} + E\{Y(t)\} \tag{A.3.3}$$

A constant factor k can be taken outside the expectation symbol:

$$E\{kX(t)\} = kE\{X(t)\} \tag{A.3.4}$$

Applying these rules to the expression (A.3.2) for the variance yields

$$\sigma_X^2 = E\{(X(t))^2\} - \mu_X^2 \tag{A.3.5}$$

Covariance and correlation

Let $X(t)$ and $Y(t)$ be stationary, stochastic processes. The cross-covariance $\kappa_{XY}(\tau)$ is defined by

$$\kappa_{XY}(\tau) = E\{(X(t) - \mu_X)\,(Y(t+\tau) - \mu_Y)\} \tag{A.3.6}$$

Due to stationarity, $\kappa_{XY}(\tau)$ is independent of t. Then we can use $t - \tau$ in place of t, which gives

$$\kappa_{XY}(\tau) = E\{(Y(t) - \mu_Y)\,(X(t-\tau) - \mu_X)\} \tag{A.3.7}$$

since, according to the definition, the last expression equals $\kappa_{YX}(-\tau)$, we have the rule

$$\kappa_{XY}(\tau) = \kappa_{YX}(-\tau) \tag{A.3.8}$$

If $Y(t)$ is the same process as $X(t)$, then (A.3.6) gives

$$\kappa_X(\tau) = E\{(X(t) - \mu_X)(X(t+\tau) - \mu_X)\} \tag{A.3.9}$$

and expression (A.3.8) gives

$$\kappa_X(\tau) = \kappa_X(-\tau) \tag{A.3.10}$$

indicating that the covariance is an even function of time difference τ. Taking $\tau = 0$, a comparison between expressions (A.3.2) and (A.3.9) shows that

$$\sigma_X^2 = \kappa_X(0) \tag{A.3.11}$$

Thus, the variance equals the covariance at a zero time difference. It can be verified that $\kappa_X(\tau)$ satisfies the inequalities:

$$-\kappa_X(0) \leqslant \kappa_X(\tau) \leqslant \kappa_X(0) \tag{A.3.12}$$

The correlation function $\rho_X(\tau)$ is a normalized version of the covariance function

$$\rho_X(\tau) = \frac{\kappa_X(\tau)}{\sigma_X^2} \tag{A.3.13}$$

and from (A.3.11) and (A.3.12) it follows that $-1 \leqslant \rho_X(\tau) \leqslant 1$. In particular, $\rho_X(0) = 1$.

Cross-correlation function $\rho_{XY}(\tau)$ is correspondingly defined by

$$\rho_{XY}(\tau) = \frac{\kappa_{XY}(\tau)}{\sigma_X \sigma_Y} \tag{A.3.14}$$

Derivatives of a stochastic process

Next, $\kappa_X(\tau)$ is assumed to be a differentiable function of τ, and it is further assumed that the stochastic process $X(t)$ can be differentiated with respect to t. The following symbols are introduced

$$\dot{X}(t) = \frac{dX(t)}{dt} \tag{A.3.15}$$

$$\ddot{X}(t) = \frac{d^2X(t)}{dt^2} \tag{A.3.16}$$

Consider the expression

$$X(t_2) - X(t_1) = \int_{t_1}^{t_2} \dot{X}(t)\, dt \tag{A.3.17}$$

The mean value of an integral is the integral of the mean value. As $X(t)$ is stationary, the expected value of the left-hand side of (A.3.17) is zero, from which the following important rule is found:

$$\mu_X = 0 \tag{A.3.18}$$

As the derivative of the mean value is the mean value of the derivative, then from (A.3.9), (A.3.15) and (A.3.18)

$$\frac{d\kappa_X(\tau)}{d\tau} = E\{(X(t) - \mu_X)\dot{X}(t+\tau)\}$$
$$= E\{(X(t) - \mu_X)(\dot{X}(t+\tau) - \mu_{\dot{X}})\} = \kappa_{X\dot{X}}(\tau) \tag{A.3.19}$$

As $\kappa_X(\tau)$ is an even function of τ, its derivative is zero when $\tau = 0$. Then using (A.3.19):

$$\kappa_{X\dot{X}}(0) = 0 \tag{A.3.20}$$

This result shows that simultaneous values of a stationary process $X(t)$ and its derivative $\dot{X}(t)$ are statistically uncorrelated.

In (A.3.19) the stationarity is used to replace t with $t - \tau$

$$\frac{d\kappa_X(\tau)}{d\tau} = E\{(X(t-\tau) - \mu_X)(\dot{X}(t) - \mu_{\dot{X}})\} \tag{A.3.21}$$

and further differentiation and use of (A.3.18) yields

$$\frac{d^2\kappa_X(\tau)}{d\tau^2} = E\{(-\dot{X}(t-\tau))(\dot{X}(t) - \mu_{\dot{X}})\}$$
$$= -E\{(\dot{X}(t) - \mu_{\dot{X}})(\dot{X}(t+\tau) - \mu_{\dot{X}}\} \tag{A.3.22}$$

which gives the rule

$$\frac{d^2\kappa_X(\tau)}{d\tau^2} = -\kappa_{\dot{X}}(\tau) \tag{A.3.23}$$

and especially by taking $\tau = 0$

$$\frac{d^2\kappa_X(\tau)}{d\tau^2}\Big|_{\tau=0} = -\sigma_{\dot{X}}^2 \tag{A.3.24}$$

Spectra

In wind engineering, the one-sided spectrum $S_X(n)$ for process $X(t)$ is defined by the cosine transform

$$S_X(n) = 4\int_0^\infty \kappa_X(\tau)\cos 2\pi n\tau\, d\tau \tag{A.3.25}$$

which only implies positive values of frequency n. It can be proved that the inverse transformation is valid:

$$\kappa_X(\tau) = \int_0^\infty S_X(n)\cos 2\pi n\tau\, dn \tag{A.3.26}$$

If $\tau = 0$ is used in (A.3.26), then according to (A.3.11)

$$\sigma_X^2 = \int_0^\infty S_X(n)\, dn \tag{A.3.27}$$

The autospectrum $S_X(n)$ indicates how the variance is distributed at the frequency axis. It can be proved that $S_X(n) \geqslant 0$ for all values of n.

Equations (A.3.25) and (A.3.26) can be written in complex form (the Fourier transformation)

$$S_X(n) = 2\int_{-\infty}^{\infty} \kappa_X(\tau) e^{-i2\pi n\tau}\, d\tau \tag{A.3.28}$$

$$\kappa_X(\tau) = 1/2\int_{-\infty}^{\infty} S_X(n) e^{i2\pi n\tau}\, dn \tag{A.3.29}$$

where i is the imaginary unit, $i^2 = -1$, and $S_X(n)$ is an even function in the frequency.

The cross-spectrum $S_{XY}(n)$, corresponding to two different processes $X(t)$ and $Y(t)$, is defined by the complex transformation

$$S_{XY}(n) = 2\int_{-\infty}^{\infty} \kappa_{XY}(\tau) e^{-i2\pi n\tau}\, d\tau \tag{A.3.30}$$

with the inverse transformation

$$\kappa_{XY}(\tau) = 1/2\int_{-\infty}^{\infty} S_{XY}(n) e^{i2\pi n\tau}\, dn \tag{A.3.31}$$

In general, the cross-spectrum $S_{XY}(n)$ is complex, whereas the spectrum $S_X(n)$ is real. The cross-spectrum may be written

$$S_{XY}(n) = |S_{XY}(n)| e^{i\Phi_{XY}(n)} \tag{A.3.32}$$

where $|S_{XY}(n)|$ is called the cross-amplitude spectrum and $\Phi_{XY}(n)$ is called the phase spectrum.

In wind engineering, the concept of the coherence spectrum or just coherence is frequently used. Coherence is defined as

$$\mathrm{Coh}_{XY}(n) = \frac{|S_{XY}(n)|^2}{S_X(n) S_Y(n)} \tag{A.3.33}$$

and from (A.3.31) and (A.3.32) it follows that

$$S_{XY}(n) = \sqrt{S_X(n) S_Y(n)}\sqrt{\mathrm{Coh}_{XY}(n)} e^{i\Phi_{XY}(n)} \tag{A.3.34}$$

Coherence is a measure of the correlation between the processes. A comparison of formula (A.3.33) and formula (A.2.13) shows that at each frequency n there is an analogy between the square root of the coherence for stochastic processes and the correlation coefficient for random variables.

Example A.3.1

A stochastic process represented by realizations can be expressed as

$$X(t) = A_1 \sin \omega_1 t + A_2 \cos \omega_1 t$$

where ω_1 is a deterministic angular frequency and A_1 and A_2 are mutually independent random variables with the same probability density function. Let the mean value be

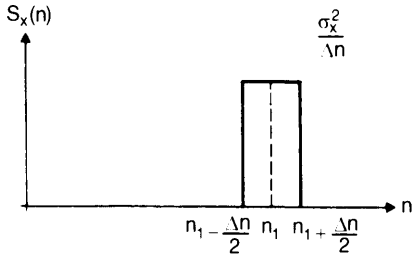

Fig. A.3 *Autospectrum for the process in Example A.3.1. (Reproduced by permission of Danish Building Research Institute).*

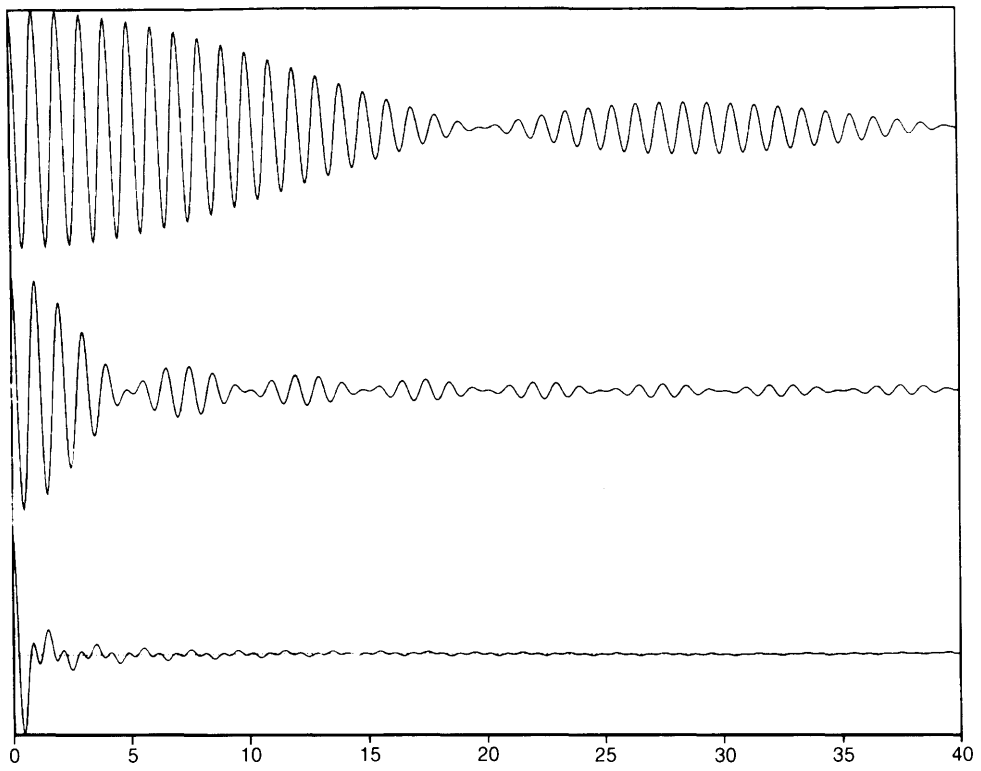

Fig. A.4 *Examples of the autocovariance corresponding to the autospectrum in Figure A.3. The upper figure corresponds to* $\Delta n = n_1/20$, *the middle to* $\Delta n = n_1/4$ *and the lower to* $\Delta n = n_1$. *When* $\Delta n = n_1/20$, *quite high values are found for relatively high values of* $n_1\tau$, *but when* $\Delta n = n_1$, *the autocovariance is only important at relatively small values of* $n_1\tau$.

$\mu_A = 0$ and the variance be σ_A^2. According to (A.3.9) the covariance function is

$$\kappa_X(\tau) = E\{(A_1 \sin \omega_1 t + A_2 \cos \omega_1 t)(A_1 \sin \omega_1 (t+\tau) + A_2 \cos \omega_1 (t+\tau)\}$$
$$= E\{A_1^2\} \sin \omega_1 t \sin \omega_1 (t+\tau) + E\{A_2^2\} \cos \omega_1 t \cos \omega_1 (t+\tau)$$

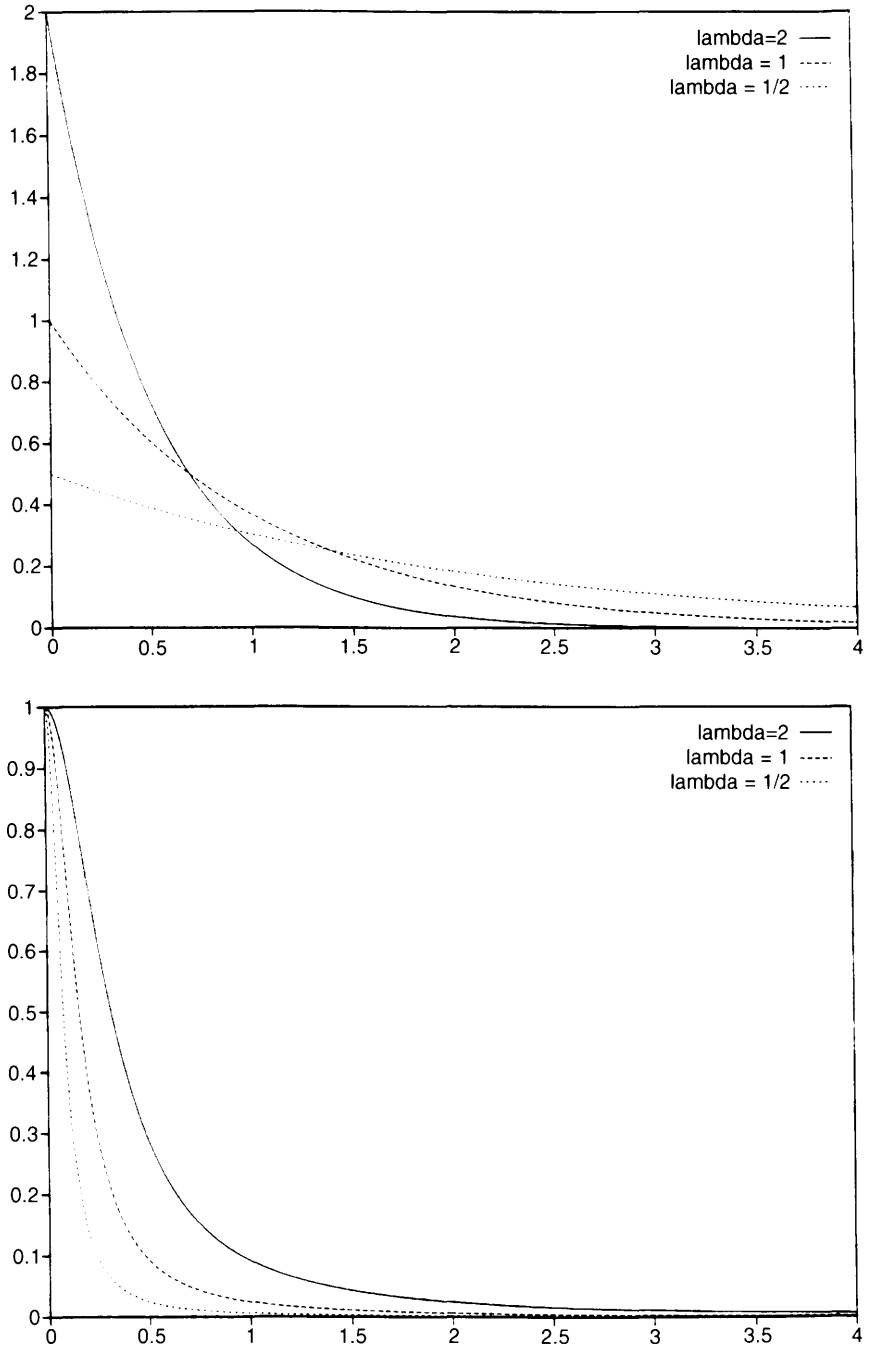

Fig. A.5 *Autospectrum (at the top) and autocovariance (at the bottom) for the variation in Example A.3.2 with* $\sigma_X = 1$. *A steeper decrease of the autospectrum is reflected in a less steep decrease of the autocovariance. (Reproduced by permission of Danish Building Research Institute).*

$$= \sigma_A^2[\sin\omega_1 t \sin\omega_1(t+\tau) + \cos\omega_1 t \cos\omega_1(t+\tau)]$$
$$= \sigma_A^2 \cos\omega_1 \tau$$

since the independence between A_1 and A_2 implies $E\{A_1A_2\} = 0$.

Due to convergence problems, the spectrum cannot be derived using formula (A.3.25).

However, let us start with a spectrum such as that shown in Figure A.3, which is only nonzero in an interval Δn around the central frequency $n_1 = \omega_1/2\pi$. In this interval with the value $S_X(n) = \sigma_X^2/\Delta n$, we can form a picture of the spectrum.

It follows from (A.3.26) that the covariance corresponding to this spectrum is

$$\kappa_X(\tau) = \int_{n_1-\Delta n/2}^{n_1+\Delta n/2} \frac{\sigma_X^2}{\Delta n} \cos 2\pi n\tau \, dn$$
$$= \frac{\sigma_X^2}{\Delta n 2\pi\tau}\left(\sin 2\pi\left(n_1 + \frac{\Delta n}{2}\right)\tau - \sin 2\pi\left(n_1 - \frac{\Delta n}{2}\right)\tau\right)$$
$$= \frac{\sigma_X^2}{\pi\Delta n\tau} \sin\pi\Delta n\tau \cos\omega_1\tau$$

If Δn is close to 0, then $\kappa_X(\tau)$ will be close to $\sigma_X^2 \cos\omega_1\tau$, and thus the spectrum related to this covariance is expressed by means of a Dirac delta function $S_X(n) = \sigma_X^2\delta(n - n_1)$.

Figure A.4 shows some examples of the covariance connected with the spectrum in Figure A.3.

Example A.3.2

With a spectrum

$$S_X(n) = \sigma_X^2 \lambda e^{-\lambda n}$$

where λ is a constant, and equation (A.3.27) is satisfied, the covariance is

$$\kappa_X(\tau) = \int_0^\infty \sigma_X^2 \lambda e^{-\lambda n} \cos 2\pi n\tau \, dn = \sigma_X^2 \frac{\lambda^2}{\lambda^2 + 4\pi^2\tau^2}$$

corresponding to $\lambda = 1/2$, 1 and 2, spectra and covariance functions are shown in Figure A.5.

A.4 THRESHOLD CROSSINGS AND EXTREME VALUES

In relation to phenomena which are described by means of stochastic processes, it is often important to know the probability of the process making an upcrossing of a certain threshold during a specific time interval. In practice, high thresholds with rare events are most important. Figure A.6 shows a realization of a stochastic process. An upcrossing of the threshold ξ at the time t_1 means that $X(t) < \xi$ immediately before and $X(t) > \xi$ immediately after the time t_1.

Let an upward crossing take place between the times t and $t + \Delta t$, where Δt is so small that

$$X(t + \Delta t) \cong X(t) + \dot{X}(t)\Delta t \qquad \text{(A.4.1)}$$

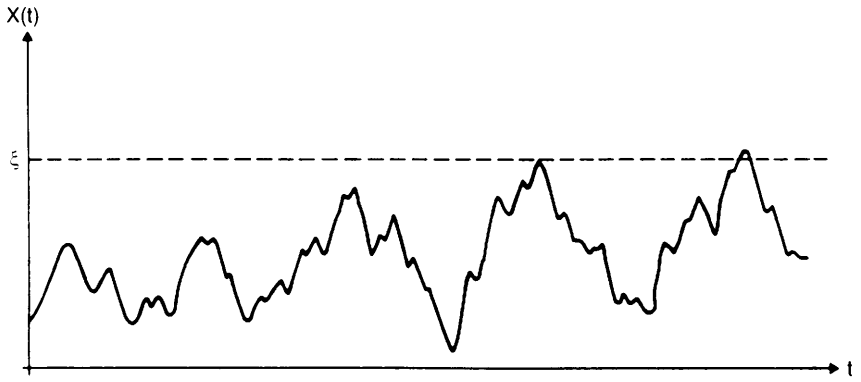

Fig. A.6 *A realization of the stochastic process X(t). (Reproduced by permission of Danish Building Research Institute).*

The expected number of upcrossings of the threshold ξ per unit of time is called ν_ξ. The probability P of an upcrossing during the time interval Δt is given by

$$\nu_\xi \Delta t = P\{X(t) < \xi \text{ and } X(t) + \dot{X}(t)\Delta t > \xi\} \tag{A.4.2}$$

The probability density function for the combined event $X(t)$ and $\dot{X}(t)$ is $f_{X\dot{X}}(x, \dot{x})$, and from (A.4.2) it follows that

$$\nu_\xi = \lim_{\Delta t \to 0} \frac{1}{\Delta t} \int_0^\infty \left(\int_{\xi - \dot{X}(t)\Delta t}^{\xi} f_{X\dot{X}}(x, \dot{x})\, dx \right) d\dot{x} \tag{A.4.3}$$

With the limit $\Delta t \to 0$, the innermost integral becomes

$$\int_{\xi - \dot{X}(t)\Delta t}^{\xi} f_{X\dot{X}}(x, \dot{x})\, dx \cong \dot{X}(t)\Delta t f_{X\dot{X}}(\xi, \dot{x}) \tag{A.4.4}$$

and consequently (A.4.3) is reduced to

$$\nu_\xi = \int_0^\infty \dot{X}(t) f_{X\dot{X}}(\xi, \dot{x})\, d\dot{x} \tag{A.4.5}$$

As X and $\dot{X}$ are taken at the same time, they are statistically independent, and according to (A.2.6):

$$f_{X\dot{X}}(\xi, \dot{x}) = f_X(\xi) f_{\dot{X}}(\dot{x}) \tag{A.4.6}$$

and the formula for ν_ξ becomes

$$\nu_\xi = f_X(\xi) \int_0^\infty \dot{x} f_{\dot{X}}(\dot{x})\, d\dot{x} \tag{A.4.7}$$

For simplicity, let $X(t)$ be a stationary, Gaussian process. Then $\dot{X}(t)$ will also be Gaussian, and according to (A.3.18) with the mean value $\mu_{\dot{X}} = 0$. Then the probability density function for $\dot{X}(t)$ is

$$f_{\dot{X}}(x) = \frac{1}{\sqrt{2\pi}\sigma_{\dot{X}}} \exp\left[\frac{\dot{x}^2}{2\sigma_{\dot{X}}^2} \right] \tag{A.4.8}$$

This is used in (A.4.7) and with the substitution $y = \dot{x}^2/(2\sigma_{\dot{X}}^2)$, ν_ξ is calculated as

$$\nu_\xi = \frac{1}{\sqrt{2\pi}} f_X(\xi)\sigma_{\dot{X}} \tag{A.4.9}$$

Formula (A.4.9) was found by Rice in 1944. If $X(t)$ is not Gaussian, the constant factor $1/\sqrt{2\pi}$ should be replaced by another value in formula (A.4.9).

$\sigma_{\dot{X}}$ can be calculated using the spectrum $S_X(n)$ for $X(t)$. From (A.3.26) and (A.3.23) it follows that

$$\kappa_{\dot{X}}(\tau) = \int_0^\infty 4\pi^2 n^2 S_X(n) \cos 2\pi n\tau \, dn \tag{A.4.10}$$

and from (A.3.11)

$$\sigma_{\dot{X}}^2 = \int_0^\infty 4\pi^2 n^2 S_X(n) \, dn \tag{A.4.11}$$

From the spectrum $S_X(n)$ and the probability density function $f_X(x)$, frequency ν_ξ of upcrossing threshold ξ is determined.

Rare upcrossing events

Next, the problems concerning upcrossings of a threshold are examined more closely. High thresholds with rare upcrossings are assumed.

The following three assumptions are made:

1. The upcrossings are mutually independent.
2. The probability of an upcrossing in the infinitesimal time from t to $t + dt$ is proportional to dt and is independent of t.
3. The probability of more than 1 passage during the differential time dt is infinitely small compared to the probability of 1 upcrossing during dt.

Let $P(r, t_1)$ be the probability of r upcrossings during a time interval t_1. From the assumptions (1) and (3) it follows that

$$P(r, t_1 + dt) = P(r, t_1)P(0, dt) + P(r - 1, t_1)P(1, dt) \tag{A.4.12}$$

and using assumption (2)

$$P(1, dt) = \nu_\xi \, dt \tag{A.4.13}$$

$$P(0, dt) = 1 - \nu_\xi \, dt \tag{A.4.14}$$

These equations are satisfied by the expression

$$P(r, t_1) = \frac{(\nu_\xi t_1)^r}{r!} \exp(-\nu_\xi t_1) \tag{A.4.15}$$

which shows that the upcrossings are described by a Poisson process.

During time interval t_1, one thing is certain, that there will be either 0 or a positive number of upcrossings and as a certain event has the probability 1, the following condition must be fulfilled:

$$\sum_{r=0}^{\infty} P(r, t_1) = 1 \tag{A.4.16}$$

which agrees with the series expansion of the exponential function

$$e^x = \sum_{r=0}^{\infty} \frac{x^r}{r!} \tag{A.4.17}$$

Let $F_X(\xi, t_1)$ denote the probability of $X < \xi$ during time interval t_1. This is the same as the probability of 0 upcrossings of the threshold ξ during t_1, given that $X < \xi$ from the beginning of the time interval.

Exponential distribution

As a specific example, let $X(t)$ be Weibull distributed with shape parameter $C = 1$, also called an exponential distribution. Then by (A.1.8) and Table A.1

$$f_X(\xi) = \frac{1}{\sigma_X} \exp\left(-\frac{\xi}{\sigma_X}\right) \tag{A.4.18}$$

and using (A.4.9)

$$\nu_\xi = \frac{1}{\sqrt{2\pi}} \frac{\sigma_{\dot{X}}}{\sigma_X} \exp\left(-\frac{\xi}{\sigma_X}\right) \tag{A.4.19}$$

From (A.4.15) it follows that the probability of 0 threshold upcrossings is

$$P(0, t_1) = \exp\left(-bt_1 \exp\left(-\frac{\xi}{\sigma_X}\right)\right) \tag{A.4.20}$$

where, for clarity, the abbreviation b is introduced as

$$b = \frac{1}{\sqrt{2\pi}} \frac{\sigma_{\dot{X}}}{\sigma_X} \tag{A.4.21}$$

In deriving formula (A.4.20), the value ξ of the threshold is assumed to be so high that the probability of finding $X(t)$ above the threshold at the start of the time interval is extremely small.

The probability of at least 1 upcrossing during a time interval t is

$$P\{X > \xi, \text{ at least once during } t\} = 1 - P(0, t) \tag{A.4.22}$$

and, corresponding to the specific threshold ξ, a probability density function $f_t(t)$ over time is found by differentiating (A.4.22) with respect to time t

$$f_t(t) = b \exp\left(-\frac{\xi}{\sigma_X}\right) \exp\left(-bt \exp\left(\frac{\xi}{\sigma_X}\right)\right) \tag{A.4.23}$$

The mean time μ_t which must be expected before a threshold upcrossing is given by

$$\mu_t = \int_0^\infty t f_t(t)\, dt \tag{A.4.24}$$

which gives the following reasonable result using formula (A.4.19):

$$\mu_t = \frac{1}{\nu_\xi} \tag{A.4.25}$$

If a threshold is crossed upwards on average once per 50 years, then $\nu_\xi = \frac{1}{50}$ year^{-1}. The corresponding threshold is called ξ_{50}. Analogously, ξ_K is a threshold which is only crossed once per K years on average. Then it is concluded from (A.4.19) and (A.4.21) that

$$\frac{\xi_K}{\xi_{50}} = \frac{\ln(bK)}{\ln(50b)} \tag{A.4.26}$$

As far as wind speeds are concerned, $b \sim 1300$ year^{-1} (Davenport, 1977). Then the 100-year velocity $U_{100} \sim 1.06U_{50}$, where U_{50} is the 50-year velocity.

The probability of crossing the K-year threshold at least once during K years follows from (A.4.19)-(A.4.22)

$$P\{X > \xi_K, \text{ at least once during } K \text{ years}\} = 1 - \frac{1}{e} = 0.63 \tag{A.4.27}$$

and this value does not depend on K.

Appendix B Calculation of Multiple Integrals

In calculating a joint acceptance function, it may be useful to find a quantity A from an integral

$$A = \int_0^1 \int_0^1 g(x_1)g(x_2)\psi(s)\,dx_1 dx_2 \tag{B.1}$$

where the parameter s is

$$s = |x_1 - x_2| \tag{B.2}$$

The following operations are straightforward:

$$\begin{aligned} A &= \int_{x_1=0}^1 \int_{x_2=0}^{x_1} g(x_1)g(x_2)\psi(x_1 - x_2)\,dx_2 dx_1 + \int_{x_1=0}^1 \int_{x_2=x_1}^1 g(x_1)g(x_2)\psi(x_2 - x_1)\,dx_2 dx_1 \\ &= \int_{x_1=0}^1 \int_{s=0}^{x_1} g(x_1)g(x_1 - s)\psi(s)\,ds dx_1 + \int_{x_1=0}^1 \int_{s=0}^{1-x_1} g(x_1)g(x_1 + s)\psi(s)\,ds dx_1 \\ &= \int_{s=0}^1 \int_{x_1=s}^1 g(x_1)g(x_1 - s)\psi(s)\,dx_1 ds + \int_{s=0}^1 \int_{x_1=0}^{1-s} g(x_1)g(x_1 + s)\psi(s)\,dx_1 ds \end{aligned}$$

Thus, an influence function $k(s)$ may be introduced (see Dyrbye and Hansen, 1988), so

$$A = \int_0^1 k(s)\psi(s)\,ds \tag{B.3}$$

$$k(s) = \int_{x_1=s}^1 g(x_1)g(x_1 - s)\,dx_1 + \int_{x_1=0}^{1-s} g(x_1)g(x_1 + s)\,dx_1 \tag{B.4}$$

In the first integral in (B.4), substitute $x_1 = x + s$, and in the second integral, substitute $x_1 = x$, from which

$$k(s) = 2\int_0^{1-s} g(x)g(x + s)\,dx \tag{B.5}$$

We recommend using (B.3) and (B.5) to calculate the integral given by (B.1).

Joint acceptance functions depend on a parameter ϕ, and are found from (B.3) using

$$\psi(s) = \exp(-\phi s) \tag{B.6}$$

Some special cases are shown in Table B.1; and values of A_j and B_{jp} are shown in Table B.2. Some of the cases are illustrated in Figure B.1.

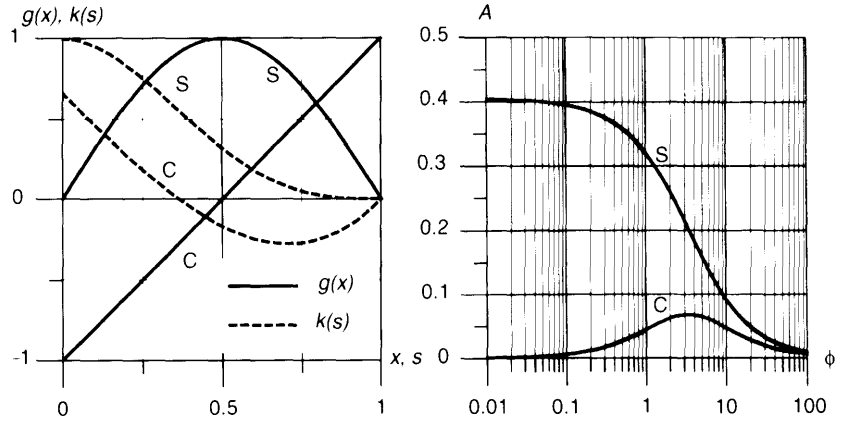

Fig. B.1 *The left-hand figure shows influence functions k for a sinusoidal (S) and a cantilever (C) distribution function g. The right-hand figure shows the corresponding integrals A from formulae (B.3) and (B.6).*

Table B.1 *Influence functions and the integral from formula (B.1) for different distribution functions g. Parameter ϕ is determined in the main text.*

Response influence function $g(x)$	Normalized co-spectrum influence function $k(s)$	A from formulae (B.3) and (B.6)
Uniform: $g = 1$	$2(1-s)$	$\frac{2}{\phi^2}(\phi - 1 + e^{-\phi})$
Linear: $g(x) = x$	$\frac{1}{3}(2 - 3s + s^3)$	$\frac{2}{3\phi} - \frac{1}{\phi^2} + \frac{2}{\phi^4} - e^{-\phi}\left(\frac{2}{\phi^3} + \frac{2}{\phi^4}\right)$
$g(x) = x^j$	$\frac{1}{A_j}(1-s)^{j+1}\sum_{p=0}^{j} B_{jp}s^p$	
Cantilever:		
$g(x) = 2x - 1$	$\frac{2}{3}(1 - 3s + 2s^3)$	$\frac{2}{3\phi} - \frac{2}{\phi^2} + \frac{8}{\phi^4}$ $-e^{-\phi}\left(\frac{2}{\phi^2} + \frac{8}{\phi^3} + \frac{8}{\phi^4}\right)$
Sinusoidal:		
$g(x) = \sin(\pi x)$	$(1-s)\cos(\pi s) + \frac{1}{\pi}\sin(\pi s)$	$\frac{1}{\pi^2+\phi^2}\left(\phi + \frac{2\pi^2}{\pi^2+\phi^2}(1+e^{-\phi})\right)$

Table B.2 *Constants A_j and B_{jp}, cf. Table B.1.*

j	A_j	B_{j0}	B_{j1}	B_{j2}	B_{j3}	B_{j4}
0	1	2				
1	3	2	1			
2	15	6	3	1		
3	70	20	10	4	1	
4	315	70	35	15	5	1

Another important problem concerns the determination of quadruple integral

$$B = \int_0^1 \int_0^1 \int_0^1 \int_0^1 g(y_1, z_1)g(y_2, z_2)\psi(|y_1 - y_2|, |z_1 - z_2|)\, dy_1 dy_2 dz_1 dz_2 \tag{B.7}$$

Using a procedure similar to that which was used for the double integral leads to the more convenient form

$$B = \int_0^1 \int_0^1 k(s_y, s_z)\psi(s_y, s_z)\, ds_y ds_z \tag{B.8}$$

in which

$$s_y = |y_1 - y_2| \tag{B.9}$$

$$s_z = |z_1 - z_2| \tag{B.10}$$

and the influence function $k(s_y, s_z)$ is

$$k(s_y, s_z) = 2\int_0^{1-s_y} \int_0^{1-s_z} (g(y, z)g(y + s_y, z + s_z) + g(y, z + s_z)g(y + s_y, z))\, dy dz \tag{B.11}$$

If, as a special case, function g(y,z) is given as

$$g(y, z) = g_y(y)g_z(z) \tag{B.12}$$

then influence function $k(s_y, s_z)$ is likewise

$$k(s_y, s_z) = k_y(s_y)k_z(s_z) \tag{B.13}$$

in which

$$k_y(s_y) = 2\int_0^{1-s_y} g_y(y)g_y(y + s_y)\, dy \tag{B.14}$$

and

$$k_z(s_z) = 2\int_0^{1-s_z} g_z(z)g_z(z + s_z)\, dz \tag{B.15}$$

Appendix C Vibrations of Linear Structures

C.1 ORTHOGONALITY OF MODE SHAPES

In the book, several applications of modal analysis are made. Modal analysis is based on the fundamental theorem of orthogonality. The theorem holds true for any kind of linear structure, but here it is only shown for beams.

We introduce the notation $y(x, t)$ for the lateral deflection of the beam at position x at time t. If damping is neglected, free vibrations may correspond to a motion

$$y(x, t) = \xi_j(x) \cos \omega_j t \tag{C.1.1}$$

ω_j is called a natural, circular frequency and $\xi_j(x)$ is the corresponding mode shape function. The motions are only possible at certain values of ω_j; they are numbered such that $\omega_1 < \omega_2 < \omega_3 < \ldots$ Mode shape $\xi_1(x)$ is as simple as possible, i.e. it has the least possible number of nodal points.

The accelerations are given by

$$\ddot{y} = \frac{\partial^2 y}{\partial t^2} = -\omega_j^2 \xi_j(x) \cos \omega_j t \tag{C.1.2}$$

At times when $\omega_j t$ is a multiple of 2π, the structure has zero velocity but is deflected in the mode shape $\xi_j(x)$. The accelerations are

$$\ddot{y} = -\omega_j^2 \xi_j(x) \tag{C.1.3}$$

and therefore the mass of the beam is acted upon by forces

$$m(x)\ddot{y} = -\omega_j^2 m(x) \xi_j(x) \tag{C.1.4}$$

This means that the mass will act upon the beam with forces of the same magnitude but opposite direction, therefore mode shape function $\xi_j(x)$ is the deflection corresponding to static loading

$$p_j(x) = \omega_j^2 m(x) \xi_j(x) \tag{C.1.5}$$

Correspondingly, the k mode shape function $\xi_k(x)$ is the deflection corresponding to a loading

$$p_k(x) = \omega_k^2 m(x) \xi_k(x) \tag{C.1.6}$$

Let us slowly, i.e. without any vibrations, load the structure first with $p_j(x)$ and then with $p_k(x)$. When the loads are increased from 0 to $p_j(x)$, the deflections increase from 0 to

$\xi_j(x)$, and the work done is

$$W_{jj} = \tfrac{1}{2}\int_0^L p_j(x)\xi_j(x)\,dx \tag{C.1.7}$$

where L is the total length of the beam.

Then, the load $p_k(x)$ is placed slowly, thus increasing the deflections with $\xi_k(x)$. The work done by the load $p_j(x)$ is

$$W_{jk} = \int_0^L p_j(x)\xi_k(x)\,dx \tag{C.1.8}$$

and the work done by the load $p_k(x)$ is

$$W_{kk} = \tfrac{1}{2}\int_0^L p_k(x)\xi_k(x)\,dx \tag{C.1.9}$$

The total work done by the load is

$$W_{\text{tot}} = W_{jj} + W_{jk} + W_{kk} \tag{C.1.10}$$

If the structure had been loaded in the opposite order, we would have found the total work as

$$W_{\text{tot}} = W_{kk} + W_{kj} + W_{jj} \tag{C.1.11}$$

where W_{kj} is the work done by the loading $p_k(x)$ as the deflections $\xi_j(x)$ from the loading $p_j(x)$ are applied,

$$W_{kj} = \int_0^L p_k(x)\xi_j(x)\,dx \tag{C.1.12}$$

Since the structure is assumed to be linear, the total work is independent of the order in which the loading is applied. Therefore, W_{jk} and W_{kj} are equal, which leads to

$$\int_0^L \omega_j^2 m(x)\xi_j(x)\xi_k(x)\,dx = \int_0^L \omega_k^2 m(x)\xi_k(x)\xi_j(x)\,dx \tag{C.1.13}$$

and if $\omega_j \neq \omega_k$, this is only fulfilled if

$$\int_0^L m(x)\xi_j(x)\xi_k(x)\,dx = 0 \qquad j \neq k \tag{C.1.14}$$

This is the condition of orthogonality of the mode shape functions with respect to the mass distribution. This condition is frequently used, and it forms the basis of modal analysis.

The mode shapes are not unambiguously determined, because if $\xi_j(x)$ is a mode shape, then $\xi_j(x)$ multiplied by any constant is likewise a possible representation of the deflections in mode number j. Usually, a principle is used. This may be a maximum value taken as 1 or a motion at a certain point taken as 1.

The modal mass m_j corresponding to mode no. j is defined as

$$m_j = \int_0^L m(x)(\xi_j(x))^2\,dx \tag{C.1.15}$$

so it depends upon the choice of the factor mentioned above.

C.2 EQUATION OF MOTION

If an elastic beam is slender, then the deflections are usually determined by the effects of bending alone. The differential equation is

$$\frac{d^2}{dx^2}\left[EI(x)\frac{d^2y}{dx^2}\right] = p(x) \tag{C.2.1}$$

where $EI(x)$ is the bending stiffness, y is the deflection and $p(x)$ is the loading. In the case of dynamic actions, a part of the loading may be thought of as used for accelerations, and (C.2.1) is changed to

$$\frac{\partial^2}{\partial x^2}\left[EI(x)\frac{\partial^2 y}{\partial x^2}\right] = p(x,t) - m(x)\ddot{y} \tag{C.2.2}$$

usually written as

$$\frac{\partial^2}{\partial x^2}\left[EI(x)\frac{\partial^2 y}{\partial x^2}\right] + m(x)\ddot{y} = p(x,t) \tag{C.2.3}$$

In the case of free vibrations, $p(x,t) \equiv 0$ and y follows from (C.1.1), hence

$$\frac{d^2}{dx^2}\left[EI(x)\frac{d^2\xi_j(x)}{dx^2}\right] = \omega_j^2 m(x)\xi_j(x) \tag{C.2.4}$$

C.3 RESPONSE TO EXTERNAL LOADING

Let a beam be subjected to a loading $p(x,t)$. The symbols indicate that the loading may vary both in space and time. The response $y(x,t)$ to the loading will also vary in time, and may be written as a sum of the contributions from the different modes:

$$y(x,t) = \sum_{j=1}^{\infty} \xi_j(x) f_j(t) \tag{C.3.1}$$

This expression is inserted into (C.2.3) and if we use (C.2.4) we reach

$$\sum_{j=1}^{\infty} (\ddot{f}_j(t) + \omega_j^2 f_j(t)) m(x)\xi_j(x) = p(x,t) \tag{C.3.2}$$

This equation is multiplied by the ith mode shape function $\xi_i(x)$ and integrated over length L. Then from (C.1.14) and (C.1.15)

$$\ddot{f}_i(t) + \omega_i^2 f_i(t) = \frac{1}{m_i} p_i(t) \tag{C.3.4}$$

where the generalized mass m_i and the generalized load $p_i(t)$ follows as

$$m_i = \int_0^L m(x)(\xi_i(x))^2\, dx \tag{C.3.5}$$

$$p_i(t) = \int_0^L \xi_i(x) p(x,t)\, dx \tag{C.3.6}$$

In the derivation, damping has been neglected. It would often be chosen to include viscous damping, thereby changing (C.3.4) to

$$\ddot{f}_i(t) + 2\zeta_i\omega_i\dot{f}_i(t) + \omega_i^2 f_i(t) = \frac{1}{m_i}p_i(t) \tag{C.3.7}$$

where ζ_i is the damping ratio in mode no. i. The solution of (C.3.7) may be written

$$f_i(t) = \int_{-\infty}^{t} p_i(\tau)h_i(t-\tau)\,d\tau \tag{C.3.8}$$

where

$$h_i(s) = \frac{1}{m_i\alpha_i}e^{-\zeta_i\omega_i s}\sin\alpha_i s \tag{C.3.9}$$

and

$$\alpha_i = \omega_i\sqrt{1-\zeta_i^2} \tag{C.3.10}$$

If the load varies harmonically in time, then the generalized load $p_i(t)$ also has a harmonic variation, and may be expressed

$$p_i(t) = a_i\cos\omega t \tag{C.3.11}$$

The time function $f_i(t)$ varies harmonically as well, but due to the damping it is not in phase with the loading. It is

$$f_i(t) = b_i\cos(\omega t - \theta_i) \tag{C.3.12}$$

where b_i is the amplitude and θ_i is a phase angle. It follows from (C.3.7) that

$$b_i = |H_i(\omega)|a_i \tag{C.3.13}$$

in which $H_i(\omega)$ is the frequency response function. It can be proved that $H_i(\omega)$ is the Fourier transform of the impulse response function $h_i(s)$. It can also be shown that

$$|H_i(\omega)|^2 = \frac{1}{m_i^2}\frac{1}{(\omega_i^2-\omega^2)^2+4\zeta_i^2\omega_i^2\omega^2} = \frac{1}{k^2}\frac{1}{(1-\Omega_i^2)^2+4\zeta_i^2\Omega_i^2} \tag{C.3.14}$$

in which $\Omega_i = \omega/\omega_i$ and $k = m_i\omega_i^2$.

Calculating the variance of a response often leads to an integral of the type

$$I = \int_0^\infty |H_i(n)|^2 F(n)\,dn \tag{C.3.15}$$

where frequency $n = \omega/2\pi$ is used.

If the following conditions are met:

- the damping is low meaning $\zeta_i \ll 1$,
- $F(n)$ has most of its values at frequencies below n_i,

then I may be approximated as

$$I \cong |H_i(0)|^2\int_0^\infty F(n)\,dn + F(n_i)\int_0^\infty |H_i(n)|^2\,dn \tag{C.3.16}$$

The last integral is found by contour integration, and

$$\int_0^\infty |H_i(n)|^2 \, dn = \frac{1}{m_i^2} \frac{n_i}{(2\pi n_i)^4} \frac{\pi}{4\zeta_i} = \frac{1}{m_i^2} \frac{n_i}{(2\pi n_i)^4} \frac{\pi^2}{2\delta_i} \tag{C.3.17}$$

For small damping ratios, i.e. $\zeta_i \ll 1$, the logarithmic decrement is

$$\delta_i = 2\pi\zeta_i. \tag{C.3.18}$$

Appendix D Solving Flutter Equations

Reference is made here to the equations of motion given in Section 8.2.2 which analyse wind loads on bridge decks.

Assuming that the vertical deflection, ξ, and the angular rotation, α, of the bridge deck are proportional to $e^{i\omega t}$, the solution obtained will, in general, be of the form $\omega = \omega_1 + i\omega_2$, and will therefore represent either a decaying ($\omega_2 > 0$) or a divergent ($\omega_2 < 0$) oscillation. The critical flutter wind velocity U_c is found for the value K_c of K where the solution is purely imaginary ($\omega = \omega_1$, $\omega_2 = 0$), see equation (8.4.5):

$$U_c = \frac{b\omega}{K_c} \tag{D.1}$$

The oscillation frequency n in hertz is equal to $\omega/(2\pi)$. This procedure has been described thoroughly by Simiu and Scanlan (1986) for the case in which H_4^* and A_4^* are both equal to 0. The expressions given below include all the aerodynamic derivatives. Larsen (1995) has also described the solution of flutter equations including the H_4^* and A_4^* terms. The printing errors in Larsen (1995) have been corrected in the formulas presented here.

Inserting the harmonic functions of ξ and α in equations (8.2.14), (8.2.15), (8.2.16) and (8.2.17), and assuming that the wind load due to air turbulence can be neglected, gives the following two equations:

$$\left[-\Omega^2 + 2i\zeta_\xi\Omega + 1 - \frac{\Omega^2}{2\gamma_m}(H_4^* + iH_1^*)\right]\frac{\xi_c}{b} - \left[\frac{C_\xi\Omega^2}{2\gamma_m}(H_3^* + iH_2^*)\right]\alpha_c = 0 \tag{D.2}$$

$$\left[-\frac{C_\alpha\Omega^2}{2\gamma_I}(A_4^* + iA_1^*)\right]\frac{\xi_c}{b} + \left[-\Omega^2 + 2i\zeta_\alpha\gamma_\omega\Omega + \gamma_\omega^2 - \frac{\Omega^2}{2\gamma_I}(A_3^* + iA_2^*)\right]\alpha_c = 0 \tag{D.3}$$

where

$$\Omega = \omega/\omega_\xi \tag{D.4}$$

$$\gamma_\omega = \omega_\alpha/\omega_\xi \qquad \gamma_m = m_e/(\rho b^2) \qquad \gamma_I = I_e/(\rho b^4) \tag{D.5}$$

and ξ_c and α_c are complex deflection amplitudes of ξ and α, respectively. In accordance with the four F-functions introduced in equation (8.2.6) and (8.2.7), the eight aerodynamic derivatives are grouped in pairs as follows:

$$H_4^* + iH_1^* \qquad H_3^* + iH_2^* \qquad A_4^* + iA_1^* \qquad A_3^* + iA_2^* \tag{D.6}$$

Setting the determinant of the coefficient matrix for equations (D.2) and (D.3) equal to zero and separating the real and imaginary parts gives:

$$R_4\Omega^4 + R_3\Omega^3 + R_2\Omega^2 + R_1\Omega + \gamma_\omega^2 = 0 \tag{D.7}$$

$$I_3\Omega^3 + I_2\Omega^2 + I_1\Omega + [2\zeta_\xi\gamma_\omega^2 + 2\zeta_\alpha\gamma_\omega] = 0 \tag{D.8}$$

where the coefficients R_i, $I_j (i = 1 \ldots 4,\ j = 1 \ldots 3)$ are given by

$$R_1 = 0 \tag{D.9}$$

$$R_2 = -\gamma_\omega^2 - 4\zeta_\alpha\zeta_\xi\gamma_\omega - 1 - A_3^*/(2\gamma_I) - \gamma_\omega^2 H_4^*/(2\gamma_m) \tag{D.10}$$

$$R_3 = \zeta_\alpha\gamma_\omega H_1^*/\gamma_m + \zeta_\xi A_2^*/\gamma_I \tag{D.11}$$

$$R_4 = 1 + H_4^*/(2\gamma_m) + A_3^*/(2\gamma_I) + (C_\xi C_\alpha A_1^* H_2^* - A_2^* H_1^* + H_4^* A_3^* - C_\xi C_\alpha A_4^* H_3^*)/(4\gamma_m\gamma_I) \tag{D.12}$$

$$I_1 = -\gamma_\omega^2 H_1^*/(2\gamma_m) - A_2^*/(2\gamma_I) \tag{D.13}$$

$$I_2 = -2\zeta_\alpha\gamma_\omega - 2\zeta_\xi - \zeta_\alpha\gamma_\omega H_4^*/\gamma_m - \zeta_\xi A_3^*/\gamma_I \tag{D.14}$$

$$I_3 = H_1^*/(2\gamma_m) + A_2^*/(2\gamma_I) + (H_4^* A_2^* + H_1^* A_3^* - C_\xi C_\alpha H_3^* A_1^* - C_\xi C_\alpha H_2^* A_4^*)/(4\gamma_m\gamma_I) \tag{D.15}$$

The solution of the flutter determinant is found by plotting curves corresponding to the roots of the real and imaginary parts of the flutter determinant as a function of the reduced velocity $U/(nb)$. The intersection point $(U_c/(n_c b), \Omega_c)$ between the real and imaginary root curves with the lowest value of U_c defines the critical flutter wind velocity, see equation (D.16) below.

Absolute critical flutter-vibration amplitudes ξ_0 and α_0 may have any value. However, the ratio $b\alpha_0/\xi_0$ and the phase angle between the vertical and angular deflection can be determined using the flutter equations.

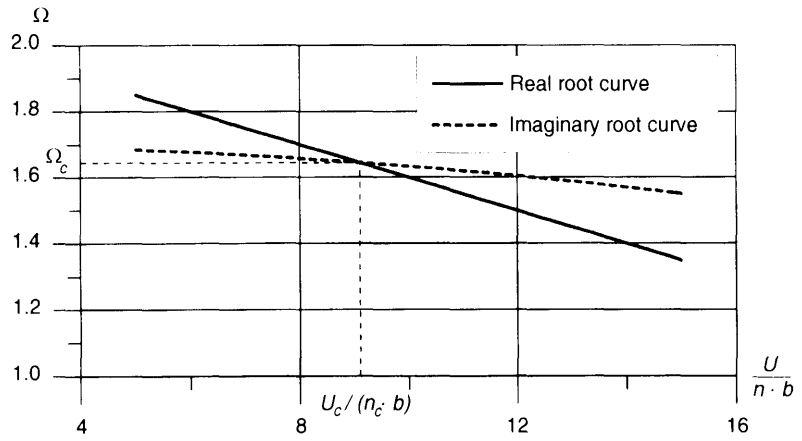

Fig. D.1 *Determination of critical flutter wind velocities from intersection of root curves.*

Flutter wind velocities

The reduced critical flutter wind velocity, $U_c/(n_\xi b)$, is equal to (see equations (D.1) and (D.4))

$$\frac{U_c}{n_\xi b} = \frac{U_c}{n_c b}\Omega_c \tag{D.16}$$

where $U_c/(n_c b)$ and Ω_c are determined as described above. The reduced critical flutter wind velocity depends on the aerodynamic derivatives, on the damping ratios ζ_ξ and ζ_α and on the non-dimensional frequency ratio γ_ω, mass ratio γ_m and mass moment of inertia ratio γ_I defined in equation (D.5).

References

Armitt, J. (1976) *Wind Structures. Lecture Series 89, Wind Effects on Buildings and Structures*. Von Kármán Institute for Fluid Dynamics, Rhode-Saint-Genèse.

Basu, R.I. (1983) "Across-wind Response of Slender Structures of Circular Cross-Section to Atmospheric Turbulence". *PhD Thesis*, BLWT-3-1983, The University of Western Ontario, London, Ontario, Canada.

Batchelor, G.K. (1953) *The Theory of Homogeneous Turbulence*. Cambridge University Press, London.

Brancaleoni, F. (1992) "The construction phase and its aerodynamic issues". *Aerodynamics of Large Bridges*. Larsen, A. (ed). Balkema, Rotterdam, pp. 147–158.

Businger, J.A. (1974) "Aerodynamic of vegetated surfaces". Chapter 10 of : *Heat and Mass Transfer in the Biosphere, Vol. I, Transfer Processes in the Plant Environment*. Scripton Book Co., Washington, DC, pp. 139–165.

Cartwright, D.E. and Longuet-Higgins, M.S. (1956) *The Statistical Distribution of the Maxima of a Random Function*. Royal Society, London.

Ciesielski, R., Gaczek, M. and Kawecki, J. (1992) "Observation results of cross-wind response of towers and steel chimneys". *Journal of Wind Engineering and Industrial Aerodynamics*, **41–44**, 2205–2211.

Cochran, L.S. and Cermak, J.E. (1992) "Full- and model-scale cladding pressures on the Texas Tech University experimental building". *Journal of Wind Engineering and Industrial Aerodynamics*, **41–44**, 1589–1600.

Cook, N.J. (1985) *The Designer's Guide to Wind Loading of Building Structures, Part 1*. Building Research Establishment, Butterworths.

Cook, N.J. (1990) *The Designer's Guide to Wind Loading of Building Structures, Part 2 Static Structures*. Building Research Establishment, Butterworths.

Counihan, J. (1975) "Adiabatic atmospheric boundary layers: a review and analysis of data from the period 1880–1972" . *Atmospheric Environment*, **9**, 871–905.

Courtney, M. and Troen, I. (1990) "Wind speed spectrum from one year of continuous 8 Hz measurements". *Ninth symposium on Turbulence and Diffusion*. Jensen, N.O. *et al.* (eds). American Meterological Society, New York, pp. 301–304.

Dalgliesh, W.A., Wright, W. and Schriever, W.R. (1967) "Wind pressure measurements on a full-scale high-rise office building". *Proceedings of the Second International Conference on Wind Effects on Buildings and Structures*, Vol. 1, Ottawa.

Daly, A.F. (1986) "Evaluation of methods of predicting the across-wind response of chimneys". *CICIND report*, **2**.

Dansk Standard DS 410 (1983) *Loads for the Design of Structures*. Translation edition, Teknisk Forlag, Copenhagen, Denmark.

Davenport, A.G. (1962) "The response of slender line-like structures to a gusty wind". *Proceedings of the Institution of Civil Engineers*, **23**, 389–408.

Davenport, A.G. (1967) "Gust loading factors". *Journal of the Structural Division, ASCE*, **93**, 11–34.

Davenport, A.G. (1977) "The prediction of the response of structures to gusty wind". *Safety of Structures under Dynamic Loading*, Holand, Kavlie, Moe and Sigbjörnsson (eds.), Tapir, Trondheim, pp. 257–284.

Davenport, A.G. (1982) "The reliability and synthesis of aerodynamic and meteorological data for wind loading". Seminar on Structural Aerodynamics, Institut Technique du Bâtiment et des Travaux Publics (ITBTP), St-Remy-Les-Chevreuse, France, April 20–22.

Davenport, A.G., King, J.P.C. and Larose, G.L. (1992) "Taut strip model tests". *Aerodynamics of Large Bridges*. Larsen, A. (ed). Balkema, Rotterdam, pp. 113–124.

Dyrbye, C. and Hansen, S.O. (1988) "Calculation of joint acceptance function for line-like structures". *Journal of Wind Engineering and Industrial Aerodynamics*, **31**, 351–353.

ESDU 74031 (1974) *Characteristics of atmospheric turbulence near the ground. Part II: single point data for strong winds (neutral atmosphere)*. Engineering Sciences Data Unit, London.

ESDU 85020 (1985) *Characteristics of atmospheric turbulence near the ground. Part II: single point data for strong winds (neutral atmosphere)*. Engineering Sciences Data Unit, London.

ESDU 86010 (1986) *Characteristics of atmospheric turbulence near the ground. Part III: Variations in space and time for strong winds (neutral atmosphere)*. Engineering Sciences Data Unit, London.

Eurocode 1 (1995) "Basis of design and actions on structures–Part 2-4: Actions on structures–Wind actions". *European Prestandard* ENV 1991-2-4.

Eurocode 3 (1992) "Design of steel structures". *European Prestandard* ENV 1993-1-1.

Feng, C.C. (1968) "The measurement of vortex induced effects in flow past stationary and oscillating circular and D-section cylinders", *MSc Thesis*, University of British Columbia, Canada.

Fortak, H. (1982) *Meteorologie*. Dietrich Reimer Verlag, Berlin, Germany.

Frandsen, S. (1979) *RISØ kontraktrapport : 'Tværsvingninger af stålskorstene. Feltmålinger*. Roskilde (in Danish).

Gartshore, I.S. (1973) "The effects of freestream turbulence on the drag of rectangular two dimensional prism". University of Western Ontario, London, Ontario, Canada.

Gerstoft, P. (1986) "An assessment of wind loading on tower shaped structures". PhD Thesis, Department of Structural Engineering, Technical University of Denmark, Report R 213.

Gerstoft, P. and Hansen, S.O. (1987) "A new tubing system for the measurement of fluctuating pressures". *Journal of Wind Engineering and Industrial Aerodynamics*, **25**, 335–354.

Gomes, L. and Vickery, B.J. (1978) "Extreme wind speeds in mixed climates". *Journal of Industrial Aerodynamics*, **2**, 331–344.

Hansen, S.O. (1981) "Cross-wind vibrations of a 130 m tapered concrete chimney". *Journal of Wind Engineering and Industrial Aerodynamics*, **8**, 145–155.

Hansen, S.O. and Krenk, S. (1996) "Dynamic along-wind response of simple structures". Submitted for publication in *Journal of Engineering Mechanics ASCE*.

Harris, R.I. (1970) "The nature of the wind". *Seminar on Modern Design of Wind-Sensitive Structures, 1970*. Construction Industry Research & Information, CIRIA, London, pp. 29–55.

Harris, R.I. (1990) "Some further thoughts on the spectrum of gustiness in strong winds". *Journal of Wind Engineering and Industrial Aerodynamics*, **33**, 461–477.

Harris, R.I. and Deaves, D.M. (1980) "The structure of strong winds". *Wind Engineering in the Eighties: Proceedings of the CIRIA Conference held on 12–13 November 1980.* London, Construction Industry Research and Information Association Paper 4.

Hjorth-Hansen, E. (1992) "Section model tests". *Aerodynamics of Large Bridges.* Larsen, A. (ed). Balkema, Rotterdam, pp. 95–112.

Hjorth-Hansen, E. (1993) "Fluctuating drag, lift and overturning moment for a line-like structure predicted (primarily) from static, mean loads", Department of Structural Engineering, University of Trondheim, Norway.

Højstrup, J., Larsen, S.E. and Madsen, P.H. (1990) "Power spectra of horizontal wind components in the neutral atmospheric surface boundary layer". *Proceedings of the Ninth Symposium on Turbulence and Diffusion, Risø, Roskilde, Denmark.*

Holmes, J.D. (1995) "Equivalent time averaging in wind engineering". *Proceedings of the Ninth International Conference on Wind Engineering, New Delhi, January*, pp. 1849–1858.

Jakobsen, J.B. (1995) "Fluctuating wind load and response of a line-like engineering structure with emphasis on motion-induced wind forces". *PhD Thesis*, Department of Structural Engineering, the Norwegian Institute of Technology, University of Trondheim, Norway.

Jain, A., Jones, N.P. and Scanlan, R.H. (1995) "Fully-coupled buffeting analysis of long-span bridges". *Proceedings of the Ninth International Conference on Wind Engineering, New Delhi, January*, pp. 962–971.

Jensen, M. (1958) "The model law for phenomena in the natural wind", Ingeniøren, International Edition, **2**, 121–128.

Jensen, M. (1959) *Aerodynamik i den Naturlige Vind* (in Danish) Teknisk Forlag, Copenhagen.

Jensen, N.O. (1985) "Luftens bevægelser". Chapter 3 in: *Luftforurening—en introduktion.* Teknisk Forlag, Copenhagen (in Danish).

Jensen, M. and Franck, N. (1965) *Model-Scale Tests in Turbulent Wind.* The Danish Technical Press, Copenhagen.

Jensen, M. and Franck, N. (1970) *The Climate of Strong Winds in Denmark.* Danish Technical Press, Copenhagen.

Jensen, G. and Petersen, A. (1994) "Erection of suspension bridges". *Proceedings of the International Conference on Cable-Stayed and Suspension Bridges, Deauville, France*, **2**, 351–362.

Jones, R.T. (1939) "The unsteady lift of a wing of finite aspect ratio". *Report No. 681*, Langley Memorial Aeronautical Laboratory, National Advisory Committee for Aeronautics, Langley Field, VA., June.

Joukowski, N. (1916) *Aérodynamique.* Paris.

Kaimal, J.C., Wyngaard, J.C., Izumi, Y. and Coté, O.R. (1972) "Spectral characteristics of surface-layer turbulence". *Journal of the Royal Meteorological Society*, **98**, 563–589.

Krenk, S. (1995) "Wind field coherence and dynamic wind forces". *Symposium on the Advances in Nonlinear Stochastic Mechanics.* Naess and Krenk (eds.), Kluwer, Dordrecht.

Kristensen, L. and Jensen, N.O. (1979) "Lateral coherence in isotropic turbulence and in the natural wind". *Boundary Layer Meteorology*, **17**, 353–373.

Larose, G.L. (1992) "The response of a suspension bridge deck to turbulent wind: the taut strip model approach". The University of Western Ontario, London, Ontario, Canada, March.

Larsen, A. (1995) "Prediction of aeroelastic stability of suspension bridges during erection". *Proceedings of the Ninth International Conference on Wind Engineering, New Delhi, January*, pp. 917–927.

Larsen, A. and Jacobsen, S. (1992) "Aerodynamic design of the Great Belt East Bridge". *Aerodynamics of Large Bridges*. Larsen, A. (ed). Balkema, Rotterdam, pp. 269–283.

Lawson, T.V. (1980) *Wind Effects on Buildings, Vol. 1, Design Applications*. Applied Science Publishers, Essex.

Lawson, T.V. (1980) *Wind Effects on Buildings, Vol. 2, Statistics and Meteorology*. Applied Science Publishers, Essex.

Lemelin, D.R., Surry, D. and Davenport, A.G. (1988) "Simple approximations for wind speed-up over hills". *Journal of Wind Engineering and Industrial Aerodynamics*, **28**, 117–127.

Liepmann, H.W. (1952) "On the application of statistical concepts to the buffeting problem". *Journal of Aeronautical Science*, **19**, 793–800.

Madsen, H.O., Krenk, S. and Lind, N.C. (1986) *Methods of Structural Safety*. Prentice-Hall, Englewood Cliffs, NJ.

Mahrenholtz, O. and Bardowicks, H. (1979) "Aeroplastic problems at masts and chimneys", *Journal of Industrial Aerodynamics*, **4**, 261–272.

Mann, J. (1994) "The spatial structure of neutral atmospheric surface-layer turbulence". *Journal of Fluid Mechanics*, **273**, 141–168.

Mann, J. and Krenk, S. (1994) "Fourier simulation of a non-isotropic wind field model". *Structural Safety and Reliability*. Schueller, Shinozuka and Yao (eds.), Balkema, Rotterdam, pp. 1669–1674.

Melbourne, W.H. (1975) "Probability distributions of response of BHP house to wind action and model comparisons". *Journal of Industrial Aerodynamics*, **1**, 167–175.

Melbourne, W.H. (1995) "Bluff body aerodynamics for wind engineering". *State of the Art Volume, Ninth International Conference on Wind Engineering, New Delhi, January*, pp. 47–64.

Nakamura, Y., Kaku, S. and Mizota, T. (1971) "Effects of mass ratio on the vortex excitation of a circular cylinder". *Proceedings of the 3rd International Conference on Wind Effects on Buildings and Structures, Tokyo, September*.

Newberry, C.W., Eaton, K.J. and Mayne, J.R. (1967) "The nature of gust loading on tall buildings". *Proceedings from the Second International Conference on Wind Effects on Buildings and Structures, Vol. 1, Ottawa*.

Newberry, C.W., Eaton, K.J. and Mayne, J.R. (1973) *Wind Loading on Tall Buildings—Further Results from Royex House*. Building Research Establishment, Current Paper 29/73. HMSO, November.

Ostenfeld, Chr., Frandsen, A.G. and Haas, G. (1970) "Motorway bridge across Lillebælt. Aerodynamic investigations for the superstructure of the bridge". *Bygningsstatiske Meddelelser*, Copenhagen, **41**, 79–98.

Petersen, E.L., Troen, I. and Frandsen, S. (1980) *Vindatlas for Danmark*. Forsøgsanlæg Risø, Danmark.

Plate, E.J. (1971) *Aerodynamic Characteristics of Atmospheric Boundary Layers*. U.S. Atomic Energy Commission, Washington, DC.

Reynolds, O. (1883) "An experimental investigation of the circumstances which determine whether the motion of water shall be direct or sinuous, and of the law of resistance in parallel channels". *Philosophical Transactions of the Royal Society* Papers II.

Roshko, A. (1961) "Experiments on the flow past a circular cylinder at very high Reynolds number". *Journal of Fluid Mechanics*, **10**, 345–356.

Ruscheweyh, H. (1982) *Dynamische Windwirkung an Bauwerken*. Bauverlag GmbH, Wiesbaden und Berlin.

Ruscheweyh, H. and Sedlacek, G. (1988) "Crosswind vibrations of steel stacks — critical comparison between some recently proposed codes". *Journal of Wind Engineering and Industrial Aerodynamics*, **30**, 173–183.

Scanlan, R.H. (1992) "Wind dynamics of long-span bridges". *Aerodynamics of Large Bridges*. Larsen, A. (ed), Balkema, Rotterdam, pp. 47–57.

Schmidt, L.V. (1965) "Measurements of fluctuating air loads on a circular cylinder". *Journal of Aircraft*, **2**, 49.

Scruton, C. and Rogers, E.W.E. (1971) "Steady and unsteady wind loading of buildings and structures". *Philosophical Transactions of the Royal Society*, **A269**, 353–383.

Sears, W.R. (1941) "Some aspects of non-stationary airfoil theory and its practical applications". *Journal of Aeronautical Science*, **8**, 104–108.

Selberg, A. and Hjorth-Hansen, E. (1966) "The fate of flat plate aerodynamics in the world of bridge decks". *Proceedings of the Theodorsen Colloquium*, Persen, L.N. (ed.), Det Kongelige Norske Videnskapers Selskap.

Sigbjörnsson, R. (1974) "On the theory of structural vibrations due to natural wind". Department of Structural Engineering, Technical University of Denmark, Report R 59.

Sill, B.L., Cook, N.J. and Fang, C. (1992) "The Aylesbury comparative experiment: a final report". *Journal of Wind Engineering and Industrial Aerodynamics*, **41–44**, 1553–1564.

Simiu, E. and Scanlan, R.H. (1986) *Wind Effects on Structures. An Introduction to Wind Engineering. Second edition*. Wiley, New York.

Smith, F.T. (1989) "Linear instability of the wake behind a flat plate placed parallel to a uniform stream". *Journal of Fluid Mechanics*, **208**, 67–81.

Smith, J.W. (1988) *Vibrations of Structures. Applications in Civil Engineering Design*. Chapman and Hall, London.

Solari, G. (1993a) "Gust buffeting I : peak wind velocity and equivalent pressure". *Journal of Structural Engineering*, **119**, 365–382.

Solari G. (1993b) "Gust buffeting II : dynamic alongwind response". *Journal of Structural Engineering*, **119**, 383–398.

Szechenyi, E. and Loiseau, H. (1975) "Portance instationnaires sur un cylindre vibrant dans un écoulement supercritique". *Recherche Aerospatiale*, **1**.

Theodorsen, Th. (1934) "General theory of aerodynamic instability and the mechanism of flutter". *NACA Report No. 496*, Washington DC.

Tieleman, H.W. (1995) "Simulation of surface winds for assessment of extreme wind loads on roofs". *Proceedings of the Ninth International Conference on Wind Engineering, New Delhi, January*, pp. 1162–1169.

Troen, I. and Petersen, E.L. (1989) *European wind Atlas*, Risø, National Laboratory, Denmark.

Van der Hoven, I. (1957) "Power spectrum of horizontal wind speed in the frequency range from 0.0007 to 900 cycles per hour". *Journal of Meteorology*, **14**, 160–164.

Vickery, B.J. (1978) "A model for the prediction of the response of chimneys to vortex shedding". *Proceedings of the 3th International Chimney Design Symposium, Munich.*

Vickery, B.J. (1981) "Across-wind buffeting in a group of four in-line model chimneys" *Journal of Wind Engineering and Industrial Aerodynamics*, **8**, 177–193.

Vickery, B.J. (1995) "The response of chimneys and tower-like structures to wind loading". *State of the Art Volume, Ninth International Conference on Wind Engineering, New Delhi, January*, pp. 205–233.

Vickery, B.J. and Basu, R.I. (1983) "Across-wind vibrations of structures of circular cross-section. Part 1. Development of a mathematical model for two-dimensional conditions". *Journal of Wind Engineering and Industrial Aerodynamics*, **12**, 49–73.

Vickery, B.J. and Basu, R.I. (1984) "Response of reinforced concrete chimneys to vortex shedding". *Engineering Structures*, **6**, 324–333.

Vickery, B.J. and Clark, A.W. (1972) "Lift or across-wind response of tapered stacks". *Journal of the Structural Division, ASCE*, **98**, 1–20.

Vickery, B.J. and Daly, A. (1984) "Wind-tunnel modelling as a means of predicting the response of chimneys to vortex shedding". *Engineering Structures*, **6**, 363–368.

von Kármán, T. (1948) "Progress in the statistical theory of turbulence", *Journal of Maritime Research*, **7**.

von Mises, R. (1945) *Theory of Flight*. Dover Press, New York.

Walshe, D.E.J. (1972) *Wind-Excited Oscillations of Structures*. National Physical Laboratory, London.

Walther, J.H. (1994) "Discrete vortex method for two-dimensional flow past bodies of arbitrary shape undergoing prescribed rotary and translational motion". *PhD Thesis*, Department of Fluid Mechanics, Danish Technical University.

Wooton, L.R. and Scruton, C. (1970) "Aerodynamic stability". *Seminar on Modern Design of Wind-Sensitive Structures, 1970*. Construction Industry Research and Information Association, CIRIA, London, pp. 65–81.

Yano, T. and Takahara, S. (1971) "Study on unsteady aerodynamic forces acting on an oscillating cylinder". *Proceedings of the 3th International Conference on Wind Effects on Buildings and Structures, Tokyo, September.*

Zdravkovich, M.M. (1981) "Review and classification of various aerodynamic and hydrodynamic means for suppressing vortex shedding". *Journal of Wind Engineering and Industrial Aerodynamics*, **7**, 145–189.